POLITECNICO DI MILANO
Physics Department
Doctoral Program in Physics
XXXII cycle

Cuprate high-T_c superconductors studied by polarization-resolved RIXS

Supervisor: Prof. Giacomo GHIRINGHELLI
Chair of the Doctoral Program: Prof. Marco FINAZZI

Doctoral Dissertation of:
Roberto Fumagalli

A. A. 2019-2020

Cuprate high-T_c superconductors studied by polarization-resolved RIXS

Roberto Fumagalli

January 24, 2020

to my family,
to Valentina

“Physics is like sex:
sure, it may give some practical results,
but that’s not why we do it.”

Richard P. Feynman

Abstract

This thesis work presents some of the results obtained on one- and two-dimensional cuprates with resonant inelastic X-ray scattering (RIXS) during my three years activity in the group held by Prof. G. Ghiringhelli of the Physics Department of the Politecnico di Milano (Italy).

In the last two decades the group has largely contributed in the development of this technique, especially in terms of realization of dedicated RIXS instrumentations. In particular, they designed three spectrometer: AXES (Advanced X-ray Emission Spectrometer) for the ID08 beamline at the ESRF - the European Synchrotron in Grenoble (France), which has been operational since 1995, and SAXES (Super-Advanced X-ray Emission Spectrometer), an evolution of AXES, installed in 2006 at the ADDRESS beamline at the Swiss Light Source (SLS) in Villigen (Switzerland). With the continuous improvements in their performances, accompanied by the need to improve the overall energy resolution, the group joined the ESRF staff for the realization of the first ultra high-resolution ERIXS (European-RIXS) spectrometer, which holds nowadays the world record of energy resolution with a combined (beamline + spectrometer) resolving power of 30,000 at the Cu L_3-edge.

Moreover, this activity has been followed by several achievements also from the scientific point of view that have been made possible thanks to the unprecedented performances offered by the dedicated RIXS end-stations available nowadays.

Here I will present some of the results achieved with the ERIXS spectrometer in the last three years on insulating and superconducting cuprates, especially focusing the attention on the possibility to perform polarization-resolved RIXS at the Cu L_3-edge.

RIXS is a synchrotron-based spectroscopy technique used to study the properties of correlated electrons systems such as cuprates, through the analysis of the elementary excitations probed by X-rays. In particular, the excitations accessible by RIXS carry information about the degrees of freedom which characterize the superconducting cuprates. In fact, with RIXS we can simultaneously study the energy, momentum and polarization of the electronic, magnetic and charge excitations of the CuO_2 planes. The latter are at the basis of the superconducting behavior and they represent the core of all the copper-based compounds. In fact, cuprates are layered materials characterized by a stacking of superconducting CuO_2 layers, consisting of Cu^{2+} ions alternated to O^{2-} ions, intercalated by so-called blocking layers that act as charge reservoirs.

Due to the strong electron-electron interaction typical of the transition metal oxides, the parent compounds of the high-T_c superconducting cuprates are characterized by a strong antiferromagnetic (AFM) correlation which persists upon doping. As a consequence, undoped cuprates are usually described as Mott insulators where the valence *d* electrons are localized on the Cu atomic sites. Here, the Cu^{2+} ions are in a $3d^9$ electronic configuration with the unpaired spin $1/2$ per Cu site coupled via superexchange (which is exceptionally high in cuprates), that is mediated by the surrounding oxygen ions. The net result of this interaction is reflected in the two-dimensional (2D) nature of the electronic and magnetic physical properties.

A system can become a superconductor with an increasing of the critical temperature by adding holes or electrons in the CuO_2 planes of insulating parent compound: in this way T_c has a maximum in correspondence of the so-called optimal doping. Superconductivity in cuprates is usually achieved by altering the number of mobile carriers (holes or electrons) in the parent compounds via chemical substitution or by varying the oxygen content. The transition from the insulating to the superconducting regime is triggered by the dopant charges in the CuO_2 planes which alter the local physical properties. In this context, long-range orders are rapidly destroyed giving way to new intriguing scenarios.

High-T_c superconductivity is a fascinating phenomenon, which still needs to be understood. In the last thirty or more years, physicists deployed all sorts of experimental and theoretical efforts to shed light on the mechanism behind it. In recent years, RIXS contributed enormously to the debate by providing information complementary to existing techniques (including inelastic neutron scattering, resonant X-ray diffraction, angle-resolved photoemission, etc.). RIXS is a spectroscopic technique capable of probing orbital, charge and spin excitations and the possibility of measuring the polarization of scattered photons gives access to further crucial information that is usually unavailable in polarization-integrated RIXS spectra, such as the interplay between charge, spin and orbital excitations.

The ability to disentangle the spectral features of complex RIXS spectra is crucial to pinpoint the various contributions to the lattice, magnetic and electronic dynamics at play in high-T_c systems. Nowadays, only at the ID32 beamline of the ESRF it is possible to perform polarization resolved RIXS measurements which have played a crucial role in many cases, such as in the confirmation of the charge nature of the ordering discovered in the overdoped region of $(Bi,Pb)_2(Sr,La)_2CuO_{6+\delta}$, in the assignment to spin excitations the enhanced dynamic response at the charge order vector of $Nd_{2-x}Ce_xCuO_4$ and finally in the confirmation of the charge nature of the zone-center fast-dispersing excitations in $La_{2-x}Ce_xCuO_4$. The polarization analysis has been applied also to systems other than cuprates, that is the case of $CeRh_2Si_2$. All these works will be discussed as an example of the potentialities offered by polarization-resolved RIXS.

The main objective of this thesis work regards the study of insulating and superconducting layered cuprates, using resonant inelastic X-rays scattering technique, with special emphasis on the possibility to infer about the polarization state of the scattered photons. With regard to this, we present a systematic RIXS study of orbital, magnetic and vibrational excitations in a prototypical cuprate system belonging to the “123” family ($NdBa_2Cu_3O_{7-\delta}$). We measured Cu L_3-edge RIXS spectra of undoped, underdoped and optimally doped $NdBa_2Cu_3O_{7-\delta}$ thin films at different in-plane momenta with both perpendicular and parallel (with respect to the scattering plane) polarization of the incident X-rays. The experimental dataset allows to unequivocally determine the polarization dependence and the evolution of electronic *dd* excitations as a function of doping and scattering geometry. Moreover, we show that the polarimetric device, a polarization-selective optical element based on a multilayer, can provide crucial insights to disentangle the different contributions in the low energy scale due to spin and phonon excitations. Finally, we discuss the interpretation of the experimental data within the framework of the single-ion model and in terms of Stokes parameters. Our results will be of interest to the large scientific community interested in correlated electron systems because they provide important insights into the interpretation of polarization resolved RIXS data of cuprates.

Besides the polarimetric study of the excitations probed by RIXS in cuprates, we present a detailed study of the dispersing behavior of orbital excitations in quasi-one dimensional (1D) systems. It is known that in correlated oxides orbital excitations tend to have a localized character and are usually described by orbital and spin quantum numbers in a symmetry adapted atomic picture: thus orbital excitations do not disperse, irrespective of their spin character. However, theory predicts that at low dimensionality, *dd* excitations can split their orbital and spin components, giving rise to complex dispersion in momentum space. Indeed, orbital excitations with sizable dispersion, called ‘orbitons’ due to their collective character, were observed with RIXS on quasi-1D cuprates.

Our results on the quasi-1D spin = $1/2$ AFM Heisenberg chain Ca_2CuO_3 are consistent with those of Sr_2CuO_3 but they are analyzed with an improved theoretical model. In particular, we verify how the Hund’s exchange affects the observed spectra and whether a predicted interaction between spinon and orbiton can be observed.

Moreover, our RIXS dataset on the insulating 2D infinite layer $CaCuO_2$ suggests that *dd* excitations may disperse also in 2D systems. Unfortunately, the theoretical model adopted for the interpretation of the dispersing orbital excitations in quasi-1D cuprate cannot takes into account the the sizable dispersion measured in the 2D $CaCuO_2$. It is worth mentioning that $CaCuO_2$, differently from all the other well known 2D cuprates, it is characterized by the absence of apical oxygens. It has been demonstrated that the apical oxygens largely influence the possibility of valence electrons to ‘jump’ from site to site in the CuO_2 planes. This affects the magnetic spectra of the insulating parent compounds, where the in-plane hopping is larger in compounds where there are no apical oxygens, that is the case of $CaCuO_2$. Regarding the dispersing behavior of orbital excitations in this material, and without a theoretical model that explain this phenomenon, we believe that the role of the apical oxygens could be relevant also in the orbital excitations physics.

Finally, motivated by the recent synthesis of the high temperature superconducting cuprate with putative $d_{3z^2-r^2}$ ground state symmetry $Ba_2CuO_{3+\delta}$ (BCO), we investigated its electronic structure by means of X-ray absorption (XAS) and RIXS techniques on a polycrystalline sample. We show that the XAS profile of BCO is characterized by two peaks that we ascribe to inequivalent Cu sites, a scenario that is reminiscent of the double Cu sites in $YBa_2Cu_3O_{6+\delta}$. By tuning the incident X-rays energy to the peak ascribable to the Cu ions in the planes, the RIXS response features a single, sharp peak associated to crystal-field excitations, and argue that these observations are incompatible with the previously proposed crystal structure of BCO. We thus propose an alternative structure, which accounts for our results and previous powder X-ray diffractions experiments. Based on this, we analyze the low-energy spectral range of the RIXS spectra and estimate the magnitude of the magnetic interactions in BCO.

Contents

List of Tables

List of Figures

Introduction

The aim of this thesis is to show how the recent developments of the resonant inelastic X-ray scattering (from now on RIXS) technique in the soft X-ray energy range have made possible the realization of a novel kind of experiments. In particular, we will show that RIXS can be used to probe several degrees of freedom in insulating and superconducting cuprates, such as spin, charge and orbital. The improvements in the soft RIXS instrumentation (beamline optics and spectrometers) at the third generation synchrotron facilities allow to reach unprecedented performances, especially in terms of energy resolution and photon flux. After the successful era driven by the AXES [1, 2] and SAXES [3] spectrometers, most of the synchrotron facilities have or are realizing high quality RIXS end-stations.

RIXS is a synchrotron-based spectroscopy technique used to study the properties of correlated electrons systems such as cuprates, through the analysis of elementary excitations. RIXS is based on a second order process that makes it a "photon *in*-photon *out*" technique [4]. The excitations accessible by RIXS span from phonons and magnons, at the meV energy scale, to orbital (or *dd*) and charge transfer excitations at few eV. What makes RIXS an extremely powerful technique is the possibility to simultaneously study all these excitations. The incident photon energy is chosen such that it corresponds to the binding energy of one element in the compound, in our case the the Cu L_3-edge ($\simeq 931\,$electronvolt), greatly enhancing the scattering cross-section.

In the specific case of cuprates, the incident X-ray energy is tuned to match exactly the absorption edge promoting a $2p$ electron into a bound state just above the Fermi level. At this stage the system is in an unstable state: although the de-excitation is mostly through Auger processes, the radiative decay of the core hole produces the emission of an X-ray photon that carries information about the excitation left in the system. The whole process can be thus viewed as the inelastic scattering of X-ray photons, *i.e.* an energy loss spectroscopy holding several similarities to Raman and electron energy loss spectroscopies. Therefore, by analyzing the inelastic features one can infer about the energy, momentum dependence, symmetry and physical origin of the excitations left in the sample. In particular, the excitation in the final state is characterized by an energy $E = \hbar\omega_{\mathrm{i}} - \hbar\omega_{\mathrm{o}}$, which is defined as the energy difference between the incident and emitted photon. Moreover, the final state of the RIXS process has an intrinsic transferred momentum, mainly dictated by the adopted scattering geometry, defined as $\hbar\mathbf{q} = \hbar\mathbf{k}_{\mathrm{i}} - \hbar\mathbf{k}_{\mathrm{o}}$. Often, in cuprates the relevant transferred momentum is only the projection onto the CuO_2 *ab* plane $\mathbf{q}_{\parallel}$ because of the intrinsic two-dimensional (2D) nature of these materials. RIXS preserves the neutrality of the measured system since during the scattering process there are no charges added or removed from the sample. Moreover, RIXS provides an element and chemical selectivity because of the incident photon energy is tuned to a specific absorption edge. RIXS even in the soft X-ray range does not require complicated cleaning procedures for the sample surface because the penetration depth of X-rays varies from 10 nm in case of soft X-rays to few micron in the hard X-rays energy range.

The recent development of this technique was particularly favored by the discovery done by Braicovich *et. al.* in 2010 [5], where they showed that using RIXS it is possible to measure the magnon dispersion at the Cu L_3-edge. This has been an important turning point because dispersion of magnons were traditionally studied using inelastic neutron scattering (INS) which typically requires large single crystal samples of several cm^3 in volume. With X-rays, instead, one can do experiments with very small samples. Finally, RIXS has $\mathbf{q}$-resolution: at the Cu L_3-edge the incident X-ray wavelength is $\lambda \approx 10\,\text{Å}$, value comparable with the typical inter-atomic distances. So that, a sizable portion of the first Brillouin zone can be investigated.

In this thesis work we have mainly performed RIXS measurements at the Cu L_3-edge in several insulating and superconducting cuprates. RIXS allows us to access electric-dipole forbidden transitions, such as the $3d \rightarrow 3d$ one, that involved the most relevant properties of these materials. Cuprates are classified as strongly correlated electron systems and show unusual electronic and magnetic properties. These systems cannot be described by using a one-particle theory because electrons are strongly influenced by the other ones and their collective motion is deeply correlated. Notably, CuO_2 layers exhibit an insulating antiferromagnetic (AFM) phase and, when chemically doped, a superconducting state below a specific critical temperature. Cuprates are also characterized by a very strong in-plane superexchange coupling that stabilizes a 2D AFM order. The interest in these superconducting materials has grown during last decades, especially due to their physical properties and to the possible future powerful technology applications. Since their discovery in 1986 [6] many progresses were done in order to understand the mechanisms beyond the high temperature superconductivity, but an exhaustive and complete explanation is still unknown [7]. The scenario is open to novel discoveries due to the development of theoretical models and new experimental setup.

In particular, in this work we have taken advantage from the possibility to perform the polarization analysis of the scattered X-rays. The aim is to show how the polarization state of the scattered photons can add crucial information in the understanding of the spectral features. The capability to carry out polarization-resolved RIXS measurements is available solely at the ID32 beamline at the ESRF - the European Synchrotron [8]. The ERIXS spectrometer, jointly designed by our group at the Politecnico di Milano and the ESRF staff, is equipped with a graded multilayer mirror which allows the determination of the degree of linear polarization of scattered photons while preserving the energy resolution of the spectrometer.

In Chapter 1 we will give a brief introduction on the materials object of this thesis, the copper-oxides high-T_c superconductors. In particular, we will describe the electronic, magnetic and crystal structure of cuprates highlighting their importance for the manifestation of high critical temperature superconductivity. In the last section of this Chapter, the phase diagram of cuprates will be presented underlying its richness and complexity.

Chapter 2 is dedicated to the description of RIXS. We start giving an overview about all the capabilities offered by this technique. Then we describe the scattering process and its implications in terms of conservations laws, which make possible the definition of the energy, momentum and even the polarization state of a specific excitation left in the system during the scattering process. We describe the main excitations probed by RIXS and the experimental setup of the ID32 beamline, which has been widely used during the three years of my PhD. We will give a brief description of the ERIXS spectrometer, whose main innovations regard the energy resolution (30 meV of combined bandwidth at the Cu L_3-edge) and the polarization analysis of the scattered beam which allows a better insight on the symmetry of the excited states. Other relevant characteristics are the possibilities to have a continuous regulation of the scattering angle and of the sample orientation which permits to investigate the reciprocal space. Moreover, ERIXS is characterized by a high luminosity due to the presence of a specific optical layout. Here we will stress the importance to achieve an energy resolution of ≈ 30 meV, giving some examples of works made possible solely thanks to such performances. That is the case, for example, of the first detection of the superconducting energy gap by RIXS, the systematic study of low-energy phonons and the discovery of charge density fluctuations characterized by an energy of few meV. In the last sections of this Chapter we give the theoretical background for the understanding of the polarization analysis, where we have adopted the approach based on the Stokes parameters and Poincaré sphere [9, 10] to interpret the polarization state of the light.

In Chapter 3 we present a systematic RIXS study of orbital, magnetic and vibrational excitations in a prototypical cuprate system ($NdBa_2Cu_3O_{7-\delta}$). We measured Cu L_3-edge RIXS spectra of undoped, underdoped and optimally doped $NdBa_2Cu_3O_{7-\delta}$ thin films at different in-plane momenta with both perpendicular and parallel (with respect to the scattering plane) polarization of the incident X-rays. The experimental dataset allows to unequivocally determine the polarization dependence and the evolution of *dd* excitations as a function of the scattering geometry and doping. Moreover, we show that the polarimeter can provide crucial insights to disentangle the different contributions in the low energy scale. Finally, we discuss the interpretation of the experimental data within the framework of the single-ion model [11] and in terms of Stokes parameters [9, 10].

Chapter 4 gives an overview of all the polarization-resolved RIXS measurements performed at the ID32 beamline of the ESRF, showing some of all the feasible and potential applications of polarization-resolved RIXS. Here we demonstrate how this kind of experiments allowed us to infer about the many and different mechanisms at play in the low energy scale of undoped and hole doped cuprates, such as charge order and magnetic excitations. Moreover, we show that in the case of electron doped cuprates the outgoing polarization analysis of the RIXS spectra has been also crucial for the assignment of a fast dispersing mode to a plasmonic excitation and for the existence of dynamic correlations at the charge-order wave vector which primarily involves spin-flip excitations. In the last section of this Chapter we report the systematic work done for the assignment, with unprecedented accuracy, of the crystal field excitations in a Ce-based compound.

In Chapter 5 we present a systematic high-resolution RIXS study at the Cu L_3-edge on the quasi-1D spin $= 1/2$ AFM Heisenberg chain Ca_2CuO_3 and on the insulating 2D infinite layer $CaCuO_2$. The idea behind this work is to investigate the dispersing behavior of orbital excitations as a function of the dimensionality. In correlated oxides electronic excitations tend to have localized character and are usually described by orbital and spin quantum numbers in a symmetry adapted atomic picture: usually *dd* (*i.e.* orbital) excitations do not disperse, irrespective of their spin character. On the contrary, pure spin excitations have collective nature: spin-waves (or magnons) display large energy dispersion *vs* momentum. Theory predicts that at low dimensionality *dd* excitations can split their orbital and spin components, giving rise to complex dispersion. Starting from the quasi-1D Ca_2CuO_3 (Section 5.1.4), besides the magnetic excitations, being well-described by the two-spinon continuum, we observe two dispersive orbital excitations, the $3d_{xy}$ and the $3d_{yz}$ orbitons. A quantitative comparison of the RIXS spectra, obtained with two distinct incident polarizations, with the theoretical model is performed. We show that a realistic spin-orbital model needs to contain a finite, but realistic, Hund's exchange $J_\mathrm{H} \approx 0.5$ eV. Differently from the 1D case, in 2D cuprates *dd* excitations do not usually show any sizeable energy dispersion *vs* momentum. On the contrary, pure spin excitations (or magnons) display large energy dispersion thanks their collective nature. However, our data on $CaCuO_2$ (Section 5.2.4) suggest that *dd* excitations disperse also in 2D systems. It turns out that the theory model based on the Hund's exchange used in the 1D case cannot account for the orbital excitation dispersion seen in the 2D $CaCuO_2$.

Finally, in Chapter 6, we discuss the first RIXS results obtained on a polycrystalline $Ba_2CuO_{3+\delta}$ sample. This novel high-T_c copper-based superconductor, supposedly isostructural to the well known $(La_{2-x},Ba_x)CuO_4$, has challenged the common belief about the $d_{x^2-y^2}$ symmetry of the ground state in the insulating parent compounds, which eventually gives rise to *d*-wave superconductivity upon doping [12]. It is well known that the electronic structure of cuprates is characterized by a ground state of predominant $d_{x^2-y^2}$ symmetry [13], due to the structural elongation of the CuO_6 octahedra. This fact that is widely accepted to be a key ingredient for *d*-wave superconductivity observed in these materials. On the contrary, it has been proposed that $Ba_2CuO_{3+\delta}$ is characterized by a $d_{3z^2-r^2}$ ground state due to a slightly compressive distortion of the CuO_6 octahedra. After the discovery of this new material, many theoretical models have been already proposed trying to explain the implication of a $d_{3z^2-r^2}$ ground state in the manifestation of superconductivity, also because it apparently undermines the role of the $d_{x^2-y^2}$ ground state. We decided to carry out RIXS at the Cu L_3 absorption edge to shed new light on the electronic and magnetic structure of this material. Unfortunately, a powder sample cannot allow a systematic study playing with the photons polarization and the scattering geometry. Nevertheless, we are able to extract useful information about the in-plane magnetic interaction and, surprisingly, on the crystal structure.

In this thesis I will present only some of the important results achieved by myself together with my group and collaborators among these years. Obviously, all the results presented in the following could not be achieved by one single person. However, all the experimental data discussed in this thesis, except few cases, have been taken by myself. Moreover, for the results reported in Chapter 3, 5 and 6, I have personally taken care of the data analysis, and in the specific case of Chapter 3, I have also calculated the RIXS cross-sections within the framework of the single-ion model which had a fundamental role in the understanding of the experimental data. Regarding Chapter 4, I contributed in different ways to the data analyses done by my collaborators and coworkers (except in the cases of Chapter 4.5 and Chapter 4.6). Finally, I had the chance to join many other experiments not discussed hereafter, whose results are somewhat enclosed in my list of publications reported at the end of this thesis work.

CHAPTER 1

Superconducting cuprates

In this first Chapter we will give a generic introduction about the historical importance of high critical temperature (T_c) superconductors in the field of condensed matter physics. We will describe the crystal structure together with the electronic and magnetic properties of high-T_c superconducting cuprates summarized by their impressively rich phase diagram. Finally, a brief introduction to their superconducting properties will be given.

Contents

1.1 High T_c superconductors

For 40 years, the interest in strongly correlated electrons systems, such as $3d$ transition metal oxides (TMOs), has increased because of the emergence of novel quantum ground states. These materials show many interesting phenomena, as for example high critical temperature (T_c) superconductivity in cuprates [6], colossal magnetoresistance in perovskite manganites [14] and multiferroicity [15]. These properties result from the strong electronic correlation that significantly affects the physics of these compounds. This leads to a variety of novel exotic properties, *i.e.* Mott insulators, broken symmetry orders, high-temperature superconductivity and metal-insulator transitions [16].

In this scenario, cuprate superconductors have played a big role attracting the attention of the entire scientific community since their discovery by J. G. Bednorz and K. A. Müller in 1986 (awardees of the Nobel Prize in 1987) [6], representing a breakthrough in condensed matter physics. One of the most fascinating properties of superconducting cuprates is that they show a critical transition temperature much higher than the one predicted by the BCS theory and measured in conventional superconductors where it could not exceed 30 K at the time [17]. J. G. Bednorz and K. A. Müller demonstrated that ceramic materials such as copper oxides, if chemically doped, can reach a critical temperatures well above the boiling point of liquid nitrogen (77 K), making high temperature (or “unconventional”) superconductors highly significant for possible technological applications, as liquid nitrogen is far less expensive than liquid helium, which is needed to cool conventional superconductors in order to achieve their superconducting state. The fact that the BCS theory can neither predict nor explain the high superconducting transition temperature of unconventional superconductors suggests that these materials are characterized by uncommon physical properties. For example, the mechanism beyond superconductivity in cuprates cannot be explained with the s-wave pairing mediated by the electron-phonon coupling that characterized conventional superconductors.

After the discovery of superconductivity in $La_{2-x}Ba_xCuO_4$, many other materials have been found to be superconductors. In Figure 1.1 we report a summary of the most important high-T_c superconductors (HTS) discovered in the last 40 years, together with their critical temperatures and their most common crystal structures. In specific conditions, such as under high pressure, the highest superconducting transition temperature has been measured in a mercury-based copper-oxide ($T_c = 165$ K), which is unfortunately still too low for possible technological applications. The interest in this new fascinating phenomenon brought the scientific community to discover other materials that display unconventional superconductivity, and among these the most important to mention are the layered iron-based superconductors.

The discovery of unconventional superconductors generated an enormous amount of scientific investigation: despite the countless experiments and theoretical models proposed in more than 30 years since their discovery, there

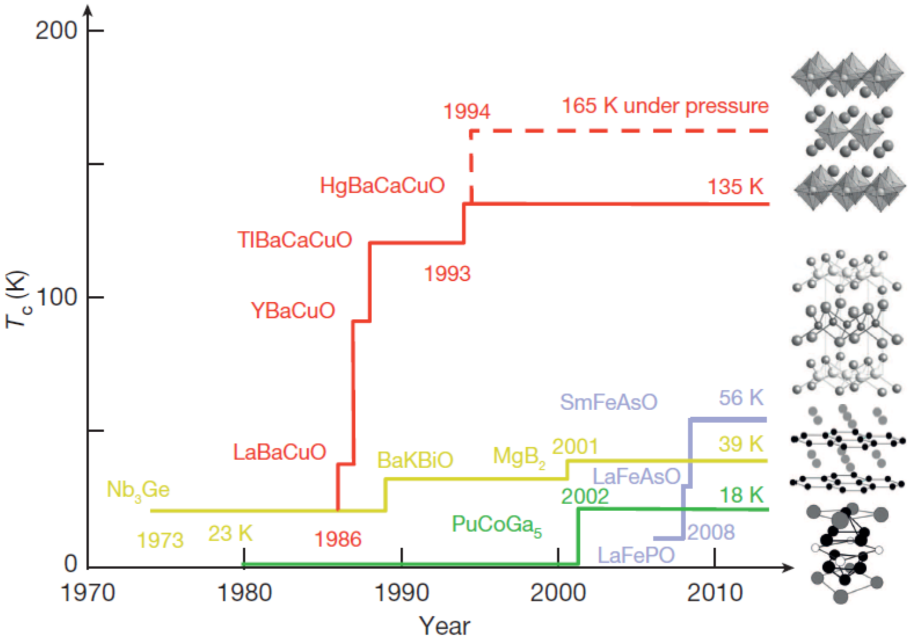

Figure 1.1: Superconducting transition temperatures versus year of discovery for different families of superconductors. On the right side the crystal structures of some of them is shown. Figure from Ref. [7].

is not yet a convincing and conclusive explanation of high-T_c superconductivity [7].

1.2 Superconducting cuprates

Copper-based superconductors belong to the 3d transition metal oxides family. They are layered materials characterized by CuO_2 layers, which play the major role for the superconducting properties, separated by spacer layers that generally differ from one compound to another. In the following we will summarize their crystal, electronic and superconducting properties.

1.2.1 Crystal structure

Most of the HTS cuprate families are characterized by having a two dimensional (2D) layered crystal structure made of CuO_2 planes, where superconductivity is induced. They are usually separated by the so-called "charge reservoir" layers: the interaction between these intermediate layers and the CuO_2 planes plays an important role in the physical properties of cuprates.

In fact, superconductivity is usually achieved in doped samples, that are obtained by chemical substitution (or oxygen stoichiometry) in the spacing layers.

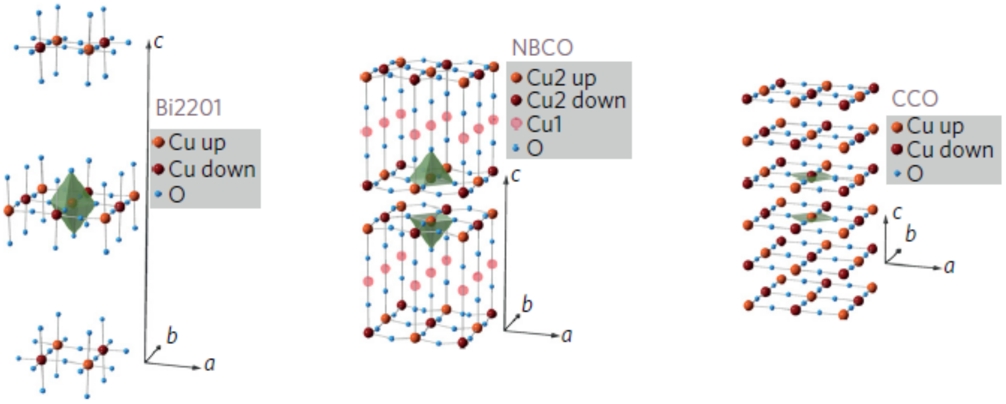

Figure 1.2: Partial representation of the crystal structures of some representative 2D cuprate families. Figure from Ref. [18].

In Figure 1.2 we report the partial schematic representation of the crystalline structures of some 2D cuprate families: the compounds reported here differ by the number of apical oxygens, which play an important role in the physics of HTS, as we will explain later. In particular, from the left to the right of Figure 1.2, we show the single-layer $Bi_2Sr_2CuO_{6+\delta}$ (Bi2201), the bilayer $NdBa_2Cu_3O_{7-\delta}$ (NBCO) and the infinite layer $CaCuO_2$ (CCO). As we can see, all these structures of square plaquettes are characterized by the common 2D CuO_2 planes divided by spacing layers which can contain different chemical elements. Usually, the copper ions in 2D layered cuprates are nominally divalent (Cu^{2+}) and are coordinated with four in-plane O^{2-} (in the case of filled $2p$ orbitals) ions which leads to the formation of squared plaquettes (see Figure 1.4). The presence of the out-of-plane apical oxygens is responsible for the creation of Cu-O polyhedra: in particular, one apical oxygen leads to the formation of a pyramid, while an octahedron is arranged by the presence of two apical oxygens. The typical in-plane Cu-O distance is of the order of 1.91-1.94 Å, whereas the distance between the apical oxygen and the CuO_2 planes can span in the range of 2.3-2.7 Å [19].

1.2.2 Electronic and magnetic properties

Regarding the electronic structure of HTS cuprates, in a pure ionic picture the copper ions (Cu^{2+}) in the CuO_2 planes are nominally in a $3d^9$ electronic configuration [20] with one unpaired electron in the $3d_{x^2-y^2}$ orbital [13]. For this reason, their electronic properties are generally described considering a one hole system with $d_{x^2-y^2}$ symmetry. The occupied $3d$ orbitals, depending on the symmetry group (which is in general tetragonal or orthorhombic) and on the ligands coordination are non-degenerate in energy. In fact, considering the crystal field model, the surrounding oxygens atoms break the pure spherical symmetry of the crystalline potential leading to a splitting of the $3d$ states.

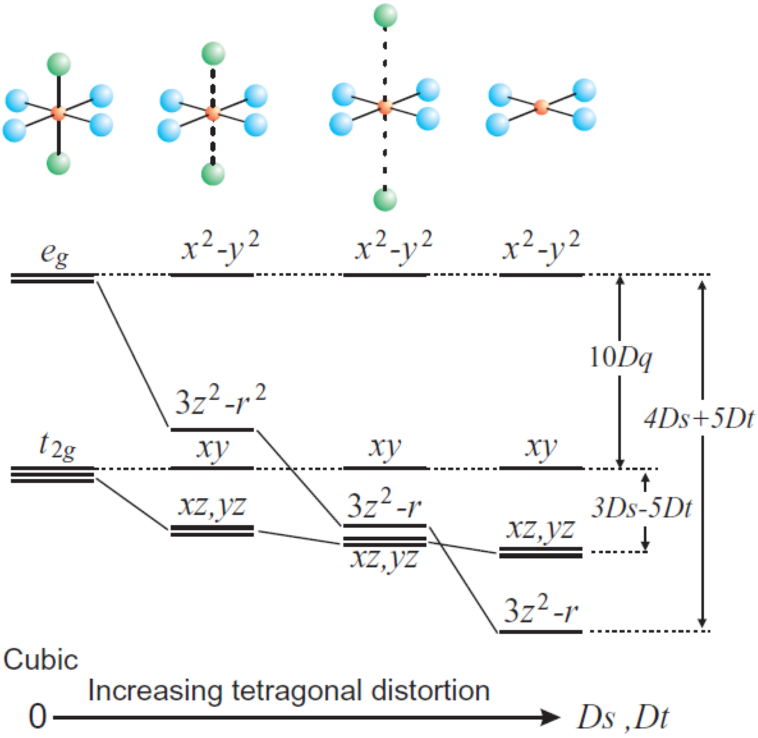

Figure 1.3: Illustration of the Cu $3d$ levels split by the crystal field and the energy level diagram for $3d$ orbitals in spherical, cubic and tetragonal symmetry. Figure from Ref. [11].

In Figure 1.3 we report the diagram of the energy level in the present case of $3d$ orbitals as a function of the crystalline distortion. The parameter $10Dq$, called crystal field splitting, is defined as the energy difference between the double degenerate e_g ($d_{x^2-y^2}$ and $d_{z^2-r^2}$) and the triply degenerate t_{2g} (d_{xy}, d_{xz} and d_{yz}) orbitals, whereas the terms $4D_s$+$5D_t$ and $3D_s$-$5D_t$ give the energy splitting between the e_g and the t_{2g} states. Moving from a cubic (O$_h$) to a tetragonal (D$_{4h}$) symmetry, the degeneracy of the e_g and t_{2g} levels is removed leading to a more complicated energy level diagram where the orbitals separation is mainly dictated by the distance between the apical oxygens and the Cu ion.

The symmetry and energy of the Cu-3d states have been recently revealed in a large number of HTS cuprates thanks to the new unique properties offered by the spectroscopic resonant inelastic X-ray scattering (RIXS) technique (see Chapter 2). The determination of the electronic configuration has been done by combining the RIXS experimental results together with the calculated RIXS cross-sections in a pure ionic picture in order to assign the crystal field parameters mentioned above [11]. Throughout most of the experimental results discussed in this thesis we will extensively use this method for the study of orbital excitations.

Concerning the magnetic properties, layered copper-oxides can be classified as 2D Heisenberg antiferromagnets. In fact, below the Néel temperature T_N (that is of the order of ~300 K in layered cuprates), the Cu^{2+} spins $1/2$ are ordered antiferromagnetically (AFM) via super-exchange interaction, mainly mediated by the surrounding oxygens present in the CuO_2 planes. The insulating behavior of the undoped cuprates originates from the electron-electron repulsion (U) at each Cu atom. Being the 2D layered cuprates Mott insulators, the super-exchange constant is generally of the order of $\sim$ 130 meV and it is inversely proportional to the Coulomb repulsion U. Moving from the undoped cuprates (which are the insulating parent compounds of the HTS) to doped compounds, the AFM long-range order is progressively destroyed by the added charges and superconductivity appears. Since all the superconducting cuprates are characterized by having an AFM ordering in the CuO_2 planes, many ideas have been proposed in the literature trying to link antiferromagnetism and superconductivity [21]. More recently, many theories supported by experiments suggest that coherent collective excitations of the electrons spin structure in a 2D square lattice, quasi-particles usually called magnons that are the eigenstates of the 2D AFM ordered CuO_2 planes, could be the acting force that drives the pairing mechanism instead of the one where superconductivity is mediated by the electron-phonon coupling. Since magnons are classified as collective modes, they involve more than one Cu site and can propagate through the planar lattice. The weak dispersion visible also along the perpendicular direction has attracted much less interest, since the coupling between the CuO_2 planes is almost absent.

More recently, dispersing spin-wave-like excitations (hereafter paramagnons) in doped compounds have been discovered firstly in the underdoped $La_{2-x}Sr_xCuO_4$ [5] and subsequently in $YBa_2Cu_3O_{6+\delta}$ HTS [22]: here, they demonstrated that paramagnons persist up to the optimally doped regime, preserving the spectral weight and the dispersing character of magnons in insulating cuprates. This important breakthrough in the knowledge of HTS cuprates opened the path to new theories in support of a magnetic-mediated high-T_c superconductivity. In fact, even in the absence of the AFM long-range order, magnetic fluctuations persist in the superconducting state, and for this reason they have attracted a lot of interest in the recent years [21].

Putting all together the properties mentioned above, we can say that HTS cuprates show a 2D character that allows us to restrict the study solely to the bidimensional first brillouin zone (BZ). In the right of Figure 1.4 we report the schematic representation of the first BZ highlighting the high symmetry points marked in reciprocal lattice units (r.l.u.): Γ represents the center of the BZ, while M the AFM scattering vector.

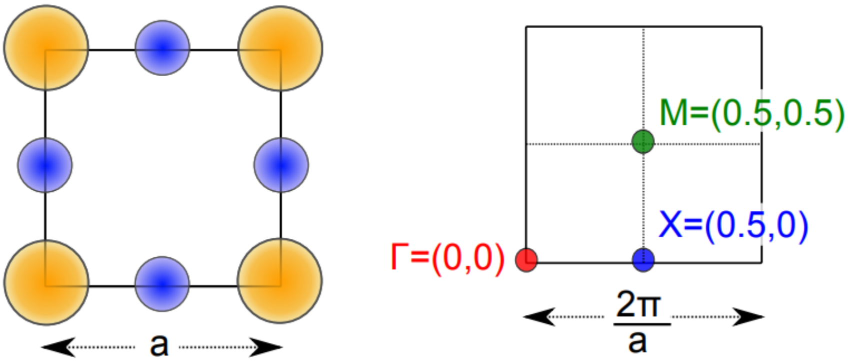

Figure 1.4: Generic scheme of a CuO_2 plaquette: copper atoms are in orange, while oxygens in blue. On the right side the reciprocal lattice together with its high symmetry points is illustrated. The points Γ, X and M are reported in reciprocal lattice units (r.l.u.). Figure from Ref. [23].

Besides the 2D cuprates introduced in this chapter, a special mention has to be made also for the family of the quasi-one dimensional (1D) cuprates, which will be discussed in greater detail in Chapter 5. These compounds, such as for example Sr_2CuO_3 and Ca_2CuO_3, are particularly interesting due to their peculiar electronic and magnetic properties. Both materials show the same crystalline structure [24, 25, 26], characterized by the quasi-1D CuO_3 chains of corner-sharing CuO_4 plaquettes along one particular crystallographic axis. Concerning the electronic properties, they can be classified as charge-transfer (CT) insulators due to the presence of an unoccupied O $2p$ band between the Cu $3d$ upper and lower Hubbard bands [27], while the strong on-site Coulomb repulsion U results, as in the 2D case, in a ground state with one localized hole per Cu ion in the $3d_{x^2-y^2}$ orbital. From the magnetic point of view, Sr_2CuO_3 and Ca_2CuO_3 constitute probably the best representation of the quasi-1D spin $1/2$ AFM Heisenberg chain [26]. The strong anisotropic interaction comes from the Cu-O-Cu bonds along the chains direction, while the coupling along the other crystallographic directions is almost negligible: as a consequence, these materials are 1D magnetic systems with a particularly large super-exchange interaction.

As we will explain much more in detail in Chapter 5, quasi-1D cuprates host one of the most fascinating phenomena in condensed matter, the electron spin-orbital (or spin-charge) fractionalization (or separation). A separation usually occurs when an electron fractionalizes into its constitutive parts, such as charge, orbital and spin. The quasi particles that describe these three degrees of freedom of an electron in solids are named holon, spinon and orbiton and they can be independently studied [28]. In Chapter 5 we will focus the attention on the case of the spin-orbital fractionalization in the quasi-1D Ca_2CuO_3 material.

1.2.3 Superconducting properties

As previously mentioned, superconductivity is achieved into the CuO_2 planes by changing the carrier concentration in the interstitial layers. Limiting the discussion to the hole doped case, it is widely accepted that the doping holes mainly occupy the oxygen states that surrounded the Cu atom in the plaquette. Having an opposite spin direction with respect to the one of the Cu^{2+} ion, the increase of the doping concentration breaks the long-range AFM order, although the short range spin-spin correlation is largely preserved. In this scenario, where the system has one more hole and a zero net spin with respect to the AFM ground state, the quasi-particle known as Zhang-Rice singlet (ZRS) [29, 30] is formed by the Cu $3_{x^2-y^2}$ hole hybridized with the delocalized added doped ligand hole on the planar O $2p_x$ and $2p_y$ orbitals. The propagation of the ZRS along the CuO_2 planes as a Cooper channel has been proposed to be one possible explanation of the mechanism beyond the high-T_c superconductivity in cuprates.

Knowing that electrons in solids can form pairs, another important aspect that has to be taken into account is their pairing mechanism responsible of the conductivity in HTS cuprates [31]. It is widely accepted that in conventional superconductors the pairing mechanism has a s-wave symmetry with a spin-singlet pairing due to the phonon-mediated many-body electron-electron interaction [17]. Since we know that this theory cannot work in the case of high-T_c superconductors, another model is needed. Historically, the starting point for the understanding of this complex scenario is the Hubbard model, where the main ingredients are the on site electron-electron Coulomb repulsion U and the hopping parameter t (usually expressed in form of the bandwidth $W = 8t$). Unfortunately, especially in the doped cases, an analytic solution of this model cannot be provided. Nevertheless, approximate solutions can be obtained revealing a d-wave superconducting ground state [7], which differs from the *s*-wave type proposed by the BCS theory. This hypothesis has been experimentally investigated in single crystals and *c*-axis oriented films of YBCO: SQUID, magnetometry and single/tricrystal junction interferometry have confirmed this assumption [32, 33, 34, 35], and subsequently these evidences have become a common feature to all the HTS cuprates. In reality, as discussed in the previous section, the ground state of the cuprates is antiferromagnetic, a property that has been successfully captured by the so-called $t-J$ model, one of the developments of the single-band Hubbard model. This model works especially in the strong-coupling limit considering a large U/t ratio [36], that is the case of strongly correlated electrons systems such as cuprates.

Despite the several models and theories proposed in the last decades, the high temperature superconductivity is still a mystery, but its solution must be built on a number of features common to all the HTS cuprates. As previously mentioned, one of the most and widely accepted interpretations is based on the fact that the symmetry of the ground state in the insulating parent compounds has a $d_{x^2-y^2}$ character, due to the structural elongation of the CuO_6 octahedron, which leads to a *d*-wave superconductivity upon doping.

1.2.4 Phase diagram

The complexity of the physics of cuptrates is summarized in the phase diagram shown in Figure 1.5. This phase diagram, characterized by unique features, displays the temperature behavior as a function of the hole concentration in copper oxides. Here the superconducting phase is one of the several phenomena that take place, and a complete explanation of this abnormally rich phase diagram is still missing [37].

It has to be underlined that the phase diagram as a function of the electron doping is similar (with some exceptions, such as for example the absence of the pseudogap phase) to the one sketched in Figure 1.5. As mentioned above, the hole (or electron) doping level can be varied via chemical substitution or by introducing extra oxygen atoms in the CuO_2 planes, and as a result doped compounds with different doping level (and T_c) can be obtained. More specifically, hole (electron) doped compounds are obtained when electrons are removed (added) from (to) the CuO_2 layers. At zero (or extremely low) doping level, cuprates can be classified as Mott-Hubbard insulators with a long range AFM order having an optical gap of the order of $\sim$2 eV. By increasing the hole concentration, the AFM order is substantially destroyed and superconductivity appears: the superconducting critical temperature T_c increases up to its maximum at a doping level defined as optimal (OP).

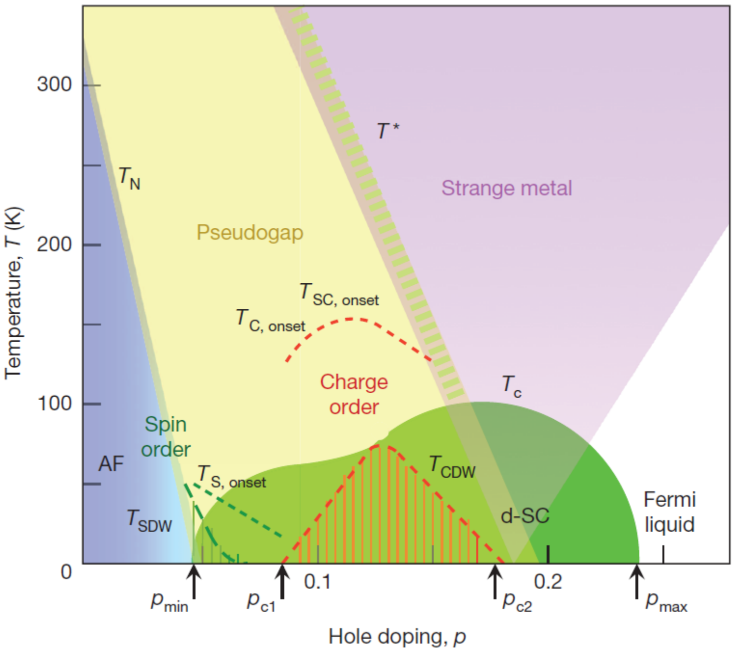

Figure 1.5: Schematic illustration of the phase diagram of HTS cuprates as a function of the hole doping, where the main phases that occur int these materials are highlighted. Figure from Ref. [7].

Between the AFM and the OP region, a phase denoted as underdoped (UD) region has attracted much attention due to its unusual properties. Here, above the superconducting dome (the region in the phase diagram where $T_c \neq 0$), the so called *pseudogap* phase persists up to temperature well above T_c. From the experimental point of view, a hint of the presence of this phase is given by a partial energy gap in the proximity the Fermi energy (where there is a substantial reduction of the density of states) usually seen in spectroscopic data. Furthermore, its presence can be related to the formation of Fermi arcs along the nodal direction in the Brillouin zone [38]. Despite the several experimental investigations, the interplay between this phase and superconductivity remains unclear [39]. Though the origin of this intriguing phase is still under debate, recent experimental evidences show that at these doping levels the system is characterized by several and different incipient orders that occur on intermediate length scales, such as charge order or charge density waves (CDW), spin density waves (SDW), electron nematic order and probably pair density waves (PDW).

The charge order, common to all the HTS cuprates, has been firstly discovered in the form of stripe order in the "214" cuprate families (*i.e.*

$La_{2-x-y}(Sr,Ba)_x(Nd,Eu)_yCuO_4$) [40, 41, 42] where it is strictly related to the uniaxially modulated AFM of the CuO_2 planes. This competing order is characterized by commensurate modulation of period $4a$ in the case of charges, while it is twice in the case of the spins modulations (here a is the lattice parameter which indicates the distance between neighboring Cu atoms). Their interplay is responsible of the suppression of T_c at a hole concentration $p \sim 1/8$ (doping level $p = 0.125$). This is the experimental evidence of the competition between stripes and superconductivity.

In other cuprate families, such as "123" compounds, the signature of charge density in the underdoped regime has been initially detected solely in the presence of magnetic field [43, 44]. Subsequently, in 2012 the presence of long-range incommensurate charge density waves in $(Y,Nd)Ba_2Cu_3O_{6+\delta}$ has been discovered [45]. The incommensurability (with respect to the underlying lattice) of the CDW wave vector has been found thanks to X-ray experiments, that after this discovery became one of the most widely used techniques for the investigation of charge order in cuprates. In fact, resonant X-ray scattering (RXS) experiments demonstrate that the presence of CDW in both hole [46, 47, 48] and electron [49] doped cuprates can be considered as a generic property common to all the HTS cuprates. Finally, as in the case of stripe-ordered cuprates, the experimental signature of the CDW signal strengthens the idea of a competition between charge ordering phenomena and superconductivity. In particular, the CDW signal shows a maximum at the superconducting transition temperature T_c followed by a considerable drop below T_c.

The phase diagram reported in Figure 1.5 summarizes all the physical properties discussed above. The presence of competing order is mainly in the underdoped regime: the onset temperatures of these phenomena are present in the pseudogap phase and it seems that their evolution can affect the superconducting dome. Going towards higher level of hole doping, at high temperatures doped cuprates in the OP and in the overdoped (OD) regions act as strange metals, the enigmatic normal state from which superconductivity emerges that does not follow the conventional transport properties. In fact, at temperatures higher than T_c, the conductivity is significantly smaller than the one registered in normal metals, and in addition to that its temperature and frequency dependences are incompatible with the conventional theory of metals.

Despite the extensive scientific inquiry, both from the experimental and theoretical point of view, an overall and accepted understanding of the superconducting mechanism in cuprates is lacking, making the unresolved problem of superconductivity one of the biggest challenges in the solid state physics.

We would like to remark that the scope of this thesis is to present the results with a phenomenological and empirical approach. In most of the cases, the measurements reported hereafter are often interpreted using calculations and theories: being an experimental thesis, we will provide to the reader a qualitative description of the theoretical background supported by references, without going into the details since this is not the scope of this work.

CHAPTER 2

Resonant inelastic X-rays scattering

In this chapter we will introduce the resonant inelastic X-ray scattering (from now on RIXS) spectroscopic technique. Due to the recent improvements in the performance of the instrumentation, especially in terms of energy resolution and efficiency, this technique has gained a lot of attention in the study of transition metal oxides, such as high-T_c cuprate superconductors. RIXS is particularly suitable to investigate the elementary excitations in solids related to all the degrees of freedom in solids, *i.e.* lattice, spin, charge and orbital. After discussing the main features of this spectroscopic technique, such as the scattering process, the RIXS cross sections and the several excitations that can be probed, we will focus on the advantages brought by the polarization analysis of the scattered X-ray photons.

Contents

2.1 Introduction

Resonant inelastic X-ray scattering is a "photon *in* - photon *out*" energy loss synchrotron-based spectroscopic technique [4] which has gained, especially in the last two decades, the interest of the scientific community due to the possibility of studying a wide range of excitations in solids. What makes RIXS a powerful and unique technique for the study of the electronic and magnetic properties in a large variety of materials lies in the following characteristics:

- ***element*** (and ***chemical***) ***selectivity***: in a typical RIXS measurement, the energy of the incident X-ray photons is chosen to match a specific absorption edge of the system under study. In this way, the inelastic scattering cross-sections are enhanced and, consequently, it is possible to probe with remarkable accuracy the different degrees of freedom (charge, magnetic and orbital) for the selected atom. Furthermore, being the absorption line shapes and the peak energies affected by the chemical environment, one can selectively choose among the different oxidation states or coordination symmetries. Once the photons are scattered by the sample, an excitation is created and the system is left in a state different from the initial one. The RIXS spectra and their polarization and geometrical dependencies carry valuable information on the symmetry and momentum of the excitations in the solid.

- ***momentum resolution***: X-ray photons carry a larger momentum than the one of the optical photons. As a consequence, the transfered momentum is enough to probe a large portion of the reciprocal space.

- ***neutrality***: the overall neutrality of the system is preserved during the scattering process, since there are no charges added or removed from the sample. As a result, we can avoid charging problems when studying insulating compounds. Moreover the experiment can be made in the presence of electric and magnetic fields and, when using hard X-rays, under high pressure.

- ***bulk sensitivity***: already in the soft X-rays energy range (400-1500 eV) RIXS is considered a bulk sensitive technique because the penetration depth inside the material spans from tens of nm to few μm.

Exploiting this capability, it is possible to study the bulk properties even in the presence of surface contamination.

- ***small samples***: differently from inelastic neutron scattering (INS), where the neutron-matter interaction is relatively weak requiring big sample volumes, RIXS measurements are possible in the case of small sample volumes, such as, for example, thin films and nano-samples.

In a RIXS spectrum the scattered photon intensities are usually reported as a function of the energy transferred to the sample, which is representative of the excitations occurred in the material during the process. The spectral features of interest in RIXS generally involve low-energy excitations in the quasi-elastic region ($\sim$ O energy loss), phonons and magnons in the meV scale, orbital excitations and charge transfer at few eV. Throughout the thesis, we will discuss each of them showing different experimental works.

Focusing on the soft X-rays regime, that is the case for example of RIXS at the Cu $L_{2,3}$-edges, one of the main limitations has been the energy resolution, often not good enough to disentangle low-energy excitations. A quite impressive work in the last few years has been done to overcome some technical issues. A new era for this technique was born thanks to the realization of the ERIXS spectrometer at the ID32 beamline of the ESRF - The European Synchrotron [8]. This instrument has set new standards conceiving a new generation of RIXS experiments, especially where all the low-energy excitations are detectable and with full access to the two- and three-dimensional reciprocal space. Equivalent, and in some cases more ambitious, projects in other facilities all over the world are going to be operational in the next years, that is the case, for example, of the SIX beamline at NSLS in Brookhaven National Lab. and I21 at Diamond Light Source.

Hereafter in this Chapter we will give a general description of RIXS technique, together with an introduction to the theoretical description of its cross-sections mainly following Refs. [4] and [50]. In the last part of this Chapter we will concentrate the attention on the instrumentation needed to perform the polarization analysis of the scattered radiation: about this topic, we will also describe the physical interpretation of polarization-resolved RIXS describing the different spectral contributions in terms of Stokes parameters and within the framework of the single-ion model.

2.2 Scattering process

RIXS is well described as a second order process where the intermediate state is not observed: initially, an incident monochromatic X-ray photon, with momentum $\hbar\mathbf{k}_i$ and energy $\hbar\omega_i$ dictated by the resonant condition, is absorbed by the sample. As a direct consequence, a core electron is promoted to an empty state above the Fermi level leaving a deep core hole. At this stage, the system is in an unstable condition with a lifetime of the order of $\sim$1 fs, and rapidly decays filling the core hole emitting another X-ray photon with energy $\hbar\omega_o$ and momentum $\hbar\mathbf{k}_o$.

The energy diagram of the RIXS process is reported in Figure 2.1, where we can easily identify RIXS as a two-steps process.

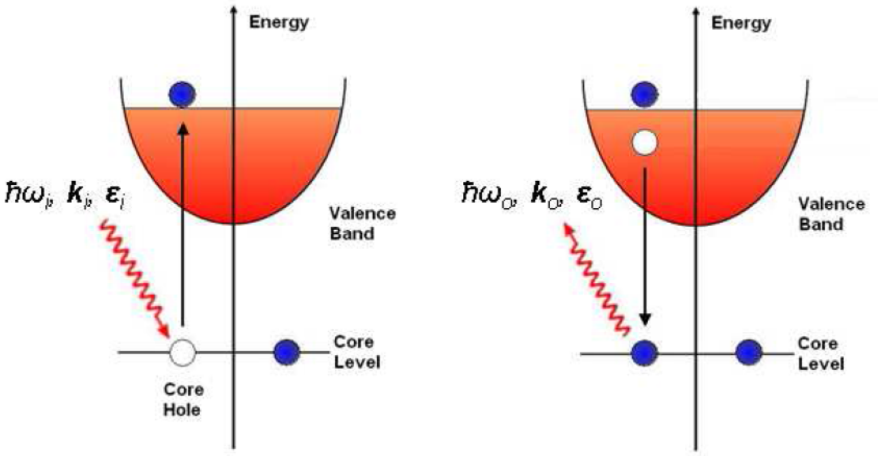

Figure 2.1: Scheme of the RIXS two-steps process: a core electron is promoted to an empty state above the Fermi level after being absorbed. The system rapidly decays by filling the core-hole created during the first step emitting a photon characterized by an energy $\hbar\omega_o$ and momentum $\hbar\mathbf{k}_o$. Figure from Ref. [51].

In general, $\hbar\omega_o \neq \hbar\omega_i$, which means that the final state of the RIXS process does not coincide with the ground state: the energy difference $\hbar\omega_i - \hbar\omega_o$ is thus the energy of the final state. If $\hbar\omega_o = \hbar\omega_i$, no excitations are left in the system: the final state coincides with the initial one, and we will refer to it as elastic scattering. Due to the conservation laws of energy and momentum during the scattering process, each final state has an intrinsic energy loss E and momentum $\hbar\mathbf{q}$

$$E = \hbar\omega_i - \hbar\omega_o \tag{2.1}$$

$$\hbar\mathbf{q} = \hbar\mathbf{k}_i - \hbar\mathbf{k}_o \tag{2.2}$$

In Figure 2.2 the conservation laws of energy and momentum are schematically illustrated. By applying the conservation law of the total angular momentum involved during the RIXS process, we can also retrieve information about the polarization state of the ingoing and outgoing photons ($\epsilon_{i,o}$). As a matter of fact, the analysis of the RIXS spectrum is done by fully characterizing the incident and scattered photons in terms of their energy, momentum and, when possible, polarization.

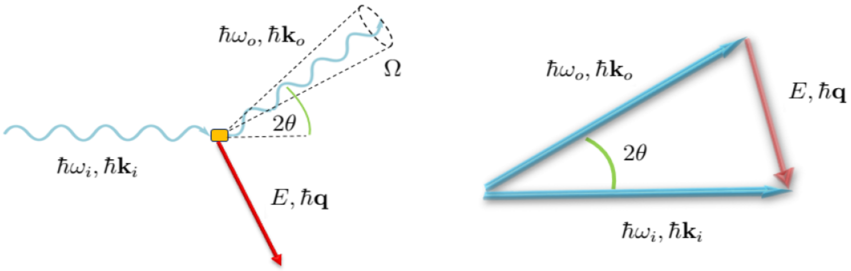

Figure 2.2: Schematic illustration of the kinematic (left) and conservation laws (right) in the RIXS process. The energy E transferred to the sample in a solid angle Ω is given by the energy difference between the incident and scattered photons ($\hbar\omega_i - \hbar\omega_o$). Here 2θ represents the scattering angle, which defines the transferred momentum to the sample $\hbar\mathbf{q} = \hbar\mathbf{k}_i - \hbar\mathbf{k}_o$.

2.3 Features in a RIXS spectrum

As previously mentioned, RIXS is capable to probe several degrees of freedom of the system under study, such as charge, spin and orbital. In the specific case of RIXS at the Cu L_3-edge ($\hbar\omega_i \sim 931$ eV), an electron from the $2p_{3/2}$ states is promoted to the empty $3d_{x^2-y^2}$ orbital, which is the only one valence state above the Fermi level [13] and the radiative decay can involve all the other $3d$ states.

The energy diagram of RIXS performed at the Cu L_3-edge is schematically represented in Figure 2.3. Since the copper atom in the layered cuprates usually has valence 2+, its electronic configuration can be described with 9 electrons filling the $3d$ orbitals, and the only $3d$ unoccupied orbital has usually a $d_{x^2-y^2}$ symmetry. This assumption will help us in the following discussion avoiding the problem related to the particle-particle interaction. In Figure 2.3 we highlight the presence of an highly unstable intermediate state, where the spin state is mixed due to the large spin-orbit interaction between the $2p$ states (~20 eV). The very short lifetime of this state is mainly driven by the Auger decay processes, although it is not directly observable during a RIXS experiment. Finally, an excitation is left in the solid when we have a hole in one of the $3d$ orbitals and the energy and momentum of the emitted photon differs from the incident one.

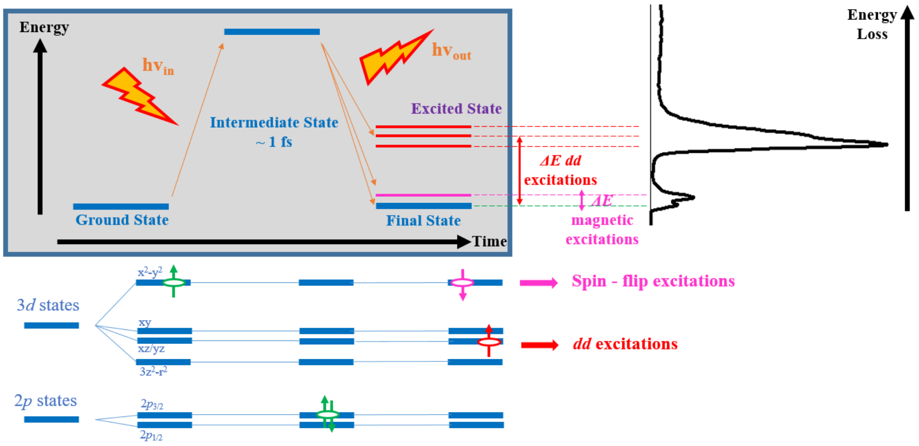

Figure 2.3: Energy scheme of the RIXS process at the Cu L_3-edge and associated typical RIXS spectrum.

In the left side of Figure 2.4 we report the Cu L_3-edge absorption spectrum measured in total electron yield (TEY) on a CaCuO$_2$ single crystal. As explained before, this measurement is essential to exactly tune the incident energy on the main L_3 absorption peak. Once the incident energy is set, the RIXS spectrum (shown in the right side of Figure 2.4) can be measured.

In a RIXS experiment it is possible to tune the incident photon energy across the resonance and see how the excitations evolve. By keeping the same momentum transfer, the energy of the emitted photons ($\hbar\omega_o$) relative to a specific excitation can be constant or changing as a function of the incident one ($\hbar\omega_i$). We will refer to Raman-like excitations when the spectral features have a constant energy loss $\hbar\omega_i - \hbar\omega_o$, while for those characterized by the constant energy of the scattered photons (independently from the incident energy) we will refer as fluorescence-like excitations. Hereafter we will restrict the study to solely the Raman-like excitations accessible by RIXS.

As previously mentioned, a finite momentum $\hbar\mathbf{q}$ is transferred from the incident photons to the system under study during the RIXS process. By changing the scattering geometry, it is possible to track the momentum dependence of the Raman-like features allowing us to single out their local or collective character. The main differences between them lies in the fact that the latter show a dispersion in the reciprocal space, usually symmetric with respect to the $\mathbf{q}$ inversion, whereas for localized excitations the momentum transferred is not a good quantum number. In the latter case no dispersion can be observed.

As we will better describe in the last part of this Chapter, one can also infer about the polarization state of the emitted photons. In this way, by

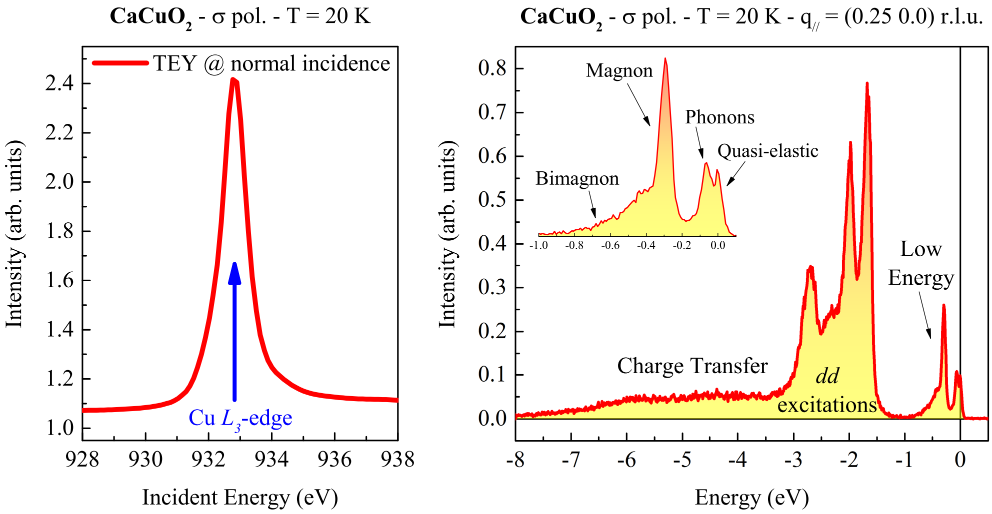

Figure 2.4: Left panel: X-ray absorption spectrum at the Cu L_3-edge measured in total electron yield (TEY) on a $CaCuO_2$ thin film. Right panel: example of a typical $CaCuO_2$ RIXS spectrum: in the low-energy range (inset) we can distinguish the quasi-elastic peak at ∼0 eV, phonons and magnetic excitations (single-and bi-magnon). At higher energies the spectrum is dominated by the *dd* and charge transfer excitations.

exploiting the possibility of controlling either the polarization (linear and circular) of the incident and scattered photons, a total control on the symmetry of both the initial and final states can be achieved. In fact, due to the conservation of the total angular momentum during the RIXS process, the photon polarizations $\epsilon_{i,o}$ have to obey to well defined selection rules.

Regarding the instrumentations that make this kind of experiments possible, with the installation of the insertion devices in synchrotrons, the polarization of the incident X-rays can be easily set either linear or circular. Much more problematic, especially in the soft X-ray energy range, is the control of the outgoing polarization ϵ_o: differently from the hard X-rays case, where the detection of the polarization of the scattered photons is achievable thanks to the Bragg optics, in the soft X-rays one has to depend on multi-layered mirrors characterized by a lower polarization sensitivity and reflectivity. However, a polarimeter for the detection of the polarization of the scattered radiation has been installed on the ERIXS spectrometer of the ID32 beamline at the ESRF and it is currently available to users [8]. As it will become clear later on, this device allowed us to disentangle the nature of almost all the spectral features present in a typical Cu L_3-edge spectrum.

Starting from the low energy region shown in the top-left inset of Figure 2.4, we can distinguish four different contributions. The quasi-elastic peak at ∼0 energy loss is mainly limited by the energy resolution and by the quality of the sample. In fact, thermal diffuse scattering, defects and roughness of the surface can generally give additional intensity. Despite this, the study of the elastic peak intensity has become a well established routine: it has been demonstrated that the evolution of the elastic signal as a function of the in-plane momentum reveals the presence of charge density waves in cuprates [45]. Moreover, with a pioneering work published in *Science* we have recently demonstrated that short-range dynamical charge density fluctuations (CDF) exist throughout the cuprate phase diagram and are characterized by finite energies of few meV (below the limit of the resolving power of the spectrometer) [52].

Below 100 meV, the spectrum is dominated by the phononic peaks. During the RIXS process, and in particular in the intermediate state, the electron promoted from the deep core $2p$ to the $3d$ states plays a fundamental role: it alters the charge distribution of the Cu ions repelling the nearby oxygen ions. As a consequence, the phonon peaks observed with RIXS are related to the lattice distortions characterized by different symmetries.

It has been demonstrated that RIXS can probe magnetic excitations [5], that can be classified as single and multiple magnons. Braicovich *et al.* demonstrated that the momentum-dependence of the single magnon in the undoped La_2CuO_4 exactly corresponds to the one measured with INS [5], as shown in Figure 2.5. This has been an important turning point since the magnon dispersion was traditionally studied using INS, which typically requires large single crystal samples of several cm^3 in volume.

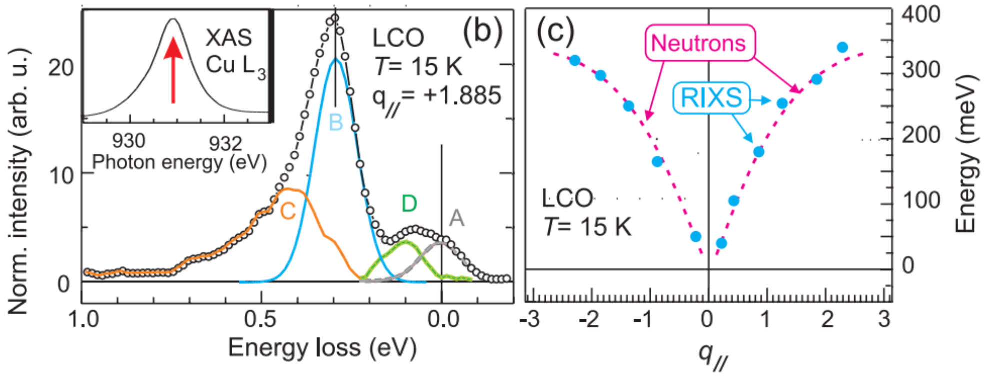

Figure 2.5: Left panel: decomposition (A elastic, B single magnon, C multiple magnons, D optical phonons) of the La_2CuO_4 (LCO) RIXS low-energy range spectrum at $q_{\|} = 1.85$. In the inset we report the Cu L_3-edge absorption spectrum highlighting the excitation energy with the red arrow. Right panel: comparison between RIXS (blue circles) and INS (magenta lines from Ref. [53]) single magnon extracted energies. Figure from Ref. [5].

A single magnon can be excited by the RIXS process thanks to the large spin-orbit coupling of the $2p$ states involved in the intermediate state which mix the spin, whereas multiple magnons excitations, such as bimagnons (multiple magnons characterized by two spin waves), can be seen as single magnons propagating in different directions at the same time. The possibility to probe bimagnons lies in the transitory $3d^{10}$ configuration of the intermediate state accompanied by a 0 net spin. This transient "non-magnetic" impurity quenches the Cu ions super-exchange in the AFM lattice giving rise to magnetic excitations that can be seen in the RIXS spectrum since during this process a finite amount of energy and momentum is transferred from the system to the outgoing photon. Moreover, magnetic excitations probed by RIXS show a collective character, which means that their energy changes as a function of the transferred momentum.

It has been also demonstrated that RIXS is a valuable tool for probing low energy collective excitations such as acoustic plasmons [54]. The possibility to perform the polarization analysis of the scattered radiation gave us the confirmation of its charge origin.

Moving towards higher energies, from Figure 2.4 we can clearly notice that most of the total spectral weight is given by the *dd* (or orbital) excitations. In the simplest picture, a *dd* excitation is created by the transition of an electron from one $3d$ level to another one. Since RIXS is based on a second order process, a $\Delta l = 0$ transition, such as a *dd* excitation, is allowed. In fact, RIXS can probe a two-dipole transition $d \rightarrow p$ and $p \rightarrow d$ having $\Delta l = 1$. The study of orbital excitations has a fundamental importance in the understanding of the main crystal field parameters. By comparing quantum chemistry calculations together with systematic measurements of the *dd* excitations, it is possible to assign the energy and symmetry coordination of the Cu $3d$ states, giving useful information about the crystal field and the octahedral distortion [11]. It is also worth mentioning that orbital excitations in 2D systems do not show momentum dependence due to their local character. Contrarily, 1D compounds such as Sr_2CuO_3 [55] and Ca_2CuO_3 (see Chapter 5) show sizable dispersions interpreted in terms of spin-orbital separation. Finally, at even higher energies usually in the range of few eV, the RIXS spectrum is characterized by charge transfer excitations that can be explained in terms of molecular orbital excitations from bonding to antibonding states which involve the oxygens ligands.

2.4 Experimental set-up

In the previous Sections we have discussed about the ability offered by RIXS technique to probe several degrees of freedom in materials such as HTS cuprates. In a RIXS spectrum, the typical energy range of low energy excitations is below 400 meV. Regarding phonons, the energy range is approximately between 0 and 100 meV of energy loss, rendering impossible their observation with the typical RIXS instrumentations. For this reason, in the last decades many efforts have been made for the development of the instrumentations in order to overcome some technical limitations, especially in terms of energy resolution, scattering intensity, outgoing polarization analysis and sample control. Much progress has been recently made especially thanks to the realization of dedicated optical layouts and spectrometers in the third generation synchrotrons. In this section we will introduce the essential concepts at the base of a RIXS beamline that allow the study of elementary excitations in solids with unprecedented control. In particular, we will briefly describe the main features of the ERIXS spectrometer at the new ID32 soft X-ray beamline of the ESRF - the European Synchrotron, where we measured most of the data discussed in this thesis work.

2.4.1 ID32 beamline and the ERIXS spectrometer

The ID32 beamline has been inaugurated in 2015 after the ESRF Upgrade Phase I and represents the state-of-the-art for the inelastic soft X-rays scattering. The beamline has been conceived primarily for the investigation of the magnetic and electronic structures of several compounds that show properties well suitable for the study in the soft X-rays energy range. That is the case of the O K absorption edge and the $L_{2,3}$-edge for the $3d$ transition elements and, finally, the $M_{4,5}$-edge in the case of rare earths-based materials.

Besides RIXS, at ID32 it is possible to carry out X-ray absorption spectroscopy (XAS), X-ray magnetic circular dichroism (XMCD) soft X-ray diffraction and coherent scattering measurements. Regarding the optical layout, ID32 is one of the longest beamlines of the ESRF ($\sim$ 125 m) and it is constituted by two main branches having different optical schemes.

Figure 2.6 shows the beamline floor plan, where the distances are referred to the X-ray source. The three insertions devices (APPLE-II undulators [56]) provide the full control of the two linearly (horizontal and vertical with respect to the plane of the synchrotron) and circular polarized emitted radiations in the 400-1600 eV energy range. Once the X-rays are generated at a specific wavelength and with a chosen polarization, they are forced to go through many optical elements along the beam path (here not discussed because their treatment is beyond the purpose of this thesis). Their functionality is to provide a monochromatic, collimated and focused (4×50 microns of full-width at half-maximum in the vertical and horizontal direction) beam on the sample. Since the beamline operates in the soft X-rays energy range,

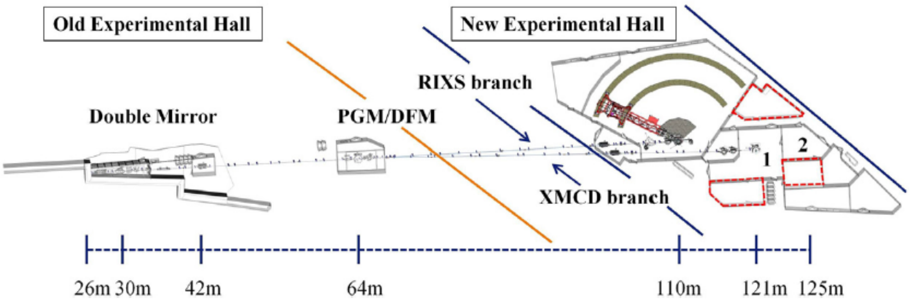

Figure 2.6: Top view of the ID32 beamline at the ESRF. The distances are calculated from the source. Figure from Ref. [8].

it is windowless and all the elements are kept in vacuum.

Hereafter we will discuss more in detail the RIXS branch, briefly describing the design and the main performances of the ERIXS spectrometer and finally focusing the attention on the unique possibility offered by this beamline to detect the polarization of the scattered X-rays in a RIXS experiment.

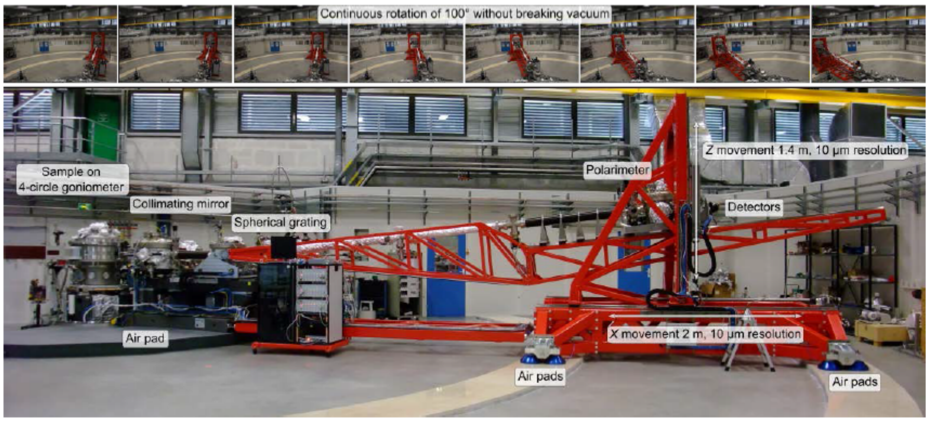

Figure 2.7: The ERIXS spectrometer at the ID32 beamline of the ESRF. Figure from Ref. [57].

The realization of the ERIXS spectrometer (shown in Figure 2.7) is the result of a long and very fruitful collaboration between the ID32 beamline staff and the group at Politecnico held by Prof. G. Ghiringhelli and the Prof. Emeritus of the ESRF L. Braicovich. Conceptually, this spectrometer is the evolution of the AXES [1, 2] (previously installed at the old ID08 at the ESRF) and SAXES spectrometer at the ADDRESS beamline of the Swiss Light Source in Switzerland [3]. The main goal was to achieve an improvement of at least a factor 2-3 in combining resolving power with respect to SAXES spectrometer while keeping a comparable count rate.

Since its inauguration, ERIXS has offered to the users unprecedented capabilities, such as:

- ***energy resolution***: the resolving power ($E/\Delta E$) at the Cu L_3-edge is 30,000, allowing to reach an overall (beamline + spectrometer) bandwidth of 30 meV (see Figure 2.10). With respect to the SAXES spectrometer, the improvement in terms of energy resolution is more than a factor 3 keeping the same count rate. The implications of such a result will be explained later on.

- ***scattering angle***: the possibility to continuously rotate around the sample the 11 meter-long scattering arm (entirely supported by air pads) from 50° to 149.5° without breaking the ultra high vacuum offers unique potentialities in terms of accessible zones in the reciprocal space.

- ***polarization control***: thanks to the multi-layered mirror installed along the scattered beam path, ERIXS offers the unique capability to fully control the symmetry of the excited states by studying the polarization-dependence of the scattered photons.

- ***sample control***: the sample chamber hosts a four-circle UHV diffractometer which allows the full control of the sample orientation and the regulation of the scattering angle (see Figure 2.8).

- ***high luminosity***: differently from the AXES and SAXES spectrometers, ERIXS houses a parabolic collimating mirror and two exchangeable spherical gratings that allows a gain of a factor ~5-7 in angular acceptance, and thus in count rate, at any given energy resolution.

The possibility to continuously rotate the spectrometer scattering arm has been made possible thanks to the innovative design of the RIXS sample chamber, which is furnished by a double-differentially steel ribbon with a nozzle that allows a 100° free rotation. Regarding the sample control and orientation, the chamber is equipped with an in-vacuum 4-circle sample goniometer that allows both the motorized translation (sub-micron) and rotation (~0.01° resolution) in vacuum (see Figure 2.8). The samples are usually mounted on a shuttle and then inserted in the chamber via a load-lock system. Once the sample is on the sample stage inside the chamber, it is electrically insulated in order to measure the total electron yield (TEY) signal thanks to the connection of a wire to an ammeter that registers the drain current coming from the sample.

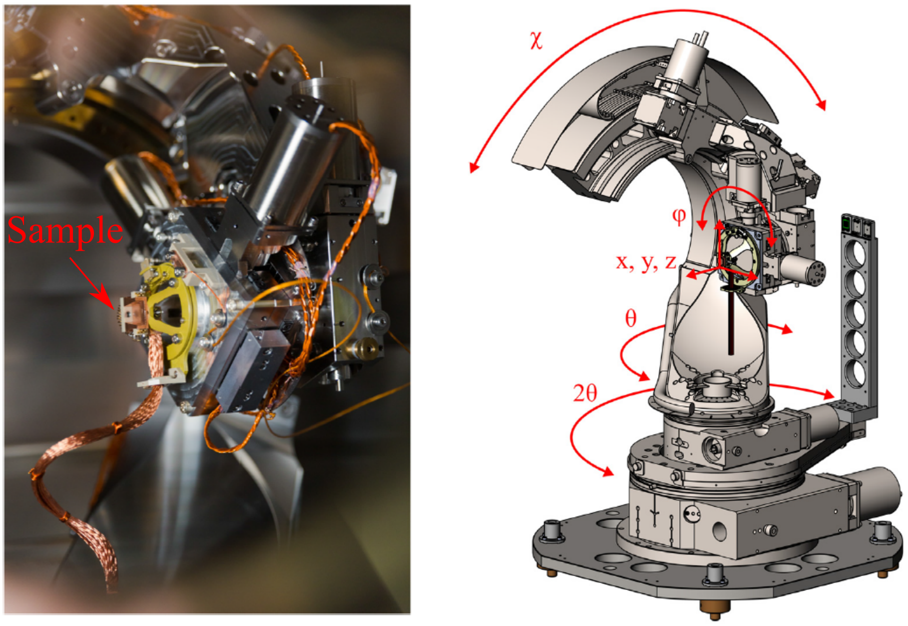

Figure 2.8: Picture and schematic representation of the RIXS sample chamber. In the right panel all the sample motions are illustrated. Figures from Ref. [8].

The ability to have a complete control of the sample orientation made the ID32 beamline the fist one in the soft-RIXS spectroscopy capable of measure dispersion relations in 3D materials.

Regarding the ERIXS spectrometer, the main idea behind it is the capability to collect the scattered photons at a certain solid angle and then infer about their energy. In the present case of soft X-ray regime, this is usually obtained thanks to the presence of a dispersive grating in the spectrometer.

The ERIXS optical layout is schematically illustrated in Figure 2.9. The first two in-vacuum chambers, supported on a granite base, host a collimating parabolic mirror in the horizontal direction with 2° of incidence angle (CM) and two interchangeable variable line spacing (VLS) spherical gratings (G1 and G2), respectively. The collimating mirror is located at 1.1 m from the sample and collects $\sim$20 mrad at $\sim$88° incidence angle.

Regarding the VLS grating, its main function is to focus and disperse the photons at the same time. After the action of the grating, the photons of different energies are focused in different vertical positions on the detector defining in this way the focal plane. Moreover, the grating is motorized in order to be moved along the spectrometer axis and to minimize the aberrations that occur at each energy. Concerning the two gratings, they are characterized by a different groove density, 1400 lines/mm (G2) for high efficiency and

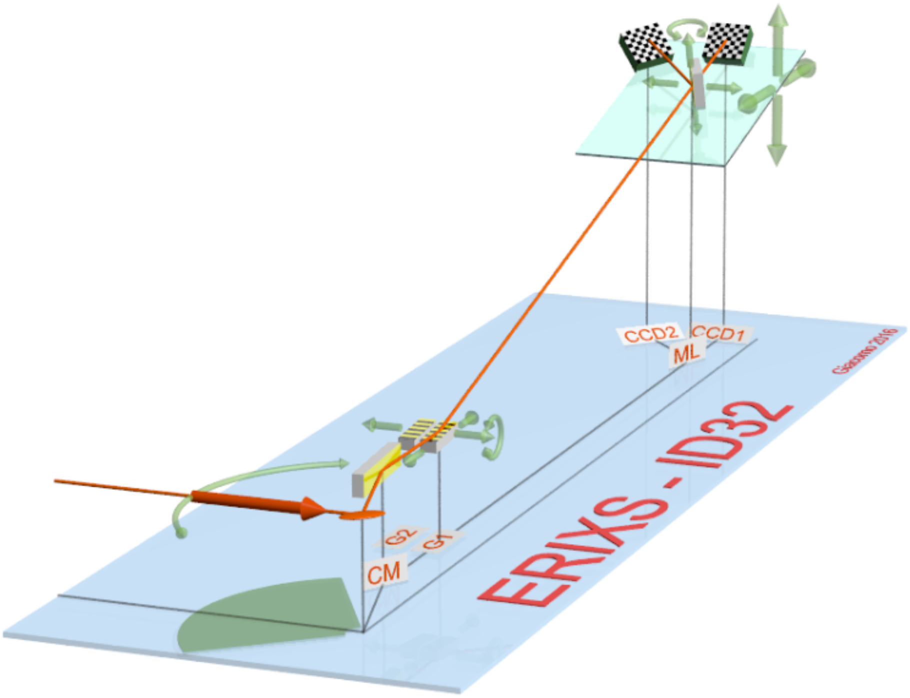

Figure 2.9: Optical layout of the The ERIXS spectrometer. Figure from Ref. [8].

2500 lines/mm (G1) for the high resolution mode and can be independently moved. They both work at the first internal diffraction order and they are optimized for a resolving power of 25,000 and 40,000 for the optimum flux and high resolution mode, respectively.

The main goal behind the realization of the ERIXS spectrometer was to achieve an overall energy resolution of ≈30 meV at the Cu L_3-edge, which is obtained by combining the resolution of the beamline and the spectromter. The main contributions to the overall energy resolution given by the beamline are dictated by the diffraction properties of the beamline gratings, the aperture of the monochromator's exit slit and by the aberrations and slope errors that affect the focusing properties. Concerning the spectrometer, its resolution is provided by the vertical beam size on the sample, the diffraction and focusing properties of the grating, and finally, by the intrinsic detector resolution.

By combining the two gratings of the spectrometer with the gratings of the beamline, three configurations are normally used. The results, in terms of combined (beamline + spectrometer) energy resolution, are reported in Figure 2.10. In particular, the high resolution mode is achieved by using the high line density for both the gratings. This configuration gives unprecedented performances in terms of energy resolution but with low intensity. It is worth mentioning that the low resolution/high flux configuration gives a reasonable resolution (56 meV) while keeping a good intensity. Finally, the medium setup gives instead a reasonable compromise between resolution and intensity.

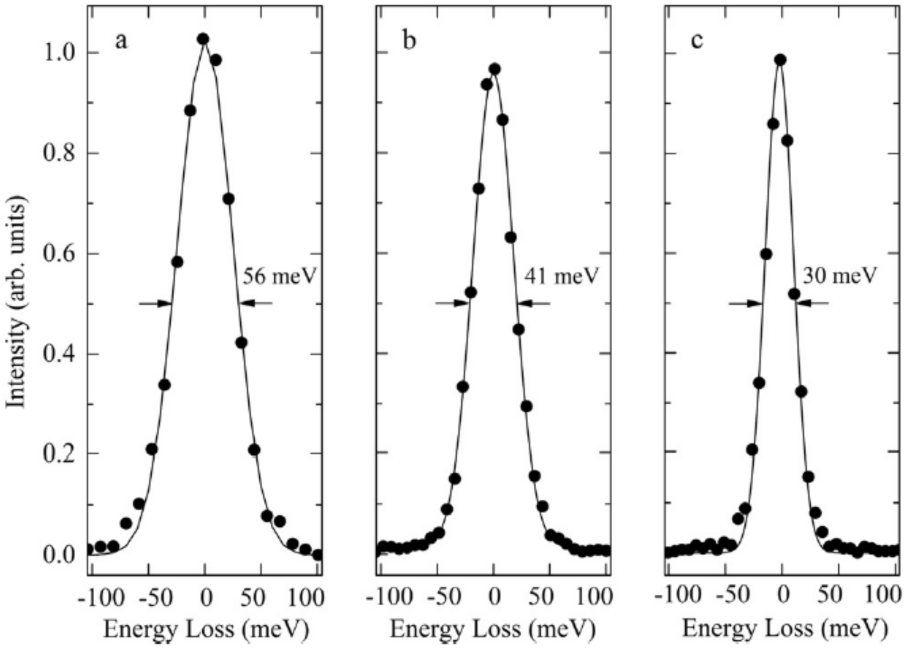

Figure 2.10: Energy resolution of the ERIXS spectrometer obtained in three different grating configurations of the beamline and spectrometer. Dots represent the data point of the elastic peak measured from a carbon tape with an incident energy of 932 eV (Cu L_3-edge). Continuous lines are the Gaussian fits. Figures from Ref. [8].

The main performances and characteristic of ERIXS are reported in Figure 2.11. Here we show the resolving power, band-width, pixel to energy conversion and total energy window as a function of the incident photon energy for the two gratings.

The third and last chamber is situated at the end of the scattering arm, where two Andor Ikon L soft X-ray direct illumination CCD detectors (CCD1 and CCD2) are located. Moreover, just before the two CCDs, there is the multi-layered mirror (polarimeter) which allows the polarization analysis, which will be discussed in the next section. CCD2 is used for the detection of the photons scattered by the ML (when inserted along the beam path for polarimetric experiments), while CCD1 is used for standard measurements being positioned along the straight path of the scattered radiation.

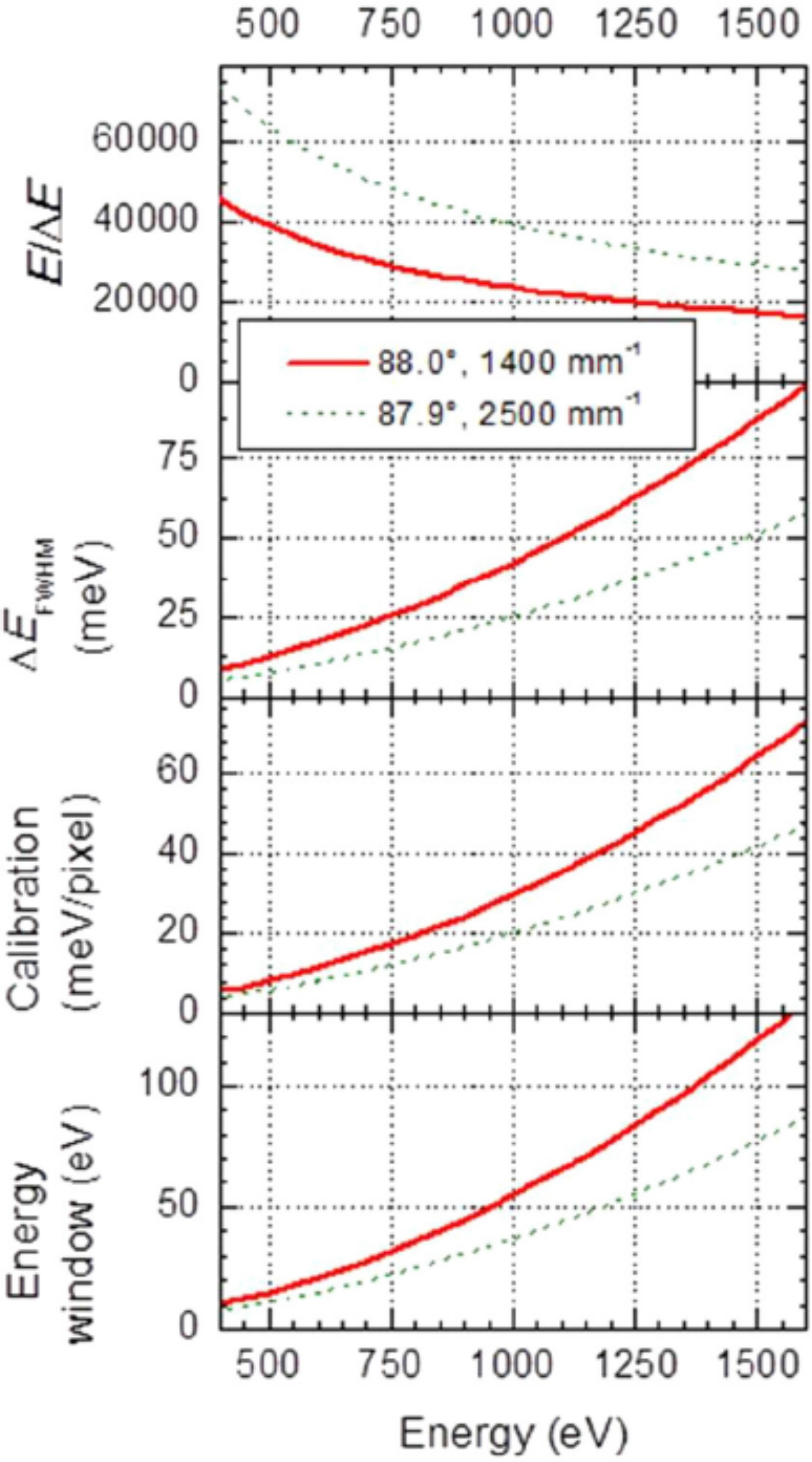

Figure 2.11: The resolving power, band-width, pixel to energy conversion and total energy window for the two gratings of ERIXS. Figure from Ref. [8].

High-sensitivity two-dimensional position sensitive detectors are needed alongside the recent improvements in energy resolution and efficiency in soft RIXS experiments. In fact, the spatial resolution of a CCD camera is intrinsically limited by the dimension of the so-called charge cloud. This phenomenon is attributable to the absorption-process of a photon in Si that generates a number of electrons proportional to its energy that spread by diffusion over several pixels [58], giving another not negligible contribute to the overall energy resolution. This limitation has been solved using the Single Photon Counting algorithm [59], a centroid reconstruction method based on single events acquisition. With this method, the position of the absorption event is reconstructed by evaluating the accumulated intensities in the pixels subjected to the charge cloud.

2.4.2 The standard experimental geometry

For all the measurements reported hereafter we have used the experimental geometry shown in Figure 2.12, where both the real and reciprocal spaces are illustrated. In panel a) of Figure 2.12 the meaningful angles are reported: 2θ is the scattering angle, while δ is defined as the angle between the sample c-axis and the bisector of the $\mathbf{k}_{in}$ and $\mathbf{k}_{out}$ vectors which represent the wave vectors of the incident and scattered X-ray photons. $\mathbf{q}$ is the total transferred momentum to the sample during the RIXS process, while $q_{\|}$ represents its projection onto the ab plane. $\mathbf{k}_{in}$ is defined by the energy of the incident X-rays, while the maximum reachable $\mathbf{q}$ is given by 2θ. These considerations can be summarized by the following equation, where the analytical definition of $q_{\|}$ is given: $q_{\|} = 2|\mathbf{k}_{in}| \sin\left(\frac{2\theta}{2}\right) \sin(\delta)$. In fact, the 2D nature of cuprates greatly simplifies the study of elementary excitations because the most interesting physics of these materials takes place in the CuO_2 planes. The direct consequence of the bi-dimensionality of cuprates makes $q_{\|}$ the meaningful quantity to be studied, allowing to restrict the investigation to solely the 2D first Brillouin zone shown in Figure 2.12(b).
Here Γ represents the [0 0] point in the 2D Brillouin zone, while the other points of the momentum space are expressed in reciprocal lattice units (r.l.u.), usually defined in units of reciprocal lattice vectors $2\pi/a$, $2\pi/b$ and $2\pi/c$, where a, b and c are the lattice constant of the material under study.

Regarding the possibility to measure the momentum dependence of a selected spectral feature, the $q_{\|}$ can be easily tracked by keeping fixed the scattering angle 2θ and gradually changing the angle δ (lying in the scattering plane) by rotating the sample around its b axis perpendicular to the scattering plane. From the 3D representation of the scattering geometry reported in Figure 2.12(c) we can see that the polarization is another degree

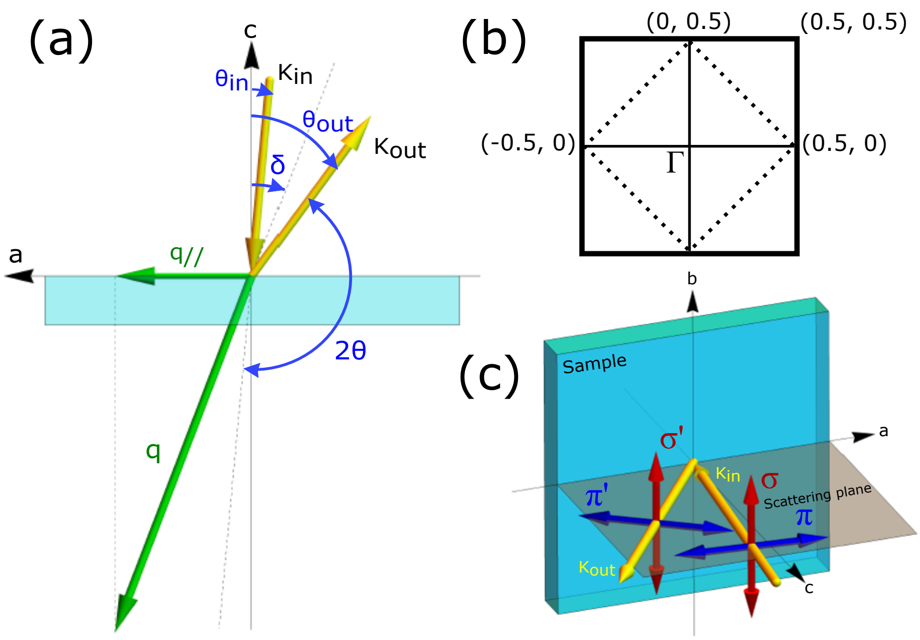

Figure 2.12: a) Sketch of the scattering geometry. b) Schematic illustration of the first 2D nuclear and magnetic Brillouin zone. c) Representation of the experimental geometry which highlights the possibility to perform the polarization analysis of the scattered light. Figure adapted from Ref. [60].

of freedom that can be exploited. In fact, at the ID32 beamline the incident polarization (direction of the electric field vector **E**) can be set either parallel (π) or vertical (σ) with respect to the scattering plane. As explained before, ERIXS is the only spectrometer that, thanks to the polarimeter device inserted along the beam path, allows the possibility to disentangle these two linearly polarized channels of the scattered X-rays.

.

2.5 Examples of RIXS measurements carried out at ID32

In this Section we will give some examples about RIXS measurements on HTS cuprates and their parent compounds which show the capability of ERIXS to study with unprecedented detail the spectral features in the low energy range. We will briefly present three different cases, where the high energy resolution (keeping a reasonable count rate) played a crucial role.

Probing the energy gap of HTS cuprates

The summary of the data and analyses discussed in this Paragraph have been published in "*Probing the energy gap of high-temperature cuprate superconductors by resonant inelastic X-ray scattering*", by H. Suzuki, M. Minola, Y. Lu, Y. Y. Peng, R. Fumagalli, E. Lefrancois, T. Loew, J. Porras, K. Kummer, D. Betto, S. Ishida, H. Eisaki, C. Hu, X. Zhou, M. W. Haverkort, N. B. Brookes, L. Braicovich, G. Ghiringhelli, M. Le Tacon and B. Keimer, *npj Quantum Materials* **3**, 65 (2018).

Being RIXS sensitive to the charge response of the system, it has been theoretically proposed as a tool that can be used to probe the phase and the excitations of the superconducting (SC) order parameter in cuprates [61]. The possibility to experimentally quantify the SC order parameter is very challenging for several reasons. First of all, different order parameters coexist and compete with superconductivity, involving both spin and charge degrees of freedom [7]. Secondly, in unconventional superconductors the SC order parameter is momentum-dependent, and for this reason it has been widely investigated with angle-resolved photoemission spectroscopy (ARPES), a momentum-resolved spectroscopic technique that probes single-particle excitations, and by scanning tunneling spectroscopy (STS).

Figure 2.13 (left panel) shows the typical angular dependence (restrict to solely one quadrant of the first Brilluoine zone) of the energy of the superconducting gap and pseudogap in doped cuprates. The presence of the pseudogap (top-right panel) is reflected by the appearance of Fermi arcs (gapless region around the *d*-wave superconducting node) in the antinodal region of the Fermi surface (shown in the bottom-right panel). The SC state is characterized by an anisotropic behavior typical of a standard *d*-wave form $\Delta_{\mathrm{SC}} = (\Delta_0/2)|\cos(k_x a) - \cos(k_y a)|$, where Δ_0 is the maximum energy of the gap. In the particular case of cuprates, ARPES measurements contributed in the understanding of the SC gap symmetry, which clearly shows a *d*-wave order with a $d_{x^2-y^2}$ symmetry [46, 62].

However, there are two major limitations related to ARPES: the first one is related to the fact that ARPES needs single crystals with a natural cleavage plane, restricting the number of compounds that can be investigated with such technique. The other one is connected to the intrinsic surface sensitivity of ARPES, so that one has to accept that ARPES results are relevant for the bulk electronic structure despite being acquired at the surface of the materials. For these reasons, among all the cuprate families, the Bi-based cuprates represent the best candidates for the investigation of the energy gap through RIXS, especially because they can be easily cleaved and they show a quite large energy gap.

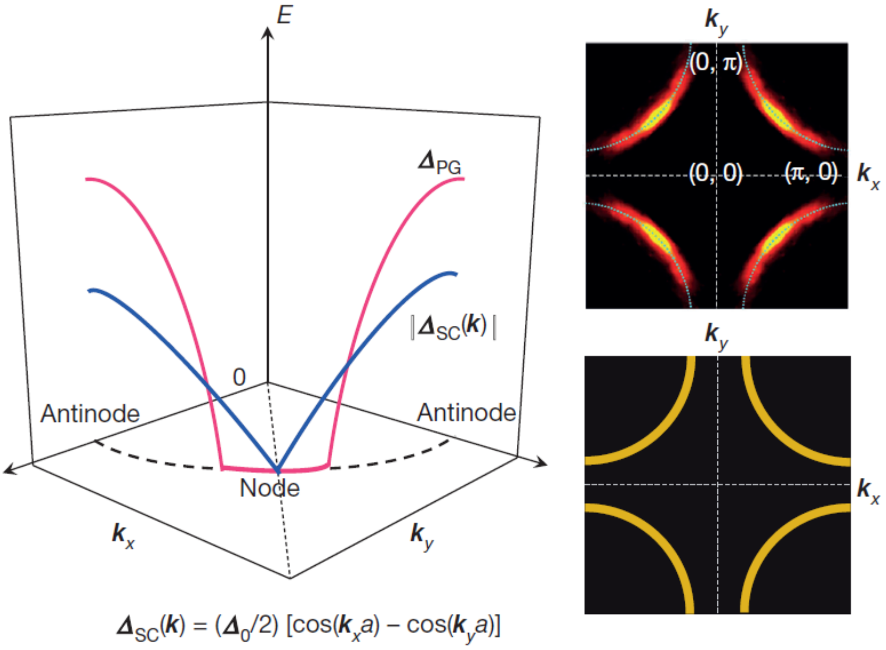

Figure 2.13: The left panel shows the angle dependence revealed by ARPES and STS of the energy of the superconducting Δ_{SC} and pseudogap Δ_{PG} as a function of the in plane momenta k_x and k_y. In the right panels the Fermi surface of overdoped cuprates is shown (bottom panel). The effect of the pseudogap is highlighted in the top–right panel by the presence of Fermi arcs. Figures from Ref. [7].

By taking advantage of the high-energy resolution offered by the ERIXS spectrometer, accompanied by the possibility to measure the alterations of charge and spin susceptibilities induced by the opening of the SC gap with RIXS, we investigated the optimally doped double-layer $\mathrm{Bi_2Sr_2CaCu_2O_{8+\delta}}$ (Bi2212, T_c = 90 K) and the triple-layer $\mathrm{Bi_2Sr_2Ca_2Cu_3O_{10+\delta}}$ (Bi2223, T_c = 110 K) compounds. These systems have already been investigated by ARPES revealing an energy gap (including the pseudogap) of the order of 40 and 80 meV, respectively [64, 65]. This means that the energy resolution available nowadays at the ID32 beamline facilitates the detection of the SC order parameter.

In the top panels of Figure 2.14 we report the Cu L_3-edge RIXS spectra measured at $\mathbf{q}_{\|}$ = (0.15, 0.0) r.l.u. with σ incident polarization for both Bi2212 (left panels) and Bi2223 (right panels). The choice of the momentum has been made evaluating the charge susceptibility $\chi_c(\mathbf{q},\,\omega)$ of the system. Figures 2.15(a-b) show the calculated imaginary part of $\chi_c(\mathbf{q},\,\omega)$ in the normal and SC state for Bi2212 using a tight-binding band structure. The constant-$\mathbf{q}$ cut of $\mathrm{Im}\chi_c(\mathbf{q},\,\omega)$ reported in panels c-e suggest that solely at

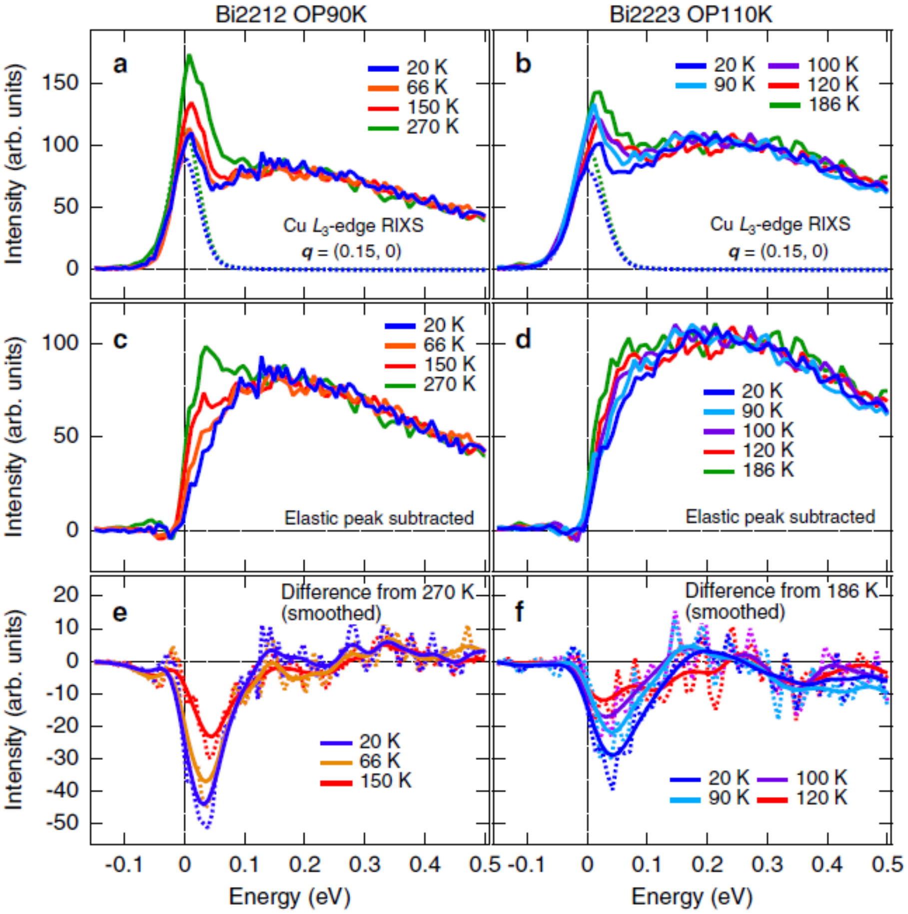

Figure 2.14: a-b) Low energy spectral range of Cu L_3-edge RIXS spectra for Bi2212 and Bi2223 measured at $q = (0.15\ 0.0)$ r.l.u with σ polarization of the incident light at different temperatures, respectively. c-d) RIXS spectra after the subtraction of the elastic lines. e-f) Difference (dotted lines) of the spectra reported in panels c-d) from the highest temperature. Smoothed data are represented by continuous lines. Figure from Ref. [63].

$\mathbf{q}_{\parallel}$=(0.15, 0.0) a clear spectral weight transfer is visible. In fact, this particular momentum value is close to that connecting the antinodal region of two neighboring Fermi surfaces [66]. At $\mathbf{q}_{\parallel}$=(0.4, 0.0) (panel d) the SC-induced changes are almost negligible since at this momentum there are no connection between different part of the Fermi surface. Finally, along the diagonal direction (panel e) the spectral weight transfer is moderate.

The crucial point of our investigations in the study of the SC gap is based on the differences between RIXS spectra taken at temperatures below and above the superconducting critical temperature T_c at different transferred momenta. Since we are looking at differences in the spectral weight in the

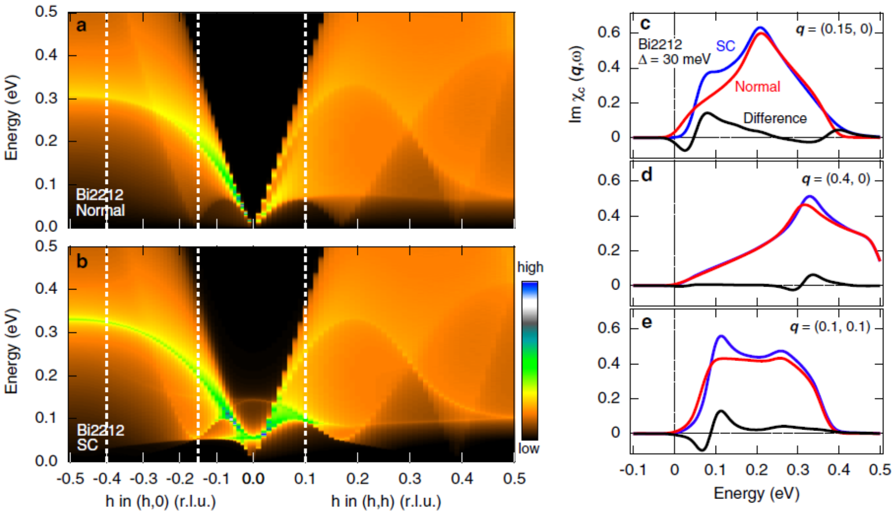

Figure 2.15: Calculated imaginary part of the charge susceptibility χ_c ($\mathbf{q}$, ω) for Bi2212 in the normal (panel a) and in the SC (panel b) states. Panels c-e) show constant-$\mathbf{q}$ cut of Imχ_c ($\mathbf{q}$, ω) in both the normal and SC states together with their difference at selected momenta. Figure from Ref. [63].

energy range below 100 meV, the subtraction of the elastic lines is needed. This procedure has been done by fitting the peak at 0 energy loss with a Gaussian lineshape having a FWHM equal to the energy resolution. The middle panels of Figure 2.14 show the RIXS spectra after the subtraction of the elastic lines. It has to be noted that the remaining spectral weight, where the low-energy electronic excitations give the biggest contribution, is clearly temperature-dependent. By subtracting the spectra from the one measured at highest temperature we can infer about the energy of the SC gap (where we have the maximum spectral reduction), which is around 32 meV in Bi2212 and 42 meV in Bi2223 (bottom panels of Figure 2.14). Moreover, we note the monotonic decrease of the spectral weight as a function of the temperature, according to the monotonic closing of the SC gap and the residual opening of the pseudogap at higher temperature.

With this method we have demonstrated that high-resolution RIXS allows the detection of the SC gap opening which is accompanied by the reduction of the spectral weight across T_c in the low energy spectral range. This experimental determination of the SC order parameter opens the way to new interesting scenarios, such as the possibility to investigate the energy gaps in HTS cuprates where reliable ARPES measurements are absent (*e.g.* YBCO).

Dynamical charge density fluctuations

The summary of the data and analyses discussed in this Paragraph have been published in "*Dynamical charge density fluctuations pervading the phase diagram of a Cu-based high-T_c superconductor*" by R. Arpaia, S. Caprara, R. Fumagalli, G. De Vecchi, Y. Y. Peng, E. Andersson, D. Betto, G. M. De Luca, N. B. Brookes, F. Lombardi, M. Salluzzo, L. Braicovich, C. Di Castro, M. Grilli, and G. Ghiringhelli, *Science* **365**, 6456 (2019).

Charge density waves have been intensively studied in both electron- and hole-doped cuprate families, but their connection (intertwining/competition) with the mechanism of superconductivity remains unclear. More in general, their role in determining the physics of HTS compounds, both at low temperatures, where superconductivity occurs, and at high temperature, where the strange metal phase sets in, has been strongly questioned: the main argument is that they have been found until now only in a limited portion of the HTS phase diagram, both in oxygen doping and in temperature. In the following we will present our recent discovery of charge density fluctuations over a sizable portion of the phase diagram in $Nd_{1+x}Ba_{2-x}Cu_3O_{7-\delta}$ (NBCO) and $YBa_2Cu_3O_{7-\delta}$ (YBCO) thin films, as a function of both doping and temperature [52].

In the three left panels shown in Figure 2.16 we report the quasi-elastic integrated intensity at different temperatures as a function of the in-plane momentum for optimally doped (OP) NBCO, and underdoped (UD) YBCO and NBCO [67, 68]. The quasi-elastic peak in all these samples present two distinct regimes: below 170-190 K, it has a rather strong temperature dependence; above this temperature range it is almost temperature independent. The temperature dependence of the peak at lower temperatures, at the incommensurate wave vector $\mathbf{q}_{\parallel} = (0.31, 0.0)$ r.l.u., is the clear signature of the already well-known charge density waves (CDWs) [45]. Here we have addressed the presence of a not negligible component of the charge order revealed in the quasi-elastic region of the RIXS spectra, even at temperatures well above the CDW onset. In previous works, this quasi-T independent contribution has been treated as a high-temperature background and, as a consequence, not carefully investigated.

In the central panels of Figure 2.16 we explore more in detail the line shape of the quasi-elastic integrated signal. Here we report the fitting results for the sample NBCO UD60 after the subtraction of the background, that has been evaluated from the scan measured along the nodal direction. The fit at low temperature clearly shows the presence of two peaks in momentum space, one broader than the other one. The narrow peak (NP) shows all the characteristics (temperature and doping dependence, correlation length)

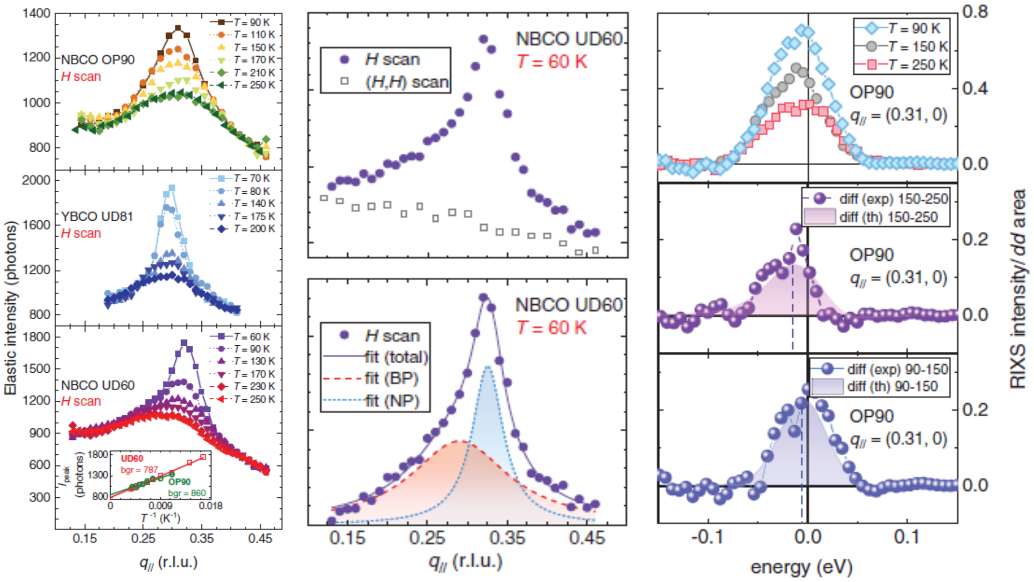

Figure 2.16: Left panels: quasi-elastic integrated intensity extracted from the Cu L_3-edge RIXS spectra measured at different temperatures on optimally doped NBCO ($p \sim 0.17$, $T_c = 90$ K), underdoped YBCO ($p \sim 0.14$, $T_c = 81$ K) and underdoped NBCO ($p \sim 0.11$, $T_c = 60$ K). Middle panels: quasi elastic scan measured along the anti-nodal (H scan) and along the nodal ((H, H) scan) at 60 K. In the bottom panel the fitting procedure (after the background subtraction) underlying the presence of two distinct peaks is illustrated. Left panels: low energy spectral range RIXS measurements on the sample OP90 carried out at different temperatures and centered at the BP wave vector. The bottom panels show the experimental difference spectra. Figure reproduced from Ref. [52].

previously observed in several underdoped cuprates and attributed to the incommensurate CDWs. Whereas the broad peak (BP), which shares with the NP almost the same position in the reciprocal space, can be associated to very short-ranged charge density fluctuations (CDF) having a relatively weak (and almost constant) temperature dependence.

To better characterize the nature of this broad peak we carried out high-resolution RIXS measurements on the sample NBCO OP90 at selected temperatures and at the BP wave vector (top left panel in Figure 2.16). The main idea was to observe a possible dynamical character of the BP, and consequently, assign its energy. Below 100 meV the main spectral contributions are given by phonons and electronic excitations related to charge fluctuations. For this reason, after the subtraction of the phonon contribution, measured on the nodal direction, we have isolated the contribution coming from the charge order. In the bottom left panels reported in Figure 2.16 we have subtracted the high-temperature spectrum from the low temperature ones. The low energy peak of the two spectra at T = 150 K and T = 250 K, where the broad peak dominates the total charge order of the system, is centered at finite energy. As a consequence, also the difference between these two spectra is centered at a finite energy loss ($\sim$ 15 meV), revealing therefore a dynamical character of the BP. Contrarily, the NP shows a static behavior being the spectral difference at low temperature almost negligible. On the contrary, the difference between T = 90 K and T = 150 K is centered almost at zero energy loss, since at low temperatures the charge order is dominated by quasi-static CDW.

In conclusion, despite their intensity, being at low temperatures (*i.e.* below T_{c}) weaker than that of CDW, dynamic CDF do not compete with superconductivity and are pervasive in the HTS phase diagram: they are present even at oxygen doping range, as the overdoped one, where CDW are absent, and up to room temperature. For this reason, CDF are believed the long-sought mechanism which mediates the scattering mechanism in the normal state of HTS and which can therefore explains the anomalous properties of the strange metal phase [69, 70]

Experimental determination of momentum-resolved electron-phonon coupling

The summary of the data and analyses discussed in this Paragraph have been published in "*Experimental determination of momentum-resolved electron-phonon coupling*" by M. Rossi, R. Arpaia, R. Fumagalli, M. Moretti Sala, D. Betto, G. M. De Luca, K. Kummer, J. Van Den Brink, M. Salluzzo, N. B. Brookes, L. Braicovich, and G. Ghiringhelli, *Physical Review Letters* **123**, 027001 (2019).

In this paragraph we will show that thanks to high-resolution RIXS we can estimate the momentum dependence of the electron-phonon coupling (EPC) by taking advantage of the possibility to carry out energy detuned measurements. Already in the BCS theory, the EPC is known to be the key ingredient for the formation of the Cooper pairs in conventional superconductors [17]. In HTS cuprates, as in all the other unconventional superconductors, the role played by the EPC is still under debate and not completely understood [7, 37, 71, 72, 73]. In this scenario, a purely phonon-mediated superconductivity cannot explain the high T_c displayed by optimally doped cuprates, and for this reason the interaction between the electrons with the underlying lattice with the formation of Cooper pairs has to be driven by other mechanisms. Up to now, the EPC has been experimentally investigated by several spectroscopies such as INS [74] and IXS [75], Raman spectroscopy [76] and ARPES [62].

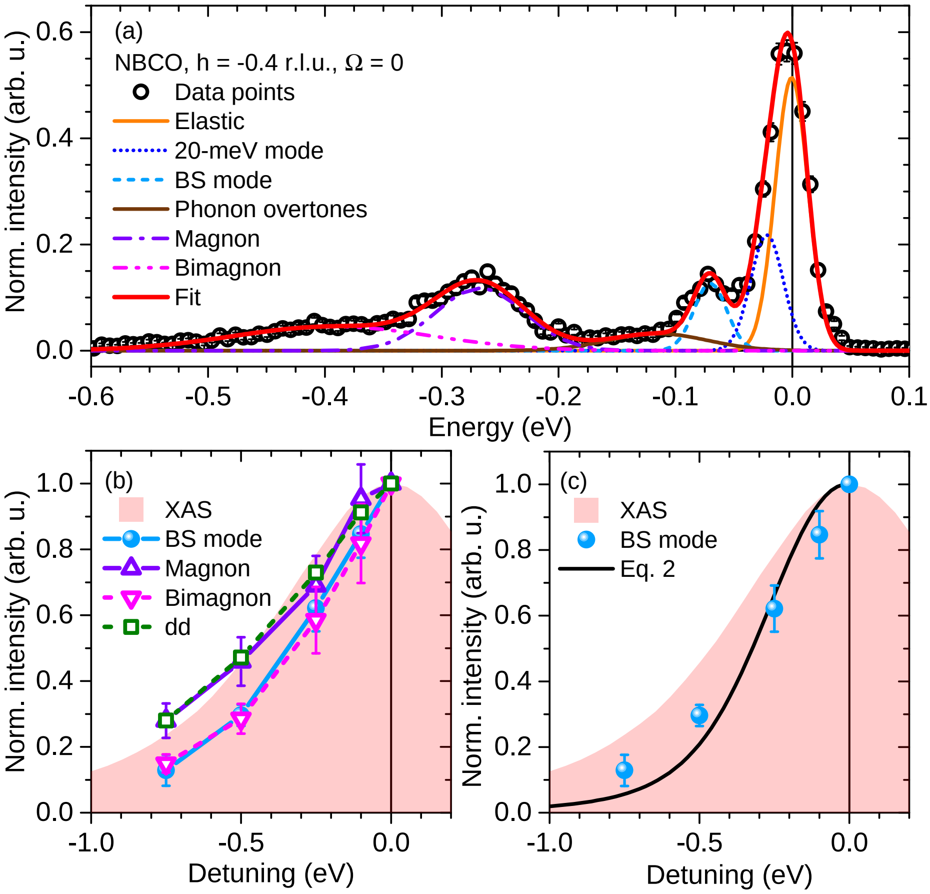

Figure 2.17: a) Representative $NbBa_2Cu_3O_6$ Cu L_3-edge RIXS spectrum (circles) at $q_{\parallel} = 0.4$ r.l.u. measured with σ polarization of the incident radiation. The continuous red line represents the fit of the low-energy spectral range. The single Gaussian features are also plotted. b) The shaded area is the X-ray absorption spectrum while with the detuning dependence of the main spectral features is reported with symbols. Error bars represent 95% confidence intervals on the fitting results. c) Detuning dependence in the particular case of the BS mode (filled circles) and expected theoretical phonon intensity dampening. Figure from Ref. [77].

Recently, it has been theoretically proposed [4, 78] that RIXS can be used for the direct evaluation of the momentum-dependent coupling strength between a given vibrational mode and the photoexcited electron during the RIXS process. Vibrational modes can be probed by RIXS due to the presence of an highly excited intermediate state: at this stage, the presence of an extra-electron in the valence states alters the charge density and consequently the equilibrium positions of the nearby ions, which can be simply described by a superposition of phonons. As a consequence, the intensity of the RIXS phonon peak can be related to the coupling between the photoexcited electron and the phonon [4].

The first approach to determine the EPC from RIXS measurements exploited the ratio between the phonon intensities and their overtones [4, 79, 80, 81, 82, 83]. Unfortunately, this method cannot be applied to cuprates at the Cu L_3-edge, where the phonon overtones are hidden by the other spectral features in the low energy range (charge, magnetic and particle-hole excitations). We thus proposed a novel method suitable for the detection of the EPC in cuprates, by means of RIXS experiments where the incident X-rays energy is detuned away from the Cu L_3 absorption resonance peak [77]. This approach is therefore based on energy-detuned systematic RIXS measurements that allow us to quantify the momentum dependence of the EPC by comparing the measured incidence-energy dependence of a given phonon intensity with predictions based on available theoretical models.

In panel a) of Figure 2.17 we show a representative Cu L_3-edge RIXS spectrum measured at $q_{\|}$ = -0.4 r.l.u.. Beside the magnetic excitations (single- and bi-magnon) we see that the spectrum in the energy range below 0.2 eV is populated by at least two resolution limited phonon modes and their overtones. In this work we focused our attention to the phonon centered at -70 meV, attributed to the in plane Cu-O bond stretching (BS) mode, usually labeled as breathing mode. In the bottom panels of Figure 2.17 we report the integrated intensities (normalized to their intensity value at resonance) of the features highlighted in panel a) as a function of the incident photon energy. Surprisingly, both the intensities of the bimagnon (broad feature at ~-0.4 eV) and of the BS mode deviate from the expected intensity damping given by the XAS (shaded area). On the other hand, the intensity of the magnon and *dd* excitations (not shown in Figure 2.17(a)) follow the the Cu L_3 resonance.

The estimation of the EPC from the detuned peak intensities is based on consideration concerning the effective duration of the scattering process, given by the lifetime of the intermediate state, and its relationship with the detuning energy. The detailed explanation of this approach, which is far beyond the scope of this work, is reported in Ref. [77, 84].

In summary, the main result obtained by applying this pioneering method is in agreement with previous works; moreover, it shows that RIXS can be used for the study of vibrational modes giving access to essential information about the electronic coupling to the lattice and its momentum dependence in quantum materials.

2.6 RIXS cross-section

In this section we will give a general overview of the theoretical background at the basis of the RIXS cross-section. In particular, following the work done by Ament *et al.* [4], we will present and comment the Kramers-Heisenberg relation obtained within the dipole approximation. Finally, we will show how to derive the RIXS cross-section by implementing the Kramers-Heisenberg equation considering solely a single Cu^{2+} ion. In this case, the fact that cuprates can be classified as one-hole systems greatly helps the calculations of the RIXS cross-section for undoped cuprates. The results obtained within this model, usually labeled as single-ion, will be widely used in this thesis for the interpretation of the experimental results.

2.6.1 The Kramers-Heisenberg formula

The Kramers-Heisenberg (KH) formula for a second order process such as RIXS in dipole approximation is written in the following way:

$$\frac{d^2\sigma}{d\hbar\omega d\Omega} = r_e^2 m^2 \omega_{\mathbf{k}_i} \omega_{\mathbf{k}_o}^3 \sum_f \left| \sum_n \sum_{j,j'}^{N} \frac{\langle f|\, \mathcal{D}^\dagger \,|n\rangle \langle n|\, \mathcal{D} \,|g\rangle}{E_g + \hbar\omega_{\mathbf{k}_i} - E_n + i\Gamma_n} \right|^2 \delta(E_g - E_f + \hbar\omega). \tag{2.3}$$

This equation represents the cross-section for the scattering of a photon of energy $\hbar\omega$ by an electron in an atom. In other words, it is an expression of the probability to have the emission of a photon with energy $\hbar\omega + (E_g - E_f)$ in a solid angle $d\Omega$ (here E_g and E_f represent the energy of the initial and final state, respectively). $|g\rangle$, $|n\rangle$ and $|f\rangle$ are the three states involved during the RIXS process characterized by the energies E_g, E_n (energy of the intermediate state) and E_f, respectively. The summations run all over the possible intermediate and final states and all over the electrons (N), while $\mathcal{D}$ represents the dipole operator. Finally, Γ_n takes into account the intrinsic lifetime broadening of the core hole created in the intermediate state, whereas the delta function ensures the overall energy conservation during the process.

2.6.2 Single-ion model and RIXS cross-section calculations

In the straightforward case of cuprates, the KH equation (Eq. 2.3) can be easily implemented especially if we consider that Cu^{2+} ions are in a $3d^9$ electronic configuration, and therefore we can reason in terms of one-hole system. In fact, both the initial and final $3d$ states involved during the RIXS process are filled by one hole, and the same happens in the intermediate state, where a hole is present in the spin-orbit coupled $2p_{3/2}$ states. For the sake of simplicity, the two-steps RIXS process (with three states involved) at the Cu L_3-edge can be readily expressed using the following short notation: $2p^4_{3/2}3d^9$ (initial state) $\rightarrow$ $2p^3_{3/2}3d^{10}$ (intermediate state) $\rightarrow$ $2p^4_{3/2}3d^{9*}$ (final state). The symbol * is related to the final state and denotes that the hole can either occupy the ground state $3d_{x^2-y^2}$ or another $3d$ orbital with different symmetry and/or spin direction. Regarding the spin, each $3d$ state is split due to the super-exchange interaction between the neighboring Cu^{2+} ions, while the weak spin-orbit coupling of the $3d$ states is negligible.

In the following we will assume a $3d_{x^2-y^2}, \downarrow$ ground state, where the arrow is related to the spin direction ($\downarrow$ for spin down and $\uparrow$ for spin up). With this hypothesis, the elastic scattering is characterized by the $3d_{x^2-y^2}, \downarrow$ final state, while the other possible final states involved in the inelastic scattering can be a single spin-flip excitation ($3d_{x^2-y^2}, \uparrow$), a different $3d$ orbital (*e.g.* $3d_{xy}, \downarrow$) or both (*e.g.* $3d_{xy}, \uparrow$).

It is worth mentioning that the Cu^{2+} single-ion model has been widely exploited in the study of the electronic, magnetic and crystal structure in the parent compounds of the HTS cuprates. First of all, it explained the possibility to experimentally probe single spin-flip excitations in layered cuprates [5, 85] where the Cu^{2+} spins always lie in the ab-plane [86, 87, 88, 89, 90]. The explanation is mainly tied to the large spin-orbit coupling of the core-hole in the $2p_{3/2}$ states. Regarding the electronic structure, this model has been successfully applied for the assignment of the energy and symmetry of the Cu $3d$ states, by means of the systematic study of the local dd excitations [11, 91, 92].

Recalling the KH equation (Eq. 2.3), the matrix element of the RIXS amplitude for a given final state f at the Cu L_3-edge can be conveniently written in the following way:

$$\mathcal{A}_f \propto \left| \sum_m \langle f| \mathcal{D}^\dagger_f |2p_{3/2,m}\rangle \langle 2p_{3/2,m}| \mathcal{D}_a |3d_{x^2-y^2}, \downarrow\rangle \right|^2 . \tag{2.4}$$

With this notation we clearly see that the KH formula captures the double RIXS step, where we firstly have the absorption process ($\mathcal{D}_a$) followed by the emission ($\mathcal{D}^\dagger_f$) of a photon carrying information about the specific crystal field excitation. Moreover, it allows to express the scattering probabilities in terms of atomic scattering tensors [93]. The atomic scattering tensor depends on the Cartesian axes (that coincides with the crystallographic axes a, b and

c) in the following way:

$$\mathcal{A}^{\mathrm{RIXS}} = \begin{pmatrix} xx & xy & xz \\ yx & yy & yz \\ zx & zy & zz \end{pmatrix} . \tag{2.5}$$

A detailed analysis of this irreducible representation brings information about the symmetry of a specific excitation.

Here we report the atomic scattering tensors for the elastic $\mathcal{A}^{\mathrm{RIXS}}_{3d_{x^2-y^2},\downarrow}$ and spin-flip $\mathcal{A}^{\mathrm{RIXS}}_{3d_{x^2-y^2},\uparrow}$ excitations probed by RIXS in cuprates:

$$\mathcal{A}^{\mathrm{RIXS}}_{3d_{x^2-y^2},\downarrow} = \begin{pmatrix} 2 & 0 & 0 \\ 0 & 2 & 0 \\ 0 & 0 & 0 \end{pmatrix} \tag{2.6}$$

$$\mathcal{A}^{\mathrm{RIXS}}_{3d_{x^2-y^2},\uparrow} = \begin{pmatrix} 0 & -i & 0 \\ i & 0 & 0 \\ 0 & 0 & 0 \end{pmatrix} . \tag{2.7}$$

These two cases have a relatively simple form, since for elastic and spin-flip excitations probed by RIXS there is no change in the orbital symmetry between the initial and final state. By carefully studying the scattering tensors it is possible to retrieve a lot of information about the excitation under study. In the case of the elastic scattering, for example, there is no transfer of angular momentum from the photon to the system due to the conservation of the total angular momentum. As a consequence, the atomic scattering tensor (Eq. 2.6) is diagonal. Whereas in the case of a single spin-flip excitation, an angular momentum transfer is needed in order to actually rotate the spin, and not surprisingly the scattering tensor reported in Eq. 2.7 shows non zero off-diagonal elements [89, 90].

Regarding excitations accompanied by a change of the orbital symmetry, that is the case off *dd* excitations, the scattering tensors have a more complex form and they will be widely discussed in Chapter 3.

In order to extract useful information by comparing the calculations with the experimental results, we have to take into account also the scattering geometry and the photons polarization. For this purpose, we can express the RIXS amplitudes as in the following

$$\mathcal{A}^{\mathrm{RIXS}}_{f} \equiv \boldsymbol{\epsilon}'^{*}_{o} \, \mathcal{A}_{f} \, \boldsymbol{\epsilon}_{i} \tag{2.8}$$

where the terms $\boldsymbol{\epsilon}_{i,o}$ bring information about the scattering geometry and the polarization of the ingoing and outgoing photons.

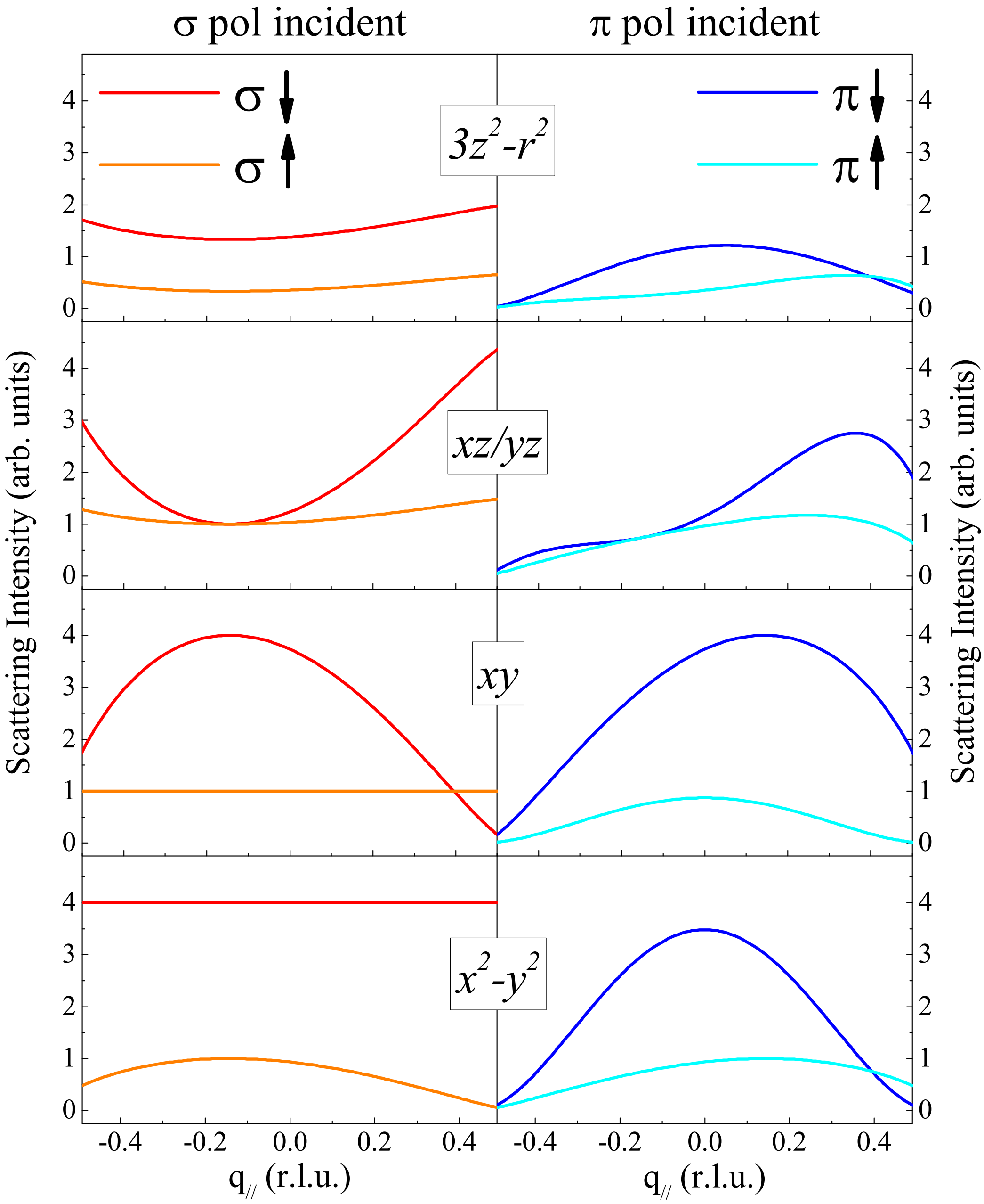

Figure 2.18: In-plane momentum dependence of single ion Cu^{2+} L_3-edge RIXS cross-sections for σ (left) and π (right) polarization of the incident light. For these results the scattering angle was fixed at $2\theta = 150°$ and the scattering plane parallel to the *ac* sample plane. The arrows denotes the direction of the Cu spin. All the possible RIXS final states are reported.

The results of the RIXS cross-sections calculations applied to the cuprates case have been widely discussed in Refs. [11, 50] and as a function of different scattering geometries. In Figure 2.18 we report the results of the calculations for all the possible RIXS final states as a function of the in-plane momentum $q_{\|}$. It has to be underlined that most of the cuprates have a tetragonal (D_{4h}) symmetry, and consequently the t_{2g} $3d_{xz}$ and $3d_{yz}$ states are degenerate. To facilitate the comparison between the calculations and the experimental results presented in this thesis, the scattering angle has been fixed to 150° and we have also considered both the incident linear polarizations of the light (σ and π).

In the last Section of this Chapter we will recall the RIXS cross-sections calculated within the single-ion model interpreted in terms of Stokes parameters. This novel approach will be extremely useful for the understanding of the polarization-resolved experimental findings.

2.7 Polarization analysis

As introduced in the previous Section, the possibility to perform the polarization analysis of the scattered X-rays greatly helps the disentanglement of selected spectral features, especially when their intrinsic broadening or quasi-degeneracy makes high-energy resolution partially insufficient.

The main idea behind the polarization analysis of the scattered photons in the soft X-ray regime lies in the possibility to exploit the polarization dependence of the reflectivity. In fact, differently from the hard X-rays, Bragg optics based on crystals cannot be implemented due to their low efficiency. To overcome this limitation, a prototype of a polarimeter device based on a graded multi-layered (ML) mirror had been successfully installed and tested on the AXES spectrometer of the old ID08 beamline of the ESRF [94, 95].

The idea behind the new polarimetric device installed on the ERIXS spectrometer follows the same concepts: the W/B_4C graded ML mirror exploits the different sensitivity of the reflectivity for the two linearly polarized channels, namely π and σ. In order to keep the reflectivity constant over several eVs, the graded ML has been designed with a period that changes linearly along one specific direction on its surface, consistently with the photon energy dispersion of ERIXS at the position of the ML.

Differently from AXES, however, this new device delivers horizontally collimated radiation, which means that the incident angle is the same for all the photons. The polarimeter is installed just before the CCD cameras (see Figure 2.9): in this way, the multilayer can be translated to intercept the straight path of the scattered photons by the sample and used to deflect them towards the second CCD camera (CCD2). In order to fulfill these requirements, the period of the ML changes along the dispersion direction to match the energies of the photons scattered by the grating G2, as schematically shown in Figure 2.19.

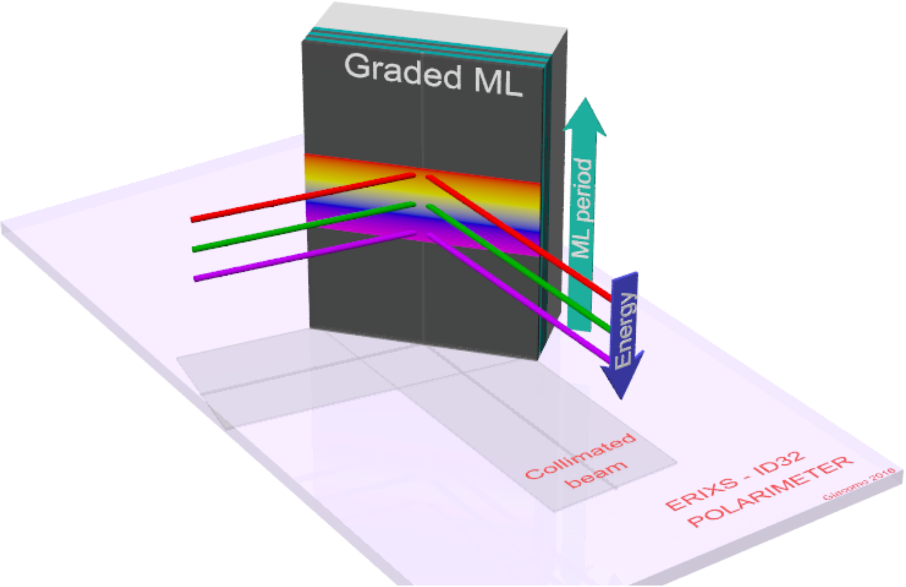

Figure 2.19: Schematic representation of the polarimetric device based on a graded multi-layered mirror in a grating spectrometer such as ERIXS. Figure from Ref. [8].

Moreover, the ML works with an intermediate incident angle and fulfills the Bragg condition at the chosen photon energy in order to have a slightly larger reflectivity for the σ' channel. In fact we do not work at the Brewster angle for X-rays (45°), where we could in principle entirely suppress the π' channel, because the σ' signal would have a too much reduced reflectivity ($R_{\sigma'} \approx 0.012$). For this reason, the nominal working angle of the ML is $\sim 20°$, which leads to reflectivities $R_{\sigma'}$ and $R_{\pi'}$ for the σ and π components of the order of 0.14 and 0.085, respectively. Hereafter we will refer to the scattered polarization with an apex (*e.g.* σ' and π'), while with the unprimed symbols will be used to describe the incident polarization. We can thus define the average reflectivity of the ML mirror as $R_0 = (R_{\sigma'} + R_{\pi'})/2$, which is in our case approximately 11.2%. In summary, the overall system can be viewed as a filter with relatively small efficiency and preferred transmission of the σ' component with respect to π'.

The ability to disentangle the spectral features of complex RIXS spectra is crucial to pinpoint the various contributions to the lattice, magnetic and electronic dynamics at play in high-T_c superconducting systems. Nowadays, only at the ID32 beamline of the ESRF it is possible to perform polarization resolved RIXS measurements which played a crucial role in many cases, such as, for example, the confirmation of previous assignment of orbital and spin excitations in undoped NBCO and in the estimation of the spin-flip contribution at all dopings [60] (this work will be presented in Chapter 3). Moreover, polarization-resolved measurements confirmed the charge nature of the ordering discovered in the overdoped region of $(Bi,Pb)_2(Sr,La)_2CuO_{6+\delta}$ [96] (see Chapter 4), the assignment to spin excitations of the enhanced dynamic response at the charge order vector in $Nd_{2-x}Ce_xCuO_4$ [97] and finally the confirmation of the charge nature of the fast-dispersing zone-center excitations in $La_{2-x}Ce_xCuO_4$ [54] (see Chapter 4). The polarization analysis has been applied also to systems other than cuprates, that is the case of $CeRh_2Si_2$, where the use of the polarimeter allowed to assign the energy and symmetry of *ff* excitations [98].

Poincaré sphere and Stokes parameters

In this Section we will describe the method used to extract the information about the polarization dependence of the scattered X-rays, mainly following the procedure reported in Refs. [60, 94]. The polarization-resolved RIXS analysis is obtained taking advantage of the difference in the ML reflectivity and by combining two independent measurements: one polarization-unresolved spectrum collected on the CCD1 along the straight path of the scattered photons (I, “direct” beam) and the other one after being deflected by the ML onto the CCD2 camera (I_M).

At this point we need a method that allow us to describe the polarization state of the light. Hereafter we will adopt the approach based on the Stokes parameters and Poincaré sphere [9, 10], that will be extremely useful since Stokes parameters are measurable quantities that can be directly connected to our experimental findings.

The polarization state of the electromagnetic (EM) radiation is commonly described by an ellipse, as depicted in Figure 2.20(a). Once the orientation and the ellipticity angles are defined, any polarization state of the light can be expressed by the complex components of the electric field ($\mathbf{E}$) in the coordinate axes ($\boldsymbol{\epsilon}_\sigma$ and $\boldsymbol{\epsilon}_\pi$) perpendicularly to the propagation direction defined by the wave vector $\mathbf{K}$ [99, 100, 101, 102]. Combining appropriately the phase and amplitude of the electric field it is possible to describe the polarization state of an EM wave, including linearly (horizontal or vertical with respect to the laboratory frame), right or left circularly and linear $\pm \frac{\pi}{4}$ polarized light. The latter two cases are usually expressed as a combination of linear polarizations.

The polarization state of an electromagnetic wave is usually described by

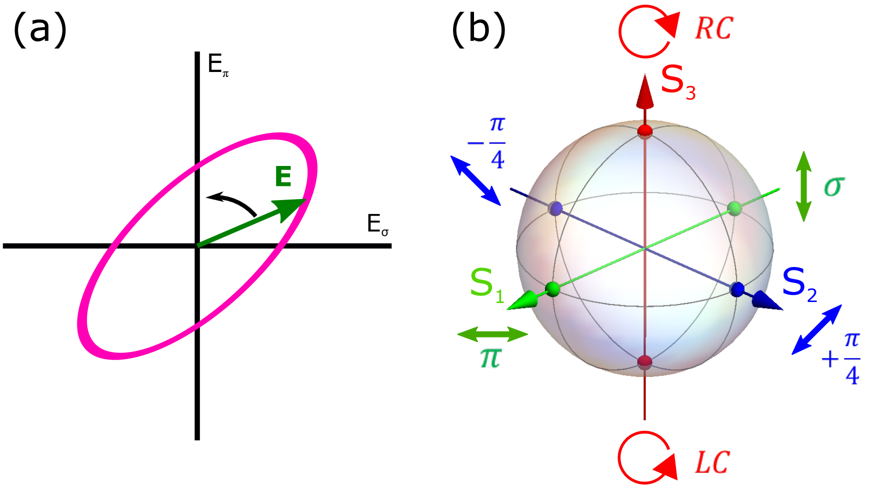

Figure 2.20: a). Polarization ellipse. All the possible light polarized states can be expressed as a function of the two linear polarized state horizontal (π) and vertical (σ). b). Schematic representation of the Poincaré sphere where the Cartesian coordinates represent the three Stokes parameters S_1, S_2 and S_3.

the quantities known as Jones vectors that can be written in the following way [103]:

$$\mathbf{E} = \begin{bmatrix} E_\sigma \\ E_\pi \end{bmatrix} = \begin{bmatrix} |E_\sigma| e^{i\delta_\sigma} \\ |E_\pi| e^{i\delta_\pi} \end{bmatrix} . \tag{2.9}$$

By applying the formalism of the Jones matrices we can easily take into account the action of any optical element, for example a graded ML mirror, on the properties of the electromagnetic radiation. In this specific case, the Jones matrix $\mathcal{J}$ for the reflection reads [104]

$$\mathcal{J}_R = \begin{bmatrix} -\sqrt{R_\sigma} & 0 \\ 0 & \sqrt{R_\pi} \end{bmatrix} \tag{2.10}$$

and the respective Jones vectors of the reflected radiation are thus given by [103, 99]

$$\mathbf{E}_r = \mathcal{J}_r \mathbf{E} = \begin{bmatrix} -\sqrt{R_\sigma} E_\sigma \\ \sqrt{R_\pi} E_\pi \end{bmatrix} = \begin{bmatrix} -\sqrt{R_\sigma} |E_\sigma| e^{i\delta_\sigma} \\ \sqrt{R_\pi} |E_\pi| e^{i\delta_\pi} \end{bmatrix} . \tag{2.11}$$

Though these quantities are not directly accessible during a RIXS experiment since the information about the phase is lost when measuring the intensities, they can be used to introduce the Stokes vector **S** based on the four Stokes parameters [9, 10]. The relationship between Stokes and Jones vectors can be written in the following way [99, 100]:

$$\begin{aligned}
\mathbf{S} &= \begin{bmatrix} S_0 \\ S_1 \\ S_2 \\ S_3 \end{bmatrix} = \begin{bmatrix} |E_\sigma|^2 + |E_\pi|^2 \\ |E_\sigma|^2 - |E_\pi|^2 \\ \frac{1}{2}\left(|E_\sigma + E_\pi|^2 - |E_\sigma - E_\pi|^2\right) \\ \frac{1}{2}\left(|E_\sigma - \imath E_\pi|^2 - |E_\sigma + \imath E_\pi|^2\right) \end{bmatrix} = \\
&= \begin{bmatrix} E_\sigma E_\sigma^* + E_\pi E_\pi^* \\ E_\sigma E_\sigma^* - E_\pi E_\pi^* \\ E_\sigma E_\pi^* + E_\sigma^* E_\pi \\ \imath(E_\sigma E_\pi^* - E_\sigma^* E_\pi) \end{bmatrix} = \begin{bmatrix} E_\sigma E_\sigma^* + E_\pi E_\pi^* \\ E_\sigma E_\sigma^* - E_\pi E_\pi^* \\ 2\,\mathrm{Re}\{E_\sigma E_\pi^*\} \\ 2\,\mathrm{Im}\{E_\sigma^* E_\pi\} \end{bmatrix} = \\
&= \begin{bmatrix} |E_\sigma|^2 + |E_\pi|^2 \\ |E_\sigma|^2 - |E_\pi|^2 \\ 2|E_\sigma||E_\pi|\cos(\delta_\sigma - \delta_\pi) \\ -2|E_\sigma||E_\pi|\sin(\delta_\sigma - \delta_\pi) \end{bmatrix}.
\end{aligned} \tag{2.12}$$

Here the four components of the Stokes vector **S** represent the total intensity of the electromagnetic radiation (S_0) and the degrees of the linear (S_1 and S_2) and circular (S_3) polarization. Since only the degenerate polarization states of the light can be expressed using an ellipse, Poincaré introduced the use of a sphere to represent and describe all possible light polarization states (see Figure 2.20(b)). Here the circular polarized light represents the north and south poles of the sphere, whereas all the linear polarization states lie on the equator.

As a consequence, one can define the Poincaré-Stokes parameters $P_i = S_i/S_0$ $(i = 1, 2, 3)$ [99, 100] where it is generally true that $S_1^2 + S_2^2 + S_3^2 \leq S_0^2$ $(P_1^2 + P_2^2 + P_3^2 \leq 1)$. The case of the equality in the last relationship means that we are dealing with fully polarized radiation, in which case the Poincaré-Stokes parameters define a point on the so-called Poincaré sphere of unit radius, as illustrated in Figure 2.20(b).

Defining the Müller matrix as $\mathcal{M} = A(\mathcal{J}^* \otimes \mathcal{J})A^{-1}$ [99], where

$$A = \begin{bmatrix} 1 & 0 & 0 & 1 \\ 1 & 0 & 0 & -1 \\ 0 & 1 & 1 & 0 \\ 0 & \imath & -\imath & 0 \end{bmatrix}, \tag{2.13}$$

one can write it down considering the action of reflection optics in the following way:

$$\mathcal{M}_R = \begin{bmatrix} \frac{1}{2}(R_\sigma + R_\pi) & \frac{1}{2}(R_\sigma - R_\pi) & 0 & 0 \\ \frac{1}{2}(R_\sigma - R_\pi) & \frac{1}{2}(R_\sigma + R_\pi) & 0 & 0 \\ 0 & 0 & \sqrt{R_\sigma R_\pi} & 0 \\ 0 & 0 & 0 & \sqrt{R_\sigma R_\pi} \end{bmatrix} . \tag{2.14}$$

The action of $\mathcal{M}_R$ is used to describe how the Stokes vector $\mathbf{S}$, that characterizes a given electromagnetic radiation, is affected by the reflection from an optical element. The result is

$$\mathbf{S}_r = \mathcal{M}_r \mathbf{S} = \begin{bmatrix} S_{R,0} \\ S_{R,1} \\ S_{R,2} \\ S_{R,3} \end{bmatrix} = \begin{bmatrix} \frac{1}{2}\left[R_\sigma(S_0 + S_1) + R_\pi(S_0 - S_1)\right] \\ \frac{1}{2}\left[R_\sigma(S_0 + S_1) - R_\pi(S_0 - S_1)\right] \\ \sqrt{R_\sigma R_\pi} S_2 \\ \sqrt{R_\sigma R_\pi} S_3 \end{bmatrix} , \tag{2.15}$$

where $S_{R,0}$ is the total intensity of the reflected electromagnetic radiation and similarly for the other Stokes parameters $S_{R,i}$ (i = 1,2,3).

Spectral decomposition

As previously mentioned, the polarization-resolved RIXS spectrum is obtained by combining the polarization-unresolved measurement I with the one reflected by the multi-layered mirror I_M. Having introduced the formalism based on the Stokes parameters, we can therefore introduce the Stokes vector that models the two different acquisitions I and I_M.

For the direct beam we have:

$$\mathbf{S} = \begin{bmatrix} S_0 \\ S_1 \\ S_2 \\ S_3 \end{bmatrix} = \begin{bmatrix} |E_{\sigma'}|^2 + |E_{\pi'}|^2 \\ |E_{\sigma'}|^2 - |E_{\pi'}|^2 \\ \frac{1}{2}\left(|E_{\sigma'} + E_{\pi'}|^2 - |E_{\sigma'} - E_{\pi'}|^2\right) \\ \frac{1}{2}\left(|E_{\sigma'} - \imath E_{\pi'}|^2 - |E_{\sigma'} + \imath E_{\pi'}|^2\right) \end{bmatrix} , \tag{2.16}$$

where $S_0 = |E_{\sigma'}|^2 + |E_{\pi'}|^2 = I$ represents the total intensity of the scattered radiation as measured on the detector. Following the general procedure introduced above, the Poincaré-Stokes parameters read $P_i = S_i/S_0$ ($i = 1, 2, 3$) [99, 100]. Whereas for the beam reflected by the multilayer the Stokes parameters can be obtained from $\mathbf{S}_M = \mathcal{M}\mathbf{S}$, where $\mathcal{M}$ is the Müller matrix for reflection by an optical elements. In this way, similarly to Eq. 2.15, we get

$$\mathbf{S}_M = \begin{bmatrix} S_{M,0} \\ S_{M,1} \\ S_{M,2} \\ S_{M,3} \end{bmatrix} = \begin{bmatrix} \frac{1}{2}\left[R_{\sigma'}(S_0+S_1)+R_{\pi'}(S_0-S_1)\right] \\ \frac{1}{2}\left[R_{\sigma'}(S_0+S_1)-R_{\pi'}(S_0-S_1)\right] \\ \sqrt{R_{\sigma'}R_{\pi'}}S_2 \\ \sqrt{R_{\sigma'}R_{\pi'}}S_3 \end{bmatrix}, \tag{2.17}$$

where $S_{M,0} = I_M$ is the total intensity of the beam after being reflected by the ML. Differently from Eq. 2.15, here we have made explicit the dependence on the polarization of the scattered photons (σ' and π').

It is important to underline that all the polarization states usually contribute to define the intensity of the spectrum I_M via their projection on the coordinate axes $\boldsymbol{\epsilon}_{\sigma',\pi'}$. In order to extract the two linearly polarized components in a RIXS spectrum we assume that the scattered X-rays are fully linearly polarized leading to have $|S_1| = S_0$ ($|P_1| = 1$) and $S_2 = S_3 = 0$ ($P_2 = P_3 = 0$). In the analysis of polarization-resolved RIXS spectra of $NdBa_2Cu_3O_{7-\delta}$ presented in Chapter 3 we will justify this assumption (except few cases). Under this hypothesis, the polarization-resolved intensities of the scattered beam by the multilayer are defined as

$$I_{\sigma',\pi'} = \frac{S_0 \pm S_1}{2} = \frac{I \pm S_1}{2}, \tag{2.18}$$

with

$$S_1 = \frac{1}{A}\left(\frac{S_{M,0}}{R_0} - S_0\right) = \frac{1}{A}\left(\frac{I_M}{R_0} - I\right) \tag{2.19}$$

and

$$A = \frac{R_{\sigma'} - R_{\pi'}}{R_{\sigma'} + R_{\pi'}} = \frac{R_{\sigma'} - R_{\pi'}}{2R_0}. \tag{2.20}$$

A represents the multilayer polarization sensitivity ($A \approx 0.25$), equivalent to the Sherman function of Mott detectors for spin-resolved photoemission experiments [105]. This formalism will be used in Chapter 3 to describe the polarization-resolved RIXS spectra in terms of Stokes parameters within the framework of the single-ion model.

Self-absorption corrections

It is well established that the knowledge of the scattered photons polarization state has a crucial relevance in the determination of the self-absorption corrections [95]. Indeed, in a RIXS experiment the self-absorption of the outgoing photons modifies the overall line shape of the spectra. Due to the resonance process, the scattered photons are in general strongly re-absorbed at small energy losses. Morevoer, the absorption coefficient depends on the photon polarization, and, as a consequence, also the self-absorption process itself. With the possibility to discriminate the polarization of the scattered beam it is therefore possible to correct this unwanted effect more carefully than in the case of unpolarized RIXS measurements.

By taking the advantage of the polarization resolution of the scattered radiation, we applied the self-absorption corrections to most of the polarization-resolved RIXS measurements discussed in this thesis following the procedure presented in the Supplemental Material of Ref. [95].

For this purpose, we define the correction factor $C_{\boldsymbol{\epsilon},\boldsymbol{\epsilon}'}(\omega_1,\omega_2)$ that depends on the energy ω_1 (ω_2) and polarization $\boldsymbol{\epsilon}$ ($\boldsymbol{\epsilon}'$) of the incident (scattered) photons.

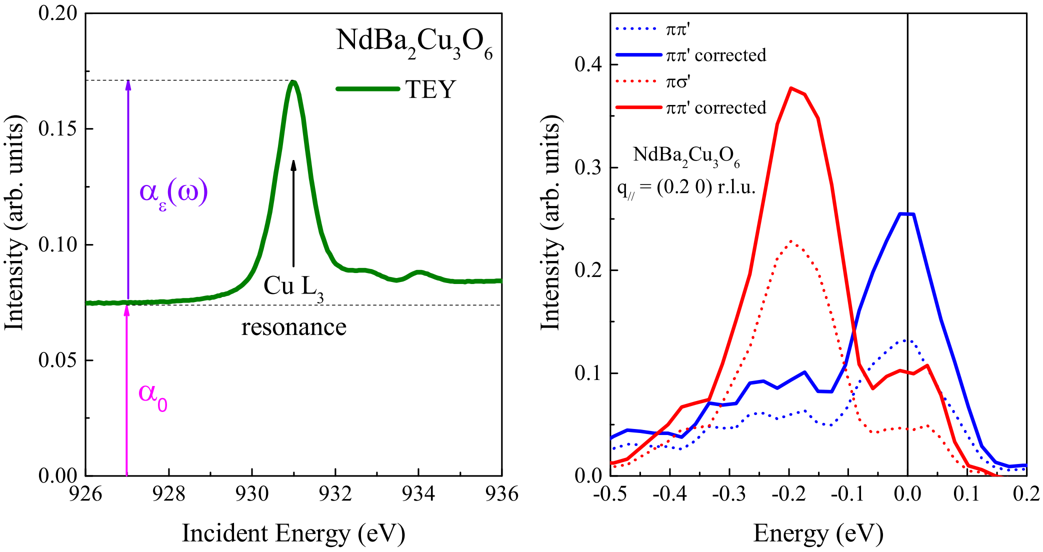

Figure 2.21: Left panel: X-ray absorption (XAS) of NBCO measured with π polarization of the incident light. Right panel: example of self-absorption correction for both the $\pi\pi'$ and $\pi\sigma'$ channels.

Hence, the intensity of the measured RIXS spectrum $I^{\text{meas}}_{\boldsymbol{\epsilon}'}(\omega_2)$ can be related to the corrected one $I^{\text{corr}}_{\boldsymbol{\epsilon}'}(\omega_2)$ by

$$I^{\text{corr}}_{\boldsymbol{\epsilon}'}(\omega_2) = \frac{I^{\text{meas}}_{\boldsymbol{\epsilon}'}(\omega_2)}{C_{\boldsymbol{\epsilon},\boldsymbol{\epsilon}'}(\omega_1,\omega_2)}, \tag{2.21}$$

where the correction factor is obtained in the following way:

$$C_{\boldsymbol{\epsilon},\boldsymbol{\epsilon}'}(\omega_1,\omega_2) = \frac{1}{1 + t_{\boldsymbol{\epsilon},\boldsymbol{\epsilon}'}(\omega_1,\omega_2)u}. \tag{2.22}$$

The experimental scattering geometry is taken into account by the geometrical factor $u = \cos(\theta_{in})/\cos(\theta_{out})$ that depends on the photon angles of incidence (θ_{in}) and scattering (θ_{out}) as measured from the normal (usually the sample c axis) to the sample surface (see Figure 2.12(a)) and by the factor $t_{\boldsymbol{\epsilon},\boldsymbol{\epsilon}'}(\omega_1, \omega_2)$, defined as

$$t_{\boldsymbol{\epsilon},\boldsymbol{\epsilon}'}(\omega_1, \omega_2) = \frac{\alpha_0 + \alpha_{\boldsymbol{\epsilon}'}(\omega_2)}{\alpha_0 + \alpha_{\boldsymbol{\epsilon}}(\omega_1)}. \tag{2.23}$$

Here α_0 and $\alpha_{\boldsymbol{\epsilon}}(\omega)$ are parameters that can be experimentally determined and are related to the non-resonant and resonant part of the absorption coefficient, respectively (right panel in Figure 2.21). Due to the large anisotropy of the $3d$ orbitals in cuprates, the absorption coefficient $\alpha_\epsilon(\omega)$ greatly differ depending on the orientation of the polarization vector with respect to the sample crystallographic directions. For example, the absorption process at resonance (Cu L_3-edge in our case) is maximized when ϵ is perpendicular with respect to the sample c axis orientation [13]. We anticipate here that at low energy losses (where phonons and magnetic excitations play the biggest role) the difference between the correction factors for the two possible linearly polarization states of the scattered light does not exceed $\approx 20\%$, while in case of dd excitations with higher energy losses the self-absorption correction is negligible.

In the right panel of Figure 2.21 we show an example of self-absorption correction applied to a polarization-resolved RIXS measurement carried out on NBCO. The correction has been applied for both the σ' and π' channels and we note how it differently affects the intensities of the decomposed spectra. In Chapter 3 we will show the $C_{\boldsymbol{\epsilon},\boldsymbol{\epsilon}'}(\omega_1, \omega_2)$ factor obtained for different selected in-plane momenta for both the cases with σ and π incident polarizations.

Error bars

The uncertainty related to the error propagation in the polarization analysis of a RIXS spectrum is non-trivial. The main reason is that the spectral decomposition in its linearly polarized components is indirectly obtained from the measurements of two independent spectra, the direct beam (I) and the one reflected by the multi-layered mirror (I_M). In this Section we will derive the procedure to calculate the error bars for polarization-resolved RIXS measurements mainly following the same approach used for spin-resolved photoemission with Mott detectors [105].

Due to the low efficiency of the multi-layered mirror, the two RIXS spectra I and I_M are usually collected with different acquisition times ($\tau < \tau_M$). Recalling the multilayer reflectivities $R_{\pi'}$ ($R_{\sigma'}$) for the π (σ) polarization channel, and assuming that $n_{\pi'}$ and $n_{\sigma'}$ are the energy-dependent numbers of photons impinging the detectors per unit time in the two different polarization cases, we have that

$$\begin{aligned} I &= (n_{\pi'} + n_{\sigma'})\tau = n\tau && (2.24) \\ I_M &= (R_\pi n_{\pi'} + R_{\sigma'} n_{\sigma'})\tau_M = n_M \tau_M && (2.25) \end{aligned}$$

are the total numbers of photons detected on the two CCD cameras (CCD1 and CCD2, see Figure 2.9). The reflectivity of the ML can be written as $R_{\sigma,\pi} = R_0(1 \mp A)$, where A is the Sherman constant (Eq. 2.20) and R_0 is the average reflectivity of the multilayer previously defined. In order to get the formulas for the error bars, we define the degree of linear polarization as

$$P = \frac{n_{\sigma'} - n_{\pi'}}{n_{\sigma'} + n_{\pi'}}, \tag{2.26}$$

and thus the measured asymmetry between I and I_M in the following way

$$D = AP = \frac{I_M \tau}{I \tau_M R_0} - 1. \tag{2.27}$$

Since $I + I_M$ gives the total number of the detected photons during an outgoing polarization-resolved RIXS measurement, and considering a Poisson statistical distribution of uncertainties, the error bars for both π and σ polarization channels are given by

$$\begin{aligned} \Delta D &= \left[\left(\frac{\partial D}{\partial I} \right)^2 \left(\Delta I \right)^2 + + \left(\frac{\partial D}{\partial I_M} \right)^2 \left(\Delta I_M \right)^2 \right]^{1/2} = \\ &= \frac{\tau}{\tau_M R_0} \sqrt{\frac{{I_M}^2 + I_M I}{I^3}}. && (2.28) \end{aligned}$$

Here ΔI and ΔI_M are the different error bars of the direct beam and the beam past the multilayer intensities, respectively. Having introduced the degree of photon polarization P, we can rewrite the two terms $n_{\pi',\sigma'}$ as

$$n_{\pi',\sigma'}(\omega_2) = (1 \mp P) \frac{I}{2\tau}. \tag{2.29}$$

Since $\Delta P = \Delta D / A$, Eq. 2.28 can be casted in the form

$$\Delta n_{\pi',\sigma'} = \frac{1}{2A\tau_M R_0} \sqrt{\frac{{I_M}^2 + I_M I}{I}}, \tag{2.30}$$

or, alternatively,

$$\begin{aligned} \Delta I_{\pi',\sigma'} &= \tau \Delta n_{\pi',\sigma'} = \\ &= \frac{\tau}{2A\tau_M R_0} \sqrt{\frac{{I_M}^2 + I_M I}{I}}. && (2.31) \end{aligned}$$

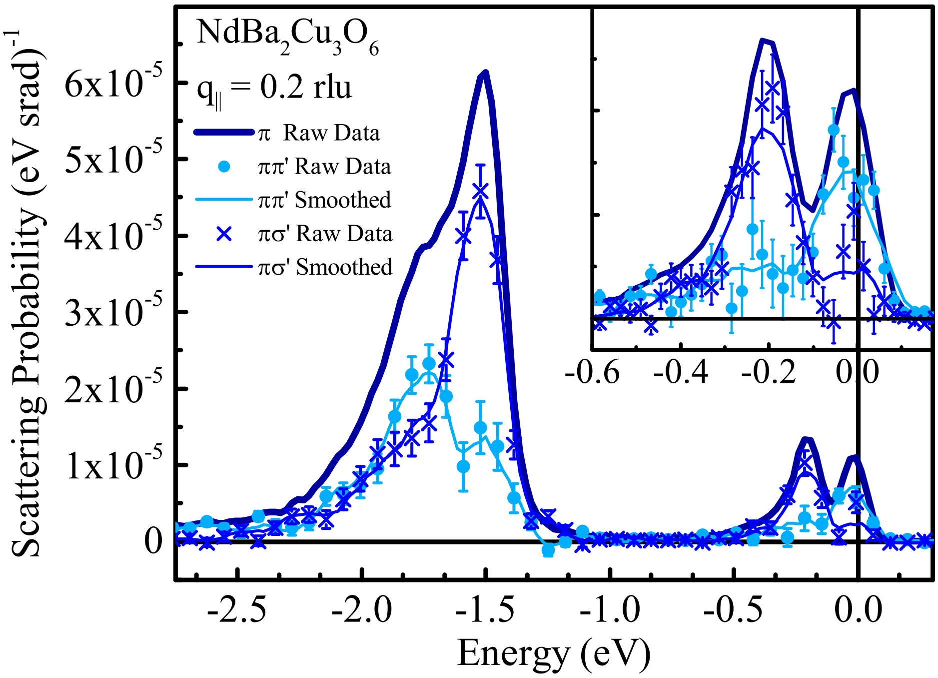

Figure 2.22: Example of polarization-resolved RIXS spectrum of $\mathrm{NdBa_2Cu_3O_6}$ measured with incident π polarization at in-plane momentum $q_{\|}$=0.2 r.l.u.. In the inset the close view of the low-energy excitations is shown. The error bars are calculated on raw data, while continuous lines represent data smoothed on seven points. For clarity, we show only every second data point (symbols).Figure from Ref. [60].

Figure 2.22 shows an example of polarization-resolved RIXS spectrum of undoped NBCO where we report the error bars calculated with the procedure described in this section. The interpretation about the polarization state of the different spectral features will be discussed in Chapter 3. Finally, from Eq. 2.31 we notice that if the total number of accumulated counts is roughly the same for the direct beam and the beam reflected by the multilayer, we have $I \simeq I_M$, implying that $\tau_M \simeq \tau/R_0$ and $\Delta I_{\pi',\sigma'} \simeq \sqrt{n(\omega_2)}/(A\sqrt{2})$.

CHAPTER 3

Polarization resolved Cu L_3-edge resonant inelastic X-ray scattering of orbital and spin excitations in $NdBa_2Cu_3O_{7-\delta}$

The data and analyses discussed in this Chapter have been published in "*Polarization resolved Cu L_3-edge resonant inelastic X-ray scattering of orbital and spin excitations in $NdBa_2Cu_3O_{7-\delta}$*", by R. Fumagalli, L. Braicovich, M. Minola, Y. Y. Peng, K. Kummer, D. Betto, M. Rossi, E. Lefranois, C. Morawe, M. Salluzzo, H. Suzuki, F. Yakhou, M. Le Tacon, B. Keimer, N. B. Brookes, M. Moretti Sala, and G. Ghiringhelli, Physical Review B **99**, 134517 (2019) and selected as an Editor's Suggestion.

In this Chapter we present a systematic RIXS study of orbital, magnetic and vibrational excitations in a prototypical cuprate system ($NdBa_2Cu_3O_{7-\delta}$, from now on NBCO). We measured Cu L_3-edge RIXS spectra of undoped, underdoped and optimally doped NBCO films at different in-plane momenta with both perpendicular and parallel (with respect to the scattering plane) polarization of the incident X-rays. The experimental dataset allows to unequivocally determine the polarization dependence and the evolution of electronic *dd* excitations as a function of doping and scattering geometry. Moreover, we show that the polarimetric device, a polarization-selective optical element based on a multilayer, can provide crucial insights to disentangle the different contributions in the low energy scale due to spin and phonon excitations. Finally, we discuss the interpretation of the experimental data within the framework of the single-ion model [11] and in terms of Stokes parameters [9, 10].

Contents

3.1 Introduction

Since the discovery of high T_c copper-based superconductors [6] many vigorous attempts have been deployed to the understanding of the microscopic mechanism beyond unconventional superconductivity. Despite several experimental findings and theoretical models proposed, an exhaustive and generally accepted explanation of this phenomenon is still missing.

In Chapter 1 we have introduced the general properties of superconducting cuprates, especially underlying the complexity of their phase diagram [7], which is the result of the interplay between antiferromagnetism (AFM), strong electronic correlation, different incipient orders and low dimensionality. Since the advent of RIXS technique as a powerful tool for the study of different degrees of freedom such as spin, charge and orbital in copper-based superconductors, a step forward has been taken in the understanding of these fascinating materials. Besides the discovery of incommensurate long-range charge density fluctuations in the "123" family [45] and subsequently in all the other hole [46, 47, 48] and electron [49] doped cuprates, it has been demonstrated that RIXS is a valuable tool to probe magnetic excitations in the parent compounds of HTS cuprate [85]. Furthermore, RIXS has shown that a short-range antiferromagnetism persists up to a very high doping level, even above the optimal one [22]. Therefore, whereas some orders such as charge density waves seem to compete with superconductivity and magnetic fields are known to suppress it, the presence of spin fluctuations even in doped compounds suggest that magnetism can have a crucial role in the formation of Cooper pairs [71].

The recent impressive developments in soft RIXS instrumentations and optics have opened new scenarios regarding the accessible excitations. In particular, thanks to the high quality performances of the ERIXS spectrometer in terms of efficiency and energy resolution ($\sim$ 30 meV at the Cu L_3-edge, an energy scale where most of the low energy excitations can be studied, see Chapter 2.4.1), we have recently demonstrated that RIXS can get insights into the low energy region where phonons play a crucial role: in particular, we proposed a new methodology for the experimental determination of the electron-phonon coupling in the insulating $NdBa_2Cu_3O_6$ [77]. Finally, RIXS can also give information about the crystal field and the electronic configuration of the valence electrons: in the specific case of cuprates, RIXS has been used in the determination of the energy and symmetry of the Cu $3d$ states by studying the *dd* (or orbital) excitations in almost all the insulating cuprates [11, 91, 92, 106].

Mainly due to technical limitations, the degree of freedom related to the polarization of the scattered photons has not been exploited before the inauguration of ERIXS, except for a pioneering work done by my Minola *et al.* in the study of the polarization dependence of spin-flip excitations [95]. By using a prototype [94] of the polarimeter device installed nowadays in the ERIXS spectrometer, they demonstrated that magnetic excitations flip the spin of the ground state and they necessarily lead to a change in the angular momentum of the photons: from law conservation of angular momenta this yields also a change in the photon polarization which can be detected with a device sensitive to different linearly polarized light [89].

The examples of excitations accessible by RIXS just mentioned suggest that a full characterization of the excitations is needed in order to better understand the fascinating and intriguing physics that characterize HTS cuprates. For example, studying the polarization dependence of spectral features gives access to further crucial information that is usually unavailable in polarization-integrated RIXS spectra. In particular, understanding the polarization dependence of electronic and magnetic excitations could be helpful to learn how charge, spin and orbital orders interact with each other.

In this Chapter we report the first systematic high-resolution polarization-resolved soft RIXS study of low energy (magnons and phonons) and orbital excitations in the high-T_c superconductor $NdBa_2Cu_3O_{7-\delta}$ and we prove the capability and reliability of polarimetric measurements. In this work we used a pure ionic picture to study the experimental results calculating the theoretical RIXS cross-sections for all the possible excitations (for further details see Chapter 2.6.2). This model can be easily applied to the case of cuprates because these are one-hole systems, where the Cu atoms are in a $3d^9$ configuration (Cu^{2+}), *i.e.* having only one hole normally residing in the $3d_{x^2-y^2}$ orbital. With respect to previous works, we added in the calculations the polarization dependence of all the possible RIXS final states which greatly helps the understanding of measured polarization-resolved spectra. In particular, we are able to describe and interpret the different polarized resolved contributions in terms of Stokes parameters [9, 10] which can be also calculated using a single-ion model.

3.2 Experimental methods

Samples

The $NdBa_2Cu_3O_{7-\delta}$ (hereafter NBCO) thin films investigated in this chapter were grown by our collaborators at the CNR/SPIN lab located in Napoli. NBCO belongs to the "123" family and shares the same crystal structure of the most well studied $YBa_2Cu_3O_{7-\delta}$ (YBCO). As shown in Figure 3.1(a), the NBCO crystal structure is characterized by CuO_2 bilayers separated by insulating blocks composed by BaO layers and CuO chains and the central CuO_2 sheets are separated by a Nd ion each.

NBCO thin films have been epitaxially grown by a high oxygen pressure diode sputtering on a (001) surface of $SrTiO_3$ single crystal, and as a consequence the lattice parameters a and b are almost identical ($= 3.9$ Å, while $c = 11.7$ Å) since the almost in-plane matching with the substrate and a tetragonal description will be conveniently used. Whereas in the case of YBCO $a \neq b \neq c$, since it belongs to the D_{2h} point group with a crystalline structure composed by a rhombic dipyramidal. Superconductivity in the CuO_2 planes with a maximum T_c of 95 K is achieved through the control of the holes density (hole doping) by adjusting the excess of Nd at the Ba sites ($Nd_{1+x}Ba_{2-x}Cu_3O_{7-\delta}$) and the oxygen content in the CuO chains.

In this work we have measured undoped (AF), underdoped (UD, $T_c = 63$ K and hole concentration $p = 0.11$) and optimally doped (OP, $T_c = 90$ K and $p = 0.17$) NBCO thin films. More details on samples growth and characterization can be found in Refs. [107] and [108].

RIXS measurements

RIXS spectra have been acquired with the new high-resolution ERIXS spectrometer (for further details see Chapter 2.4.1) with a combined energy resolution (beamline and spectrometer) of ~ 80 meV, evaluated by measuring the full width at half maximum of the non-resonant response from silver paint deposited on a corner of the sample surface, for both the direct beam and the beam measured through the multi-layered mirror. The incident photon energy was tuned at the Cu L_3-edge (~ 931 eV) where the scattering cross-section is greatly enhanced, while the polarization of the incident X-rays could be set either parallel (π, horizontal) or perpendicular (σ, vertical)

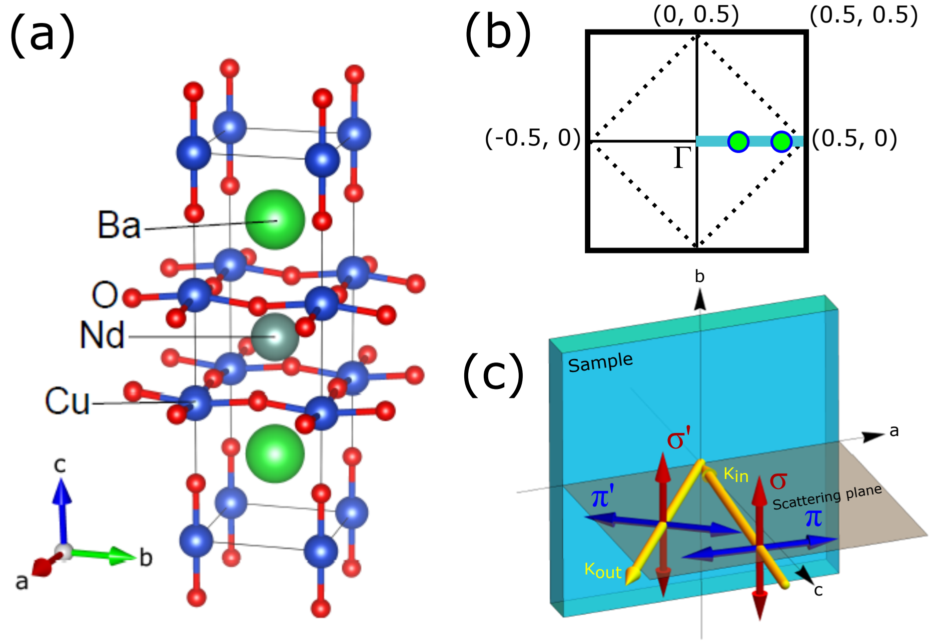

Figure 3.1: a) $NdBa_2Cu_3O_{7-\delta}$ crystal structure. b) First Brillouin zone where the two circles along the [1 0] direction represent the in-plane momentum values of the experimental data discussed in this chapter (h = 0.2 and 0.4 r.l.u.). c) Sketch of the experimental scattering geometry adopted for the RIXS measurements reported here which underlines the possibility to perform polarization analysis of the scattered light. Figures from Refs. [77] and [60].

with respect to the scattering plane (see panel c in Figure 3.1). All the measurements were collected at 20 K and the scattering angle 2θ was fixed at 149.5° with the scattering occurring in the sample ac plane. Experimental data have been taken at two fixed in-plane momenta, namely at $q_{\|}$=0.2 r.l.u. and 0.4 r.l.u. along the anti-nodal direction $\Gamma \longrightarrow X$ (or [1 0], parallel to the Cu-O bonds in the CuO_2 planes), as indicated in Figure 3.1(b). In order to change the absolute value of the in-plane transferred momentum $q_{\|}$ the sample could be rotated azimuthally around the b axis perpendicular to the scattering plane.

All the polarization-resolved RIXS spectra presented in this Chapter have been corrected for self-absorption as explained in Chapter 2.7 and their intensities express as "scattering probability" in units of $eV^{-1}srad^{-1}$. For that the measured RIXS intensities were thus normalized to the collection solid angle of ERIXS ($5{\cdot}10^{-5}$, obtained from the product of the angular acceptance of the grating and of the collimating mirror, which are ∼2.5 mrad and 20 mrad, respectively) and to the incident photon flux obtained by measuring the drain current generated by the incident beam in the last optical element before the sample ($\sim 10^{12}$ photons/s in a typical bandwidth of 45 meV). Moreover, we have taken into account the spectrometer efficiency, where the limiting factor is mainly given by the reflectivity of the grating (0.1 for the 1400 mm^{-1} grating used for the measurements reported here [8]) and the sampling channel width, 10 meV in the present case.

The use of the scattering probability to express the RIXS intensities will facilitate in the future a direct comparison between spectra acquired in different working conditions (experimental setups) and in different synchrotons (beamlines, spectrometers, etc.).

Self-absorption corrections

As mentioned in the previous Section, the RIXS spectra presented hereafter were corrected for self-absorption. As explained in detail in Chapter 2.7, the knowledge of the scattered photon polarization allows us to correct the spectra without uncertainty. For the specific case of the data discussed here, and since the self-absorption strongly depends on the scattering geometry, we

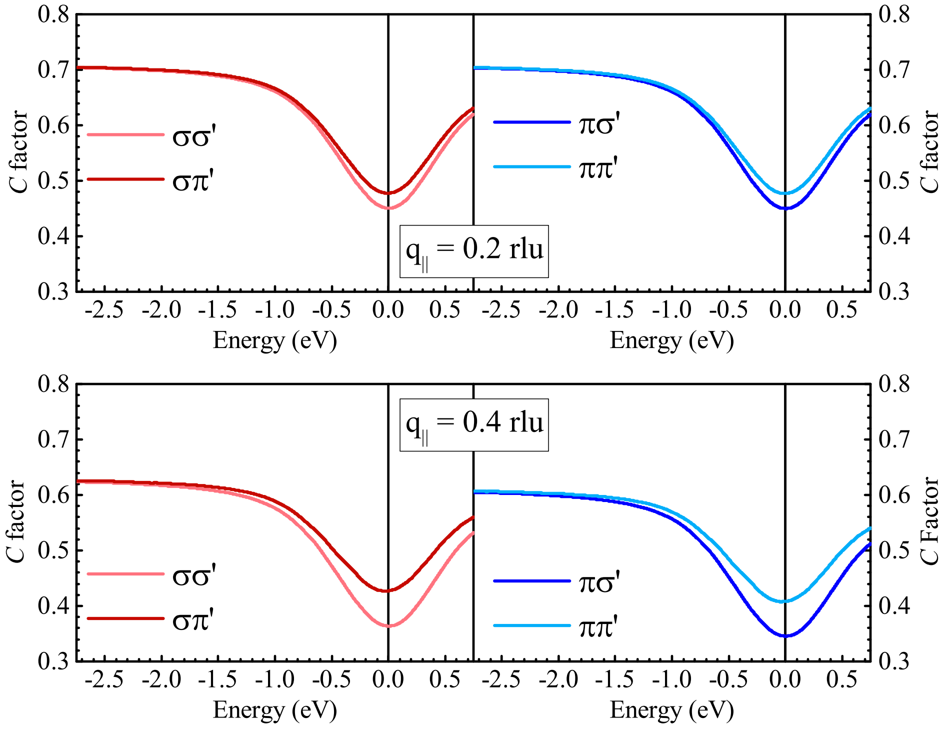

Figure 3.2: Self absorption correction factors at selected transferred momenta ($q_{\|}$ = 0.2 and 0.4 r.l.u.) for both σ and π polarization of the incident and scattered light. These results were calculated from the x-ray absorption spectra measured by total electron yield on the AF NBCO sample. Figures from Ref. [60].

calculated the correction factor $C_{\epsilon,\epsilon'}(\omega_1, \omega_2)$ (Eq. 2.22) for the two selected transferred momenta at which we measured the spectra. The results are illustrated in Figure 3.2.

Here, the correction factors for the two linearly polarized outgoing channels (σ' and π') calculated at $q_{\parallel} = 0.2$ and 0.4 r.l.u. were obtained from the X-ray absorption spectra measured by total electron yield on the AF NBCO sample. As we can note in Figure 3.2, the self-absorption mainly affects the low-energy spectral range (below 1 eV), while it remains almost polarization independent at higher energies, where orbital excitations take place. Finally, Figure 3.2 shows that the correction factor is momentum dependent, giving a bigger contribution at higher transferred momenta, obtained in a grazing out scattering geometry. The XAS spectrum and an example of the self-absorption correction applied on the $\pi\pi'$ and $\pi\sigma'$ decomposed spectra has been described in Chapter 2.7 and illusrated in Figure 2.21.

3.3 Single-ion model for the calculation of the RIXS cross-section

In Chapter 2.6.2 we have introduced the procedure to calculate the RIXS cross-sections within the single-ion model. Moreover, we have shown that the polarization of the light can be interpreted in terms of Stokes vector. Here we will combine these two approaches exploiting the possibility to explicit the outgoing polarization dependence of the RIXS cross-sections in order to calculate the Stokes vector and the corresponding Poincaré - Stokes parameters **P**. Recalling the RIXS amplitudes obtained in the framework of the single-ion model given by the Eq. 2.8, the Stokes vector **S** (Eq. 2.16) can be rewritten in the following way

$$\mathbf{S} = \begin{bmatrix} S_0 \\ S_1 \\ S_2 \\ S_3 \end{bmatrix} \propto \begin{bmatrix} |\mathcal{A}_{\sigma'}|^2 + |\mathcal{A}_{\pi'}|^2 \\ |\mathcal{A}_{\sigma'}|^2 - |\mathcal{A}_{\pi'}|^2 \\ |\mathcal{A}_{\sigma'} + \mathcal{A}_{\pi'}|^2 - |\mathcal{A}_{\sigma'} - \mathcal{A}_{\pi'}|^2 \\ |\mathcal{A}_{\sigma'} - \imath\mathcal{A}_{\pi'}|^2 - |\mathcal{A}_{\sigma'} + \imath\mathcal{A}_{\pi'}|^2 \end{bmatrix}. \tag{3.1}$$

Poincaré-Stokes parameters $P_i' = S_i/S_0$, $i = 1, 2, 3$ are reported in Tables 3.1 and 3.2 for the scattering geometry adopted in our measurements and reported in Chapter 2.12(a) and in Figure 3.1 for both σ and π polarization of the incident photons.

As we explained in Chapter 1.2.2, being the Cu^{2+} ions in the CuO_2 planes in a $3d^9$ configuration, the ground state of cuprates is assumed to be $3d_{x^2-y^2}\downarrow$, where the arrow denotes the spin state. As a consequence, in our calculations

	P_1	P_2	P_3
$x^2-y^2\downarrow$	1	0	0
$x^2-y^2\uparrow$	-1	0	0
$xy\downarrow$	-1	0	0
$xy\uparrow$	1	0	0
$xz\downarrow$	-1	0	0
$xz\uparrow$	-1	0	0
$yz\downarrow$	$\frac{4\cos(2\theta_{out})-3}{1+8\sin^2\theta_{out}}$	0	$\frac{4\sqrt{2}\sin\theta_{out}}{1+8\sin^2\theta_{out}}$
$yz\uparrow$	1	0	0
$3z^2-r^2\downarrow$	$\frac{1}{2}\frac{\cos(2\theta_{out})+3}{2+\sin^2\theta_{out}}$	0	$\frac{2\sqrt{2}\sin\theta_{out}}{2+\sin^2\theta_{out}}$
$3z^2-r^2\uparrow$	-1	0	0

Table 3.1: Poincaré-Stokes parameters of scattered radiation calculated within the Cu^{2+} single-ion model with σ incident photon polarization for all the possible final states. θ_{out} is the angle between the scattered photons and the normal to the sample surface (see Figure 2.12(a)).

the final state $3d_{x^2-y^2}\downarrow$ always refers to a pure elastic scattering, whereas a pure spin flip excitation is characterized by having a $3d_{x^2-y^2}\uparrow$ final state. The other final states that can occur during the RIXS process involve an orbital change ($3d_{xy}\downarrow$, $3d_{xz}\downarrow$, $3d_{yz}\downarrow$ and $3d_{3z^2-r^2}\downarrow$) or both an orbital change and spin flip ($3d_{xy}\uparrow$, $3d_{xz}\uparrow$, $3d_{yz}\uparrow$ and $3d_{3z^2-r^2}\uparrow$).

Differently from previous works where the single-ion model has been used to study the angular dependence of the RIXS final states (especially for *dd* excitations [11]), in Tables 3.1 and 3.2 give a direct information about their polarization dependence in terms of Poincaré-Stokes parameters. Having a close look at both Tables 3.1 and 3.2, we can extract useful indications that will be used in the understanding of the experimental data. For example, we note that if the scattering process occurs in the sample *ac* (xz) plane (see Figure 3.1) in both the cases with σ and π polarization of the incident radiation, the scattered photons are fully σ' and π', respectively. This affirmation comes from the fact that $P_1 = 1$ or -1, respectively, and $P_2 = P_3 = 0$ for all the excited states except for $yz,\downarrow$ ($yz,\uparrow$) and $3z^2-r^2,\downarrow$ ($3z^2-r^2,\uparrow$) for σ (π) incident photon polarization, where $S_3 \neq 0$ ($P_3 \neq 0$).

In the description of the polarization analysis given in Chapter 2.7 we have underlined that the polarimetric device installed on the ERIXS spectrometer can separate solely the two pure linearly polarized states of the scattered light σ' and π'. The fact that some final states are characterized by $P_3 \neq 0$ and $S_3 \neq 0$ could make, sometimes, the interpretation of the polarization resolved RIXS spectra ambiguous. For example, if we assume that the scattered

	P_1	P_2	P_3
$x^2-y^2\downarrow$	-1	0	0
$x^2-y^2\uparrow$	1	0	0
$xy\downarrow$	1	0	0
$xy\uparrow$	-1	0	0
$xz\downarrow$	-1	0	0
$xz\uparrow$	-1	0	0
$yz\downarrow$	1	0	0
$yz\uparrow$	$\frac{1-2\sin^2\theta_{out}}{1+2\sin^2\theta_{out}}$	0	$\frac{2\sqrt{2}\sin\theta_{out}}{1+2\sin^2\theta_{out}}$
$3z^2-r^2\downarrow$	-1	0	0
$3z^2-r^2\uparrow$	$\frac{1-2\sin^2\theta_{out}}{1+2\sin^2\theta_{out}}$	0	$\frac{2\sqrt{2}\sin\theta_{out}}{1+2\sin^2\theta_{out}}$

Table 3.2: Poincaré-Stokes parameters of scattered radiation calculated within the Cu^{2+} single-ion model with π incident photon polarization for the various final states. θ_{out} is the angle between the scattered photons and the normal to the sample surface (see Figure 2.12(a)).

radiation is fully circularly polarized, then $|S_3| = S_0$ ($|P_3| = 1$) and $S_1 = S_2 = 0$ ($P_1 = P_2 = 0$): the intensity recorded on the detector after reflection from the multilayer mirror will be $S_{M,0} = R_0 S_0$. Eqs. (2.18) and (2.19) will provide $I_{\sigma'} = I_{\pi'} = S_0/2$, *i.e.* the scattered intensity is equally distributed between the two polarization channels. Here we have thus demonstrated that by expressing the RIXS cross-sections calculations in terms of Poincaré-Stokes parameters is of crucial importance to determine the effective polarization state of the excited states.

In the upper panels of Figure 3.3 we show the polarization-resolved RIXS cross-sections obtained with the single ion model for all the excited states that involve an orbital change. The results are plotted as a function of the in-plane transferred momentum $q_\parallel$ along the [1 0 0] direction of the Brillouin zone with both σ (left) and π (right) incident photon polarization and having considered the scattering angle $2\theta = 150°$. In the calculations we have summed over all the two possible spin final states (up and down) since the super-exchange coupling is negligible for all the $3d$ orbitals except for the ground state ($3d_{x^2-y^2}$) [11]. Moreover, in the measured RIXS spectra of all the 2D cuprate families there is no evidence of a possible spin splitting for *dd* excitations (and if present, it is not resolved). Therefore, in Chapter 3.3 we have considered as degenerate the final states with $\Delta S = 0$ and $\Delta S = 1$, which are related to spin-conserving ($\Delta S = 0$) and single spin-flip excitations ($\Delta S = 1$), respectively.

Following the same procedure adopted by Moretti *et al.* [11], we simulate

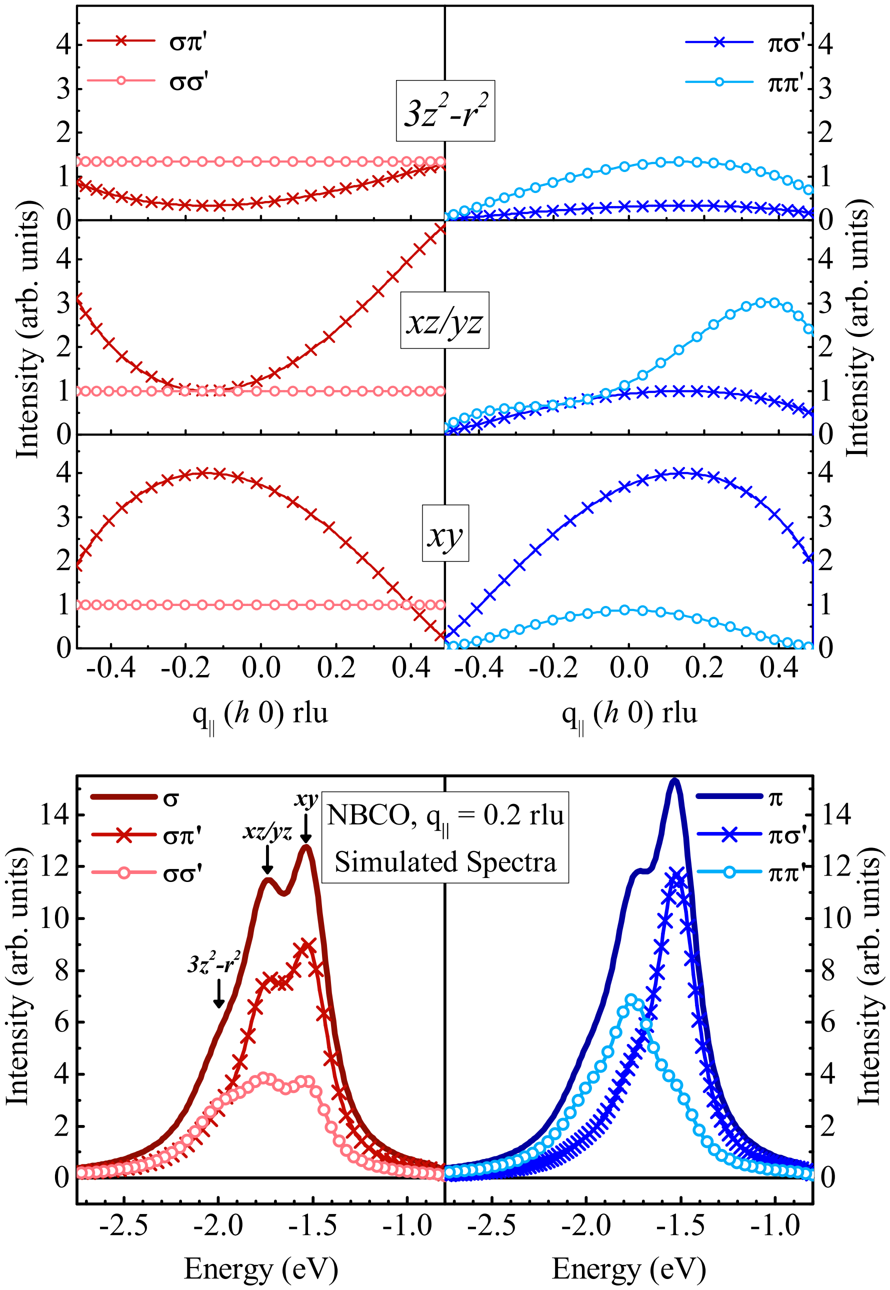

Figure 3.3: The top panels show the in-plane momentum dependence of Cu L_3-edge polarized RIXS cross-sections calculated in the framework of the single-ion model for dd excitations ($3d_{xy}$, doubly degenerate $3d_{xz/yz}$ and $3d_{3z^2-r^2}$ orbitals). For each curve we consider as degenerate the final states with $\Delta S = 0$ and $\Delta S = 1$. For all cases the scattering angle (2θ) has been fixed at 149.5°. In the bottom panels we report the simulated spectra with outgoing polarization analysis of AF NBCO (the energy positions of the 3 dd excitations are taken from Ref. [11]) at $q_{\parallel} = 0.2$ rlu along [1 0 0] direction of the Brillouin zone with both σ (left) and π (right) incident photon polarization of the light. Figure from Ref. [60].

the RIXS spectra of AF NBCO at $q_{\parallel} = 0.2$. The energy positions and the intrinsic Lorentzian lifetime broadening of the three *dd* excitations have been taken from Ref. [11]: the transition from the ground state to the $3d_{xy}$ orbital is the one at lower energy loss (-1.52 eV), the doubly degenerate final state $3d_{xz/yz}$ at -1.75 eV, while the other e_g final state $3d_{3z^2-r^2}$ at -1.98 eV. In order to allow a direct comparison with the experimental data (shown in Chapter 3.4), the calculated spectra were convoluted with a Gaussian function having a full width at half maximum of 80 meV which takes into account the experimental energy resolution. The simulated spectra, including their polarization-resolved decompositions, show an excellent agreement with the measured polarized-RIXS spectra of undoped NBCO illustrated in the upper panels a-b) of Figure 3.4. The capability offered by the single-ion model to assign the energy and symmetry of the Cu $3d$ states in undoped cuprates has been confirmed by several works [11, 92], while in this work we also demonstrate how this tool allows the study of the polarization dependence of the excited states. Therefore, we will use in the following the combination of the Poincaré-Stokes parameters together with the RIXS cross-sections to discuss the polarization and doping dependence of the main spectral features in the NBCO RIXS spectra.

3.4 Results and discussion

Figure 3.4 shows the polarization-resolved RIXS spectra of AF (upper panels) and OP (bottom panels) NBCO measured with both σ and π at two selected in-plane transferred momenta ($q_{\parallel} = 0.2$ and 0.4 r.l.u.). For clarity, we show only every second data point (symbols), while the continuous lines represent data smoothed on seven points. The four different polarization combinations ($\pi\pi'$, $\pi\sigma'$, $\sigma\sigma'$ and $\sigma\pi'$) have been obtained by applying the procedure described in Chapter 2.7 (here the spectrum acquired after being reflected by the ML is not shown). The low energy region is characterized by dispersing inelastic excitations and by a resolution limited (quasi)elastic peak, while at higher energy losses (between-1 and -3 eV) the spectral weight is dominated by the crystal field excitations. All the spectral feature intensities show momentum and polarization dependence, while the effect of the doping is reflected in a significant broadening of all the spectral lineshapes. In the following, we will detail our analysis on each of the excitations.

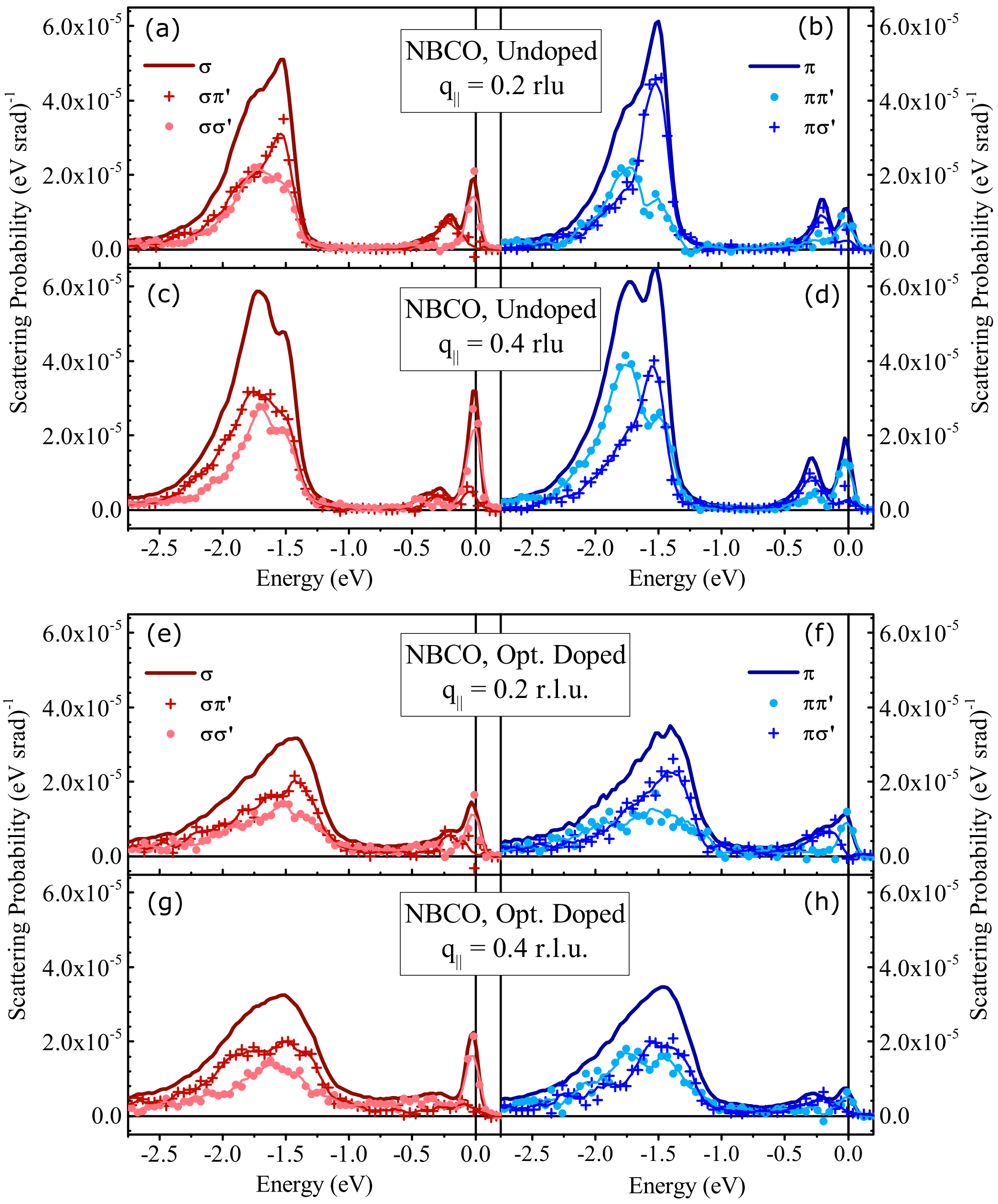

Figure 3.4: Polarization-resolved RIXS spectra of undoped (top panels) and optimally doped (bottom panels) NBCO. The measurements were carried out at the two selected momenta $q_{\|} = 0.2$ and 0.4 r.l.u. with both σ (panels a,c,e,g) and π (panels b,d,f,h) polarization of the incident light. In the decomposed spectra symbols represent raw data while continuous lines are smoothed data on 7 points. Figure from Ref. [60].

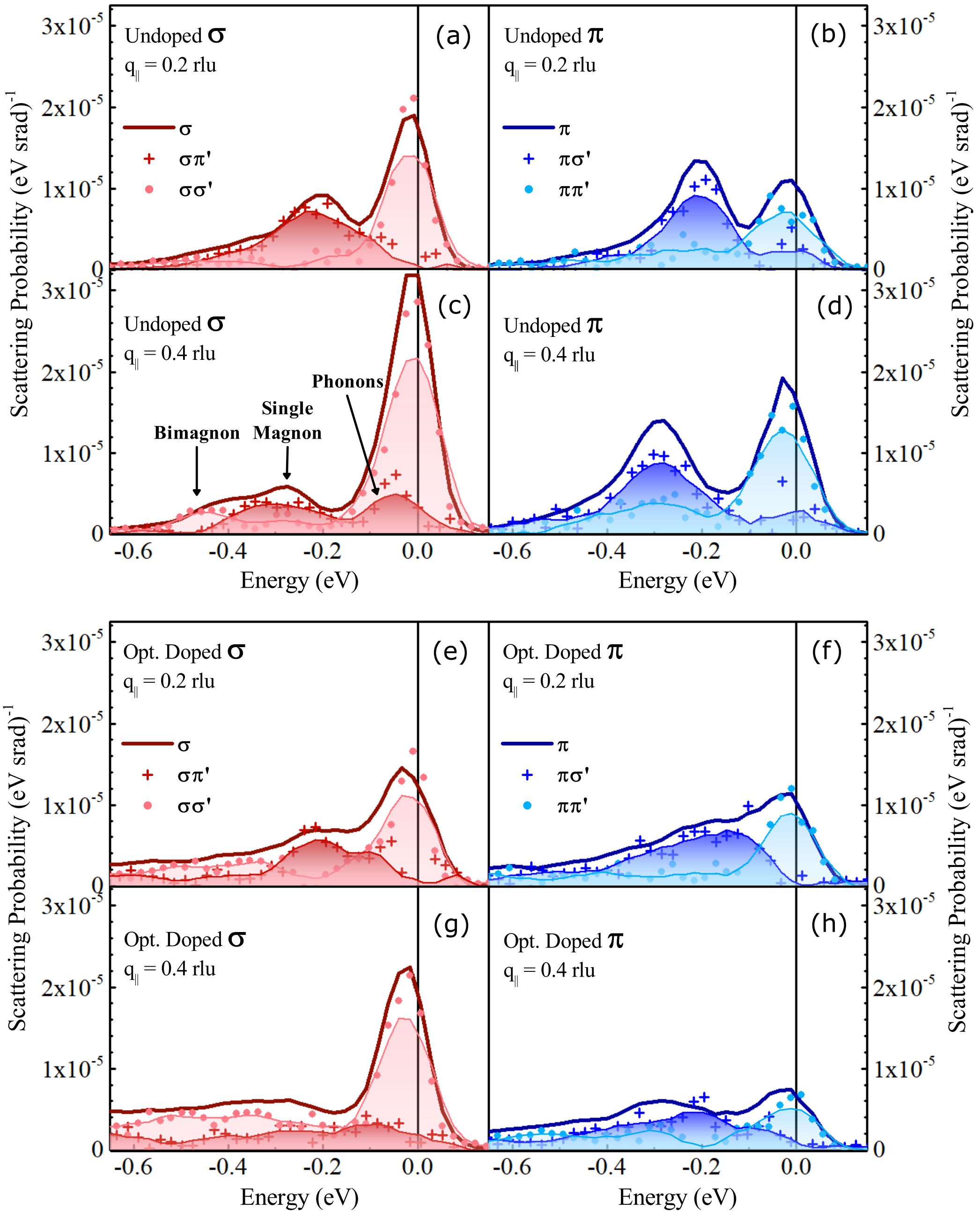

Figure 3.5: Low energy spectral range of the polarization-resolved RIXS spectra of undoped (top panels) and optimally doped (bottom panles) NBCO at the two selected momenta $q_{||} = 0.2$ and 0.4 r.l.u. and measured with both σ (panels a,c,e,g) and π (panels b,d,f,h) polarization of the incident light. In the decomposed spectra symbols represent raw data while continuous shaded areas are smoothed data on 7 points. Figure from Ref. [60].

(Quasi)elastic line and phonons

In Figure 3.5 we highlight the low-energy spectral range of the RIXS spectra shown in Figure 3.4. As mentioned above, the undoped NBCO spectra are sharper than optimally doped cases, facilitating the distinction of the spectral features. Although the (quasi)elastic peak (centered at ~ 0 energy loss within the uncertainty related to the finite energy resolution) in all the spectra of the undoped and optimally doped NBCO mainly belongs to the non-crossed polarization channels ($\pi\pi'$ and $\sigma\sigma'$), a non negligible crossed ($\pi\sigma'$ and $\sigma\pi'$) contribution is clearly visible. This experimental finding seems to be in contradiction with the well established RIXS cross-sections calculated within the single-ion model, especially in the case of undoped cuprates. As a consequence of the total angular momentum conservation law, the spin-conserving elastic scattering ($\Delta S = 0$) without orbital character in cuprates ($x^2 - y^2$ ground state) is purely non-crossed, as illustrated in the top panels of Figure 3.6.

Since the energy resolution of the present experiment is ≈ 80 meV, excitations such as phonons might help in the understanding of this apparent inconsistency. In fact, the two main phonons probed by RIXS are the buckling (out-of CuO_2 planes vibrations of the planar O atoms) and breathing (Cu-O bond-stretching vibrations) mode, which for the present case of NBCO have an energy of ≈-35 and ≈-70 meV, respectively [77]. In the spectra reported in Figure 3.5 we can not resolve the two distinct phonon contributions due to the intrinsic broadening given by the finite energy resolution. Although an accurate and detailed systematic study of the vibrational modes requires an energy resolution at least twice better than the present one, the polarization-resolved measurements clearly reveal their presence in the low energy region. We thus exploit this analysis to note that specific phonons can give a contribution in the crossed-polarization channel, as seen in Raman measurements [109]. Nevertheless, a systematic investigation of polarization and doping dependence of the buckling and breathing mode accessible by RIXS is out of the scope of this work. However, our work suggests that a further improvement in the energy resolution in RIXS experiments, specifically in the polarization-resolved ones, could in principle provide essential hints about the symmetry of the different phonon modes and eventually greatly contribute to uncover the nature of the electron-phonon coupling in undoped and superconducting cuprates.

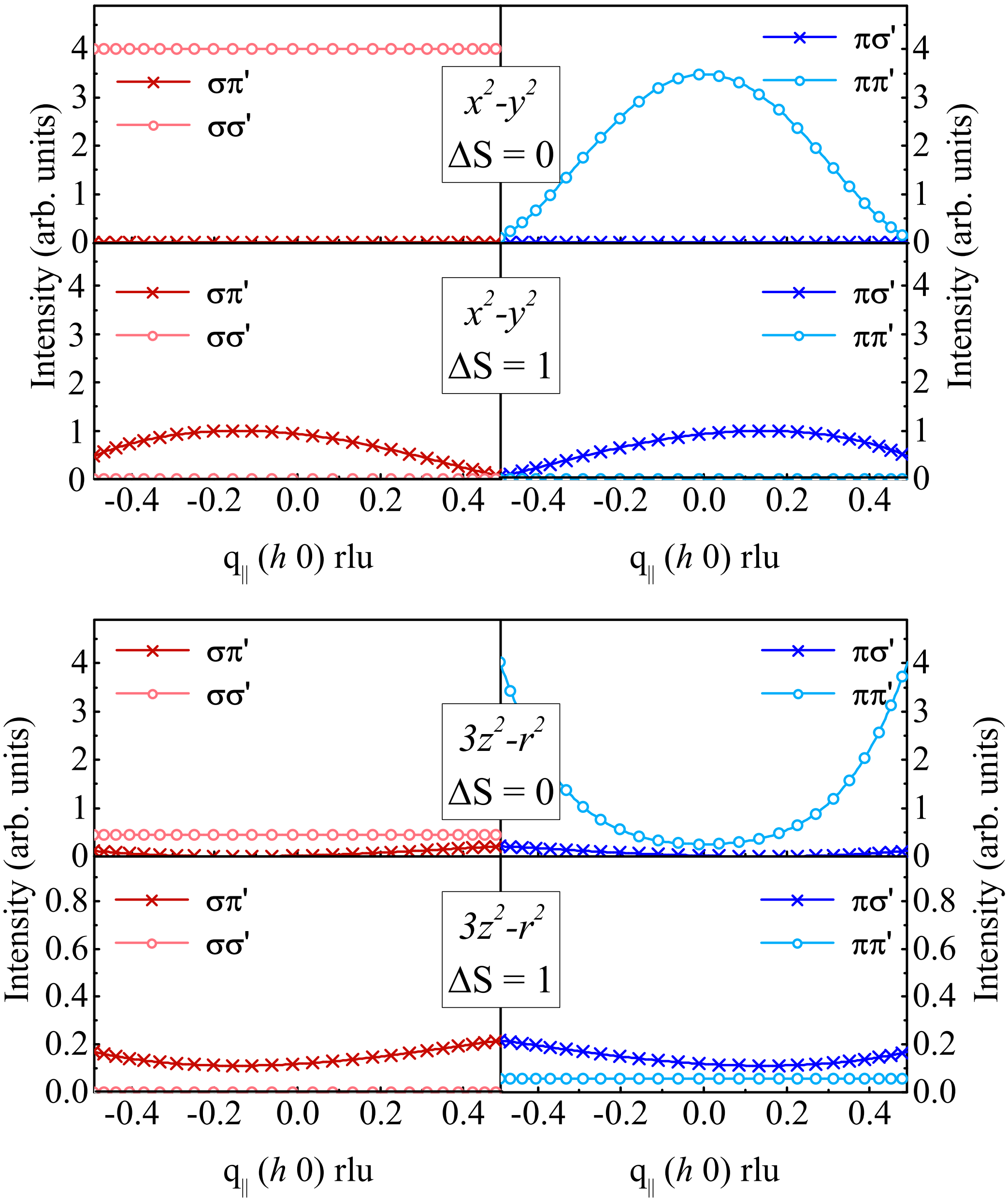

Figure 3.6: $q_{\parallel}$-dependence of the polarization-resolved RIXS cross-sections within the single-ion model for spin-conserving ($\Delta S = 0$) and pure spin-slip ($\Delta S = 1$) excitations without orbital change. In the top panels the ground state is considered to have a $x^2 - y^2$ symmetry, while in the bottom panels a $3z^2 - r^2$ symmetry. For these calculations the scattering angle 2θ is 149.5° and we consider both the incident polarizations of the light (σ and π). Figure from Ref. [60].

Magnetic Excitations

Magnetic excitations (single and/or multi-magnons) are usually described as collective due to their dispersing character in the reciprocal space. Starting our discussion from the undoped case illustrated in the top panels of Figure 3.5, the sharp peaks found at $\approx$-250 meV at $q_{\|} = 0.2$ r.l.u. and at -300 meV at $q_{\|} = 0.4$ r.l.u. are single-spin flip (magnon) excitations and occur predominantly in the crossed-polarization channels. Previous theoretical [89] and experimental [95] works have already shown that spin-flip excitation ($\Delta S = 1$) leads to a rotation of the scattered light polarization with respect to the incident one. However, as in the case of the (quasi)elastic peak, our polarization-resolved RIXS spectra seem to slightly contradict this common belief, showing a sizable spectral weight with non-crossed character behind the magnon peaks.

Nevertheless, it is well known that the shoulder of the magnon peak seen in the spectrum measured with σ polarization is usually ascribed to the bimagnon (excitation of two interacting magnons) continuum, that in the specific case of RIXS at Cu L_3-edge is characterized by a dispersive branch of its continuum [110] and, as a consequence, more visible at larger momentum. In fact, at $q_{\|} = 0.4$ r.l.u. the bimagnon can be easily recognized at -450 meV, and contrarily to single magnons, it mainly occurs in the non-crossed polarization channels. The tail of the bimagnon can therefore extend up to the single magnon energy justifying the $\pi\pi'$ and $\sigma\sigma'$ contributions. Another plausible explanation that can be taken into account is the consideration of a $3d_{x^2-y^2}$ ground state mixed with the $3d_{3z^2-r^2}$, a scenario that has already been considered before [111]. To check the feasibility of this hypothesis, we calculated the $\Delta S = 0$ and $\Delta S = 1$ RIXS cross-sections within the single ion model assuming a $3z^2 - r^2$ ground state. The results, sketched in the bottom panels of Figure 3.6, show that spin-flip transitions are allowed in the $\pi\pi'$ and not $\sigma\sigma'$ case.

Both of the hypotheses discussed here can simultaneously be at play, however the non-crossed contribution coming from the bimagnon seems more likely to dominate.

Let's now have a look to the low energy spectral range of the optimally doped NBCO spectra illustrated in the bottom panels (e-h) of Figure 3.5. If compared to the undoped NBCO discussed above, the first thing that stands out is that OP spectra are broader, making the distinction of the spectral features more difficult, and sit on an unpolarized continuum. This spectral weight is related to the presence of added charges in the system and it is usually ascribable to an electron-hole pair excitation continuum. The single magnon excitations (usually called paramagnons in doped compounds) are heavily damped but persist when mobile holes are added to the system [5, 22, 23, 112, 95, 113, 114]. Finally, our measurements demonstrate that, especially in the case of π polarization of the incident photons, paramagnons still belong to the crossed-polarization channel preserving the polarization dependence of single spin-flip excitations as in the undoped NBCO.

Crystal-field excitations

The study of crystal-field (or *dd* excitations) in undoped cuprates with RIXS has been extensively done in the past by our group to assign the energy and symmetry of the $3d$ Cu^{2+} orbital states by examining the momentum-dependence of the *dd* peak intensities and compared with the RIXS cross-sections [11]. As we pointed out in the introduction of this work, and differently from the magnetic excitations case, the spectral features related to orbital excited states usually do not show any energy-momentum dispersion. In addition to that, the noticeable agreement with simulated RIXS spectra obtained within the single-ion model underline the localized (non-collective) nature of orbital excitations in NBCO, as already demonstrated by some of us *et al*. [11].

It could therefore be interesting to track their evolution upon doping, as we show in the top panels of Figure 3.7. Here we show the doping dependence of the polarization unresolved AF, UD and OP NBCO spectra taken with both π and σ incident polarization at $q_{\parallel} = 0.2$ r.l.u. and $q_{\parallel} = 0.4$ r.l.u.. Moving towards higher doping levels we observe two major effects:

- the overall *dd* lineshapes broaden and the different orbital peaks increasingly overlap with each other, making almost impossible their assignment;
- the energy position of the resulting broad distribution shifts towards lower energy loss.

In order to quantify the latter effect, we estimated the *dd* spectral centroid (center of mass) by integrating the distribution of orbital excitations in the energy range between -3 and -1 eV. While regarding the overall shift to lower energy loss of the *dd* distribution, we assessed the energy of the d_{xy} peak (the one at lowest energy loss) by computing the second derivative of the spectra. We decided to not implement a multi-peak fitting procedure because in the case of OP NBCO RIXS spectra the results are affected by a considerable uncertainty of the fitting parameters due to the broadening of the *dd* excitations. However, with this approach we obtain the same value of the d_{xy} energy position (1.52 eV) in the AF NBCO reported in Ref. [11]. These two quantitative analyses are summarized in the bottom panel of Figure 3.7. The average softening of the overall *dd* distribution amounts to ≈50 meV from the AF to the OP case and seems to be mostly caused by a ≈150 meV shift of the d_{xy} peak towards lower energy losses. By taking advantage of the

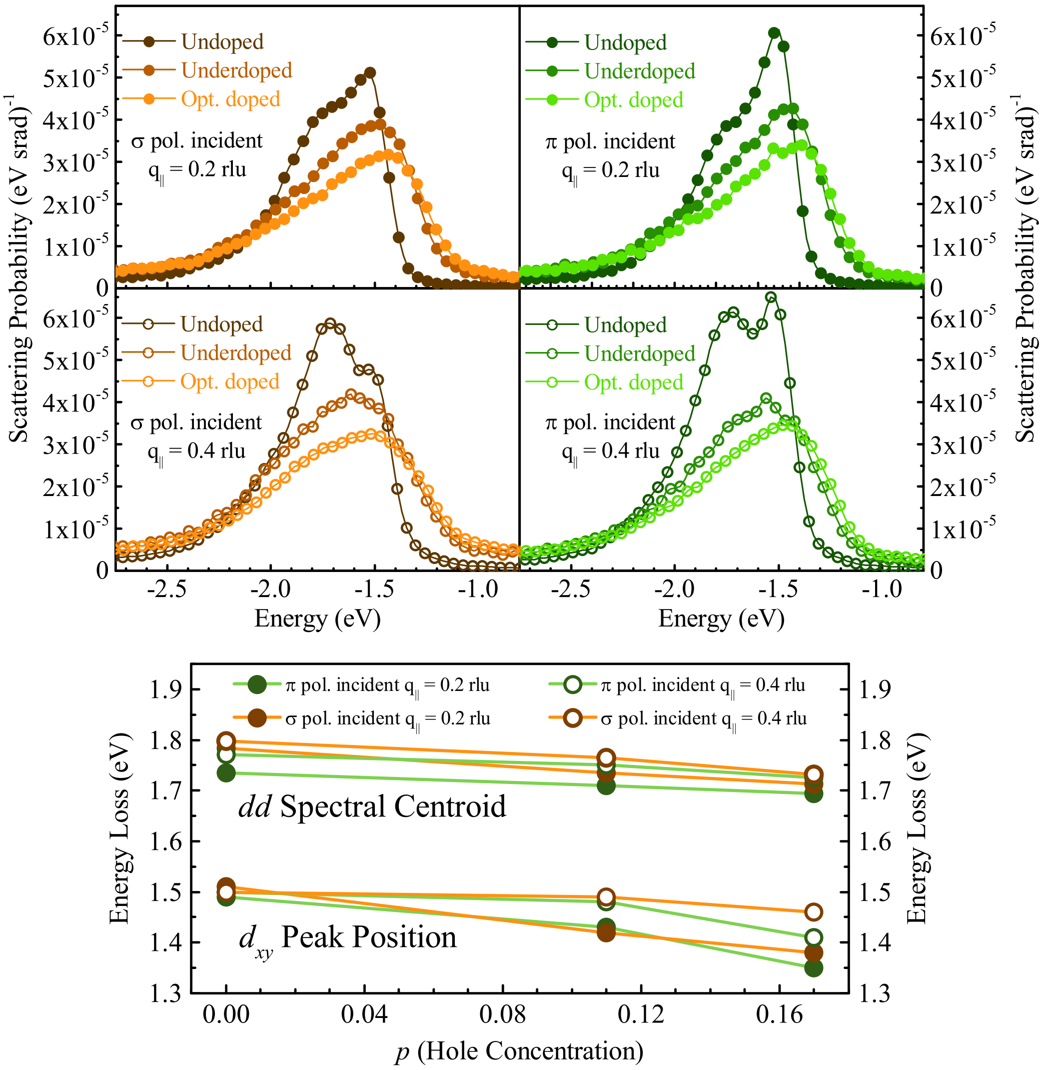

Figure 3.7: Top panels: doping dependence (undoped, underdoped and optimally doped NBCO) of *dd* excitations at $q_{\parallel} = 0.2$ and 0.4 r.l.u. measured with π and σ incident light polarization. The bottom panel shows the doping dependence of the *dd* spectral centroids and the xy peak positions. Figure from Ref. [60].

polarization resolution we further inspected these properties in the AF and OP NBCO polarization-resolved RIXS spectra.

In particular, we concentrated on the cross-polarization $\pi\sigma'$ and $\sigma\pi'$ spectra taken at $q_{\parallel} = 0.4$ r.l.u.: in this scattering geometry, our RIXS cross-sections calculations suggest that we can follow the evolution upon doping of the two different d_{xy} and $d_{xz/yz}$ states. In fact, the former is enhanced by the $\pi\sigma'$ polarization channel, while the latter has a predominant $\sigma\pi'$ contribution. The feasibility of these considerations are supported by the fact

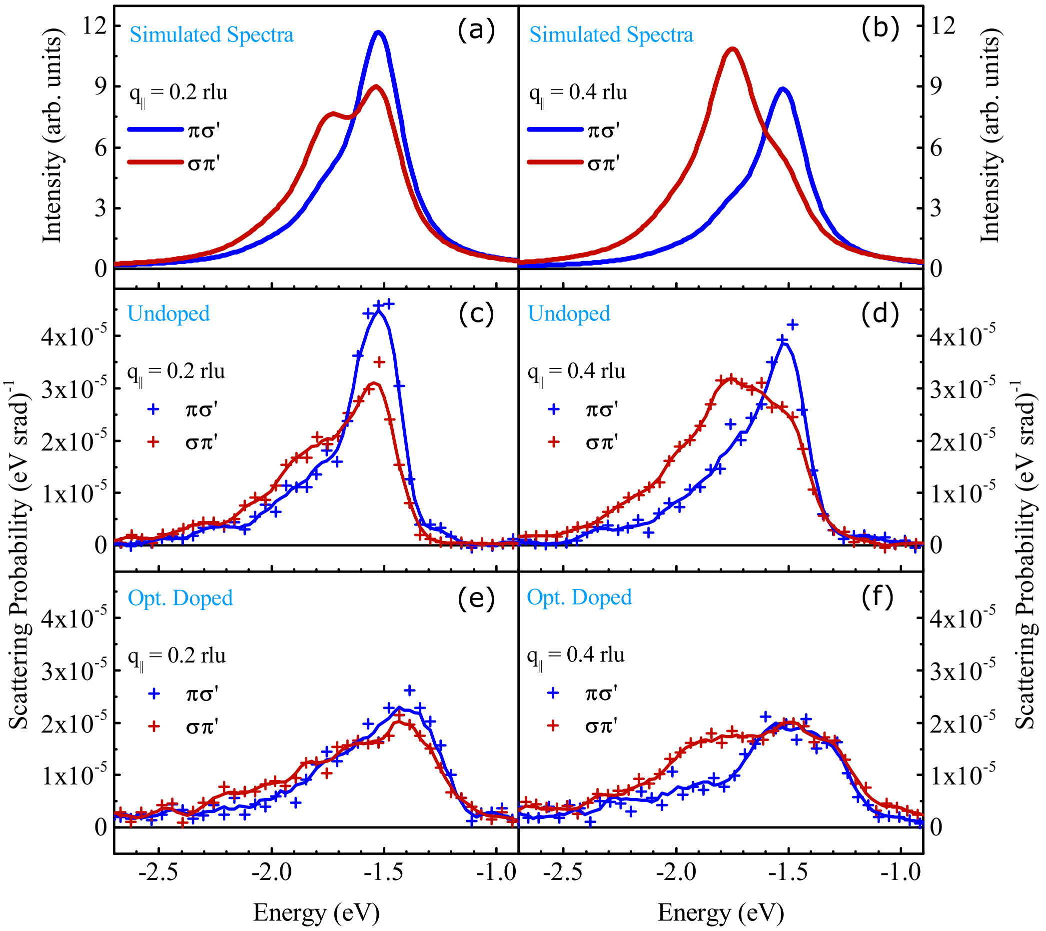

Figure 3.8: (a-b) Simulated $\pi\sigma'$ and $\sigma\pi'$ (cross-channels polarization) spectra of AF NBCO for momentum transfers of $q_{\|} = 0.2$ r.l.u. and $q_{\|} = 0.4$ r.l.u. (orbital energies are taken from Ref. [11]). Comparison between cross-channels polarization spectra of AF (c,d) and OP (e,f) NBCO at $q_{\|} = 0.2$ r.l.u. (left panels) and $q_{\|} = 0.4$ r.l.u. (right panels). Continuous lines are smoothed data on 7 points. Figure from Ref. [60].

that simulated RIXS spectra shown in Figure 3.8(b) nicely reproduce the experimental data of AF NBCO sketched in Figure 3.8(d). Figure 3.8(f) shows that the main effect given by the added holes is the broadening of both the d_{xy} and $d_{xz/yz}$ states, while the previously discussed shift of the spectral centroid of the entire *dd* distribution could be ascribable to the additional spectral weight visible in the low-energy side of the d_{xy} peak in both $\pi\sigma'$ and $\sigma\pi'$ channels. The spectra taken at $q_{\|} = 0.2$ r.l.u. (Figure 3.8(c) and (e)) confirm what we have determined in the spectra at $q_{\|} = 0.4$ r.l.u.. An additional spectral weight can also be observed in the high-energy side of the $d_{xz/yz}$ state, but its effect seems to be smaller with respect to the one related to the d_{xy} and therefore we can confirm that the shift to lower energy losses of the *dd* center of mass is substantially provided by the d_{xy} softening.

The shift of *dd* excitations distribution can be explained by the reduction of the effective crystalline electric field given by the partial screening of the (negative) oxygen charges by doping holes. The effect seems to be larger for the in-plane d_{xy} orbital consistently with the formation of the Zhang-Rice singlets [29] which mainly take place in the CuO$_2$ planes, thereby providing a more effective screening of the in-plane O charges.

3.5 Conclusions

In the work presented and discussed in this Chapter we provided a systematic analysis of high-resolution polarization-resolved RIXS spectra of NBCO as a function of doping. In particular, we we studied with unprecedented accuracy the polarization dependence of all the main features accessible to Cu L_3-edge RIXS, such as phonons, single- and multiple magnon excitations, and finally orbital excitations. Thanks to the polarization resolution of the scattered photons from the sample, by simply tracking the evolution of the various excitations as a function of doping we were able to disentangle all the spectral components.

As a result of our analysis on the *dd* excitations, we reported a broadening and shift of the spectral centroid (center of mass) of the whole *dd* excitations distribution towards lower energy losses. In particular, the analysis of the doping dependence of the cross-polarization $\pi\sigma'$ and $\sigma\pi'$ channels allowed us to discriminate between d_{xy} and $d_{xz/yz}$ excited states and ascribe the shift of *dd* excitations to the softening of the d_{xy} state. Moreover, we show that a proper correction for self-absorption effects can be done only if we have a complete knowledge about the scattering geometry and of the polarization of the scattered radiation. This fact could have relevant repercussions especially when investigating little intensity differences, as in the case of the low energy spectral range where phonons are detected.

Finally, we interpret the polarization-resolved RIXS spectra in terms of Poincaré-Stokes parameters that can be evaluated from calculations of the RIXS cross-sections within the framework of the single-ion model. We find out that the decomposition in the σ' and π' components is accurate solely when the scattered photons are fully σ' or π' polarized, namely $|S'_1| = S'_0$ ($|P'_1| = 1$), that is the case of most of the excited states. In general, we have demonstrated that by carrying out systematic polarization-resolved measurements it is possible to add fundamental information on the nature of all the excitations probed by RIXS. As an example, it might help in the future to single out phonon modes with different symmetries.

In addition, polarization resolution of the scattered light reduces issues related to the intrinsic broadening of the RIXS spectral features upon doping, for which a high energy resolution does not necessarily help, *e.g.* for magnetic excitations, phonons and electron-hole pair excitations sharing the same energy range or for orbital excitations, which broaden and merge into a single feature.

CHAPTER 4

Review of polarimetric measurements

In this Chapter we report a summary of all the polarization-resolved RIXS measurements carried out at the ID32 beamline of the ESRF. The idea behind this Chapter is to show some of all the possible applications of polarization-resolved RIXS in cuprates and rare-earth materials.

In the previous Chapter we have shown how polarimetric measurements can help the disentanglement of the low energy spectral features and how they can permit a systematic study of orbital excitations, for example their doping dependence. Here we will concentrate our attention on the study of different mechanisms at play in the low energy scale of undoped and superconducting cuprates, such as charge order and magnetic excitations. The outgoing polarization analysis of the RIXS spectra in the case of electron doped cuprates was also crucial for the detection of a fast dispersing mode ascribable to a plasmonic excitation and for the existence of dynamic correlations at the charge-order wave vector which primarily involves spin-flip excitations.

Finally, in the last Section we will show that the analysis of the scattered photons polarization helped in the unique assignment of the crystal field excitations in a Ce-based compound.

I would like to underline that I have been involved in all the experiments and data analyses discussed in this Chapter, except for the works reported in Chapters 4.5 and 4.6. We decided to include these two works in order to provide to the reader the most complete review about the polarization-resolved soft-RIXS measurements carried out at the ID32 beamline.

Contents

4.1 Re-entrant charge order in overdoped $(Bi,Pb)_{2.12}Sr_{1.88}CuO_{6+\delta}$

The data and analyses discussed in this Section have been published in "*Re-entrant charge order in overdoped* $(Bi,Pb)_{2.12}Sr_{1.88}CuO_{6+\delta}$", by Y. Y. Peng, R. Fumagalli, Y. Ding, M. Minola, S. Caprara, D. Betto, M. Bluschke, G. M. De Luca, K. Kummer, E. Lefranois, M. Salluzzo, H. Suzuki, M. Le Tacon, X. J. Zhou, N. B. Brookes, B. Keimer, L. Braicovich, M. Grilli and G. Ghiringhelli, Nature Materials **17**, 697 (2018).

In high-T_c cuprate superconductors the doping of either hole or electron carriers to the Mott insulator parent compounds introduces superconductivity and a number of instabilities [7]. Charge density waves (CDW) have emerged as a universal feature of underdoped materials but their relevance to pseudopgap and superconductivity is less clear. Early evidence of charge order had come from stripe formation in La-based cuprates near the doping level $p = 1/8$ hole/Cu [40, 115, 42]. Only later incommensurate charge order, competing with superconductivity, has been observed in the "123 family" [45, 116] and in Bi- and Hg-based cuprate families [46, 117]. In Bi-based cuprates the onset temperature is similar to the pseudogap temperature T^*

and the wavevector is comparable to the distance between the Fermi arc tips, therefore hinting at a link between CDW and the pseudogap in hole-doped systems [48, 118]. In contrast, in electron-doped cuprates CDWs extend well above T^*, with an onset temperature close to that of the AF fluctuations, thus suggesting a possible connection between the two [49, 119].

Based on these observations, it is largely accepted that the charge order phenomenon is present in all the cuprate families but it is restricted inside in the underdoped portion of the phase diagram. Contrarily to this common belief, by employing RIXS at the Cu L_3-edge we have discovered a strong and very sharp incommensurate quasi-elastic peak along the Cu-O bond directions (see Figure 4.1(d)) in the overdoped single-layer cuprate $(\mathrm{Bi,Pb})_{2.12}\mathrm{Sr}_{1.88}\mathrm{CuO}_{6+\delta}$ (Bi2201). This RIXS signal, reported in Figure 4.1 (panels a-c), can be ascribable to very long-range charge density modulations. The Fermi surface (FS) measured by angle resolved photoemission spectroscopy (ARPES) allows us to exclude the nesting scenario as origin of the CDW (see panels e-f of Figure 4.1). This finding suggests the ubiquity of charge ordering also in the Fermi liquid region of overdoped cuprates.

From the energy/momentum intensity map illustrated in Figure 4.1(a) on the OD11K Bi2201 we can distinguish two main spectral regions: the one centered at ∼0 energy which exhibits a maximum at $q_\parallel = 0.14$ r.l.u. (reported in Figure 4.1(c)) and the inelastic features related to orbital excitations in the energy range between -1.4 and -2.5 that do not show any momentum dependence [11]. In particular, as shown in Figure 4.1(b), the RIXS spectrum measured at $q_\parallel = 0.14$ r.l.u. is completely dominated by the elastic signal, that is at least 20 times more intense than *dd* peaks. In the following we will refer to this feature as EI-RXS (energy integrated resonant X-ray scattering) peak since in all our measurements we have found it to be elastic within our experimental uncertainty, that is ∼10 meV.

ARPES, measured on the OD11K sample at T = 20 K, suggest that the FS nesting in not the origin of the strong intensity of the quasi-elastic peak. In fact, photoemission data in panel e of Figure 4.1(b) do not display any replicas of the Fermi surface. Moreover, the shape of the FS does not give parallel segments suitable for a good nesting at $q_\parallel = 0.14$ r.l.u. and the band in the antinodal region (Cu-O bond direction) lies close to the Fermi energy level E_f offering no space for a possible nesting (Figure 4.1(f)). Figure 4.1(g) shows that there is no opening of a gap at E_f, which should be expected in a folded FS due to the presence of charge order [120]. Finally, a strong Van Hove singularity (vHs) is situated slightly below the Fermi energy level at the M point in the Brillouin zone boundary [121], as shown in Figure 4.1(h).

Regarding the RIXS data, this strong and sharp quasi-elastic peak has been measured at three different doping levels (OD17K, $p \sim 0.205$; OD11K,

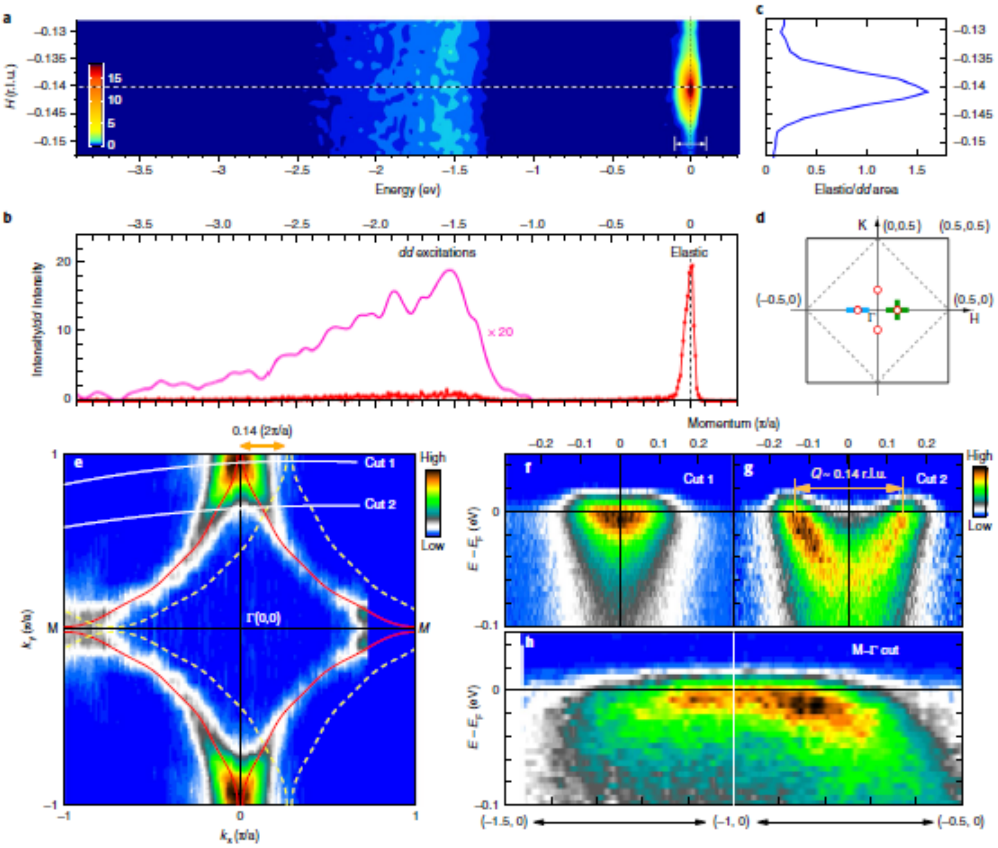

Figure 4.1: Observation of a quasi-elastic peak by RIXS in overdoped $(Bi,Pb)_{2.12}Sr_{1.88}CuO_{6+\delta}$ (OD11K, $T_c = 11$ K, $p \sim 0.215$). a) RIXS intensity color map as a function of both energy and transferred momentum. Spectra have been measured at T = 20 K and with σ polarization of the incident photons along the (-0.5 0) → (0 0) symmetry direction in the first Brillouin zone indicated by the light blue line in panel d. b) RIXS spectrum measured at H≃0.14 r.l.u. (white dashed line in panel a). c) Integrated intensity of the quasi-elastic peak in the energy range indicated in panel a). d) Schematic representation of the 2D Brillouin zone. The open red circles represent the position of the observed quasi-elastic peak. e) Photoemission intensity at the Fermi energy (E_F) as a function of the in-plane momenta k_x and k_y measured on the OD Bi2201 ($T_c = 11$ K). The red lines have been obtained by fitting the data with a tight-binding model and have been illustrated as a guide of the eyes, while the dashed yellow lines are related to the Fermi surface shifted horizontally by 0.14 r.l.u.. f-g) Electronic dispersions for the cuts 1 and 2 indicated by the continuous white lines in panel e). h) Electronic dispersion for the cut along the M-Γ high symmetry direction near the Brillouin zone boundary. Figure from Ref. [96].

$p \sim 0.215$; OD0K $p \sim 0.23$ and OD5K $p \sim 0.225$) and shows all the typical characteristics of the charge order signal present in the underdoped region. In fact, it has been found at both negative and positive $q_{\parallel}$ values with comparable intensity and both along H and K, as shown in Figure 4.2(a), and not along the (H,K) directions of the reciprocal space.

In panel b) of Figure 4.2 we report the doping dependence of the integrated intensity of the quasi-elastic peak measured along both the H and K directions. All the samples were obtained by post-annealing treatments of as-grown samples OD5K, and as a consequence, the latter displays a large and anisotropic peak width since it is characterized by a higher structural disorder. Furthermore, in order to check if this signal arises from structural orders, we have measured its energy dependence (not shown here). In fact, a modulation of the valence charge density is detectable only at the resonance, and our data demonstrate that the incident photon energy dependence of the quasi-elastic peak resembles the Cu L_3-edge X-ray absorption spectrum.

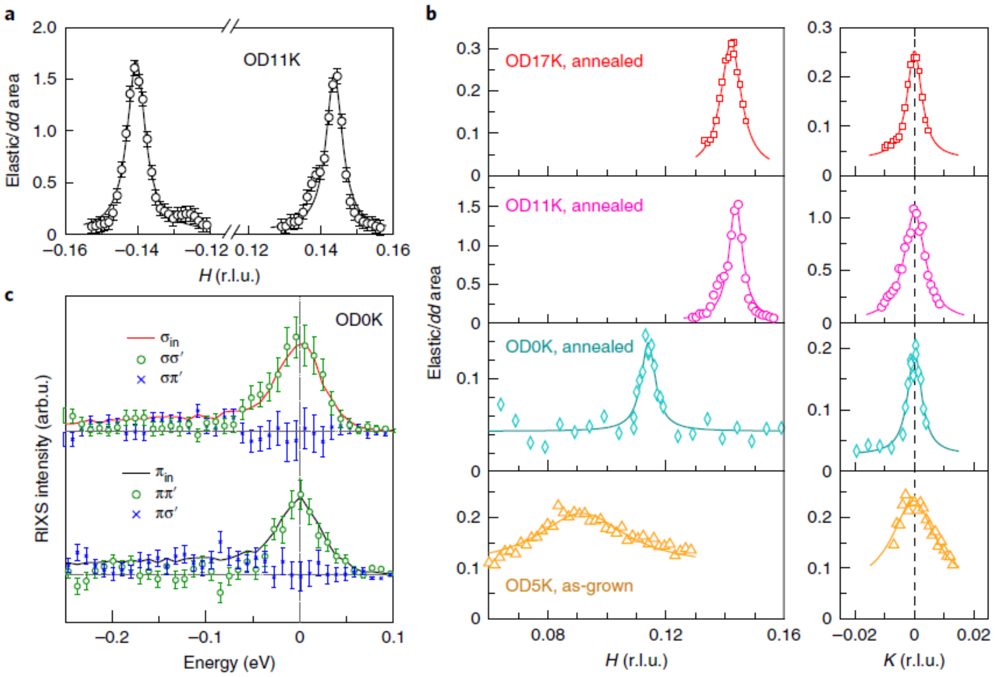

Figure 4.2: a) Quasi-elastic integrated intensity of the EI-RXS signal measured with σ polarization of the incident photons in the OD11K Bi2201 at both negative and positive values of H. b) Integrated intensities at the H and K cuts for all the overdoped Bi2201 that we have investigated. Continuous lines represent the fits made by using a Lorentzian lineshape. c) Polarization-resolved RIXS spectra for OD0K measured at $q_{\parallel} = 0.115$ r.l.u. with both σ (top panel) and π (bottom panel). Error bars have been calculated following the procedure discussed in Chapter 2.7. Figure from Ref. [96].

Finally, in order to determine the character of the EI-RXS peak, we have exploited the possibility to perform polarization-resolved RIXS measurements with the polarimetric device installed at the ERIXS spectrometer (see Chapter 2). Being the EI-RXS peak characterized by an energy of ∼0 eV, its nature could be ascribable solely to be charge or spin, since it is very unlikely that orbital changes are involved at so low energy losses. We know that a scattering that implies a flip of the spin in the ground state without involving an orbital change has to be followed by a 90° rotation of the photon polarization due to the conservation of the total angular momentum of the system [89]. On the contrary, in the absence of a spin-flip event, a pure charge scattering conserves the photon polarization during the RIXS process. As illustrated in Figure 4.2(c), the strong and sharp elastic peak in the OD0K spectra measured at $q_{\parallel} = 0.115$ r.l.u. with both σ (top panel) and π (bottom panel) completely belongs to the non-crossed polarization channels $\sigma\sigma'$ and $\pi\pi'$ within the experimental error bars, while the signal coming from $\sigma\pi'$ and $\pi\sigma'$ spectra displays no intensity in the quasi-elastic spectral range. This experimental finding tells us that the EI-RXS peak arises from charge order, since its scattering conserves the photon polarization.

4.2 Dispersion, damping, and intensity of spin excitations in the monolayer (Bi,Pb)$_{2.12}$Sr$_{1.88}$CuO$_{6+\delta}$ cuprate superconductor family

The data and analyses discussed in this Section have been published in “*Dispersion, damping, and intensity of spin excitations in the monolayer (Bi,Pb)$_{2.12}$Sr$_{1.88}$CuO$_{6+\delta}$ cuprate superconductor family*”, by Y. Y. Peng, E. W. Huang R. Fumagalli, M. Minola, Y. Wang, X. Sun, Y. Ding, K. Kummer, X. J. Zhou, N. B. Brookes, B. Moritz, L. Braicovich, T. P. Devereaux, and G. Ghiringhelli, Physical Review B **98**, 144507 (2018).

We carried out Cu L_3-edge measurements on a large doping range ($0.03 \lesssim p \lesssim 0.23$) of high-$T_c$ (Bi,Pb)$_{2.12}$Sr$_{1.88}$CuO$_{6+\delta}$ (Bi2201) cuprate superconductor. In particular, we focused our attention to the damping and dispersion of magnons and paramagnons along both the nodal (Cu-Cu) and anti-nodal (Cu-O) directions. One of the most important results is that, thanks to the possibility to infer about the polarization of the scattered photons, we demonstrated the spin-flip nature of damped magnetic excitations (paramagnons) in the overdoped region of the phase diagram.

In 2D layered cuprates, high critical temperature superconductivity is obtained by adding charge carriers into the CuO$_2$ planes with a subsequent rapid suppression of the longrange antiferromagnetic (AFM) order of the insulating parent compounds [37]. However, the exceptionally large nearest-neighbor super-exchange interaction among Cu sites helps the preservation of the short and mid range spin correlation, even at very high doping. Antiferromagnetism is a ubiquitous wallpaper for any scenario aiming to explain high-T_c superconductivity, therefore its detailed and complete understanding is necessary. In the absence of long-range AFM order, the most insightful information is encoded in the dispersion, broadening and intensity of spin excitations. Historically, the study of magnetic order and excitations of HTS cuprates has been usually done with inelastic neutron scattering (INS) exploiting both its momentum and energy resolution.

In the last decade, RIXS experiments carried out at the Cu L_3-edge have become more than a promising alternative to INS to measure spin excitations [89, 90, 5]: in fact, thanks to the more favorable cross sections and beam flux available in the third generation synchrotron, it is possible with RIXS to measure small crystals, films and even heterostructures. INS experiments have shown that the zero-energy scattering peak at the antiferromagnetic-order wave vector $\mathbf{q}_\mathrm{AF} = (0.5, 0.5)$ rapidly loses intensity moving from the undoped cuprates to the overdoped SC compounds [122, 123]. Moreover, INS has revealed that around $\mathbf{q}_\mathrm{AF}$ both elastic and inelastic scattering related to spin order get suppressed by doping. On the contrary, RIXS experiments have demonstrated that spin excitations persist up to heavily overdoped and non-superconducting compounds in a large portion of the 2D Brillouin zone around the Γ point (0, 0) [22, 23, 113, 112, 114, 95].

There is therefore an apparent contradiction between the results obtained with INS and RIXS that can be easily explained by the fact that these two techniques probe different areas of the reciprocal space. In this context, the numerical calculations of the spin dynamical structure factor $S(\mathbf{q},\omega)$ [124, 125] show that the short-range and high-energy spin excitations measured by RIXS close to the magnetic Brillouin zone boundaries are less relevant in the pairing mechanism of HTS cuprate than the low-energy ones measured with INS around the antiferromagnetic point $\mathbf{q}_\mathrm{AF}$. All this information leads to consider spin fluctuations as a key ingredient for the explanation of superconductivity in cuprates [126, 71].

However, most of the results mentioned above obtained by RIXS concern solely the high symmetry anti-nodal direction $\Gamma \to X$ or [10] (related to the Cu-O bonds). On the contrary, in the RIXS spectra acquired along the nodal direction it is difficult to identify excitations having a collective nature. In this case, the experimental findings have been interpreted with an itinerant picture (particle-hole excitations) supported by random-phase approximation (RPA) calculations, thus questioning the mere existence of damped collective spin excitations (paramagnons) in doped cuprates [127, 128, 129, 130, 131]. An apparent dichotomy emerges between dispersing spin-excitations along the [10] direction that preserve they spectral weight upon doping and the continuum given by charge modes along the [11] direction that softens as the doping is increased [127, 128]. As a consequence, the doping evolution of magnons into paramagnons calls for revised interpretations especially regarding the microscopic description of spin fluctuations in overdoped compounds. These issues are even more interesting in consideration of the recent RIXS study of several AFM parent compounds that showed how apical oxygen ions tend to localize the in-plane exchange coupling, with detrimental effects on the optimal T_c and thus superconductivity in the respective doped materials under the assumption that doping does not modify significantly the spin excitation dispersion [18]. In support of these hypotheses, recent determinant quantum Monte Carlo (DQMC) calculations showed that the reduction of spectral weight as well as the hardening of paramagnons near $\mathbf{q}_{\mathrm{AF}}$ leads to a substantial decrease of the d-wave pairing strength in the overdoped regime [132]. Furthermore, a low-energy spin excitation was predicted along the nodal direction for overdoped $La_{1.77}Sr_{0.23}CuO_4$ (LSCO) from RPA calculations, which was proposed to be resolvable by RIXS if energy resolution is improved to ∼60 meV [129]. Overall, an extensive high-resolution study of the doping and momentum dependence of paramagnons might shade lights about the different perspectives mentioned above.

In the work presented in this section we have performed a systematic Cu L_3-edge RIXS study of magnetic excitations on four doping levels, spanning from the AFM insulator to the overdoped superconductor, of single-layer Bi2201. We have covered a sufficiently large region of the reciprocal space and we have determined the energy *vs.* momentum dispersion, damping and spectral weight as a function of both doping and momentum of the magnetic excitations. The main results obtained with this work is that both the undumped frequency and the damping factor increase from the AFM to the overdoped compound. Furthermore, a remarkable momentum dependence is displayed by the damping and the spectral weight. These observations were captured by DQMC calculations of $S(\mathbf{q}, \omega)$ for the three-band Hubbard model, which allow us to interpret quantitatively the conclusion that can be drawn from the experimental findings.

Among all these results reported in detail in Ref. [133], in this section we would like to emphasize the polarization-resolved RIXS measurements of the overdoped Bi2201 that allowed us to isolate the spin-flip contribution even at this level of doping. Panels a-b) of Figure 4.3 show the low energy range of two RIXS spectra measured on the overdoped Bi2201 (OD11K, T_c = 11 K, $p \sim 0.215$) sample at two selected in-plane momenta along the

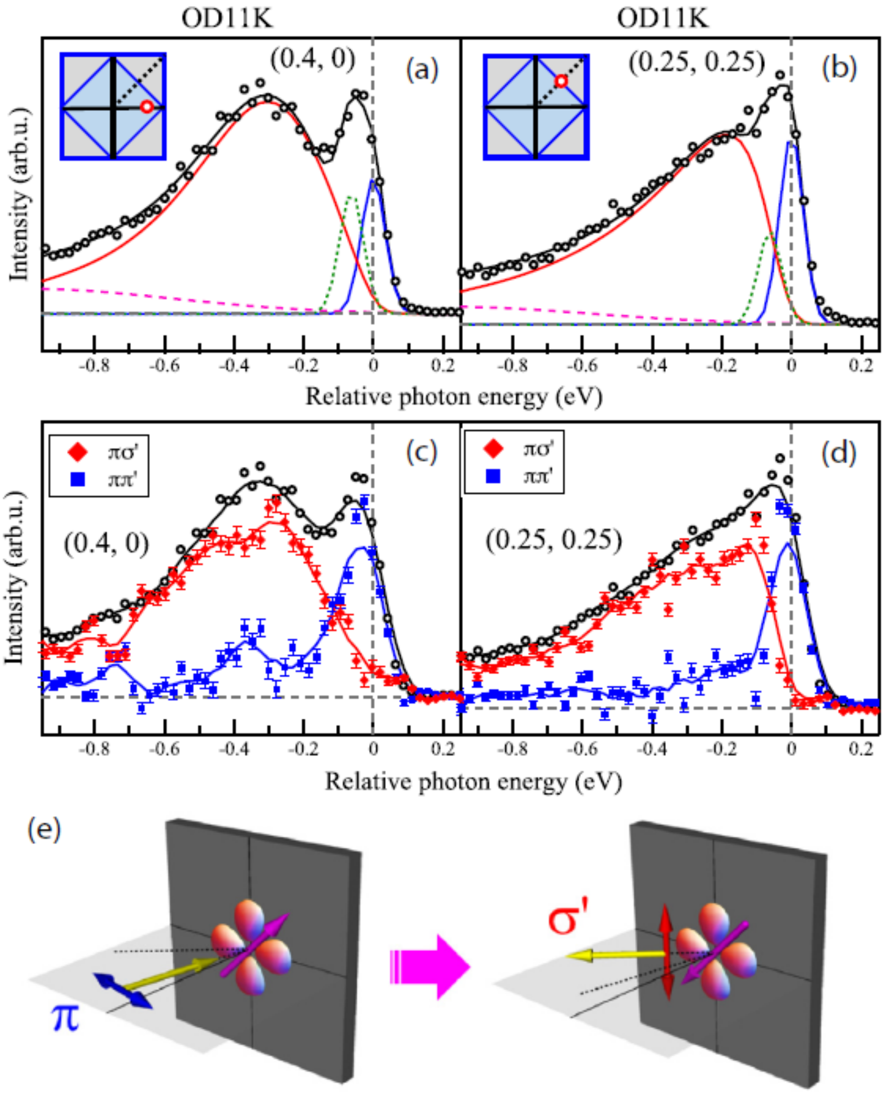

Figure 4.3: a-b) RIXS spectra of overdoped Bi2201 (OD11K, $T_{\mathrm{c}} = 11$ K, $p \sim 0.215$) at (0.4 0) and (0.25 0.25) (see the insets), respectively, measured with π polarization of the incident photons at T = 20 K. Both the two spectra illustrated have been decomposed in the following way: magnetic excitations are represented by the continuous red lines, phonons with green dotted lines and the elastic signal with continuous blue lines. The background coming from the scattering given by the continuum of charge modes is represented with the dotted magenta lines. Raw data (black dots) have been smoothed (continuous black lines). c-d) Polarization-resolved RIXS spectra of OD11K Bi2201 ($p \sim 0.23$) measured with π polarization of the incident light. Red spectra correspond to the crossed $\pi\sigma'$ polarization channels, while the blue ones to the non-crossed $\pi\pi'$. Error bars have been calculated following the procedure introduced in Chapter 2.7. e) Schematic representation of the spin-flip process probed by RIXS. Figure from Ref. [133].

anti-nodal (panel a) and nodal (panel b) direction of the first Brillouin zone (see the two insets). Both the two spectra were taken at T = 20 K and with π polarization of the incident photons and were decomposed onto a resolution limited elastic line (centered at ~0 energy, continuous blue line) and a generic phonon contribution (dashed green line). As we can clearly see, the magnetic peak (paramagnon, red line) dominates the low energy spectral range, as expected.

In analogy with INS experiments, RIXS can probe the spin dynamical structure factor $S(\mathbf{q},\,\omega)$ which is directly proportional to the imaginary part of the magnetic susceptibility $\chi''(\mathbf{q},\,\omega)$. Since RIXS and INS are characterized by a different microscopic scattering process, we can not therefore compare the absolute intensity values. However, knowing that the intensity of spin excitations has a weak dependence on the scattering angles and polarization, we can indeed make a comparison between the relative intensities [89]. We decided therefore to fit the magnetic peak using a function that has been obtained from the expression of χ and from its imaginary part $\chi''(\mathbf{q},\,\omega)$. In this way we can easily estimate the energy, width, and relative intensity of the spin-flip peak and, ultimately, of χ. A damped harmonic oscillator characterized by the undamped frequency ω_0 and damping factor γ, can be described by the complex susceptibility $\chi''(\omega) \propto 1/[(\omega_0^2 - \omega^2)+2i\gamma\omega]$. For a given momentum transferred, we can thus explicit the imaginary part of the magnetic susceptibility in the following way:

$$\chi''(\mathbf{q},\omega) \propto \frac{\gamma\omega}{(\omega^2-\omega_0^2)^2+4\gamma^2\omega^2}. \tag{4.1}$$

In the case of a not too large damping ($\gamma < \omega_0$) the shape of χ'' can be obtained in the same way by an antisymmetrized Lorentzian function $L(\omega)$ that can be expressed as the difference of two Lorentzian peaks centered at $\pm\omega_p$ and same width γ:

$$L(\omega) = \frac{\gamma}{(\omega-\omega_p)^2+\gamma^2} - \frac{\gamma}{(\omega+\omega_p)^2+\gamma^2}. \tag{4.2}$$

The use of the antisymmetrized Lorentzian function $L(\omega)$ to fit damped magnetic excitations can lead to an inaccurate estimation of ω_0 [22, 23], especially in the case of overdamped paramagnons where $\gamma > \omega_0$. Therefore, we have fitted the paramagnon peaks in a consistent way using the function χ'' reported in Eq. 4.1 after being convoluted with a Gaussian lineshape to take into account the overall experimental energy resolution (~55 meV). By using this fitting procedure we could estimate the values of γ and ω_0 for all the measured RIXS spectra. Moreover, in order to get a reliable fit, we have also included the scattering due to the particle-hole continuum given by the added charges (magenta dashed lines).

The spectral assignments have been widely confirmed by the polarization-resolved RIXS measurements reported in the panels c and d of Figure 4.3. The quasi-elastic region belongs to the non-crossed $\pi\pi'$ polarization channels due to the charge scattering that preserves the polarization during the RIXS process. Since for these measurements we had to relax the energy resolution ($\sim$80 meV) due to the low efficiency of the polarimeter, we can not distinguish the phononic peaks from the quasi-elastic line. Regarding the magnetic peak, in both the two polarization-resolved RIXS spectra reported in Figure 4.3 it is present in the $\pi\sigma'$ channels, as expected for spin-flip transitions (see Chapter 3.4). In fact, as schematically illustrated in Figure 4.3(e), since RIXS probes the flip of the ground state spin, in order to conserve the total angular momentum of the system the polarization of the scattered photons has to be rotated by 90°.

The important finding is that we demonstrate that magnetic excitations along both the [10] and [11] directions of the reciprocal space preserve their polarization dependence upon doping, even in the overdoped region of the phase diagram where paramagnons show a noticeable damping.

4.3 Multiple-magnon excitations shape the spin spectrum of cuprate parent compounds

The data and analyses discussed in this Section have been recently submitted as a part of the work "*Multiple-magnon excitations shape the spin spectrum of cuprate parent compounds*" by D. Betto, R. Fumagalli, M. Rossi, R. Piombo, K. Yoshimi, D. Di Castro, E. Di Gennaro, D. Bonn, G. A. Sawatsky, F. Miletto-Granozio, L. Braicovich, N. B. Brookes, J. Lorenzana, and G. Ghiringhelli.

In this work we measured the dispersion of spin waves using RIXS on single crystals of $Sr_2CuO_2Cl_2$ (SCOC) and thin films of La_2CuO_4 (LCO), both insulating antiferromagnets and well studied examples of the two-dimensional (2D) Heisenberg square lattice. We found that the dispersion across the 2D Brillouin zone is in very good agreement with inelastic neutron scattering (INS) data except when close to the zone boundary along the [10] direction (X-point, $q_{\parallel} = ({}^{1}\!/_{2}, 0)$). The analysis of the polarimetric data, which gives the possibility to disentangle the two linear polarizations of the scattered light, points to the existence of a continuum of excitations which couples to the spin waves, broadening and shifting them to higher energy loss. This unexpected behavior might give additional contributions to the RIXS scattering operator especially in the crossed polarization channels, shedding a light on the different line shape with respect to neutrons. The results discussed in the following draw special attention to the importance of quantum fluctuations in spin-$1/2$ systems at the zone boundary.

The 2D spin-$1/2$ antiferromagnet square lattice represents one of the most investigated quantum systems and constitutes a standard reference for quantum magnetism. Specifically, it describes the CuO_2 planes that characterize all the layered parent compounds of the high-T_c superconducting cuprates and for that reason it has been widely inspected. As discussed in Chapter 1.2.2, the ground state of the undoped parent compounds is described by a long-range antiferromagnetic order [53, 134], while, in the case of doped superconductors, damped and broadened magnons result from the short-range in-plane spin correlations [5, 23, 95]. These considerations lead to the proposal of spin-fluctuations as a candidate for the "glue" for Cooper pairs in high-T_c cuprate superconductors [71]. The most relevant coupling parameters, such as the super-exchange interactions J_{SE}, the nearest-neighbors hopping parameters t and the Coulomb repulsion U, have been estimated from the analysis of the measured momentum dependence of spin excitations on a large variety of systems [53, 134, 135, 136, 18].

We decided to carry out Cu L_3-edge RIXS measurements to study the momentum dependence of spin excitations in the LCO and SCOC parent compounds because they represent good 2D antiferromagnetic prototypes where the single-layer CuO_2 planes are separated by LaO_2 planes or Sr and Cl atoms, respectively. Historically, this kind of experiments has been done using INS and the measured dispersion usually interpreted by an improved Heisenberg model which includes higher-order terms [134, 137].

In Chapter 2 we have discussed all the advantages given by RIXS, especially for the study of magnetic excitations in cuprate superconductors [5, 22, 23, 95, 18] and other strongly-correlated compounds[138, 139, 140]. Furthermore, the resonant nature of the RIXS process allows us to investigate very small samples, such as, for example, nanometer-thick thin films. Finally, this technique includes also the possibility of retaining the energy resolution at higher energy transfer. On the other hand, the very small scattering cross-section of neutrons requires the use of bulk samples and the magnetic excitations have to be extracted by subtracting a non-magnetic background, which can lead to partially incorrect interpretations of the experimental data. Nevertheless, from the theoretical point of view the scattering process in INS is fully explained in terms of the dynamic magnetic susceptibility [141], while in the case of the RIXS cross-sections of magnetic and other collective modes, a complete theoretical explanation is still missing and further investigations are needed [142]. Recently Plumb *et al.* [137] identified some differences between INS and RIXS measurements in the magnetic dispersion of the AF SCOC close to the X-point of the Brillouin zone, where apparently RIXS overestimates the magnon energy by $\sim$ 25 meV.

In this work we report state-of-the-art high-resolution RIXS measurements, acquired with the ERIXS spectrometer at the ID32 beamline of the ESRF [8] on a SCOC single crystal and LCO thin film, focusing our attention to the spectral range where magnetic excitations take place. To better clarify the discrepancy between RIXS and INS results, we compared the extracted single magnon peak positions (for more details see below) of LCO and SCOC with the most recent INS measurements carried out on the same materials [134, 137], as shown in panels a) and b) of Figure 4.4, respectively. The agreement between the two datasets is remarkable everywhere except near $q_{\parallel} = (^1/_2, 0)$ in SCOC, as pointed out by Plumb *et al.* [137]. The amount of the discrepancy is of the order of 10-25 meV depending on the model used to fit the RIXS spectra. We underline that both the RIXS and INS measurements display a substantial decrease of the magnetic peaks intensity approaching the X-point. This behavior has been also found in other cuprates and spin-$^1/_2$ systems, but the mechanism beyond it remains still unclear.

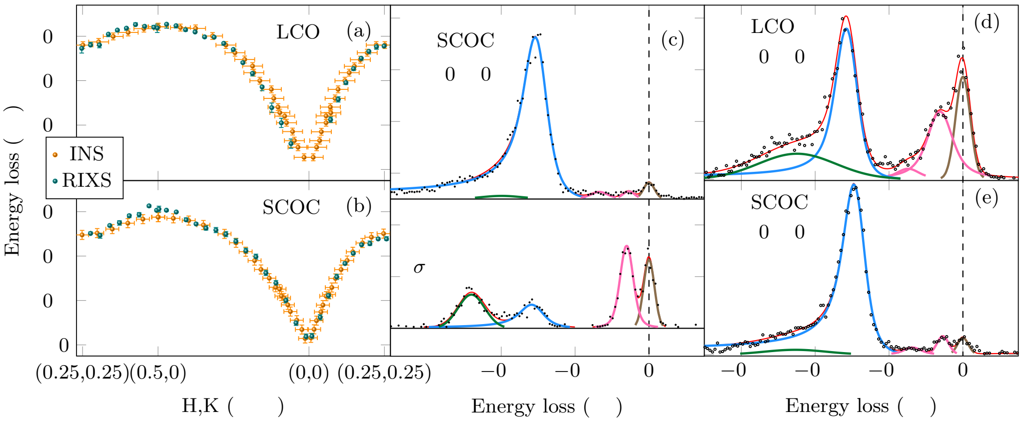

Figure 4.4: a-b) Extracted energy positions of the single magnon peak extracted from the RIXS spectra and superimposed to the ones obtained with INS in Refs. [134] and [137]. c) Incoming polarization dependence of the SCOC RIXS spectra measured at $q_{\parallel} = (0.5, 0)$. d-e) Example of the fitting procedure in the low energy spectral range applied to LCO (d) and SCOC (e) at $q_{\parallel} = (0.4, 0)$. Raw data are illustrated with the black dots and the fit with the red continuous line, while for the decomposed spectral features we have: brown curve for the elastic peak, magenta curves for the phonon contributions, blue curves for the single magnon and its tail and finally green curve for the multimagnon contribution.

Regarding the RIXS spectra, we decomposed them into a resolution limited quasi-elastic peak centered at 0 energy loss, a generic phonon contribution with its overtone and finally a single- and multi-magnon peaks. We used a Gaussian line shape to model the elastic and the multimagnon peaks, while for the phonons we adopted a Lorentzian shape convoluted with a Gaussian function in order to take into account the overall energy resolution. Regarding the single-magnon peak, the high-energy resolution offered by the ERIXS spectrometer ($\sim$ 45 meV for LCO and $\sim$ 32 meV for SCOC measurements) allowed us to clearly distinguish the asymmetry of the line shape and, therefore, we used a Fano line shape for the fitting. Using this procedure we obtained reliable results across the entire Brillouin zone, especially when matching the low-energy side of the single-magnon peak. This approach allowed us to better capture the asymmetry (single peak + tail) of this peak, especially close to the zone boundary. The results are reported in panels c-e) of Figure 4.4.

Concerning the difference between RIXS and INS spectra close to the X-point, a conceivable explanation could be due to the fact that RIXS, like for example Raman and other IR spectroscopies, is sensitive to spin-conserving ($\Delta S = 0$) excitations such as bimagnons. The presence of a sharp peak in the mid-IR spectra of insulating parent compounds is usually assigned to a bimagnon plus a phononic excitation [143], which becomes abnormally sharp at the zone boundary. Its energy is well established from IR experiments.

At this point, we decided to gain further insight on the RIXS line shape, especially at the zone boundary, thanks to the polarization analysis of the scattered photons. We performed polarization-resolved RIXS measurements on SCOC at $q_{\parallel} = (1/2, 0)$, $(1/4, 1/4)$ and $(1/4, 0)$ with both π and σ incident polarizations. The results in the low-energy spectral range are illustrated in Figure 4.5. The decomposition of the spectra into two linearly polarized outgoing channels π' and σ', and the statistical error bars have been obtained following the procedures described in Chapter 2.7.

Starting with the comparison between the spectra reported in Figure 4.5(a) and Figure 4.4(c), the polarization-resolved RIXS spectra clearly show that the main contribution to the overall line shape at $\sim$ 0.3 eV belongs to the crossed polarization channel $\pi\sigma'$. As explained above, the bimagnon excitation conserves the spin ($\Delta S = 0$) and as a consequence should give contribution solely to the $\pi\pi'$ signal. Following this consideration, we can exclude the scenario in which the bimagnon becomes dominant at $(1/2, 0)$. An unexpected complexity is revealed by carefully inspecting the spectra shown in Figure 4.5. It is often assumed that in the crossed polarization channel the scattering involves only a single magnon operator, but the RIXS spectrum should be proportional to the full transverse magnetic structure factor $S^{\perp}(\mathbf{q}, \omega)$, which also includes a three-magnon continua developing above the single

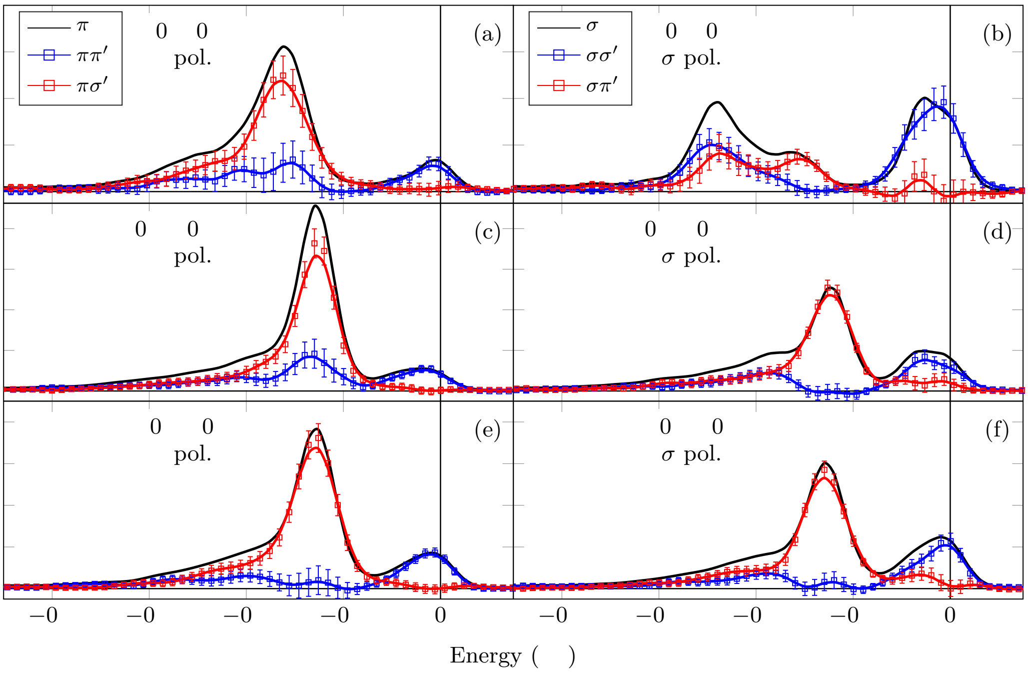

Figure 4.5: Polarization-resolved SCOC RIXS spectra measured at selected **q** along the high symmetry directions of the whole Brillouin zone. The spectra were taken with both π and σ polarization of the incident light. The unpolarized spectra (black lines) have been smoothed on 3 points.

magnon [144, 145, 146, 147] and ideally other odd number of magnons excitations with increasingly lower importance. The continuum given by the three magnons has a 21% spectral weight on average in the entire Brillouin zone [144] with a relative maximum (40%) at the boundary zone [145]. We therefore assign the high-energy tail of the single-magnon peak to a three-magnon process, which is also responsible to the asymmetric Fano line shape.

We note that these considerations are experimentally reproduced in the spectra measured with incident π polarization (left panels of Figure 4.5): in fact, at (0.25, 0.25) and (0.25, 0) the spectra are dominated by the $\pi\sigma'$ channels related to the single magnon peak accompanied by a higher energy continuum that shows an increased weight at (0.5, 0). Furthermore, if only a single magnon is considered, the $\sigma\pi'$ channel reported in Figure 4.5(b) should be proportional with the $\pi\sigma'$ one in Figure 4.5(a), which is without any doubts not the case. The direct consequence of this discrepancy implies that the scattering operator may be constituted by another spin-flip channel, *e.g.* a three magnon operator as proposed in Ref. [148]. The idea behind this claim is that these two spin-slip channels, despite being different but characterized by the same symmetry, could interfere yielding a different line shape than the neutron $S^{\perp}(\mathbf{q}, \omega)$, and therefore they might have a different directional dependence reflected in the two crossed channels $\sigma\pi'$ and $\pi\sigma'$.

Concerning the spin-conserving processes that can be seen in the non-crossed channels, the scattering operator is usually derived assuming a local approximation where the most relevant effect of the intermediate $2p^5 3d^{10}$ state probed by the RIXS process is to transiently eliminate one magnetic site, without displaying any polarization dependence. However, we note that in our data at (0.5, 0) the non-crossed polarized channels $\pi\pi'$ and $\sigma\sigma'$, reported in the top panels of Figure 4.5, show different line shapes. This calls for non-local effects of the core hole, where the polarization direction selects particular magnetic bonds in real space. The simplest spin-conserving excitation is a finite momentum generalization of Raman operators [149] which resemble the ones appearing in the theory of phonon-assisted multimagnon absorption in IR [150, 151]. These operators should not be symmetry-allowed in RIXS at the zone boundary but, nonetheless, we note that the $\pi\pi'$ spectrum at (0.5, 0) displays a peak at $\sim$ -0.3 eV which is consistent with the bimagnon peak found in IR experiments [151]. Furthermore, the $\pi\pi'$ channel is characterized by higher energy structures that we assigned to four and more (even number of magnons) processes. The breaking of the symmetry rule could be due to the resonant nature of the RIXS process or external effects such as disorder.

To summarize, we studied the spin-wave dispersion in $Sr_2CuO_2Cl_2$ and La_2CuO_4 along high-symmetry directions across the whole Brillouin zone. We compared our high-resolution RIXS spectra to that obtained with INS and we found a perfect agreement in LCO, while SCOC spectra show a discrepancy near the X-point, at the zone boundary. Across the entire Brillouin zone, our measurements clearly show that the single magnon peak is characterized by an asymmetrical line shape, reminiscent of a Fano process. In our investigation we added polarization-resolved RIXS data, where we noted that the main contribution to the spectra (single-magnon peak) belongs to the crossed polarization channels. Coming back to the discrepancy seen in RIXS and INS spectra at the X-point, our polarization-resolved measurements allow us to attribute it to the interference between two different spin-flip channels that can be probed simultaneously solely by RIXS. On the contrary, only one of them contributes to neutrons. Finally, the RIXS-INS anomaly in the crossed polarization channels and the strong multimagnon effects present in the $\pi\pi'$ channel both close to the X-point are suggestive of the proximity to more exotic ground states, as proposed by INS studies [134, 152, 153].

4.4 Three-dimensional collective charge excitations in electron-doped copper oxide superconductors

The data and analyses discussed in this Ssection have been published in "*Three-dimensional collective charge excitations in electron-doped copper oxide superconductors cuprate superconductor family*", by M. Hepting, L. Chaix, E. W. Huang, R. Fumagalli, Y. Y. Peng, B. Moritz, K. Kummer, N. B. Brookes, W. C. Lee, M. Hashimoto, T. Sarkar, J.-F. He, C. R. Rotundu, Y. S. Lee, R. L. Greene, L. Braicovich, G. Ghiringhelli, Z. X. Shen, T. P. Devereaux, and W. S. Lee, Nature **563**, 374 (2018).

Since the core of high-temperature copper oxide superconductors lies in the CuO_2 planes, the main electronic and magnetic properties have a two-dimensional (2D) nature [62, 154], whereas superconducting coherence displays a three-dimensional (3D) character. Optical measurements have revealed that, in a limited area of the reciprocal space, out-of-plane charge dynamics, such as plasmons, are incoherent in the normal state [155, 156]. Plasmons have been experimentally detected with other spectroscopic techniques [156, 157, 158] and transmission electron energy loss spectroscopy (EELS) [159]. Unfortunately, these investigations carry information solely in a restrict portion of the Brillouin zone, in particular near the Γ-point and without exploring the out-of-plane q_z-dependence. In systems with quasi-2D conducting layers, the charge dynamics are significantly affected by the poorly screened out-of-plane Coulomb interactions. The dispersion of charge collective modes changes from optical-like to acoustic-like plasmons as a function of the momentum perpendicular to the conducting planes.

In the specific case of superconducting cuprates characterized by conducting CuO_2 planes stacked along the c-axis with an almost negligible interplane Coulomb screening, an analogous charge dynamics has been proposed to be present [160, 161, 162]. In the work discussed in this Section we have exploited the capability of RIXS to probe charge excitations across all the three dimensions of the first Brillouin zone, and moreover, to infer about the polarization of the scattered photons. We found that the excitations have a pure charge nature without mixing with magnetic components, confirming their 3D character from the out-of-plane dispersion. The periodicity along the direction perpendicular to the CuO_2 planes corresponds to their relative distance, without showing a correlation with the crystallographic c-axis lattice constant. This evidence points to consider the interplane electron-electron Coulomb interaction to be responsible for the coherent out-of-plane charge dynamics. All these properties suggest that our experimental findings are the confirmation of the presence of acoustic plasmon, a distinct branch of charge collective modes that has been predicted to play a significant role in mediating the pairing in layered systems [163, 160, 161, 162].

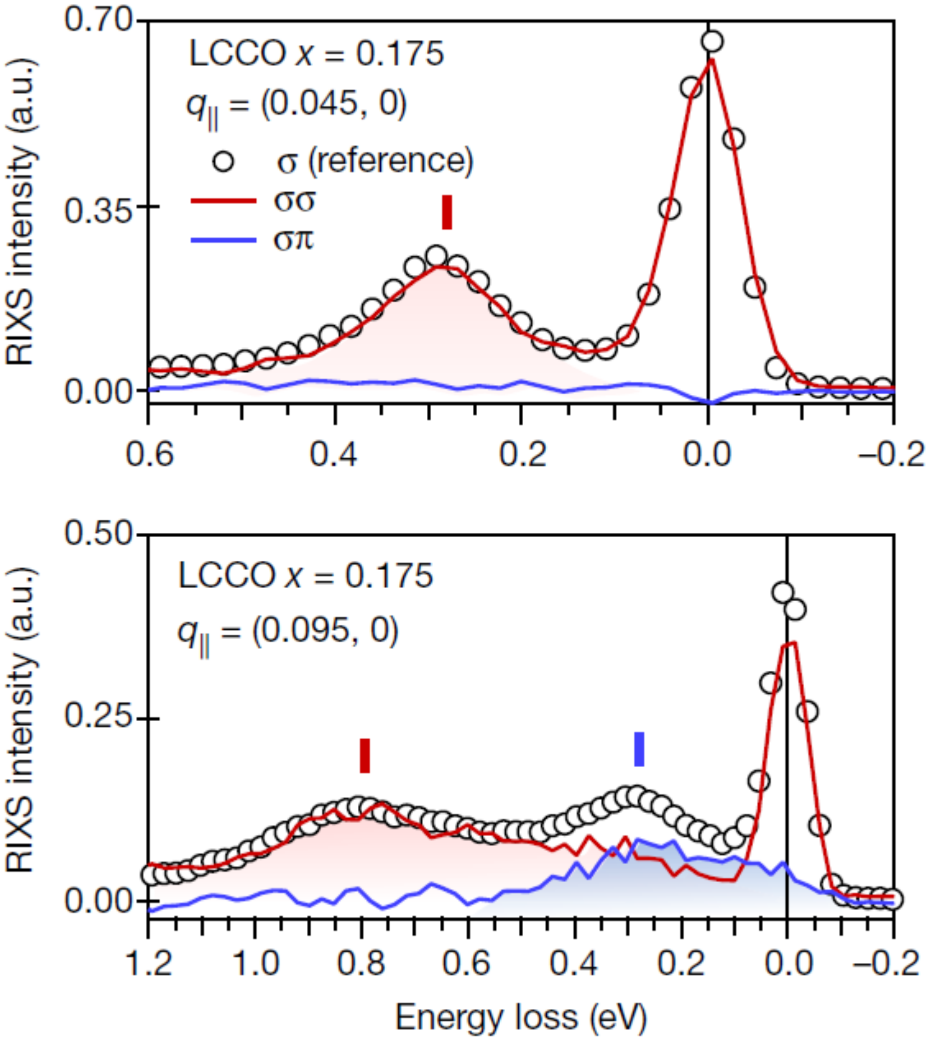

Figure 4.6: Polarization-resolved RIXS spectra of LCCO at two representative in-plane momenta $q_{\|} = (0.045, 0)$ and $(0.095, 0)$. $\sigma\sigma$ spectrum (shown in red) is related to the charge scattering, while magnetic excitation, such as paramagnons, belongs to the crossed-polarization channel $\sigma\pi$ (blue lines). Circles represent the unpolarized spectrum, which is given by the sum of the $\sigma\sigma$ and $\sigma\pi$ contributions. Figure from Ref. [54].

In this work we investigated the enigmatic "zone center" excitation previously discovered by Cu L_3-edge RIXS in the electron-doped superconductor

$Nd_{2-x}Ce_xCuO_4$ (x=0.15) [164, 165], from now on NCCO, and $Sr_{1-x}La_xCuO_2$ [166]. We found in another electron-doped compound, namely $La_{2-x}Ce_xCuO_4$ (LCCO) (x=0.15), spectral features similar to those of NCCO, suggesting the universality of this collective mode in electron-doped cuprate superconductors. Although the mode has been suspected to be of charge character, such as for example plasmons [167], collective modes of quantum phase [165] and intra-band transitions [164], a definitive assessment has not been possible due to the impossibility to disentangle the charge and magnetic nature of the excitations [4, 142].

We therefore decided to exploit the possibility to resolve the polarization of the scattered photons offered by the ERIXS spectrometer to determine the character of this excitation. As we have already explained, magnetic excitations that involve the flip of the spin necessarily yield to rotate the polarization of the scattered photons in order to conserve the total angular momentum of the system. As a result, in a RIXS spectrum, a single spin-flip excitation contributes to the crossed-polarization channels ($\sigma\pi'$ or $\pi\sigma'$). Contrarily, charge excitations conserve the polarization of the photons during the scattering event and as a consequence they are usually detected in the parallel polarization channels ($\sigma\sigma'$ or $\pi\pi'$).

In Figure 4.6 we report the low-energy range of polarization-resolved RIXS spectra measured on LCCO with σ polarization of the incident light at two representative in-plane transferred momenta. In the top panel of Figure 4.6 the spectrum is completely dominated by the $\sigma\sigma'$ spectral component: Here we can distinguish two peaks: the quasi-elastic at 0 energy loss and the other one, related to the zone center excitation, at $\sim$ 0.28 eV. At larger momentum (bottom panel of Figure 4.6), the mode disperses reaching an energy of $\sim$ 0.8 eV and, as expected, a magnetic excitation (paramagnon) appears at about 0.3 eV [164, 165, 166, 4]. As we have seen in many other cases [95, 133, 60], paramagnons mainly belong to the crossed-polarization channel. In particular, at $q_\parallel$ = (0.095, 0) the zone center excitation is well separated in energy from the paramagnon and still occurs in the $\sigma\sigma'$ spectral component. Finally, thanks to the insights given by polarization-resolved RIXS, we ascribe the zone center excitation to be a pure charge mode.

To better characterize the charge mode, we studied its momentum dependence in all the three dimensions of the reciprocal space, especially focusing the attention on the never explored q_z-dependence [163, 165, 166]. In Figure 4.7(a-b) we report the RIXS intensity maps at $l = 1$ and 1.65 r.l.u. as a function of the transferred momentum along the hh and h directions. Here l (h) indicates transferred momentum along the c (a)-axis and it is reported in units of $2\pi/c$ ($2\pi/a$), where a and c are the lattice constants of LCCO.

The charge mode shows a different dispersion depending on l and an

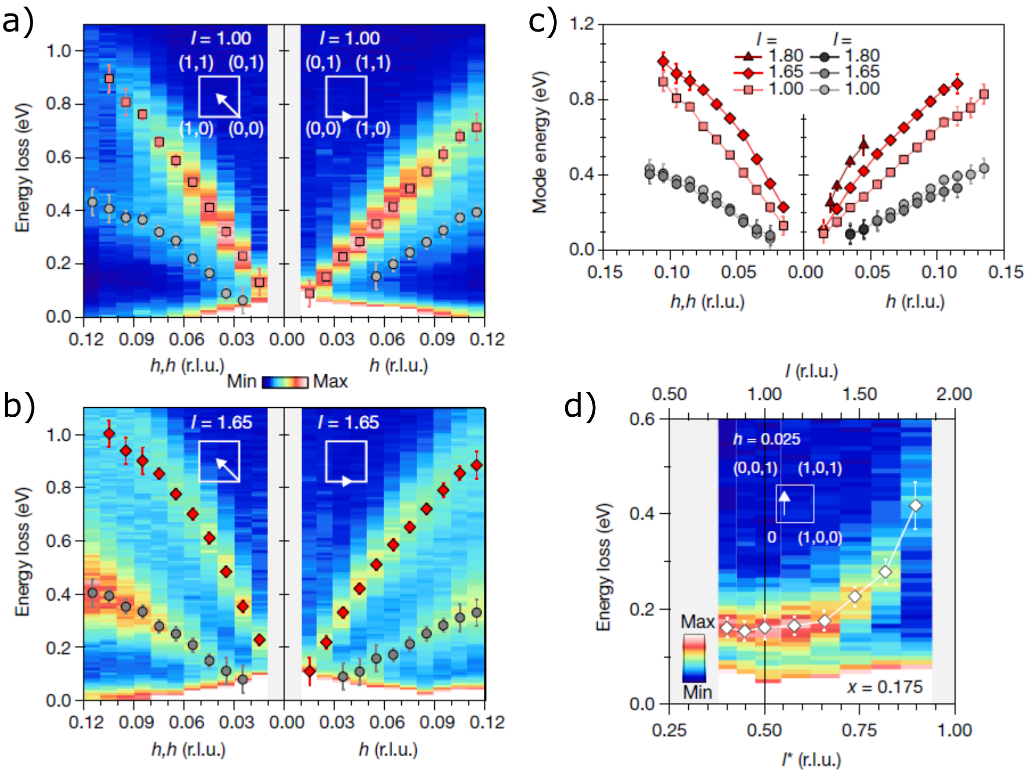

Figure 4.7: a-b) RIXS intensity maps of LCCO ($x = 0.175$) along the hh and h direction as a function of the transferred momentum along the c-axis (l). Symbols indicate the extracted energy of the zone center excitation (red) and the paramagnons (grey). Statistical error bars have been evaluated from the uncertainty in energy-loss reference-point determination ($\sim \pm$ 0.01 eV) together with the standard deviation of the fits. c) Momentum dependence at different l values of the zone center excitation (red symbols) and the paramagnon (grey symbols). The latter show no l-dependence. d) RIXS intensity map along the out-of-plane (perpendicular to the CuO_2 planes) direction at $h = 0.025$. The transferred momentum along the c-axis (l, top scale) is reported in units of $2\pi/c$, while l^* (bottom scale, units of $2\pi/d$) corresponds to the CuO_2 plane spacing. Figure from Ref. [54].

almost linear in-plane momentum dependence (in both the two cases) originating from the zone center $(0,\ 0,\ l)$, while the paramagnons, as expected since their 2D nature, do not show any l-dependence. The summary of these considerations is reported in Figure 4.7(c), where we compare the in-plane momentum dependence along the hh and h directions for three different values of l. We further investigated the out-of-plane dependence by fixing the in-plane momentum $h = 0.025$ and acquiring RIXS spectra at different l values. The results are shown in Figure 4.7(d). Here we denote the bottom scale with the index l^* (units of $2\pi/d$, where $d = c/2$ is the nearest-neighbor

CuO_2 plane spacing), useful to describe the proper periodicity of the zone center excitation. The dispersion is symmetric around the high symmetry point $l = 1$, and in particular, increasing the values of l from 1 to 1.8 (the maximum out-of plane momentum that could be reached in our experiment) the zone center disperses towards high energy.

In summary, we used the polarisation analyser of ID32 beamline to disentangle magnetic and charge contributions in the RIXS spectra and revealed a pure charge character of the zone center mode. Moreover, we were able to explore the relevant energy-momentum region thanks to the continuous rotation of the spectrometer: in particular, we probed the excitations also along the out-of-plane direction perpendicular to the CuO_2 planes, demonstrating that the coherent 3D charge dynamics are in agreement with the long-sought acoustic plasmon. The experimental findings are also supported by theoretical calculations, which change the prospective when describing the charge dynamics in copper oxides, usually described with 2D models.

Our results open new perspectives regarding the connection between acoustic plasmons and the enhanced superconducting transition temperatures. As a consequence, the layered crystal structure of copper oxides has to be taken into account when describing the superconducting properties since the Coulomb energy stored between the CuO_2 planes plays a part in the energy savings associated with the superconducting transition.

4.5 Coupling between dynamic magnetic and charge-order correlations in the cuprate superconductor $Nd_{2-x}Ce_xCuO_4$

The data and analyses discussed in this Section have been published in "*Coupling between dynamic magnetic and charge-order correlations in the cuprate superconductor $Nd_{2-x}Ce_xCuO_4$*", by E. H. da Silva Neto, M. Minola, B. Yu, W. Tabis, M. Bluschke, D. Unruh, H. Suzuki, Y. Li, G. Yu, D. Betto, K. Kummer, F. Yakhou, N. B. Brookes, M. Le Tacon, M. Greven, B. Keimer, and A. Damascelli, Physical Review B **98**, 161114(R) (2018).

Upon increasing doping the antiferromagnetic phase is suppressed and within the pseudogap region in the underdoped regime of the phase diagram all cuprate high-T_c superconductors display charge order correlations coexisting with superconducitivity and competing with it [40, 168, 169, 42, 43, 45, 116, 170, 48, 118, 46, 47, 49, 119, 117, 171]. These charge density waves (CDW) can be described by a periodic configuration of low-energy electronic states. After the first theoretical predictions about the coexistence of charge and spin stripe orders [172, 173, 174, 175] later experimentally observed in the La-based cuprates family [40], the more recent observations of charge order (CO) in other cuprate families point to new interpretations, some of which include and invoke an interplay between CO and AF fluctuations [176, 177, 178, 179, 180]. In this framework, only nuclear magnetic resonance measurements carried out on hole-doped $YBa_2Cu_3O_{6+\delta}$ (YBCO) materials shed light about a possible coupling between charge and spin fluctuations [43, 181, 182, 183], while in the case of the other cuprate families there is not yet a convincing manifestation of the co-action between the CO evolution upon doping and the AF properties [119, 181]. In this scenario, the electron-doped $Nd_{2-x}Ce_xCuO_4$, hereafter NCCO, can be considered as a prototypical system where to study the link between AF and CO fluctuations, since this compound displays both CO [49] and noticeable AF correlations that extend into the phase diagram at higher doping levels compared to the hole-doped counterparts [184].

When we talk about CO we usually refer to charge correlations having a static nature. Several experimental works conducted on a restricted doping range in YBCO revealed an impressive increase of CO intensity and correlation length above 12 T [43, 183, 185, 186, 187]. This experimental evidence has been explained by considering that, without applying a magnetic field, the short-range (≈65 Å) CO is supposedly a precursor state to the high-field one. Moreover, CO correlations of the order of ≈25 Å have been found in other hole- and electron-doped cuprates [48, 118, 47, 49, 119, 171]. The observations by static probes suggest therefore that the CO correlations found at zero field could also have a dynamic nature and could then get static due to disorder or defect pinning of the modulation [188, 189, 190].

In the recent years, Cu L_3-edge resonant X-ray scattering, energy integrated (EI-RXS) and energy resolved (RIXS) mode has become the tool of choice to investigate CO in cuprates. The main difference between RIXS and EI-RXS lies in the impossibility to extract from EI-RXS measurements information about inelastic features, such as the finite energy excitations that one would expect to be associated with dynamic CO. In the work presented in this Section [97], the high-resolution ERIXS spectrometer at the ID32 beamline [8] at the ESRF - the European Synchrotron allowed to detect the presence of finite energy (dynamic) correlations at the charge-order wave vector (Q_{CO}) in both non superconducting ($x = 0.106$) and SC ($x = 0.145$) NCCO. The authors found that a sizable contribution coming from the dynamic correlations at Q_{CO} shares the same energy range covered by magnetic excitations. By performing polarization-resolved RIXS measurements, they were able to ascribe the enhancement of the dynamic response at Q_{CO} to spin-flip processes, revealing therefore a direct link between CO and dynamic magnetic correlations in electron-doped NCCO.

Figure 4.8(a) shows Cu L_3-edge RIXS spectra of non-SC NCCO at selected in-plane momenta along the [1 0] direction, here reported in reciprocal lattice units. These spectra are extracted from the full energy-momentum RIXS color map illustrated in Figure 4.8(b), where we can identify the elastic line at 0 energy loss, the dispersive magnetic excitations (paramagnons) in the mid-infrared region (below 600 meV) and the *dd* excitations at higher energies. In Figure 4.8(c) the authors illustrate the relationship between EI-RXS and RIXS measurements, where the result of the integration of each RIXS spectrum shown in Figure 4.8(b) in the energy range spanning from -0.06 to 10 10 eV is a single momentum distribution curve. It is worth mentioning that this curve is well comparable with previous EI-RXS experiments of NCCO [119]. It must be stressed that EI-RXS measurements are affected by a huge background coming from all the elastic and inelastic features, and most importantly, that the usual CO peak contributes to solely a small fraction of the total integrated intensity [48, 118, 49, 181]. Therefore, the peak at Q_{CO} in Figure 4.8(c) (highlighted by the arrow) can also originate from spectral components that are not necessarily elastic. In this context, RIXS can greatly help to understand the possible inelastic origin of the peak at Q_{CO}.

Figure 4.8(d-e) shows the detailed comparison between the low-energy excitations in the non-SC NCCO sample taken at 25 and 300 K. The measured paramagnons dispersion reveals the same characteristics previously investigated [165]. Moreover, the measurements at 25 K reveal an enhancement of the signal at Q_{CO} above the quasi-elastic line and below the paramagnon energy. Its presence is marked by the arrow at ~100 meV and by the huge intensity enhancement at ~250 meV, suggesting a dynamical nature. This assumption is reinforced by its suppression at high temperature, as deductible from Figure 4.8(e). At this point it was of crucial importance to determine if the enhancement of the RIXS signal at Q_{CO} comes from charge scattering that coexists with paramagnons or if it arises from an additional spin-flip scattering channel. To address this issue, the authors acquired high-resolution (≈35 meV of combined energy resolution) Cu-L_3 RIXS spectra of non-SC NCCO at two distinct H values, at Q_{CO} and away from it. The two spectra, reported in Figure 4.9(a), were measured with vertical polarization of the incident light and at 25 K and clearly confirm that the enhanced signal at Q_{CO} has the same energy of the paramagnon. However, all the experimental findings mentioned here cannot demonstrate the magnetic nature of the dynamic correlations at Q_{CO}. We know that, by resolving the scattered photon polarization, it is possible to isolate the single-spin flip contributions in the low-energy range [89, 90].

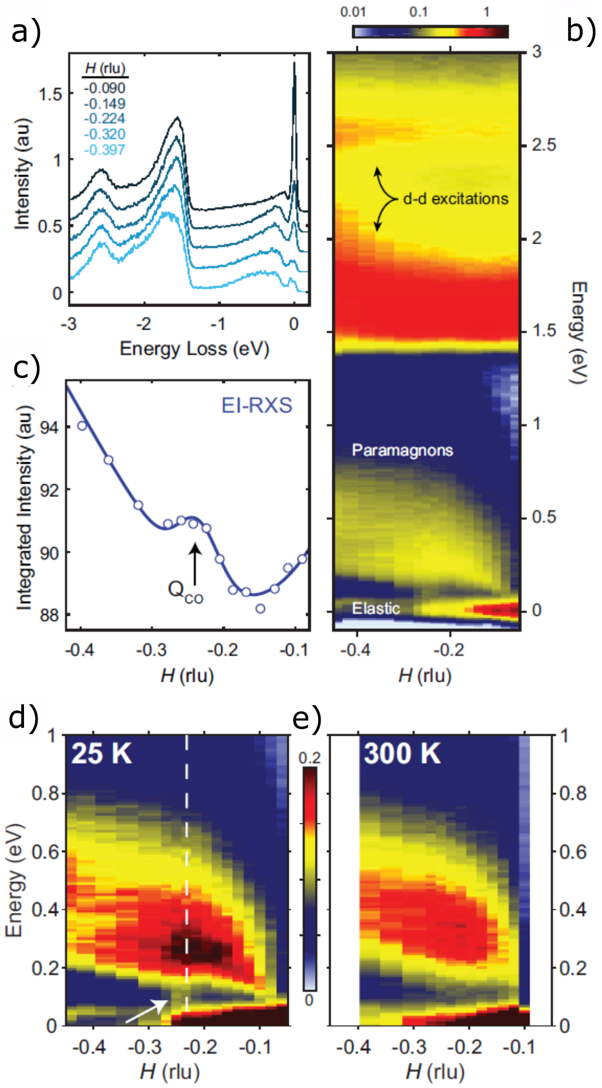

Figure 4.8: a) Cu L_3-edge RIXS spectra (vertically shifted for clarity) measured at selected in-plane momenta along the [1 0] high symmetry direction of the first Brillouin zone (H values are expressed in reciprocal lattice units). b) Energy-momentum RIXS color map in logarithmic scale. In the low-energy range the elastic line and paramagnons can be found, while the excitations at higher energies are ascribable to the transitions from the ground state to the Cu 3d orbitals (dd excitations). c) EI-RXS momentum dependence of the non-SC NCCO obtained from the integrated RIXS spectra in the energy range spanning from -0.06 to 10 10 eV. The RIXS spectra have been acquired with the polarization of the incident light vertically oriented with respect to the scattering plane (σ) and at 25 K. d-e) Close-up view of the low-energy range in the energy-momentum RIXS color map of non-SC NCCO measured with σ incident polarization at 25 and 300 K. The dashed line in d) denotes the Q_{CO} obtained from th data shown in panel c). Figures from Ref. [97].

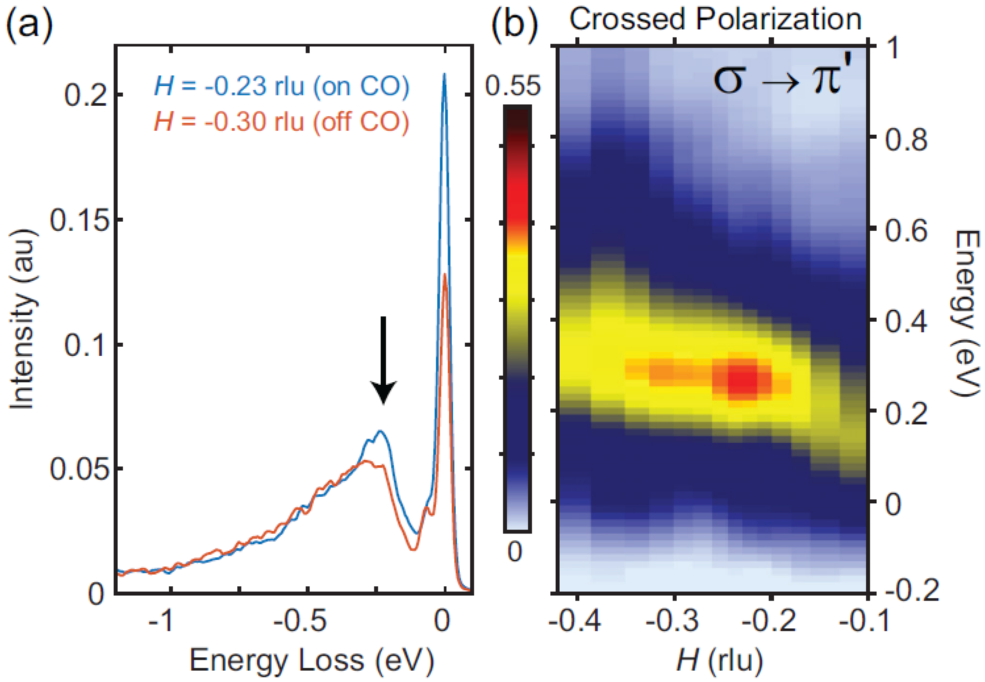

Figure 4.9: a) Comparison between two high-resolution RIXS spectra of non-SC NCCO measured on and off Q_{CO} at 25 K with σ incident polarization. b) Low-energy polarization-resolved ($\sigma\pi'$ channel) RIXS map. Figure from Ref. [97].

The $\sigma\pi'$ polarization-resolved RIXS color map is shown in Figure 4.9(b). As in the unpolarized RIXS data, here we can clearly distinguish the paramagnons dispersion which shows a remarkable enhancement exactly at Q_{CO}, not revealed in the $\sigma\sigma'$ spectra, as expected in case of single-spin flip excitations [95, 133, 60]. This result establishes, without any doubts, the magnetic nature of the dynamic correlations at the CO wave vector. Surprisingly, the increase of the $\sigma\pi'$ intensity at Q_{CO} near the paramagnons energy is not accompanied by the enhancement at ~100 meV seen in the unpolarized data (highlighted in panel d) of Figure 4.8).

The main conclusion is that the low-energy peak at Q_{CO} presumably arises from pure charge correlations at low temperatures and it is probably given by the softening of the electronic response below 150 meV that results in static charge order. At the same time, we assist to the enhancement of the magnetic spectral weight given by a pure spin-flip process at the energies that characterized the paramagnons. The simultaneous presence of charge order and dynamic spin-flip correlations could be explained considering that the fluctuations of a CO pattern necessarily require a transfer of charge between neighboring sites, regardless of the mode of fluctuation-phase shifts or amplitude enhancements. Since in electron-doped cuprates the Af correlations are strong, this intersite process is accompanied by spin-flip. As a consequence, the excitation energy will mostly affected by the paramagnon energy scale at Q_{CO}.

This work provides strong experimental evidences in support of the theoretically predicted interplay between magnetic fluctuations and charge order in cuprates [176, 177, 178, 179, 180]. Moreover, the observed softening of the low-energies electronic response could be in agreement with the prediction of a d-wave form factor of charge order in the electron-doped NCCO [191], bolstering the similarities between CO in electron- and hole-doped copper-based superconductors.

4.6 Crystal electric field in CeRh$_2$Si$_2$ studied with high-resolution resonant inelastic soft X-rays scattering

The data and analyses discussed in this Section have been published in "*Crystal electric field in CeRh$_2$Si$_2$ studied with high-resolution resonant inelastic soft X-ray scattering*", by A. Amorese, N. Caroca-Canales, S. Seiro, C. Krellner, G. Ghiringhelli, N. B. Brookes, D. V. Vyalikh, C. Geibel, and K. Kummer, Physical Review B **97**, 245130 (2018).

In this last Section we will show how high-resolution and polarization-resolved RIXS measurements can be useful for the study of materials such as rare earth compounds. In this particular case, we will present a detailed and systematic RIXS investigation that allowed the unique assignment of the crystal electric field (CEF) scheme in CeRh$_2$Si$_2$. The results discussed hereafter agree with INS and magnetic susceptibilities studies made in the past.

Rare earth based compounds can be classified as strongly correlated materials containing, in addition to rare earth elements, metallic and optionally non-metallic elements, where the resulting crystal structures strongly depend on the constituents. The main physical properties of these materials derive from the strong electron-electron correlation and from the anisotropic charge distribution mainly given by the incompletely filled d or f electron shells. Regarding CeRh$_2$Si$_2$, it is usually described as a heavy fermion compound belonging to the 122 cerium-based family. It displays a tetragonal crystal structure (D_{4h} symmetry) centered around tT_{c}he Ce ion and it is characterized by two different antiferromagnetic orders below $T_{N_1} = 37\,\mathrm{K}$ and T_{N_2}

$= 26\,\mathrm{K}$ [192, 193, 194, 195]. $CeRh_2Si_2$ has attracted a lot of attention after the discovery of a superconducting phase revealed under pressure (1.1 GPa) with a typical critical transition temperature $T_c \approx 400$ mK [196, 197].

Although $CeRh_2Si_2$ has been investigated for a long time, there is still not a complete knowledge of the CEF scheme, in particular regarding the energy splittings, symmetries and charge distribution of the Ce $4f$ states. The main effect given by the CEF is the splitting of the ground state multiplet of Ce, that has been usually studied with INS technique by probing excitations from the ground state to excited states above the Fermi level. In this way, one can infer about the energy and symmetry of the CEF levels. Over the past few years RIXS has emerged as a powerful tool for the investigations of low-energy excitations in correlated materials, especially thanks to the huge improvements in the soft X-rays instrumentations. With the ERIXS spectrometer at the ID32 beamline at the ESRF [8] it is possible nowadays to achieve a combined energy resolution of ~ 30 meV at 1 keV of incident photon energy. Moreover, the possibility to continuously move the spectrometer scattering arm offers the capability to investigate a large portion of the three-dimensional reciprocal space. Finally, as explained throughout this thesis, ERIXS allows also the polarization analysis of the scattered photons. All these features offered by the recent developments in RIXS technique opened novel systematic studies of orbital, spin and charge degrees of freedom in a large variety of materials. Unfortunately, due to the low energy resolution, RIXS study done in the past on rare-earth materials allowed the study of solely the high energy charge transfers, without any insight into the crystal field excitations [198].

In the work reported here [98], the authors exploited all the above mentioned capabilities offered by the ERIXS spectrometer to assign the energy splittings given by the CEF in $CeRh_2Si_2$. The aim of this work is to uniquely assign the CEF levels in this material, since the schemes reported in literature are in contradiction and still under debate [199, 200, 201, 202].

Differently from the examples reported in this thesis, where we have mainly discussed RIXS measurements at the Cu L_3-edge, here we will deal with the Ce M_5-edge at ~ 883 eV which involves the transitions from the $3d$ to the $4f$ states. The $CeRh_2Si_2$ ground state is dictated by the Hund's rule that leads to three Kramers doublets resulting from the splitting of the $^2F_{5/2}$ multiplet of the Ce^{3+} ions. In the Stevens' approximation (spin-orbit coupling of the $4f$ levels larger than the energy separation given by the CEF) with a negligible mixing between the ground state multiplet and the higher one $^2F_{7/2}$, the three Kramers doublets can be written in the following way:

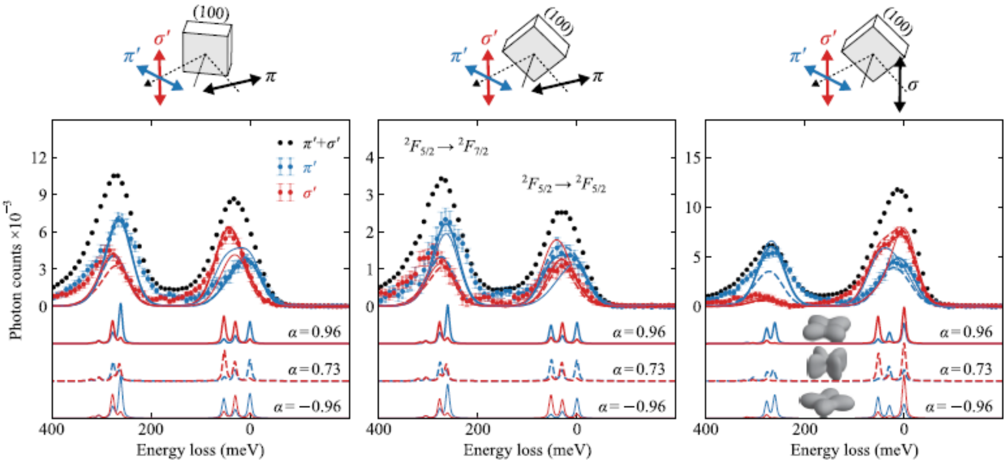

Figure 4.10: Polarization-resolved RIXS spectra measured at transferred momenta $\mathbf{q}$ = (0.0, 0.0, 0.12). On top the different adopted scattering geometries are shown. Moreover, the experimental RIXS data were compared with the calculated RIXS spectra as a function of the mixing parameter α. Figures from Ref. [98].

$$\Gamma_7^1 = \alpha\,|\pm5/2\rangle + \sqrt{1-\alpha^2}\,|\mp3/2\rangle \tag{4.3}$$
$$\Gamma_7^2 = \sqrt{1-\alpha^2}\,|\pm5/2\rangle - \alpha\,|\mp3/2\rangle \tag{4.4}$$
$$\Gamma_6 = |\pm1/2\rangle\,. \tag{4.5}$$

The Γ_6 doublet is made of pure $|\pm1/2\rangle$, while the other two can be expressed as linear combinations of the $|J_z = \pm5/2\rangle$ and $|J_z = \mp5/2\rangle$ states. The CEF parameters $A_{2,0}$, $A_{4,0}$ and $A_{4,4}$ define the energy of the three Kramers doublets as well as the mixing α in the Γ_7^1 and Γ_7^2 states. As in the case of *dd* excitations in cuprates, RIXS allows to probe transitions with $\Delta J_z = 0, \pm1, \pm2$, which are the most relevant for the investigations of the CEF in Ce-based materials. In Ref. [98], Amorese *et. al* report a detailed high-resolution (≈ 30 meV at the Ce M_5-edge) RIXS study compared with theoretical calculations in order to assign the ground state and the energies of the excited states in CeRh$_2$Si$_2$, revealing that most of the CEF schemes proposed in the past are in contradiction with their RIXS data. The main result is that the Γ_7^1 ground state has a mixing factor $\alpha = 0.96$, while the energies of the two excited states Γ_7^2 and Γ_6 are of the order of 30 and 53 meV, respectively.

In order to better estimate the correct mixing (α parameter) between the $|J_z = \pm5/2\rangle$ and $|J_z = \mp5/2\rangle$ in the Γ_7 states the authors exploited the possibility to perform the polarization analysis of the scattered photons. By carefully inspecting the polarization-resolved RIXS spectra illustrated in Figure 4.10, we clearly see that the biggest effects given by changing α can be detected solely when the outgoing photons polarization is known. This observation has been used to correctly assign both the sign and the absolute value of the mixing CEF parameter in $CeRh_2Si_2$. This result has been achieved by measuring RIXS spectra at different transferred momenta and by playing with the incident photon polarization (σ or π). The three calculated RIXS spectra as a function of α give completely different responses in the two outgoing linearly polarized channels (σ' and π'), and this information was crucial to assign the most compatible mixing CEF parameter with the experimental data.

In conclusion, Amorese *et. al* demonstrated that RIXS allows to study CEF excitations in rare earth intermetallics materials. In the particular case of $CeRh_2Si_2$, by combining high-resolution measurements and the analysis of the scattered photons polarization together with theoretical calculations it was possible to determine the energy splittings and the symmetry of the CEF levels, both the ground state and the excited states. Moreover, especially thanks to the analysis of the outgoing polarization, the mixing parameter α has been determined with unprecedented accuracy.

CHAPTER 5

Dispersing orbital excitations in quasi-1D and 2D cuprates

The data and analyses discussed in this Section will be submitted soon as a part of the work "*Mobile orbitons in Ca_2CuO_3: crucial role of the Hund's exchange*", by R. Fumagalli, J. Heverhagen, D. Betto, R. Arpaia, M. Rossi, D. Di Castro, N.B. Brookes, M. Moretti Sala, M. Daghofer, L. Braicovich, K. Wohlfeld, and G. Ghiringhelli.

In correlated oxides electronic excitations tend to have a localized character and are usually described by orbital and spin quantum numbers in a symmetry adapted atomic picture: usually *dd* (*i.e.* orbital) excitations do not disperse, irrespective of their spin character. On the contrary, pure spin excitations have collective nature: spin-waves (or magnons) display large energy dispersion *vs* momentum. Theory predicts that at low dimensionality *dd* excitations can split their orbital and spin components, giving rise to complex dispersion. So far orbital excitations with sizeable dispersion were observed and theoretically analyzed only in quasi-1D materials. In this Chapter we investigate the Cu L_3-edge Resonant Inelastic X-ray Scattering spectra of the quasi-1D antiferromagnet $\mathrm{Ca_2CuO_3}$. Beside the magnetic excitations, being well-described by the two-spinon continuum, we observe two dispersive orbital excitations, the $3d_{xy}$ and the $3d_{yz}$ orbitons. A quantitative comparison with the theoretical model reveals that a realistic spin-orbital model needs to include a finite Hund's exchange $J_\mathrm{H} \approx 0.5$ eV. As the Hund's exchange is small with respect to the values of the spin-orbital exchange processes, the spinon and orbiton can be regarded as noninteracting and the spin-orbital separation picture can well describe the orbiton motion in this compound. However, our preliminary data on the infinite layer $CaCuO_2$ suggest that *dd* excitations may disperse also in 2D systems. It turns out that the theory model used in the 1D case can hardly account for the dispersion we observed in $CaCuO_2$, and calls for a clarification.

We have exploited the unique resolution and polarization selectivity of ERIXS spectrometer at ID32 to solve this puzzle whose solution would impact on the very concept of dispersive orbital excitation, *i.e.* orbital-wave or "orbiton".

Contents

5.1 Mobile orbitons in quasi-1D Ca_2CuO_3: crucial role of the Hund's exchange

5.1.1 Introduction

The importance of the Hund's exchange and the multi-orbital character of the states lying close to the Fermi level go hand in hand in the correlated electron systems [28]. In addition to 'Hund's metallicity' in itinerant systems [203], there are Mott-insulating transition-metal compounds with almost degenerate orbitals, which can show spin and orbitally ordered ground states [28, 204]. Interestingly, the spin and orbital order in these compounds often follows a special kind of 'complementarity rule', typically known as the Goodenough-Kanamori rule [205, 206]: the bond with a dominant alternating orbital (ferro-orbital) correlation shows ferromagnetic (antiferromagnetic) correlation, respectively. Consequently and especially once the typically strong Jahn-Teller effect is included, various transition metal oxides or fluorides show strongly anisotropic magnetic ordering [207]—probably the most famous example is the cubic LaMnO$_3$ with its *ab* planes (chains along the *c* axis) showing ferromagnetic (antiferromagnetic) order [208, 209].

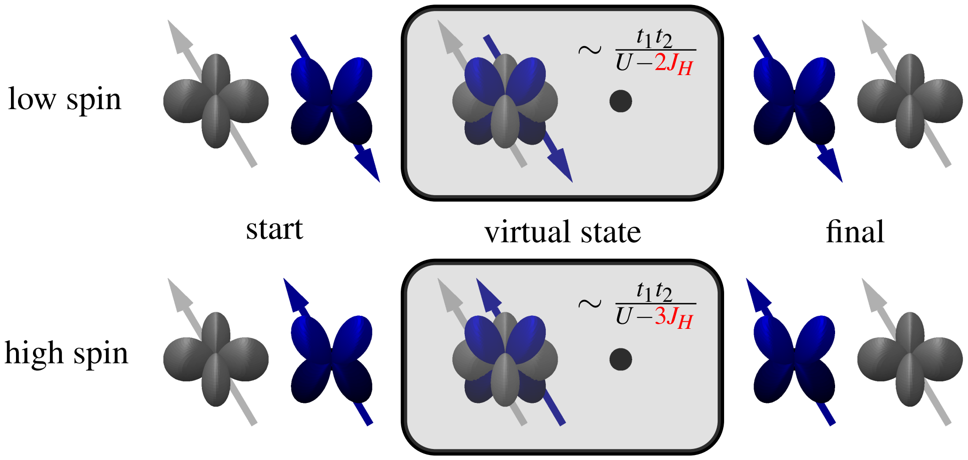

Figure 5.1: A cartoon picture of the two possible spin-orbital exchange processes along a bond with two distinct orbitals occupying the nearest neighbor sites. Whereas in the limit of vanishing Hund's exchange $J_{\rm H}$ the amplitude of such processes is solely $\propto t_1 t_2/U$ (with t_1, t_2 being the nearest neighbor hoppings between respective orbitals and U the Coulomb repulsion element on the same orbital), in a 'realistic' case it also depends on $J_{\rm H}/U$ and is larger (smaller) for the the parallel (antiparallel) spin alignment as presented on the bottom (top) panels, respectively. This not only explains the origin of one of the Goodenough-Kanamori rules but also the dependence of the orbiton velocity on the spin correlations as well as its overall increase with the Hund's exchange, as discussed in detail in this Section.

Let us understand a bit better why the Goodenough-Kanamori rules are so intimately related to the Hund's exchange. The crucial observation is that Hund's exchange is responsible for the ferromagnetic correlations suggested by the Goodenough-Kanamori rules for alternating orbital order. Without it, the singlet and triplet 'virtual' states occurring in the spin-orbital ('Kugel-Khomskii') exchange processes along an alternating-orbital bond, illustrated in Figure 5.1, would have the same energy (cf. Ref. [209] for detailed examples). This would yield the same amplitude for the two exchange processes and would thus remove all energy gain from a ferromagnetic alignment relative to the antiferromagnetic one.

Despite the fundamental importance of Hund's exchange for the ground-state ordering, little is known about its signature in dispersive collective orbital excitations (orbitons). Such excitations were observed in quasi-1D copper oxides with almost decoupled $S = 1/2$ antiferromagnetic chains [55, 210, 211] as well as in quasi-2D iridate Sr_2IrO_4 [212, 213]. In a Mott insulator, the orbiton moves via superexchange processes that are rather similar to the ones underlying the Goodenough-Kanamori rules, see the sketch Figure 5.1. Interpreting this as an 'orbiton hopping', the situation of an orbiton moving through an antiferromagnet was then described with a minimal t–J model, in perfect analogy to a hole in the same background [214]. However, this – quite successful – treatment requires the orbiton hoppings on ferro- and antiferromagnetically aligned bonds to be equal, while Hund's exchange implies that they are not.

The question of Hund's exchange becomes particularly salient in the 1D case, where the picture of spin-orbital separation was based on the above analogy to a hole: whereas an orbiton always strongly couples to the elementary spin excitations of an antiferromagnet, it can effectively separate from the spin excitation ('spinon') in a similar manner as a 'holon' separates from the spinon when a single hole is introduced into an 1D antiferromagnet [215]. The fate of spin-orbit separation in the presence of Hund's exchange was only recently addressed theoretically [216]. Fractionalization into spinon and orbiton was predicted to persist, even though Hund's exchange was concluded to mediate interactions between them. However, experimental information on the impact of Hund's exchange on orbiton propagation and spin-orbit separation is so far missing.

In this Chapter we present a systematic and detailed high-resolution resonant inelastic X-ray scattering (RIXS) study at the Cu L_3-edge on the quasi-1D spin $S = {}^1\!/_2$ antiferromagnetic Heisenberg chain Ca_2CuO_3. We assess the importance of Hund's exchange in modeling the experimentally observed orbital excitations and conclude it to be necessary for a quantitative description. To this end, we firstly discuss the experimental methods and present the main RIXS spectra in Section 5.1.2. We start the discussion with analyzing the spin excitations in great detail, see Section 5.1.3. Next, we introduce an appropriate spin-orbital model in Section 5.1.3 and compare the experimental and theoretical results in Section 5.1.3, paying particular attention to the role of the finite Hund's exchange in obtaining the results which well-describe the experiment.

5.1.2 Experimental methods

Samples

Together with Sr_2CuO_3, Ca_2CuO_3 (from now on Ca21) represents one of the best prototype of the quasi-1D spin $1/2$ AFM strongly anisotropic Heisenberg chain [26]. The dicalcium cuprate shares the common crystal structure of the better studied Sr_2CuO_3 [24, 25, 26] and it is characterized by having quasi-1D CuO_3 chains of corner-sharing CuO_4 plaquettes along the crystallographic b axis. Regarding the electronic properties, the strong on-site Coulomb U repulsion results in a ground state with one localized hole per Cu ion, located in the $3d_{x^2-y^2}$ orbital. Because of that, its $3d$ bands structure shows a Mott-Hubbard gap. The Ca21 films used for this work were grown by pulsed laser deposition, using a $\lambda = 248$ nm KrF excimer laser. We chose as the substrate for the film deposition a 5x5 mm^2 $LaSrAlO_4$ (LSAO) (1 0 0), since it has a crystal structure (K2NiF_4-type) similar to Ca_2CuO_3 and compatible in plane lattice parameters. On LSAO (1 0 0), the Ca21 grows along the c-axis and the CuO_3 1D chain lies in the ab plane along the b-axis [(see Figure 5.4(c)], with chain oxygen at corner sharing CuO_4 plaquettes. The Ca21 target for the film deposition was prepared by standard solid state reaction: stoichiometric mixtures of high-purity $CaCO_3$ and CuO powders were calcined at about 800°C in air for 20 hours, then pressed to form a disk and heated in air at 950 °C for 24 h. The distance between LSAO substrate and the target was 2.5 cm. The substrate holder was kept at T = 600 °C during the deposition at an oxygen pressure of 0.1 mbar, and cooled down to room temperature at the same pressure. High quality films with perfect c-axis orientation were grown, with thickness about 30 nm.

The structural properties of the Ca21 thin films have been determined by X-Ray Diffraction (XRD) analysis, using a Panalytical X'Pert PRO Materials Research 4-axis diffractometer. The beam from the Cu X-ray tube passes through a 2-bounce Ge220 monochromator, which includes a mirror; the diffracted beam is detected either by a rocking curve attachment or by a 3-bounce symmetric analyzer crystal, used respectively for low-resolution and high-resolution ω-2θ scans and reciprocal space maps. The XRD characterization presented in the following is focused on the same sample [30 nm thick Ca21 film on (1 0 0) oriented $LaSrAlO_4$ (LSAO) substrate] on which all the RIXS measurements presented in the paper have been taken. We have however tested that the results are reproducible among several samples of the same kind.

The ω-2θ scan [see Figure 5.2(a)] confirm that the film is crystalline and c-axis oriented, without any hint of spurious phase, or misoriented domain.

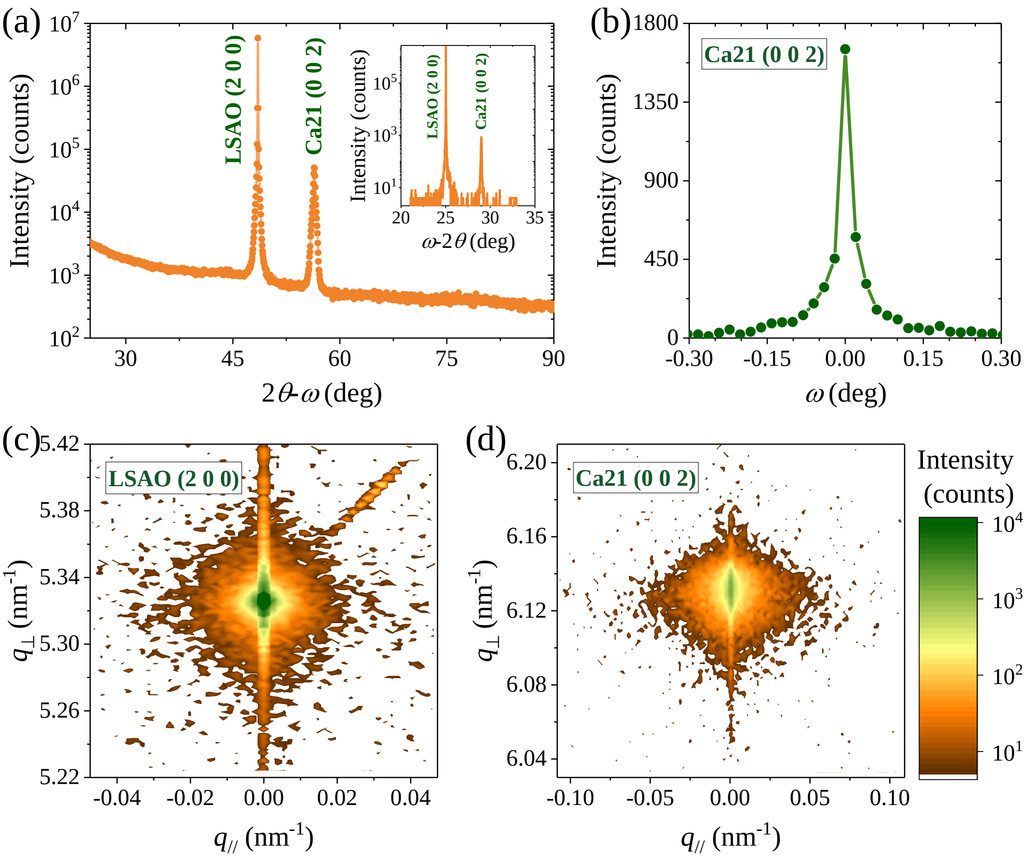

Figure 5.2: Symmetric XRD measurements on the Ca_2CuO_3 (30 nm)/$LaSrAlO_4$ (1 0 0). (a) The low resolution 2θ-ω scan shows that, beside the substrate reflection, only the Ca21 (0 0 2) reflection is present, related to the c-axis growth of the film. The absence of any other orientation or spourius phase is confirmed by the high resolution scan (inset) performed in a shorter range around the Ca21 reflection. (b) Rocking curve of the Ca21 (0 0 2) reflection. (c)-(d) High-resolution reciprocal space maps of the LSAO (2 0 0) and Ca21 (0 0 2) reflections. The c-axis of the Ca21 is perfectly aligned to the out of plane direction of the substrate (they have the same $q_{\|}$).

The high-resolution symmetric reciprocal space maps [see Figures 5.2(c)-(d)] show instead that the Ca21 (0 0 2) reflection is aligned to the LSAO (2 0 0) reflection, *i.e.* to the normal direction of the substrate ($q_{\|}^{Ca21} = q_{\|}^{LSAO}$). This occurrence, together with the full width at half maximum of only $\approx 0.03°$ for the Ca21 (0 0 2) reflection [see Figure 5.2(b)], supports the high texture of the film. Therefore the use of a substrate with such small in-plane mismatch δ^{m} with the film (with $\delta^{\mathrm{m}} = 1 - x_{\mathrm{f}}/x_{\mathrm{s}}$, and x_{f} and x_{s} in-plane lattice parameters respectively of film and substrate, see Table 5.1), prevents the distortion of the CuO_4 plaquettes within the Ca21 unit cell. Such distortion, causing a buckling of the atomic planes, is vice versa generally occurring in perovskite thin films, when they are grown on substrates with larger lattice mismatch [217, 218, 219, 220]. Finally, the length of the c-axis parameter has been estimated from the position of the Ca21 (0 0 2) reflection: its value, $q_{\perp}^{-1} = 3.262$ Å, is very close to the bulk value.

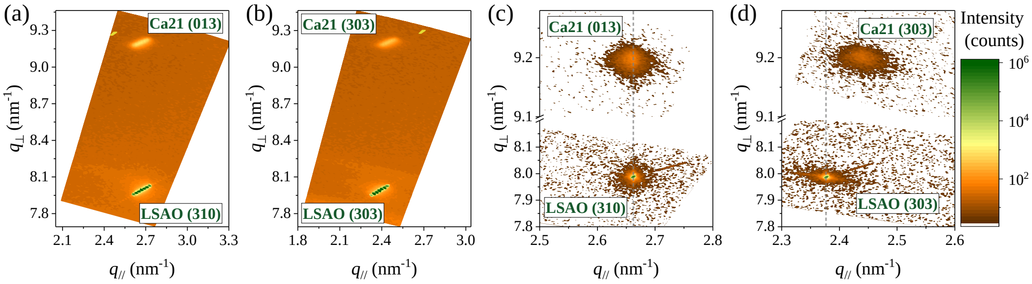

Figure 5.3: Asymmetric XRD measurements on the Ca_2CuO_3 (30 nm)/$LaSrAlO_4$ (1 0 0). (a)-(b) Low-resolution reciprocal space maps, along the two in-plane LSAO directions. Along the [0 1 0] direction [panel (a)] only the Ca21 (0 1 3) reflection (b-axis) is present, while along the [0 0 1] direction [panel (b)] the Ca21 (3 0 3) is the only measured reflection (a-axis). Where absent, the position of the Ca21 (0 1 3) and (3 0 3) reflections has been marked in the maps by a yellow cross. The film is totally detwinned, with the following film-substrate relations: Ca21(1 0 0)$\|$LSAO(0 0 1), Ca21(0 1 0)$\|$LSAO(0 1 0), Ca21(0 0 1)$\|$LSAO(1 0 0). (c)-(d) High-resolution reciprocal space maps, along the two in-plane LSAO directions, used to determine the length of the in-plane Ca21 parameters and the strain state.

To determine the twinning state of the Ca21 thin film, as well as the film-substrate orientation relations and the strain conditions, we have explored by both low- and high-resolution reciprocal space maps the asymmetrical (0 1 3) and (3 0 3) Ca21 reflections. These two reflections, associated respectively to the b-axis, where the CuO_3 chains are oriented, and to the a-axis, are characterized by almost identical $q_{\perp}$, and similar $q_{\|}$ values ($\Delta q_{\|} = 0.2$ nm^{-1}). The maps have been taken both along the [0 1 0] and the [0 0 1] in-plane LSAO directions. Along the [0 1 0] LSAO direction, only the Ca21 (0 1 3) reflection is present; vice versa, along the [0 0 1] LSAO direction, the Ca21 (3 0 3) reflection is dominant [see Figures 5.3(a)-(b)].

The film is therefore totally detwinned: the random exchange of the in-plane parameters is eliminated, and the material properties, related to the presence of CuO_3 chains along the b-axis, can be singled out. The one-dimensional nature of the Cu21 is preserved in thin film form, down to thickness of few unit cells. Such film-substrate orientation relationship has severe implications on the way the strain is applied on the Cu21 film. Along the [0 1 0] LSAO $\|$ [0 1 0] Ca21 direction, where the mismatch is negligible ($\delta^{\mathrm{m}} \approx -0.7\%$), the Ca21 (0 1 3) reflection is aligned to the LSAO (3 1 0) reflection: the b-axis of the Ca21 is totally strained on the b-axis of the

LSAO, compressing its bulk value down to $q_{\parallel}^{-1} = 3.758$ Å[see Figure 5.3(c)]. Along the [0 0 1] LSAO ∥ [1 0 0] Ca21 direction, the mismatch is instead larger ($\delta^{\mathrm{m}} \approx 3\%$): here, the Ca21 (3 0 3) reflection is misaligned with respect to the LSAO (3 0 3) reflection [see Figure 5.3(d)], since the length of the Ca21 a-axis parameter ($q_{\parallel}^{-1} = 12.288$ Å) approaches that of the LSAO a-axis, though staying much shorter than that. The tensile stain along the a-axis compensates the compressive one along the b-axis, in agreement with the negligible change of the c-axis parameter, observed via ω-2θ scan.

The Ca21 and LSAO lattice parameters, in bulk form as well as in our films, are summarized in Table 5.1.

material	a (Å)	b (Å)	c (Å)
$LaSrAlO_4$	3.756	3.756	12.617
Ca_2CuO_3 bulk [221]	12.262	3.783	3.263
Ca_2CuO_3 film	12.288	3.758	3.262

Table 5.1: The lattice parameters of our Cu21 thin films, as determined by the XRD structural characterization, are compared with those of the bulk Cu21, and of the LSAO substrate.

RIXS measurements

RIXS [4] measurements were carried out at the ID32 beamline [8] of the ESRF - the European Synchrotron. The energy of the incident beam was tuned to the maximum of the Cu L_3 absorption peak ($\sim 931\,\mathrm{eV}$) in order to fulfill the resonance condition. The polarization of the incident light was set either parallel (π) or perpendicular (σ) with respect to the scattering plane. For all the measurements discussed below, the scattering angle 2θ was fixed at 149.5° in order to maximize the in-plane transferred momentum, while the temperature was kept fixed at 20 K. To explore how the dimensionality of Ca21 affects the RIXS spectra, we were able to rotate by 90° the azimuthal angle in order to put either the bc or ac plane of the sample in the scattering plane, as shown in Figure 5.4 c) and e), respectively. Once the scattering plane is defined, by rotating the angle perpendicular to it (θ) we were able to change the in-plane transferred momentum $\mathbf{q}_{\parallel}$, defined as the projection of the momentum transfer onto the CuO_2 layers. From now on we will refer to the transferred momentum values in terms of reciprocal lattice vectors (r.l.u.) $2\pi/a$, $2\pi/b$ and $2\pi/c$. We acquired RIXS spectra along the two high-symmetry direction [0 1] [Figure 5.4(a-c)] and [1 0] [Figure 5.4(d-e)] in the first Brillouin zone. It has to be underlined that, due to the orthorombicity of the crystal structure, these two directions are not equivalent. In fact, when

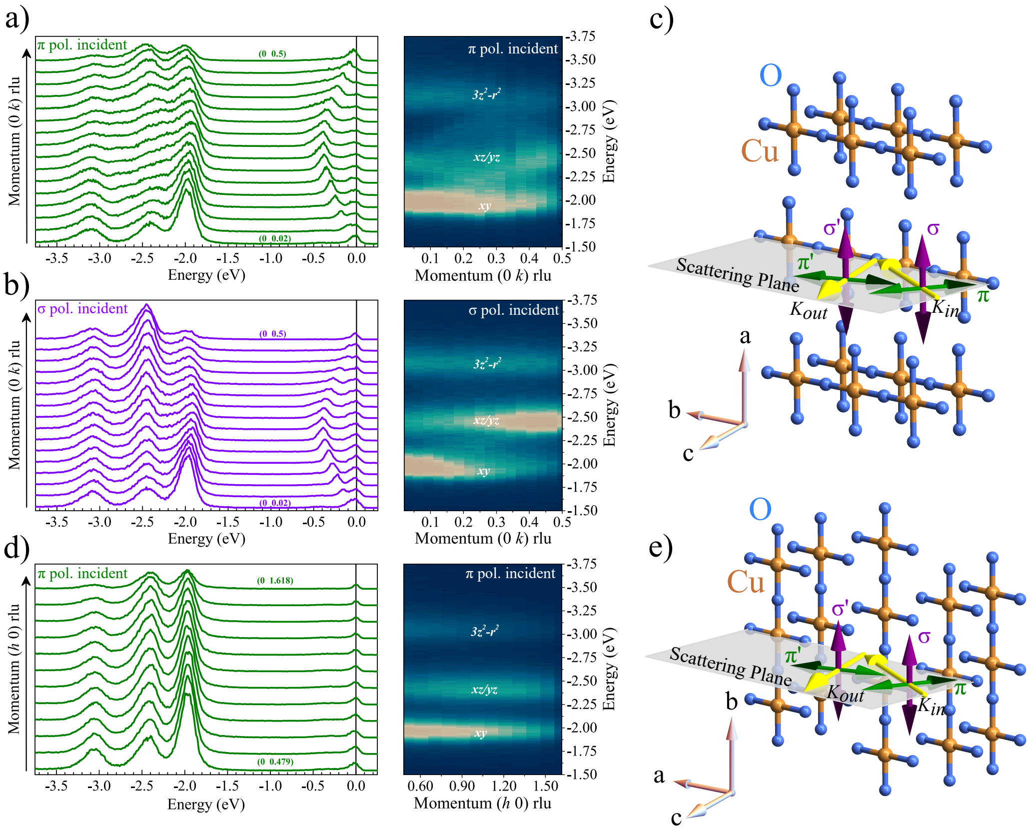

Figure 5.4: Raw RIXS spectra of Ca_2CuO_3 measured along the [0 1] direction with π (a) and σ (b) polarization of the incident light; on the right side we show a close-up view of the RIXS intensity maps in the *dd* excitations energy range. c) Sketch of the scattering and experimental geometry adopted to measure the spectra shown in a) and b) together with the crystalline structure of CuO_3 chains of Ca21. d) RIXS spectra and close-up view of the orbital excitations measured with π polarization along the direction perpendicular to the CuO_3 chains ([1 0]). e) Experimental geometry adopted for the data presented in panel b). In c) and e) the Ca atoms have been removed for clarity.

the scattering occurs in the *bc* plane, the CuO_3 chains lie in the scattering plane; on the other hand, by measuring along the [1 0] direction, the chains are perpendicular to it. These considerations on the different geometries have an important impact and significant repercussions on the physics of 1D systems, as we will explain in a more details in Section 5.1.3.

In the waterfall plots in the left panels of Figure 5.4, the spectra can be decomposed into several features. The peaks at $\sim$0 energy loss represent the quasi-elastic scattering (which includes diffuse elastic and phonons); up to -0.5 eV all the spectra reveal the presence of dispersing spin excitations and between -1.5 and $-3.5\,$eV the spectra are dominated by orbital excitations, which correspond to the final states with the Cu hole in the other $3d$ orbitals. The assignment of each orbital energy and symmetry has been done following the same procedure adopted by Moretti Sala *et al.* [11]: in a pure ionic picture, we calculated the cross sections for all the possible final states in the RIXS process, and we used them to fit the experimental data.

We also exploited the unique capability of the ERIXS spectrometer to perform polarization-resolved RIXS measurements [8, 60], disentangling the two linearly polarized channels (π' and σ') of the scattered light. The possibility of disentangling the polarization of the scattered light gives us valuable insights on the nature of the various spectral features: recently, it has been demonstrated that this method can be useful to distinguish the various orbital [60] and the low-energy excitations [94, 96, 54, 97] in different cuprate families. In particular, the polarimetric measurements confirm the orbital energies assignment given by the single ion model. In Figure 5.5 we show the polarimetric raw RIXS data of Ca21 measured with both incident π (bottom panels) and σ (top panels) polarizations at two distinct transferred momenta values (0.26 and 0.436 r.l.u.). The decomposed outgoing polarization-dependent channels and the experimental error bars have been obtained following the procedure reported in Refs. [94, 60] and in Chapter 2.7. On top of each spectrum we report the comparison between the absolute values of the polarization-resolved RIXS cross sections calculated within the single ion model as a function of the incident/scattered polarizations and the peak areas for each orbital excitation. The results are shown in the form of histograms keeping the same color code of the experimental data. We remark the good agreement between the calculations and the experimental data. Most importantly, in the spectra measured with π polarization the region which shows the larger dispersion has a predominant $d_{xz/yz}$ character. The results obtained by combining the polarimetric data and the calculations will be used in the detailed analysis presented throughout this paper.

The overall energy resolution was $\sim 60\,$meV for the unpolarized spectra, while we relaxed it to $\sim 80\,$meV for the polarimetric measurements in order to maintain an acceptable count rate. Each RIXS spectrum shown in Figure 5.4 has been acquired in 15 min. In the case of polarization-resolved measurement, the acquisition time was increased to 60 min in order to get good statistics due to the lower efficiency of the polarimeter.

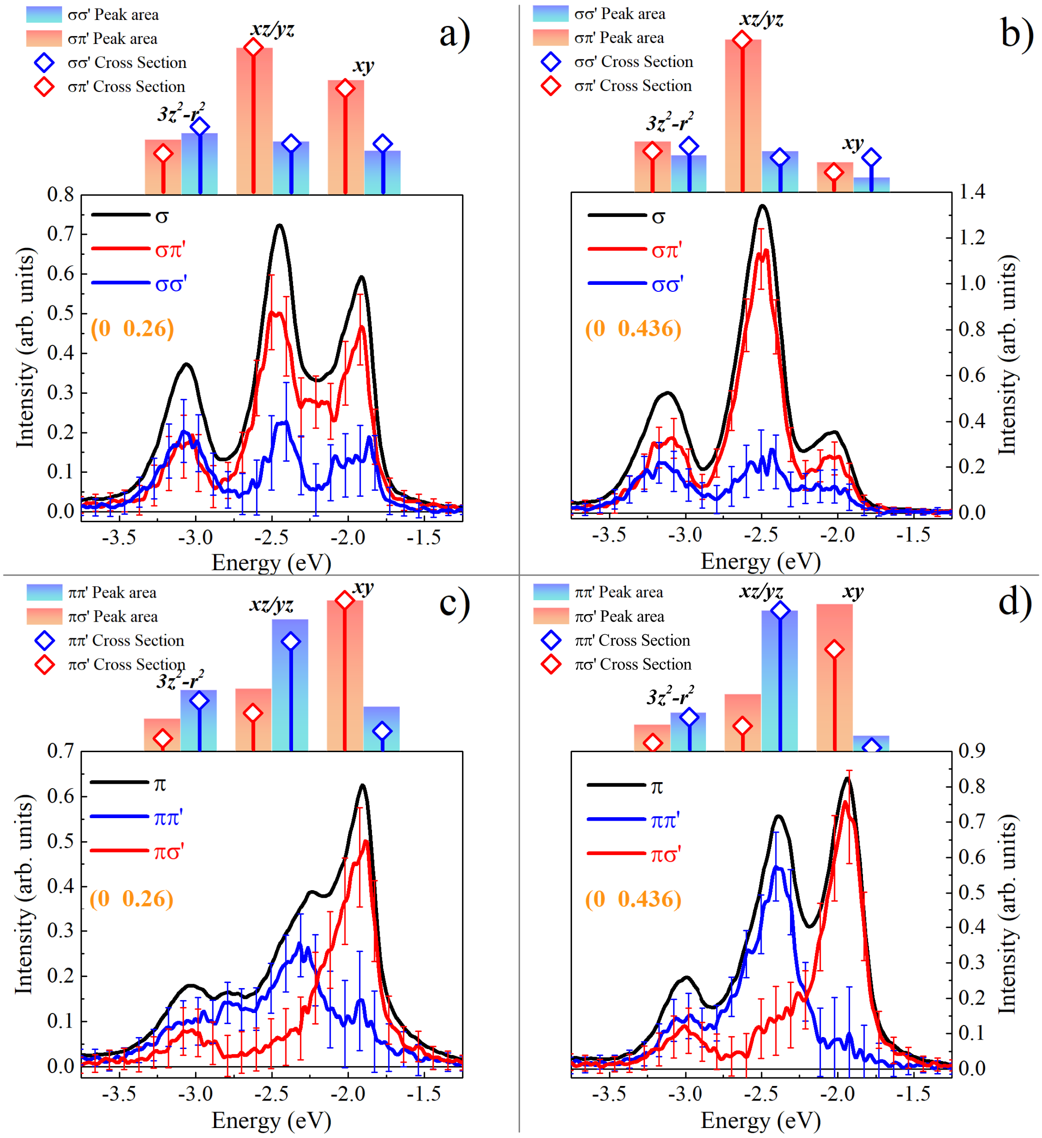

Figure 5.5: Polarimetric RIXS spectra measured with incident σ (top panels) and π (bottom panels) polarization at two selected transferred momenta (0.26 and 0.436 r.l.u.). On top of each spectrum we report the the comparison between absolute values of the polarization-resolved RIXS cross section calculations and the peak areas for each *dd* excitation. To help the reader, we use the same color code (blue for the non crossed $\pi\pi'$ and $\sigma\sigma'$ and red for the crossed $\pi\sigma'$ and $\sigma\pi'$ channels) for both the experimental data and the histograms.

5.1.3 Results and discussions

Two-spinon continuum

Spin excitations in quasi-1D systems have been intensively studied in the last decades due to their importance in the realization of the 1D Heisenberg

AFM model. The anisotropic AFM interaction of Ca21 comes from the Cu atoms within the chains, along the b axis. The coupling along the other crystallographic directions is negligible, making Ca21 a 1D magnetic system with a Néel temperature of only 9 K [26] despite the large nearest neighbor superexchange interaction along the chains. In fact, RIXS spectra measured along the [1 0] direction do not show any dispersive spin excitations.

A clear signature of the 1D nature of Ca21 comes directly from the momentum dependence of spin excitations along the [0 1] direction. Indeed, in these systems the elementary magnetic excitations with $S = 1$ fractionalize into the two-spinon continuum carrying a spin quantum number of $S = {}^{1}\!/_{2}$ [223]. In the left panels of Figure 5.6 we show the Ca21 RIXS intensity maps (between 0 and 0.8 eV of energy loss) measured with both π (top left) and σ (bottom left) polarization which display strong dispersing spin excitations characterized by two different periodicities in reciprocal space [222, 224, 225, 226, 227, 228]: π for the lower branch, 2π for the upper one. In the intensity maps we show the extracted energy positions of the main two-spinon peak from a preliminary fitting procedure (dots). In order to determine the magnetic superexchange constant (J_{SE}), we assume that RIXS probes the spin dynamical structure factor $S(\mathbf{q}, \omega)$. This approximation has been intensively used through the years in RIXS [55, 229, 4, 230, 231, 232] experiments on a large number of quasi-1D antiferromagnets. Here we used the approximated expression of the two-spinon dynamical structure factor reported in Ref. [222] to obtain a value of the superexchange coupling $J_{\mathrm{SE}} = 0.24$ eV for the present case of Ca21, which is not only close to the value found for Sr_2CuO_3 [233, 55] but also to the one reported for Ca21 [234]. The results are represented by the continuous lines shown in the left panels of Figure 5.6.

Furthermore, thanks to the good quality of our RIXS spectra, we can directly compare the RIXS line shapes with the approximated expression of the two-spinon dynamical structure factor $S(\mathbf{q}, \omega)$ of the $S = 1/2$ Heisenberg chain [222]. In the two right panels of Figure 5.6 we show the fitting results at two transferred momenta values, which have been chosen by considering the fact that here the two-spinon continuum is well separated from the other spectral features.

Theoretical model for *dd* excitations

dd excitations in 1D feature the fractionalization of spin and orbital degrees of freedom. To model the fractionalization, previous studies used an effective t-J model, which accurately described the experimental spectra. We go one step further and include the effect of Hund's coupling, which should be finite

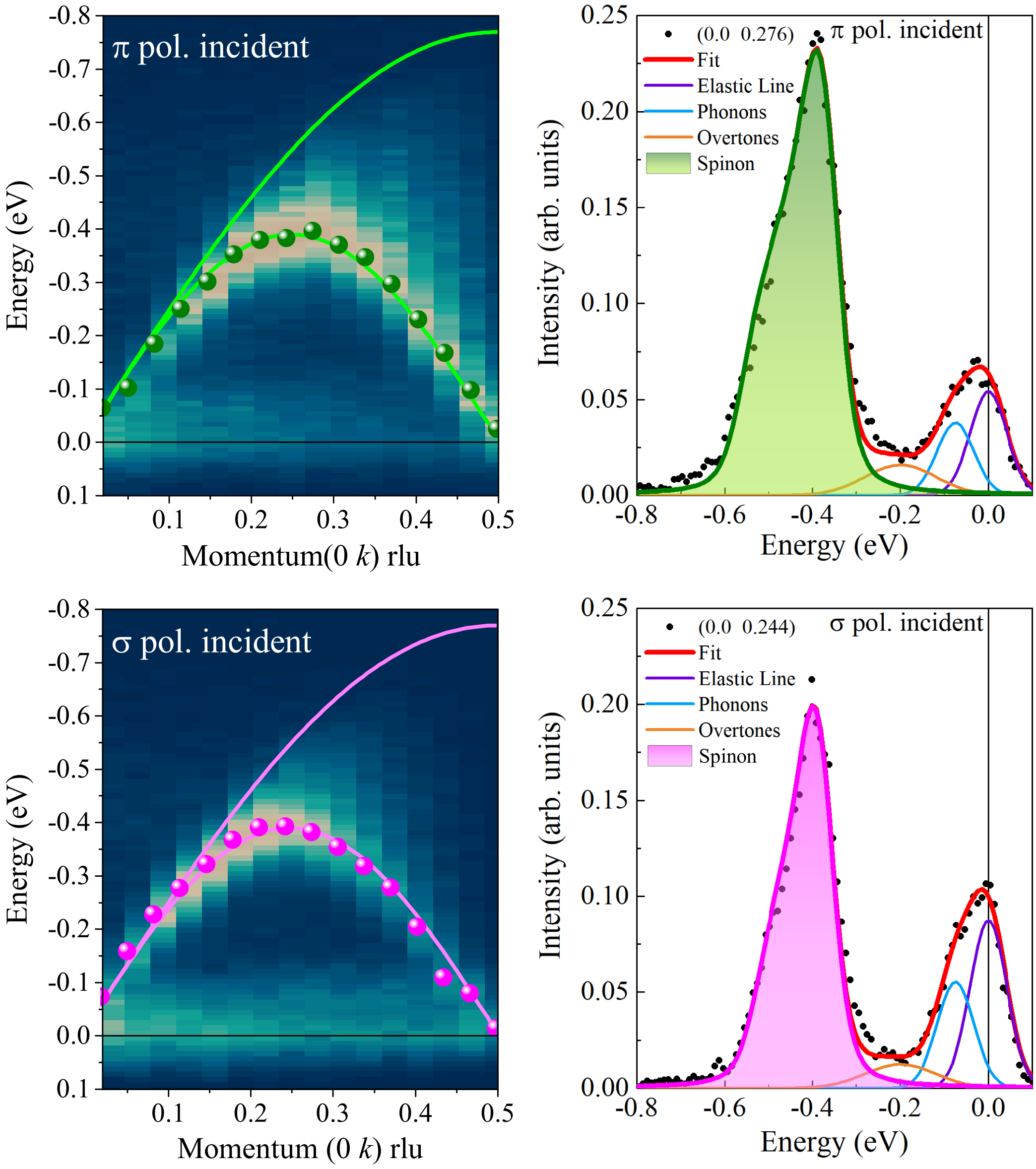

Figure 5.6: Momentum transfer dependence of the magnetic two-spinon continuum of Ca_2CuO_3 taken with π (top left panel) and σ (bottom left panel) polarization measured along the [0 1] high-symmetry direction. The results of the fittings are represented by dots (energy position of the spin excitations) while the continuous lines are related to the approximate two-spinon continuum dynamical structure factor. The right panels show the low energy RIXS line spectra at two particular momenta, which were fitted by assuming the onset of four distinct features: the quasi-elastic peak (purple), a generic phonons contribution (blue), its overtones (orange) and the spinon (green/magenta for π/σ polarization). Whereas the first three were fitted with a Lorentzian, the latter has been fitted with the approximate two-spinon dynamical structure factor $S(\mathbf{q},\omega)$ and convoluted with a gaussian lineshape [222] in order to take into account the overall experimental energy resolution.

in realistic materials. Note that finite Hund's coupling preserves fractionalization, but hinders the description with an effective t-J model and might lead to a non-negligible interaction between orbitons and spinons.

To verify the spinon-orbiton separation, we employ a Kugel-Khomskii-type Hamiltonian [28], which can be written in the following general form:

$$\begin{aligned} H = 2\sum_{\langle i,j\rangle}\left(\vec{S}_i\cdot\vec{S}_j+\frac{1}{4}\right)A(T_i^\beta,T_j^\alpha) \\ +\sum_{\langle i,j\rangle}K(T_i^\beta,T_j^\alpha)+\Delta\sum_i T_i^z\ . \end{aligned} \tag{5.1}$$

Here $\vec{S}_i$ describes a spin $S=1/2$ at site i and T_i^α is a pseudo-spin $T=1/2$ with component $\alpha\in\{x,y,z\}$ to describe the orbital degree of freedom between the ground state $|x^2-y^2\rangle$ and one of the excited orbitals $|\{xy,xz,yz\}\rangle$ (note that the 'nondispersive' $3z^2$ orbital is not taken into account in the analysis). Bonds $\langle i,j\rangle$ take nearest neighbors into account and Δ_{CF} is the crystal field splitting. Operators $A(T_i^\beta,T_j^\alpha)$ and $K(T_i^\beta,T_j^\alpha)$ only depend on the orbital degrees of freedom and account for onsite repulsion U, Hund's coupling J_{H} and nearest-neighbor hopping t_1 and t_2 for the ground state and the excited orbital, respectively (see Appendix A for details). Note that for the ferro-orbital ground state, Hamiltonian (5.1) reduces to the Heisenberg model, which describes the spin excitations discussed in the previous section.

To model the orbital excitation in the RIXS spectrum, we calculate the orbital spectral functions $O(\mathbf{q},\omega)$ and the spin-orbital $SO(\mathbf{q},\omega)$ with exact diagonalization and cluster perturbation theory for each orbital separately. The exact diagonalization results are broadened by a Lorentzian line shape of 120 meV FWHM to account for finite size effects (for details see Appendix A). For direct comparison with the experiment, they have to be multiplied by the RIXS matrix elements that can easily be obtained using the so-called fast collision approximation to the Kramers-Heisenberg formula for RIXS (for more details, see Refs. [4, 11, 60]). Finally, the results are convoluted with a Gaussian function (FWHM = 60 meV) to account for experimental resolution.

Even in the presence of Hund's coupling, the spinon-orbiton fractionalization is preserved [216], although it mediates an interaction between orbiton and spinon that can wipe out signatures of spin-orbit separation if it becomes too strong. In fact, for finite Hund's exchange the hopping of an orbiton is modified, as shown in Figure 5.1, by the distinct superexchange processes for anti-parallel and aligned spins. For anti-parallel spins an excited electron can move with superexchange constant $t_1t_2/(U-2J_{\mathrm{H}})$, which increases to

$t_1t_2/(U - 3J_\mathrm{H})$ in the case of parallel spins. Hence, orbital (O) and spin-orbital (SO) excitations are distinguishable for non-zero J_H and need to be considered separately. Additionally, the bandwidth of the excitations (W) increases for increasing J_H. Note that this intuitive picture is supported by numerical calculations [216].

Using this picture, we derived the approximate analytic relation between J_H and W (see Appendix B)

$$J_\mathrm{H} = \left(U - \frac{8t_1t_2}{W}\right)\frac{1}{3}, \tag{5.2}$$

which makes it possible to calculate J_H from the bandwidth of the excitation. This implies that a theory for spinon-orbiton separation which ignores Hund's coupling always overestimates the hopping constant of the excited orbital.

Comparison between data and theory

In Figure 5.4 we show the measured RIXS spectra of Ca21 in different experimental configurations. As mentioned above, the quasi-1D nature of Ca21 has strong repercussion on the dispersion of the spectral features seen by RIXS. This is already observed in the absence of spin excitations when spectra are measured with the CuO_3 chains oriented perpendicularly to the scattering plane. In this configuration, we do not see any kind of dispersion also in the dd excitations energy range (panel d of Figure 5.4). Therefore, let us from now on focus solely on the geometry in which the chains are parallel to the scattering plane (panels a-c of Figure 5.4). This configuration is similar to the one reported by Bisogni *et al.* [211], where in the quasi-1D AFM spin-ladder $CaCu_2O_3$, the spin-orbital separation occurs along the a direction in the d_{xz} orbital channel.

To explain the observed orbital spectra, with their peculiar dispersion relations, we use the theoretical model already described in detail in Section 5.1.3. We choose the parameters of the model in two steps. First, we start with the parameter related to the $d_{x^2-y^2}$ orbital—the hopping constant t_1 between the two nearest neighbor $d_{x^2-y^2}$ orbitals. The latter could be calculated from to the superexchange constant $J_\mathrm{SE} = 4t_1^2/U = 0.24$ eV, as obtained from the RIXS spin spectrum in Section 5.1.3. Assuming that typically for the cuprates the on-site Coulomb repulsion $U = 8t_1$ [124] we get that $t_1 = 0.49\,\mathrm{eV}$ and $U = 3.92\,\mathrm{eV}$.

We obtain the remaining model parameters—the hopping parameters t_2 describing the hopping between the excited orbitals, the Hund's coupling J_H and the on-site (crystal field) energies Δ_CF of the excited orbitals, *i.e.*

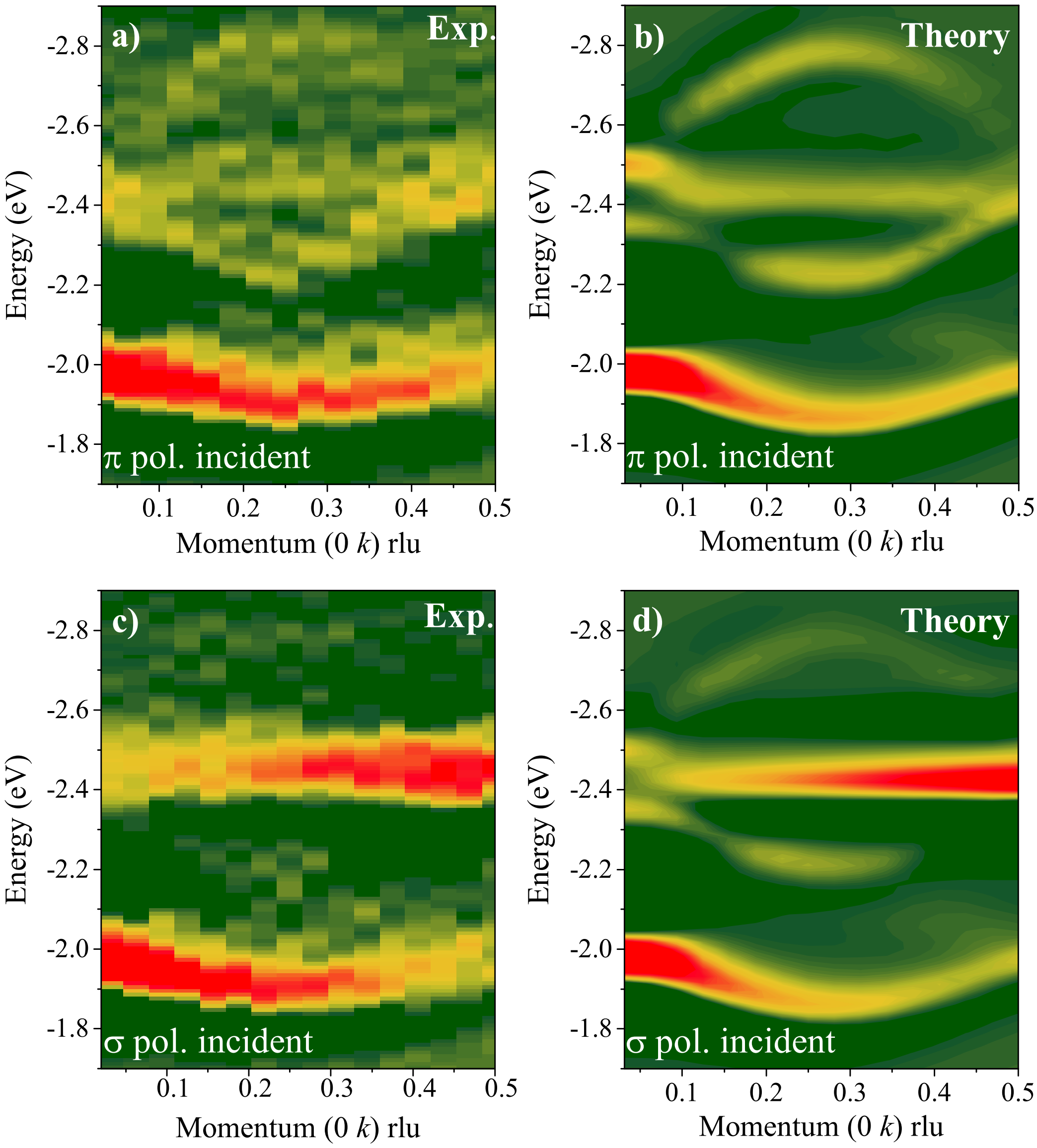

Figure 5.7: Experimental (a,c) and theoretical (b,d) second derivative RIXS intensity maps in the orbital excitations energy range.

d_{xy}, d_{yz}, d_{xz}, by directly comparing the second derivatives of the theoretical results and experimental spectra, see Figure 5.7.

The results from the 'best fit' of the theoretical model to the experimental data are given in Table 5.2.

As can be seen in Figure 5.7 the experimental and theoretical second derivative maps are in very good agreement. Let us note in passing that the second derivative curves easily track the peak position of the different spec-

	xy	xz	yz
J_{H} (in units of t_1)	0.8	1.2	1.2
t_2 (in units of t_1)	0.5	0	0.7
Δ_{CF} (eV)	1.87	2.32	2.45

Table 5.2: 'Best fit' microscopic parameters for the Kugel-Khomskii Hamiltonian. (5.1). For definitions see main text and Appendices.

tral features, making the dispersion of the orbital excitations more evident without any type of fitting. In fact, such a method has been previously used in the analysis of RIXS data to disentangle dispersive orbital excitations from the particle-hole continuum in Sr_2IrO_4 [212].

Notably, the obtained results can explain the apparent polarization dependence, as could be observed by comparing the orbital RIXS spectra obtained with π and σ polarizations [cf. Figure 5.4(a-b)]. In fact, such a result might naively suggest a possible polarization-dependence of the spin-orbital fractionalization phenomenon. This hypothesis could be supported by the fact that, up to now, in RIXS studies the orbitons have been measured solely with the incident π polarization [55]. Moreover, this apparent polarization-dependent behavior is not reflected in the low energy region: as widely discussed in Section 5.1.3, the fractionalized spinon excitations show the same momentum dependence for both π and σ incoming light. To unravel this puzzle we take a closer look at the second derivative maps in the case of σ incident polarization shown in the bottom panels (c-d) of Figure 5.7. They reveal the presence of a dispersion even for σ incoming polarization, although it is very weak. The reason for this polarization-dependent behavior lies in the fact that with σ polarization the d_{xz} RIXS cross section is enhanced, and therefore hiding the d_{yz} contribution. On the other hand, with the π polarization the d_{yz} excitation provides most of the RIXS signal. Thus, we conclude that the spin-orbital fractionalization phenomenon is indeed an intrinsic phenomenon of the material and does not depend on the polarization of the incoming light.

The theoretical RIXS spectra calculated with the 'best fit' model parameters from Table 5.2 are shown in Figures 5.8(b, e, f). Indeed, as already suggested by the second derivative maps of Figure 5.7, one can observe a very good agreement with the experimental RIXS spectrum shown *e.g.* in Figure 5.8(a): first, the dispersion of the lowest energy excitation (d_{xy}) is well reproduced in both the cases with π and σ incident light polarization. Its momentum dependence is characterized by $1/2$ r.l.u. periodicity in reciprocal space, as also shown in Sr_2CuO_3 [55]. Like in $CaCu_2O_3$, the d_{xz}

and d_{yz} energies are split by $\sim 150\,\mathrm{meV}$ [211]. Second, regarding the d_{xz} orbital excitation, assuming $t_2 = 0$ (due to the negligible overlap between nearest-neighbor d_{xz} orbitals along the y direction of the chain) results in a non-dispersive excitation. Third, the spin-orbital fractionalization is really very well-visible for the d_{yz} excitation.

Thus, the momentum dependence of the d_{yz} dispersion shows two strongly dispersive branches giving a characteristic oval shape [214, 210]. This, as discussed in detail in Appendix B, allows us to extract the bandwidth of the excitation $W \sim 0.6\,\mathrm{eV}$. The bandwidth can then be used in Eq. (11) to obtain the Hund's coupling to be of the order of $\simeq 1.14 t_1$, which is in good agreement with the above-discussed 'best fit' procedure (compare Table 5.2). Overall the values of Hund's coupling are in good agreement with the ones typically assumed for another quasi-1D cuprate (Sr_2CuO_3) [210].

Finally, we would like to stress that such a good agreement between the theoretical model (with the parameters from Table 5.2) and the experimental result cannot be achieved without a finite value of the Hund's coupling [cf. Figure 5.8(c-d)]. For instance, if $J_\mathrm{H} = 0$ and we use the same values of t_2 as reported in Table 5.2 for all the three orbitals considered we do not get a good agreement with the experimental data. It is then only when a much larger value of the hopping parameter t_2 ($t_2 > t_1$) is assumed [Figure 5.8(d)] that we obtain a satisfactory agreement with the experiment. This demonstrates that fitting the experimental results with the theoretical model with $J_\mathrm{H} = 0$ requires a non-physical, *i.e.* far too large, hopping t_2. This is due to the fact that the hopping t_2 of the excited orbital should not be larger than the hopping related to the ground state orbitals (since otherwise the hybridization would lower the energy of the excited orbital below that of the ground state orbital).

These observations remain valid also in the case of σ incident polarization; moreover, we observe [(Figure 5.8(e-f)] that also the spectral line shapes at selected transferred momenta confirm that the best way to fit our data is to include a finite, but realistic, value of the Hund's coupling.

5.1.4 Conclusions

We have studied in detail the RIXS response at the Cu L edge of a quasi-1D antiferromagnet, Ca_2CuO_3. We observed a clear signature of the dispersive spin and orbital $3d_{xy}$ and $3d_{yz}$ excitations, at first sight qualitatively resembling the ones recently found in the other quasi-1D copper oxide [55, 210, 211]. Thus, we can first conclude that also in this case it is correct to interpret the spin (orbital) excitations in terms of the onset of the two-spinon continuum (spin-orbital separation), respectively.

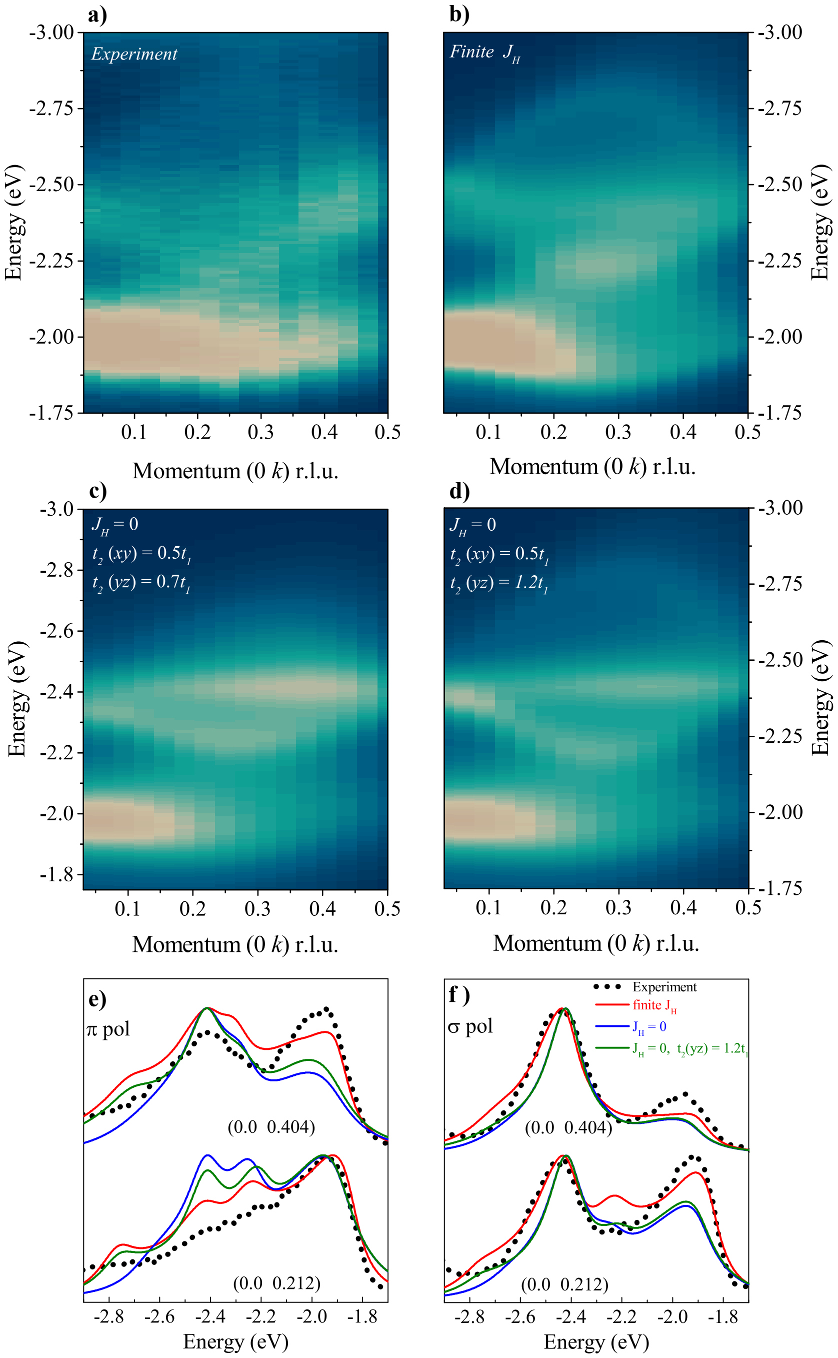

Figure 5.8: Comparison between the experimental RIXS (a) and the theoretical color maps using different set of parameters (b-d) for π polarization. Panel (b) shows the best fit with parameters listed in Table 5.2. In panel (c,d) Hund's coupling is set to zero and for panel (d) increased hopping for yz orbital was used to obtain a best fit when assuming vanishing Hund's coupling. Parameter sets used in (b-d) are compared to experimetal RIXS spectra at selected k values in panels (e) and (f) for π and σ polarization, respectively.

Next, we performed a very detailed quantitative analysis of the experimental data. First, in contrast to the previous studies, we exploit two distinct incident polarizations of the light in our analysis. Moreover, for both polarizations we managed to quantitatively describe the experimental RIXS spectra using the theoretically calculated spectrum based on the well-established spin-orbital Kugel-Khomskii Hamiltonian.

The crucial finding of this paper is that a detailed modelling of the orbital spectrum requires a finite Hund's exchange J_{H} in the Hamiltonian. Specifically, for Ca_2CuO_3 we obtain that a moderate, and *realistic*, value of $J_{\mathrm{H}} \simeq 0.5$eV best explains the experimental data. Here the main role of the Hund's exchange is to increase the velocity of the orbiton so that the theoretically predicted one matches well with the experimentally observed one. We note that the assumed value of the Hund's exchange is relatively small with respect to the calculated spin-orbital exchange constants, so that the interaction between orbitons and spinons is not that large and thus the spin-orbital separation picture can still approximately describe the physics present here, cf. Ref. [216] for details.

Altogether, this means that the Hund's exchange plays a vital role in the propagation of an orbiton.

5.2 Dispersing orbital excitations in the 2D infinite layer $CaCuO_2$

5.2.1 Introduction

The mere existence of orbitons [235, 236] is still controversial. Perhaps the clearest signatures have been recently proposed based both on experiments [55, 211, 237] and theory [214] in quasi-1D cuprates (*e.g.* Sr_2CuO_3) and in quasi-2D iridates (here as spin-orbital waves due to the large spin-orbit coupling in the $5d$ states) [213]. This is due to the fact that these two cases are rather 'special': while in the quasi-1D cuprate the large orbiton dispersion is observed thanks to the 'liberation' of the orbiton from the spin excitation (by which it is inherently dressed), the 2D iridate case is actually not a 'pure' orbiton (it is a $j_{\mathrm{eff}} = {}^3\!/_2$ excitation which carries both spin and orbital quantum numbers). Thus, an unambiguous observation of an orbiton in a quasi-2D cuprate case would constitute a real breakthrough.

On the theory side, it was suggested [214, 238] that the orbiton excitation in a quasi-2D cuprate might still be dispersive, even though its dispersion relation should be different to that in a quasi-1D cuprate (which is due to the polaronic coupling between orbitons and magnons that is absent in 1D).

In the previous Section we have provided a refinement of the theoretical models previously proposed to describe a realistic spin-orbital separation in quasi-1D materials separation by including a finite Hund's exchange [216]. Unfortunately, this model cannot explain the dispersing behavior of orbital excitations in 2D cuprates probed by RIXS, as we will show in the following.

Here we will present high resolution RIXS measurements on the 2D infinite layer $CaCuO_2$, which display a surprising dispersion of the *dd* excitations. Moreover, we exploit also the capability offered by the ERIXS spectrometer to measure the polarization of the scattered radiation. It is clear that our results can reopen a basic debate on the nature of the orbitons. One can also argue whether the 'revision' of orbiton theory in 2D would not call for a different interpretation of the result of the 1D system.

5.2.2 Experimental methods

Samples

The undoped "infinite layer" compound $CaCuO_2$ (hereafter CCO) discussed in this Section is characterized by the simplest crystal structure among all the cuprate families. In fact, CCO is composed by an infinite stack of 2D CuO_2 layers, which are essential for superconductivity in copper-based materials, separated by calcium ions (see Figure 5.9). The infinite and compact stacking of the CuO_2 planes is guaranteed by the absence of the apical oxygens, which is also of crucial importance for the electronic and magnetic properties. As it will become clearer in the following, the absence of the apical oxygens largely affects the Cu local coordination, which shows in the present case the largest splitting between the e_g states. Moreover, it has been recently demonstrated by some of us that also the magnetism is affected by the absence of apical oxygens: the main consequence is the increase of the in-plane hopping range [18].

The CCO films investigated in this work were grown by pulsed laser deposition (PLD), using a $\lambda = 248$ nm KrF excimer laser. The substrate used for the film deposition is 5x5 mm^2 $NdGaO_3$ (110) (NGO). Indeed, it has been shown that NGO, with pseudocubic in-plane lattice parameter $a = 3.87\,\text{Å}$, is the most suitable substrate to grow CCO film [239].The target with $CaCuO_2$ nominal composition, was prepared by standard solid state reaction, according to the following procedure: stoichiometric mixtures of high-purity $CaCO_3$ and CuO powders were calcined at 860° C in air for 24 h. Then the powders were pressed to form a disk and heated at 950° C for 12 h. The substrate was placed at a distance 2.5 cm from the targets on a heated holder and its temperature during the deposition of the films was $T \approx 600°$

C. The deposition chamber was first evacuated down to P ~ 10 mbar and then the deposition was carried out at 2x10^{-1} mbar oxygen pressure. At the end of the deposition, the film was cooled down at the growth pressure. A 4 nm crystalline $SrTiO_3$ (STO) cap layer was grown on top of the CCO film at the same growth conditions, using a commercial STO crystal as a target.

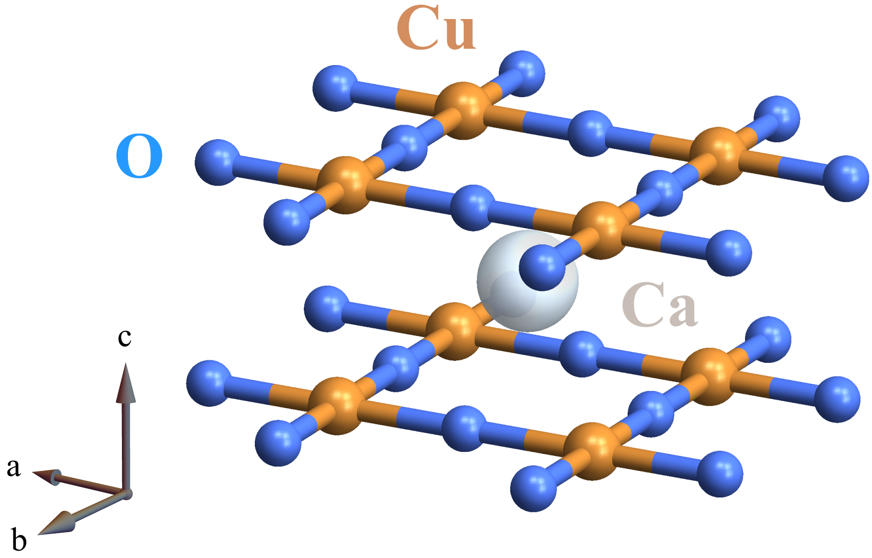

Figure 5.9: Schematic illustration of the unit cell of the 2D infinite layer $CaCuO_2$.

RIXS measuresements

In order to investigate the dispersing behavior of *dd* excitations in CCO we carried out high resolution Cu L_3-edge RIXS [4] measurements at the ID32 beamline [8] of the ESRF - The European Synchrotron. The incident energy of the X-rays photons was tuned to the maximum of the absorption peak at ~ 931 electronvolt (see Figure 2.4) and with a combined energy resolution of ~ 55 meV. We fixed the 2θ scattering angle equal to 149.5° to probe the entire first Brillouin zone. In particular, we probed the system with both π and σ polarizations measuring the high symmetry direction $\Gamma \rightarrow X$ ([1 0]). Differently from the 1D Ca21 discussed in the previous Section, the 2D infinite layer CCO shows no differences between the [1 0] and [0 1] direction in the reciprocal space due to the tetragonal crystal structure (the Cu-O distance along both the in-plane directions is 1.93 Å). Hereafter, we will express the values of the in-plane momentum $q_{\|}$ in terms of reciprocal lattice units (r.l.u.) $2\pi/a$, $2\pi/b$ and $2\pi/c$, where $a = b = 3.85$ Å and $c = 3.18$ Å are the lattice parameters of CCO During the experiments the temperature was kept fixed at 20 K.

The RIXS raw data of CCO measured along the [1 0] direction are shown in Figure 5.10. In both the waterfall plots reported here each spectrum can be decomposed into several features. In the low energy scale we can identify the elastic peak and contributions at few meV coming from phononic excitations. Up to -0.5 eV, and depending on the in-plane momentum transferred, all the spectra are characterized by the presence of dispersing magnetic (magnon and bimagnon) excitations, which reach their maximum at the zone boundary. If we compare the low energy spectral range of the 2D CCO with the one measured on the 1D Ca21 reported in Figure 5.6, we clearly note the completely different momentum dependence in the low energy magnetic spectra: the 1D system has a two-spinon continuum while the 2D system has a single dispersive peak. This experimental finding is a simple confirmation of the effective bi-dimensionality of CCO, since it shows the same dispersion of magnetic excitations detected in all the other well studied 2D cuprates [5, 18]. The absence of apical oxygens makes larger the range hopping and the exchange interaction. Moreover the infinite layer structure, with the CuO_2 planes very close to each other leads to a non negligible inter-plane direct exchange (AF), with a resulting 3D AF structure [18]. In the following we will underline the importance of the missing apicals also in the physics of the orbital excitations.

As in all the other RIXS spectra discussed in this thesis, at higher energies we find several peaks that are described in terms of *dd* (or orbital) excitations, whose energies strictly depend on the crystal structure of the compounds under study. In 2D cuprates, differently from the 1D case previously discussed (see Chapter 5.1.4), *dd* excitations are usually treated as non collective modes, and therefore described in terms of localized excitations without showing any in-plane momentum dependence [11]. Surprisingly, both the waterfall plots and the RIXS intensity maps shown in Figure 5.10 reveal the presence of dispersing orbital excitations similar to those present in the RIXS spectra of Ca21 (see Figure 5.4). Moreover, the energy range of the orbital excitations is larger than the one of NBCO reported in Figure 3.4 (a-d panels), showing, for example, a high energy peak that is ascribable to the transition from the ground state to the $d_{3z^2-r^2}$ orbital. The energy of the $d_{3z^2-r^2}$ excitation is particularly sensitive to the presence (or not) of the apical oxygens: in fact, closer (to the CuO_2 planes) apical oxygens reduce the the split-off energy of the $d_{3z^2-r^2}$ orbital and, at the same time, increase its weight in the ground state which leads to localize charges in the $d_{3z^2-r^2}$ orbitals [11].

The orbital-character has been done by fitting the experimental results with the theoretical RIXS cross-sections calculated within the single-ion

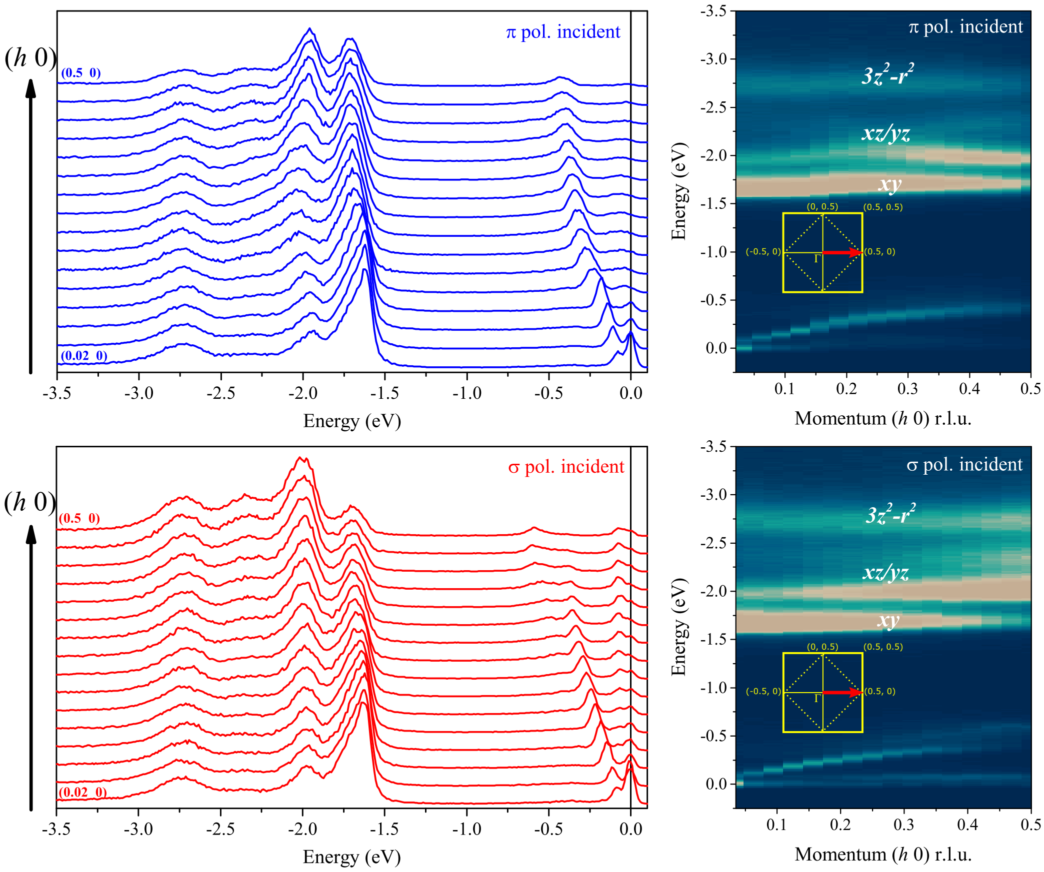

Figure 5.10: Raw RIXS spectra (left two panels) of $CaCuO_2$ measured along the [1 0] direction (as illustrated by the inset in the two color maps) with both π (top panels) and σ (bottom panels) of the incident radiation. On the right side we show the respective RIXS intensity maps.

model (for more details see Chapter 2.6.2 and Refs. [11, 50]). Our results are in agreement with the ones previously reported on CCO [11], except for the $d_{xz/yz}$ peak. In 2D cuprate characterized by a tetragonal crystal structure the d_{xz} and d_{yz} orbitals should be degenerate in energy. Apparently, in the spectra reported in Figure 5.4 it seems that at least two peaks are present in the energy range between -1.8 and -2.5 eV, which should be marked by solely one peak related to the $d_{xz/yz}$ excitation.

Finally, we have exploited the unique capability offered by the ERIXS spectrometer to distinguish the polarization of the scattered light in order to be much more confident about the assignment of the dispersing *dd* peaks and to clarify their nature. For polarization resolved measurements we relaxed the overall energy resolution to $\sim$ 70 meV by opening the monochromator exit slit to improve the data acquisition efficiency.

5.2.3 Results and discussions

As mentioned in the first part of this Section, our RIXS data on CCO reveal fascinating phenomena especially in the *dd* excitations spectral range. The two main peculiarities detected during our experiments are the presence of multiple peaks and the dispersing character of orbital excitations.

In the two left panels of Figure 5.11 we show the close-up view of the RIXS intensity maps in the *dd* excitations spectral range measured with both π (top) and σ (bottom) polarization of the incident photons along the [1 0] direction of the first Brillouin zone.

The assignment of the *dd* peaks energy has been done by fitting the experimental data with the RIXS cross-sections obtained within the framework of the single-ion model. As anticipated above, our results are in agreement with those reported in Ref. [11] for the specific case of CCO. At high energies ($\sim$2.6 eV) we find a non-dispersive peak related to the transition from the ground state to the $d_{3z^2-r^2}$ orbital, while the peak at lower energy losses is ascribable to the transition to the d_{xy} orbital. The latter displays a monotonic increase of the energy as a function of the in-plane momentum. In the energy range between -1.8 and -2.5 eV, our data surprisingly reveal the presence of a double-peak structure which clearly shows a strong momentum and polarization dependence. In particular, the dispersing behavior of the 3 d_{xy} and $d_{xz/yz}$ peaks resemble the one presented in the previous Section (1D Ca21), though with different symmetries.

In order to highlight the momentum dependence of the *dd* excitations in CCO, we compared the RIXS raw spectra with their second derivative along the high symmetry direction [1 0]. The results are illustrated in Figure 5.13. As explained in the previous Section, this method allows us to track each peaks energy without making any assumptions needed, for example, in a multiple-peaks fitting procedure. As we noticed in the case of the 1D Ca21, the $d_{3z^2-r^2}$ peak does not show neither momentum nor polarization dependence and its high energy is directly correlated to the local Cu coordination that largely affects the e_g orbitals splitting [11]. Differently from the 1D case, the 2D infinite layer CCO should present a unique peak related to the transition to the $d_{xz/yz}$ due to its tetragonal crystal structure. Contrarily to this common belief, the second derivative maps reported in the left panels of Figure 5.13 show the presence of two distinct spectral features in the energy range between -1.8 and -2.5 eV.

The analogy with the 1D case (see Figure 5.7) is reflected also in the polarization dependence: the dispersion of these two spectral features seems to be present solely when the system is probed with π polarization (top panels), while with σ polarization the momentum dependence is almost flat (bottom

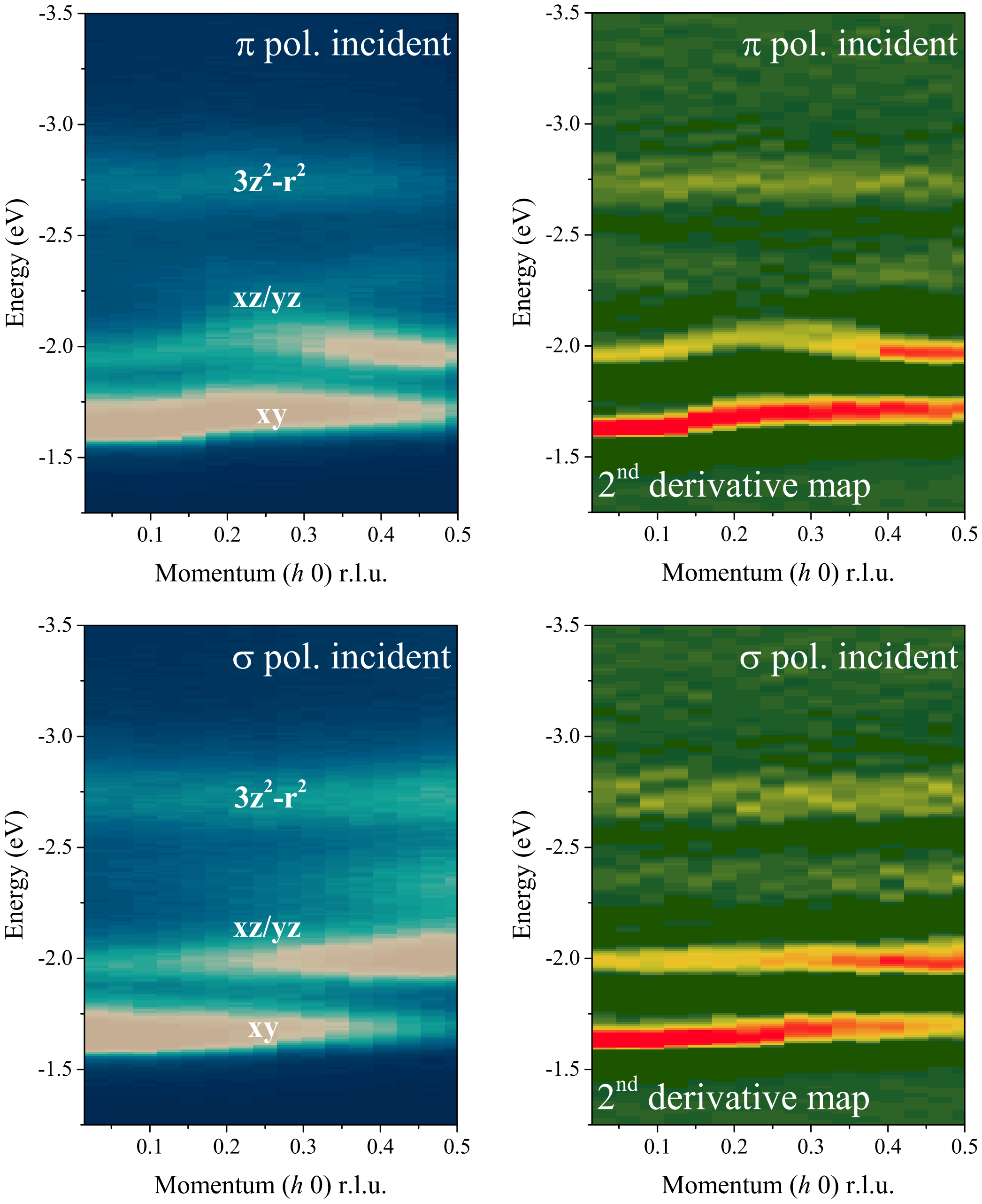

Figure 5.11: In the left panels we show the close-up view of the RIXS intensity maps in the *dd* excitations energy range measured with both π (top) and σ (bottom) polarization of the incident X-ray photons along the [1 0] direction of the first Brillouin zone. On the right side we report the respective second derivative maps.

panels). Without having a theoretical model explaining the dispersion in terms of fractionalization of orbital excitations in 2D cuprates, we can anyway observe that the dependence of the atomic RIXS cross-sections on the polarization must anyway drive the selection of the dominant components in terms of orbital final states, and those are common to the 1D and the 2D cases. Finally, the d_{xy} peak shows the same kind of momentum dependence with both the incident polarizations.

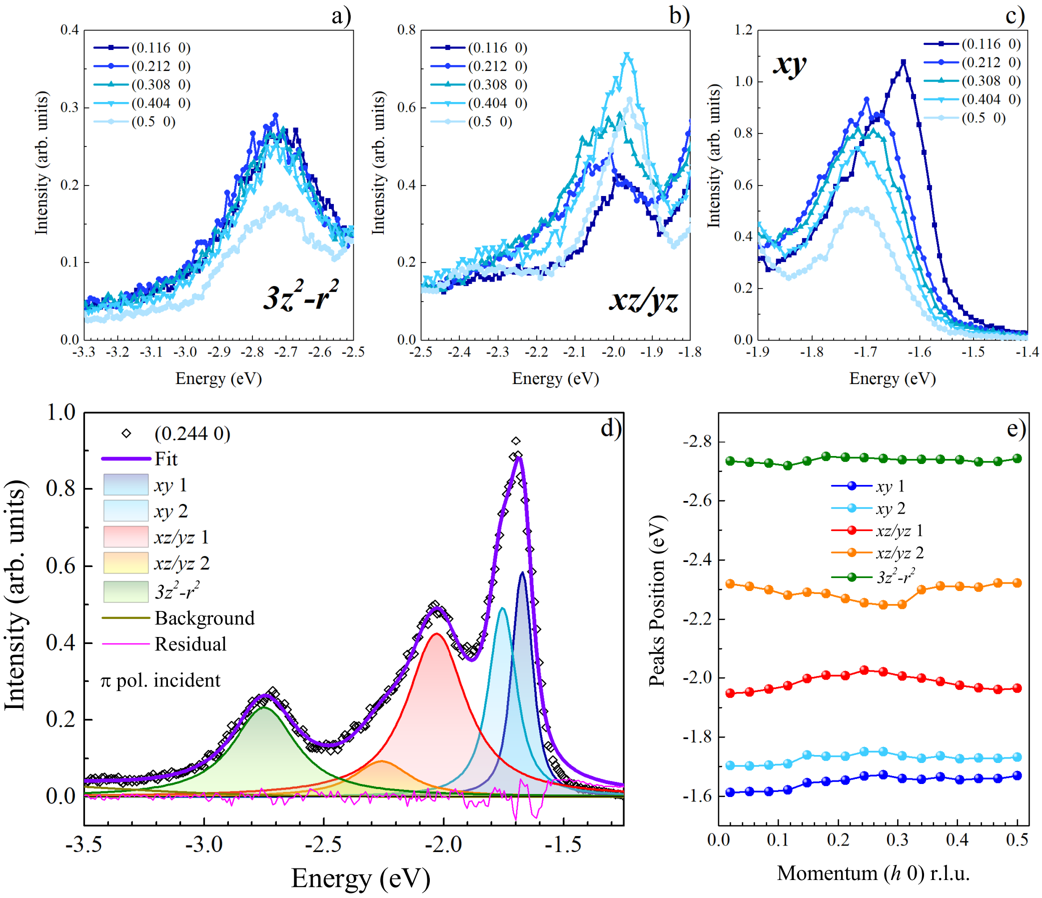

Figure 5.12: RIXS spectra measured with incident π polarization at selected in-plane momenta in the energy ranges corresponding to the $d_{3z^2-r^2}$ (a), $d_{xz/yz}$ (b) and d_{xy} (c) orbital excitations. d) Fit of the *dd* excitations spectral range of the RIXS spectrum of CCO measured at $h = 0.244$ r.l.u.. e) Peak energy positions extracted from the fitting procedure.

Since the model that we have used for the interpretation of the spin-orbital separation in the 1D case cannot explain the *dd* excitations dispersion in CCO, we decided to make a phenomenological analysis by multi-peak fitting the RIXS spectra.

Before discussing the fitting results, in the top panels (a-c) of Figure 5.12 we show the energy ranges related to the $d_{3z^2-r^2}$, $d_{xz/yz}$ and d_{xy} excitations, at selected momenta along the [1 0] direction. As previously pointed out, a closer inspection to the single RIXS spectra confirms the non dispersing character of the $d_{3z^2-r^2}$ orbital peak (panel a). On the other hand, the $d_{xz/yz}$ and d_{xy} peaks show a complex momentum dependence with different symmetries. Regarding the $d_{xz/yz}$ spectral range (panel b), the main dispersing peak lies at energies around $\sim$ -2 eV, while the second and less intense one can be found at $\sim$ -2.3 eV. Finally, the peak related to the transition to the d_{xy} (panel c) shows a monotonic momentum dependence. Furthermore, if we consider the spectrum measured at $q_{\parallel} = (0.116\ 0)$ r.l.u., its line shape seems to be asymmetric or, alternatively, composed of two features having different spectral weights. These considerations lead us to fit both the $d_{xz/yz}$ and d_{xy} spectral range with two distinct peaks, as shown in Figure 5.12(d) where we give an example of the fitting procedure at $q_{\parallel} = (0.244\ 0)$ r.l.u.. We used Lorentzian line-shapes convoluted with a Gaussian curve having a full-width at half-maximum (FWHM) equal to the energy resolution.

As expected, two peaks are needed to get the correct fitting of the $d_{xz/yz}$ and d_{xy} orbital excitations. In Figure 5.12(e) we report the extracted peaks positions. As demonstrated by taking the second derivative of the RIXS spectra, this fitting procedure confirms the non-dispersing nature of the $d_{3z^2-r^2}$ orbital excitation. Moreover, it evidences the presence of at least two dispersing spectral features in the $d_{xz/yz}$ energy range (between -1.8 and -2.5 eV) and the quasi-monotonic momentum dependence of the d_{xy} excitations. Concerning the latter, the presence of a double peaks could be explained considering two different scenarios: i) spin-orbital separation (as in 1D Ca21); ii) charge-orbital-coupling [240], where each *dd* excitation peak is assisted by phonons. For the $d_{xz/yz}$ orbital excitation, the spin-orbital separation phenomenon could probably play the bigger role, especially because the RIXS data taken on the 2D CCO are very similar to the one of the 1D Ca21. The different symmetry of the dispersion could be affected by the dimensionality, while it seems difficult to explain the sizable ($\sim$ 300 meV) splitting of the t_{2g} d_{xz} and d_{yz} orbitals.

At this point, a question naturally arises: why other 2D AF cuprates (YBCO, Bi2201, LCO etc.) do not display such dispersing orbital excitation [11]? Without the possibility to recall any theoretical model that works in the case of 2D cuprates, the only common point between CCO and Ca21 is the Cu local coordination: in fact, both the compounds have no apical oxygens. As a main direct consequence, the in-plane excitations, such as the transitions involving t_{2g} orbitals, could be less screened and more free to propagate giving rises to large dispersions in the reciprocal space.

Also due to the lack of a model, we enlarged our experimental basis set by performing polarization-resolved RIXS measurements in order to have more

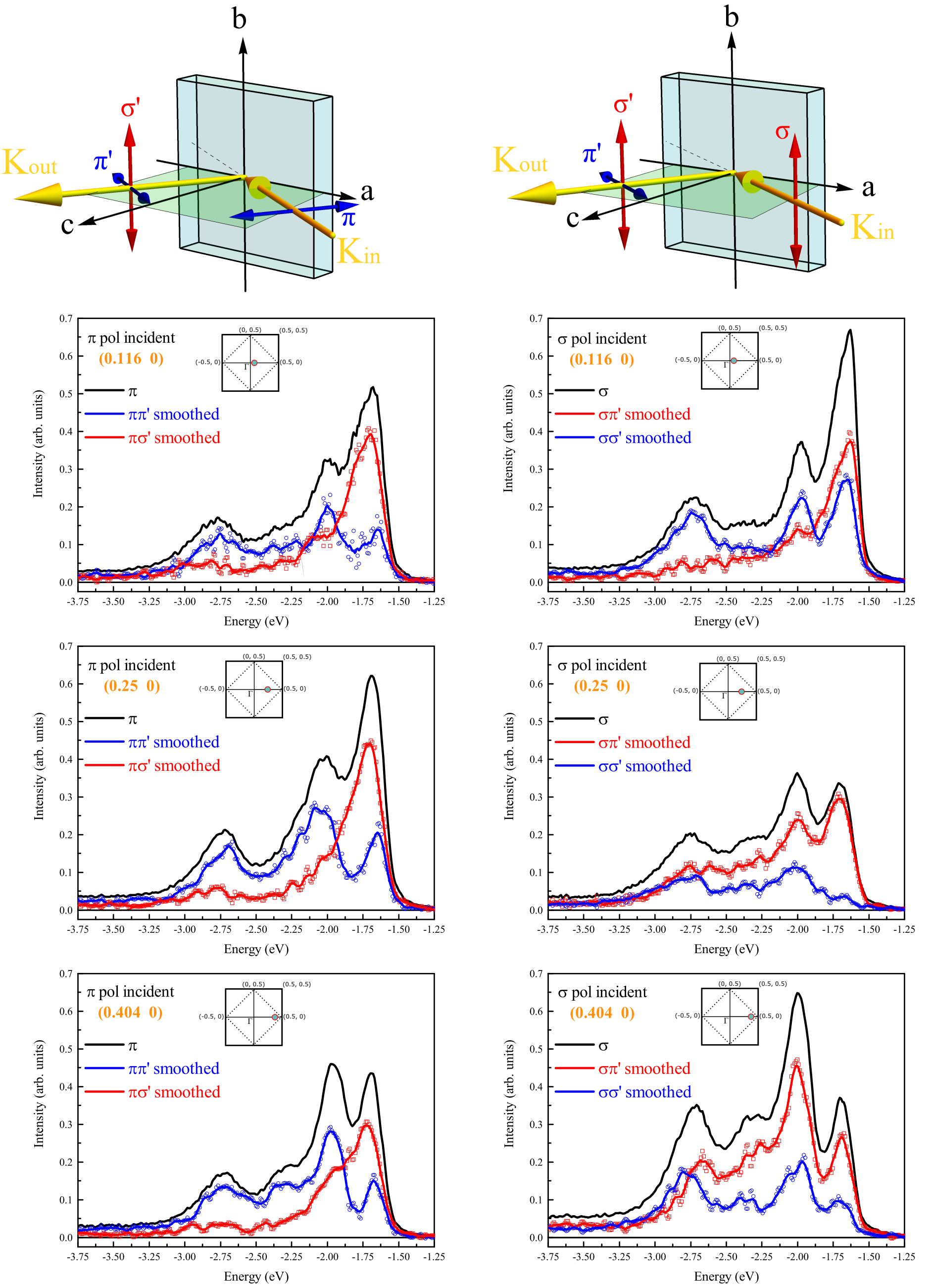

Figure 5.13: Close-up view of the *dd* excitations energy range of polarization-resolved RIXS spectra measured with both π (left panels) and σ (right panels) polarization of the incident radiation. The in-plane momenta at which we measured the spectra are illustrated in the insets present in each panel. On top we report the adopted scattering geometries highlighting the role of the incident and scattered photon polarization.

possible information about the orbital excitations in CCO. In particular, we acquired RIXS spectra at selected in-plane momenta along the anti-nodal direction [1 0] ($h = 0.116$, 0.25 and 0.404 r.l.u.) with both π and σ polarization of the incident light. The scattering geometries are schematically illustrated on top of Figure 5.13. The most relevant information that we can extract from these measurements is that in the energy range of the $d_{xz/yz}$ excitation (between -1.8 and -2.5 eV) both the peaks have the same polarization dependence. This evidence tells us that probably the unexpected dispersing double peak could be characterized by the same physical nature. Although we relaxed the energy resolution for polarimetric measurements, the d_{xy} peak (the one at lower energy losses) surprisingly reveals its asymmetric line-shape also in the polarization-resolved spectra.

5.2.4 Conclusions

The RIXS data discussed in this Section reveal the dispersing character of orbital excitations in the quasi-2D infinite layer $CaCuO_2$. Despite the dispersions in the *dd* spectral range resemble the one of Ca_2CuO_3 shown in the previous Section, their symmetry (in particular for the d_{xy} and $d_{xz/yz}$ orbitals) and periodicity is clearly different. It has been theoretically proposed that orbital excitations in quasi-2D cuprate might be characterized by a dispersing nature, even though their dispersion is expected to be different to the one revealed by quasi-1D cuprates. Our data seem to confirm this scenario. In order to make a proper comparison between the 1D and 2D case, we collected RIXS spectra along the [1 0] high symmetry direction in the reciprocal space with both π and σ polarization of the incident light. Moreover, we have also performed outgoing polarization-resolved measurements.

In Paragraph 5.1.4 we have demonstrated that, in order to explain a realistic spin-orbital model in 1D system, a finite Hund's exchange has to be taken into account. We try to explain the unexpected orbital dispersion in CCO using the same model adapted to the 2D case. Unfortunately, this model is incompatible with the experimental findings, calling for a new explanation of this unusual property manifested by CCO. Without a proper model to fit our data, we implemented a multiple-peaks fitting procedure that clearly highlights the dispersing behavior of the d_{xy} and $d_{xz/yz}$ orbital excitations. In order to obtain a reliable fit of the experimental data, we considered a double-peaks for both the dispersing d_{xy} and $d_{xz/yz}$.

The overall results about the dispersions in the *dd* spectral range have been also confirmed by the second derivative of the RIXS raw data. Finally, we added to our data set polarization-resolved RIXS measurements that clearly show, especially in the $d_{xz/yz}$ energy range, a double peak structure characterized by the same polarization dependence.

CHAPTER 6

Insights into the crystal and electronic structure of $Ba_2CuO_{3+\delta}$ from resonant inelastic X-ray scattering

Motivated by the recent synthesis of $Ba_2CuO_{3+\delta}$ (BCO), a high temperature superconducting cuprate with putative $d_{3z^2-r^2}$ ground state symmetry, we investigated its electronic structure by means of Cu L_3 X-ray absorption (XAS) and resonant inelastic X-ray scattering (RIXS) techniques on a powder sample. We show that the XAS profile of BCO is characterised by two peaks associated to inequivalent Cu sites and that its RIXS response features a single, sharp peak associated to crystal-field excitations, and argue that these observations are incompatible with the previously proposed crystal structure of BCO. We therefore propose an alternative structure, which accounts for our results and previous powder X-ray diffractions experiments. We analyze the low-energy region of the RIXS spectra and estimate the magnitude of the magnetic interactions in BCO.

Contents

6.1 Introduction

Since the discovery of high temperature superconductivity in cuprates [6], many efforts have been spent to provide a conclusive and generally accepted explanation of this phenomenon. Unfortunately, results obtained so far are only partially satisfactory [7].

The discovery of novel families of unconventional superconductors is extremely important to help distinguishing indispensable and unnecessary, or even competing, ingredients for superconductivity. In this respect, the recent synthesis of $Nd_{0.8}Sr_{0.2}NiO_2$, an infinite-layer superconducting nickelate, is extremely welcome [241] and, despite dissimilarities with superconducting cuprates, the paradigm that a $3d^9$ ground state with $d_{x^2-y^2}$ orbital symmetry of the hole is key to achieve high temperature superconductivity is further strengthened [242, 243, 244, 245]. Li *et al.*, however, challenged this belief by synthesizing $Ba_2CuO_{3+\delta}$, a high temperature superconducting cuprate with putative $d_{3z^2-r^2}$ ground state symmetry [12].

Most cuprates are layered materials, with superconducting CuO_2 planes intercalated by blocking layers that act as charge reservoirs. In their antiferromagnetic, insulating parent compounds the ground state has predominant $d_{x^2-y^2}$ symmetry [13] due to the sign of the tetragonal crystal field acting on the Cu^{2+}-derived electronic states. Moreover, it has recently been suggested that the larger the energy splitting between the $d_{x^2-y^2}$ and the $d_{3z^2-r^2}$ states, the higher the superconducting critical temperature [18]. $Ba_2CuO_{3+\delta}$ (BCO) is supposedly isostructural to the prototypical $(La_{2-x},Ba_x)CuO_4$ high-temperature cuprate superconductors, which adopt a K_2NiF_4-type structure. A small, but sizable elongation of the CuO_6 octahedra typically stabilizes the $d_{x^2-y^2}$ ground state. In BCO, instead, it was suggested that a slightly compressive distortion induces a ground state with predominantly $d_{3z^2-r^2}$ character. This scenario is intriguing, because it undermines the relevance of the $d_{x^2-y^2}$ ground state for high temperature superconductivity and, therefore, motivates further investigations. At a theoretical level, a mechanism for the pairing that heavily relies on the significant weight of both $d_{x^2-y^2}$ and $d_{3z^2-r^2}$ orbitals at the Fermi energy has been recently proposed[246]. Experimentally, instead, little has been done besides the initial work of Li *et al.*.

Here we probe BCO by means of X-ray absorption spectroscopy (XAS) and resonant inelastic X-ray scattering (RIXS) at the Cu L_3-edge to set constraints on its crystal, magnetic and electronic structure. Experimental limitations due to the use of a polycrystalline sample prevented us from exploiting all the possibilities offered by these techniques; in particular, we could not investigate the angular and polarization dependence of XAS and RIXS cross-sections and determine the symmetry of the ground and excited states in BCO, as done in the past for other cuprates [11]. Nevertheless, we show that our results are incompatible with the crystal structure previously proposed for BCO and propose an alternative, consistent with our measurements.

6.2 Experimental methods

A powder sample of $Ba_2CuO_{3+\delta}$ (BCO hereafter) has been synthesized according to the procedure described in Ref. [12], with a superconducting critical temperature $T_\mathrm{c} \approx 70$ K.

XAS and RIXS spectra were collected at the I21 beamline of the Diamond Light Source (Didcot, UK). XAS measurements were carried out in total fluorescence yield mode. RIXS spectra were measured with an overall energy resolution of ≈55 meV. The X-ray beam spot size was approximately 3 micron × 20 micron, which is probably comparable to the grain size of the sample so that the XAS and RIXS spectra were found to be partly position dependent in shape. The polarization of the incident photons was vertical in the laboratory reference frame and perpendicular to the scattering plane. The scattering angle 2θ was kept fixed at 150°. All measurements were carried out at a temperature of 20 K.

6.3 Results

We report in Figure 6.1(a) the X-ray absorption profile of BCO across the Cu L_3 absorption edge. It shows two distinct features at approximately 936.9 and 938.6 eV, respectively.

We collected RIXS spectra for incident photon energies in the energy window corresponding to the XAS spectrum and show the results in Figure 6.1(b). The strong, narrow feature at constant zero energy loss is the elastic line, while higher energy loss features correspond to inelasitc excitations which depend on the incident photon energy. The intense peak at approximately 1.5 eV energy loss is maximized in the vicinity of the first peak in the XAS spectrum (~ 936.9 eV) and its position is rather constant as the incident photon energy is scanned. In agreement with a number of RIXS studies on cuprates [4, 11], these features are assigned to crystal field (or *dd*) and charge-transfer excitations. A broader and weaker feature is observed at higher energy losses: it is strongest at incident photon energies corresponding to the second peak in the XAS spectrum and partially displays a fluorescence-like behavior as seen, for example, in $YBa_2Cu_3O_{6.99}$ (see Supplemental Materials of Ref. [95]).

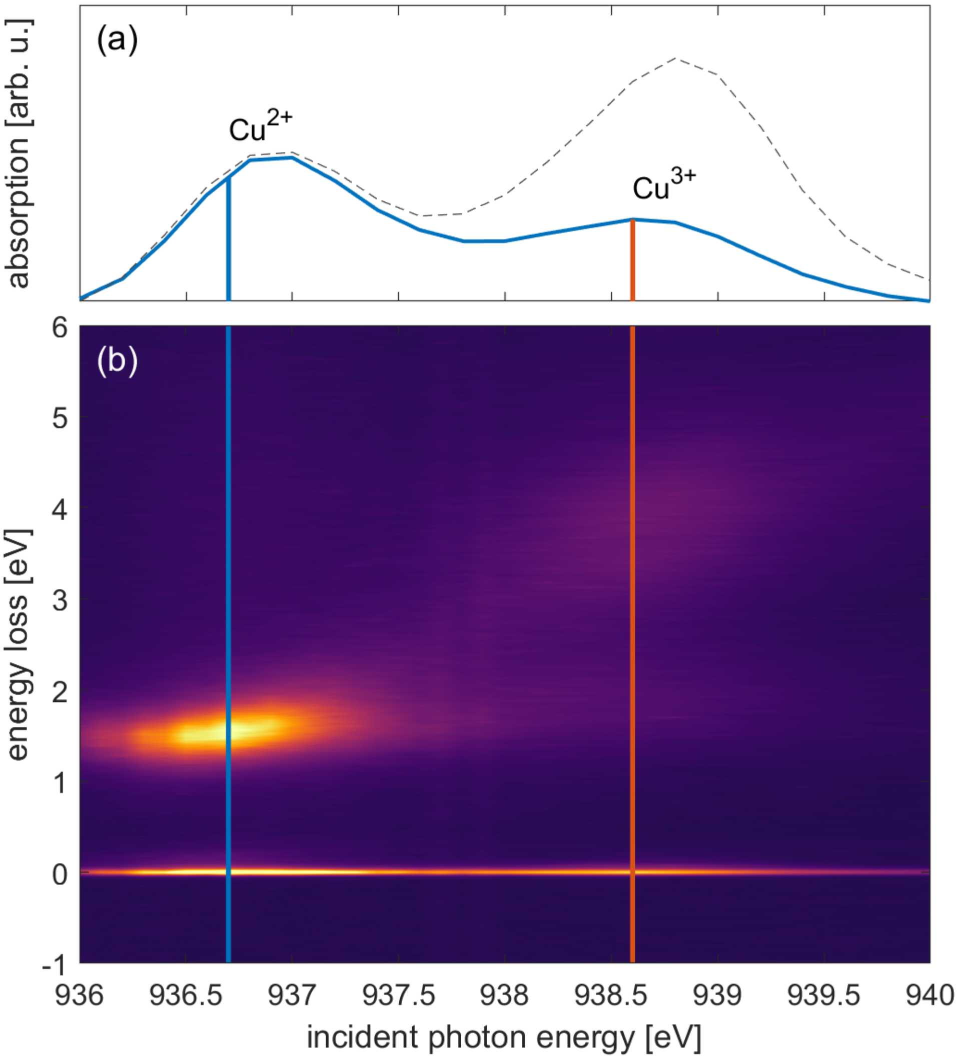

Figure 6.1: (a) Cu L_3 edge XAS and (b) RIXS map of polycrystalline BCO at 20 K. The vertical lines correspond to the cuts reported in Figure 6.2. The dashed line in panel (a) corresponds to a XAS spectrum taken on a different spot of the sample (see main text for further details).

A closer inspection of the RIXS data is provided in Figure 6.2, which shows two vertical cuts of the RIXS map of Figure 6.1(b). The overall shape of the spectra is markedly different: in particular, the RIXS spectrum taken at low incident photon energy (blue) shows a single peak at 1.5 eV energy loss, whereas the RIXS spectrum taken at high incident photon energy (red line) is characterized by two broad features at approximately 2 and 4 eV. In addition, we highlight in the inset the presence of a feature at approximately 0.2 eV, which resonates at the lower energy peak (936.7 eV) in the XAS spectrum.

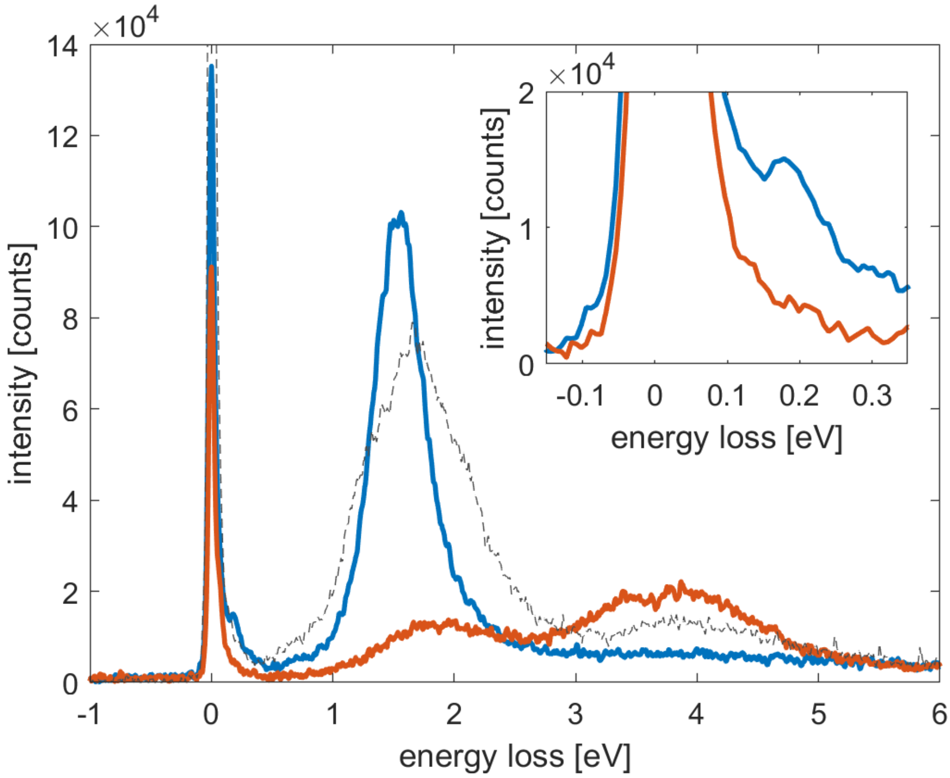

Figure 6.2: RIXS spectra of polycrystalline BCO measured at incident photon energies of 936.7 (solid blue) and 938.6 eV (solid red line), corresponding to the vertical lines in Figure 6.1, respectively. The spectrum reported with the dashed black line corresponds to the XAS in Figure 6.1 measured on a different spot of the sample. The inset shows a close-up view of the low energy loss window in logarithmic scale.

Before moving to the discussion of the experimental results, we note that the polycrystalline BCO sample was found to be rather inhomogeneous as observed with both XAS and RIXS. The black dashed lines in Figures 6.1(a) and 6.2 correspond to XAS and RIXS spectra, respectively, taken on a different area of the sample. The inhomogeneity is evidenced in the maps of

Figure 6.3: in panel (a) we show the spatial dependence of the relative intensity change of the two XAS peaks through the ratio

$$R = \frac{I(936.9\ \text{eV}) - I(938.8\ \text{eV})}{I(936.9\ \text{eV}) + I(938.8\ \text{eV})}, \tag{6.1}$$

where $I(X)$ is the XAS intensity at energy X; in panel (b) we show the spatial dependence of the full width at half maximum of crystal-field excitations in the RIXS spectra. The two maps show a clear correlation, and the first peak in the XAS is larger in the part of the sample where the crystal-field transition in RIXS is sharper. The length scale of the spatial variations amounts to a few tens of microns.

We remind here that the beam spot is much smaller than the step in the grid; and that these samples are particularly sensitive to exposure to air: different grains might have been chemically stabilized differently, leading to local variations of doping and composition. According to published results [12], the good spot is where the second XAS peak is weaker and so we focus our attention here.

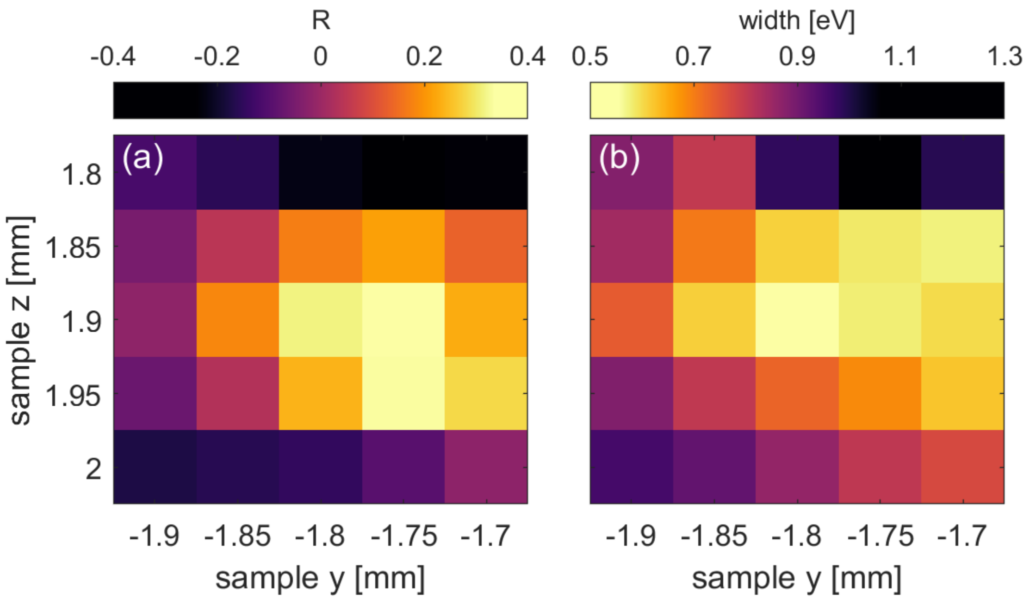

Figure 6.3: Spatial dependence of (a) the ratio between the two peaks in the XAS spectrum of Figure 6.1(a) and (b) the width of the 1.6 eV excitation in the RIXS spectrum of Figure 6.2.

6.4 Discussion

We start the discussion by commenting in the Cu L_3 edge XAS spectrum of BCO: irrespective of its detailed interpretation, the presence of two distinct features undoubtedly marks the presence of two, non-equivalent Cu sites in the system. As established in the literature on cuprates, the first and second XAS peak in Figure 6.1(a) can be associated to nominal Cu^{2+} and Cu^{3+} species, respectively [247, 95]. In the structure previously proposed for BCO, reported for convenience in Figure 6.6(a) together with additional information in Table 6.1, all the Cu sites are supposed to be equivalent at least from the structural point of view. The double XAS peak, in that scenario, would be possible only in the (unlikely) case of a strong charge discommensuration. Based on this observation we have explored other scenarios, still compatible with the powder diffraction patterns shown in Ref. [12], but also with the existence of two inequivalent Cu sites, in analogy to YBCO.

In Figure 6.4, we compare the crystal field excitations in superconducting BCO and two prototypical cuprate systems, *i.e.* the single-layer superconducting $La_{2-x}Sr_xCuO_4$ (LSCO, $x = 0.15$)[23] and the infinite-layer insulating $CaCuO_2$ (CCO) single crystals.

Crystal-field excitations arise from the redistribution of electrons within the atomic d shell. For a Cu^{2+} ion, a single particle approach is justified and dd excitations simply correspond to transitions between crystal-field split states [4, 11].

The symmetry of the crystalline electric field is primarily determined by the geometrical arrangement of the nearest neighbor oxygen ions around the central Cu^{2+} ion, whereas the Cu-O bond distances set the magnitude of the splitting. The scattering geometry and polarization dependence of the RIXS cross-sections for dd excitations have been used to determine the symmetry of the ground and excited states [11, 92, 60]. In particular, the assignment of dd excitations in CCO is as follows: the peaks at approximately 1.7, 2.0 and 2.7 eV correspond to transitions from the $d_{x^2-y^2}$ ground state to the d_{xy}, $d_{yz/zx}$ and $d_{3z^2-r^2}$ excited states, respectively; in the case of LSCO, doping causes an overall broadening of the spectrum, but one can still appreciate that the energies of the d_{xy} and $d_{yz/zx}$ transitions are similar to those in CCO, whereas the $d_{3z^2-r^2}$ excited state is found around 1.4 eV, in analogy to the single-layer insulating parent compound La_2CuO_4. We note that the energy of the d_{xy} excited state is mainly dictated by the in-plane Cu-O bond distance, which is similar for LSCO (1.91 Å) [248] and CCO (1.93 Å) [249]. Instead, the energy of the $d_{3z^2-r^2}$ excited state is mostly determined by the out-of-plane coordination of Cu [250]: in LSCO, the out-of-plane Cu-O bond

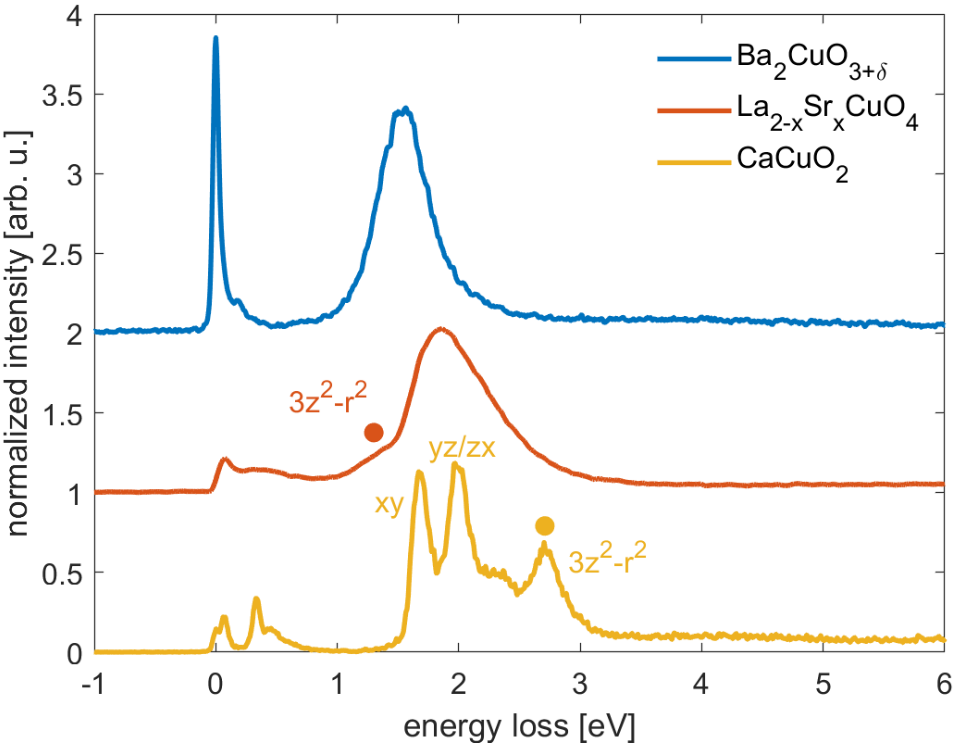

Figure 6.4: RIXS spectra of powder BCO (as in Figure 6.2, blue), compared to single-crystalline LSCO[23] (red) and CCO (yellow line) reference systems, normalized to the spectral weight of the *dd* excitations.

distance is 2.46 Å, while the infinite-layer structure of CCO features CuO_4 plaquettes with no apical oxygens (also shown in Figure 6.4), which pushes the $d_{3z^2-r^2}$ excited state at higher energies.

The RIXS spectrum of BCO is remarkably different from those of CCO and LSCO, and of all the layere cuprates studied so far. In particular, Figure 6.4 suggests three main observations: *dd* excitations in BCO are i) lower in energy than any other cuprate systems [250, 11], and are ii) sharper and iii) more symmetric than in LSCO. As we discussed above, the centre of mass of *dd* excitations is, to a large extent, determined by the in-plane Cu-O bond distance, which is considerably larger in BCO (2.00 Å [252]) than in LSCO and CCO, thus explaining i). However, we will argue in the following that, besides the XAS, also ii) and iii) cannot be accounted for by assuming the crystal structure previously proposed for BCO [12, 253].

Figure 6.5 shows the energy of the Cu 3*d* states as a function of the out-of-plane/in-plane Cu1-O distance ratio obtained from the crystal field theory reported in Ref. [251]. In this particular case, the energy of the different *d*

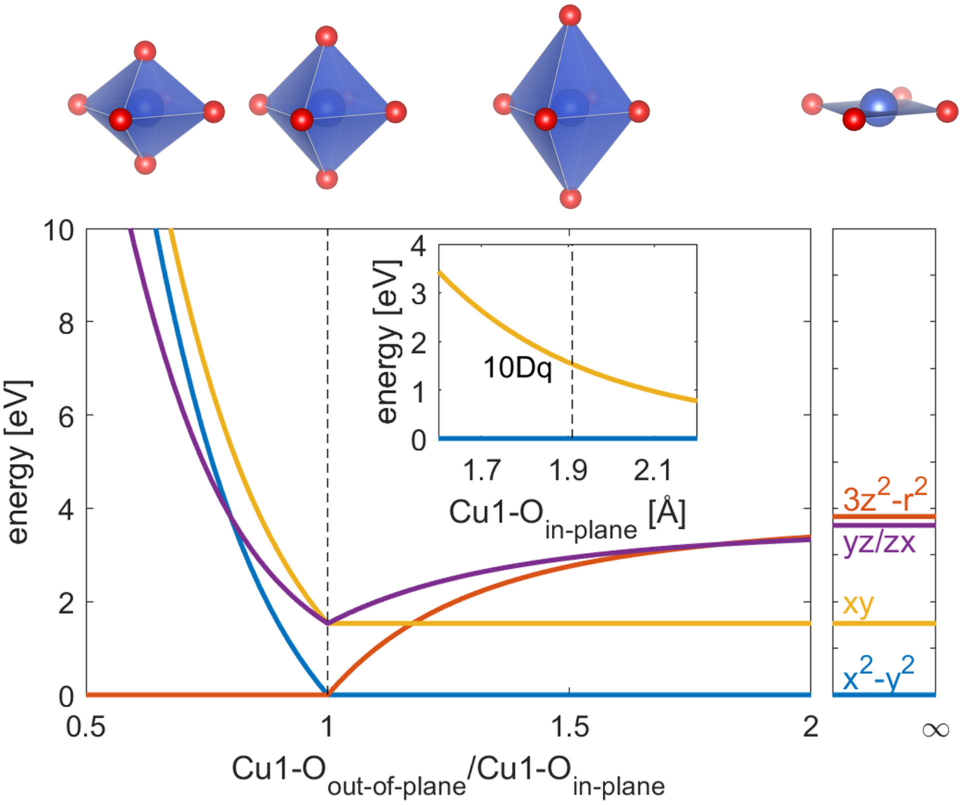

Figure 6.5: Energy of the Cu $3d$ states as a function of the out-of-plane/in-plane Cu-ligand distance [251]. In the inset we show the 10Dq energy as a function of the in plane Cu1-O distances.

states were calculated assuming an hydrogen-like picture with an effective natural charge Z such as 10Dq = 1.7 eV when the Cu1-O$_{\text{in-plane}}$ distance is 1.91 Å, as in LCO. This model gives a qualitatively picture of the energy of the Cu $3d$ states, since BCO should be characterized by a symmetry lower than D_{4h}, as it will become clearer in the following.

However, Figure 6.5 briefly summarizes the consideration previously made about the discussion of the RIXS spectra reported in Figure 6.4, where we used the energy of the dd excitations to infer about the local Cu coordination. The energy of the $3d$ states can be easily seen in the following way: in the case of compressed octahedron, the ground state has a $d_{3z^2-r^2}$ symmetry, as suggested for BCO in Ref. [12]. Whereas for an elongated octahedron (Cu1-O$_{\text{out-of-plane}}$ >Cu1-O$_{\text{in-plane}}$ distances), the ground state is characterized by a $d_{x^2-y^2}$ symmetry with the energy of the other d states that is strongly affected by the effective Cu1-O$_{\text{out-of-plane}}$/Cu1-O$_{\text{in-plane}}$ ratio. In this configuration, the theoretical model adopted in Ref. [251] confirms that the energy of the

$d_{3z^2-r^2}$ and the two-fold degenerate $d_{xz/yz}$ states is mostly influenced by the Cu-$O_{\text{out-of-plane}}$ distance. In fact, the energy of *dd* excitations in cuprates qualitatively follows the energy diagram reported in Figure 6.5 [11]. Whereas the 10Dq energy (energy difference between the $d_{x^2-y^2}$ and d_{xy} orbitals) is mostly dictated by the Cu1-$O_{\text{in-plane}}$ distance, as reported in the inset of Figure 6.5.

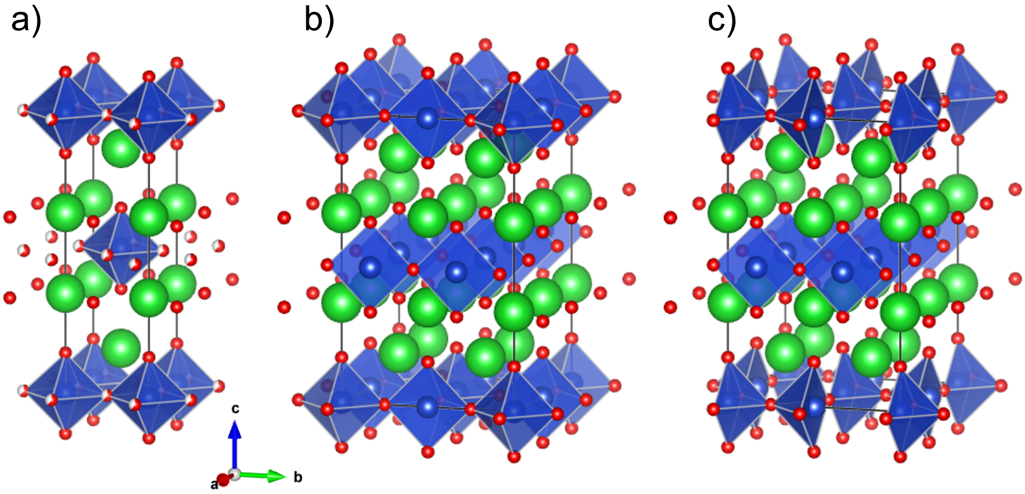

Figure 6.6: (a) Crystal structure of BCO as reported in Ref. cite??. (b) and (c), crystal structure of BCO as proposed in this work.

Space group : $I4/mmm$ (# 139)
$a = b = 4.003$ Å, $c = 12.942$ Å

label	symbol	mult.	Wyckoff	x	y	z	occupancy
Ba1	Ba	4	e	0.000	0.000	0.356	1.000
Cu1	Cu	2	a	0.000	0.000	0.000	1.000
O1	O	4	e	0.000	0.000	0.144	1.000
O2	O	4	c	0.000	0.500	0.000	0.625

Table 6.1: Principal parameters for the crystal structure of BCO as reported in Ref. [254] and shown in Figure 6.6(a).

For a nominal $\delta = 0.25$ stoichiometry the in-plane oxygens have a fractional occupancy of 62.5%, *i.e.* the Cu ions are coordinated to 4.5 randomly distributed oxygens, on average. However, disorder is known to broaden the *dd* excitation spectrum [60], such as in the case of LSCO, so the observation ii) of sharper crystal-field excitations in the RIXS spectrum of BCO does not seem to be consistent with a highly disordered system. Moreover, the average coordination of Cu imposes that a large number of CuO_4 plaquettes are formed in BCO, therefore contributing to the RIXS spectrum with an excitation at high energy losses ($\gtrsim 2.5$ eV), similarly to the $d_{3z^2-r^2}$ transition in CCO. The observation iii) of a very symmetric line shape excludes the presence of such a high energy peak, therefore suggesting that the Cu ions have a coordination number larger than 4.

Recently, Liu *et al.* [253] confirmed that oxygen vacancies prefer to reside in the planar rather than the apical sites, but suggested alternative, more stable crystals structures; in particular, they considered a $2 \times 2 \times 1$ supercell and calculated the energies associated to 26 possible crystal structures with various arrangements of 6 oxygen vacancies (corresponding to a $\delta = 0.25$ phase): they find that the most favorable structures contain 6 and 4 oxygens within layers at fractional coordinates $z = 0$ and $z = 0.5$, respectively, but none of them satisfies the structural constraints imposed by our XAS and RIXS measurements. Based on their results, we propose two alternative crystal structures for BCO as shown in Figure 6.6(b) and (c). The two structures have the following characteristics in common: i) they contain 6 and 4 oxygens within layers at fractional coordinates $z = 0$ and $z = 0.5$, respectively, as prescribed by theoretical calculations; ii) they feature two, inequivalent Cu sites. In particular, we tentatively distinguish between Cu^{2+} and Cu^{3+} within the $z = 0$ and $z = 0.5$ layers, respectively; iii) Cu^{2+} ions, contributing to the RIXS spectra of Figure 6.4, are coordinated in pyramids, while Cu^{3+} ions (which corresponds to Cu $3d^8$ or Cu $3d^9\underline{L}$), silent for RIXS, are coordinated in plaquettes. The two structures only differs in the relative orientation between pyramids and plaquettes in the $z = 0$ and $z = 0.5$ layers. Tables 6.2 and 6.3 report additional information about the crystal structures we propose for BCO.

We note that the crystal structure originally proposed for BCO was obtained by fitting the powder x-ray diffraction (pXRD) pattern [12]. The corresponding simulated pXRD pattern is reported in Figure 6.9 as a solid blue line, which we use as a reference for comparison with the simulated pXRD patterns of the crystal structures we proposed in this work: it turns out that the pXRD patterns of the crystal structures reported in 6.6(a), (b) and (c) largely overlap. When the intensities are plotted on a logarithmic scale (inset), little discrepancies can be appreciated, but only below the detectability limit of the pXRD experiment (red line).

Having established the crystal structure of BCO, we finally discuss the low-energy excitations in Figure 6.8. The RIXS spectrum is simultaneously fit to three symmetrical, energy resolution-limited curves (grey lines) and one asymmetrical curve (dashed red line); in agreement with existing literature on cuprates [77, 84], the peaks at 60 and 110 meV are tentatively assigned to

Space group : $Cmmm$ (# 65)
$a = b = 8.006$ Å, $c = 12.942$ Å

label	symbol	mult.	Wyckoff	x	y	z	occupancy
Ba1	Ba	8	n	0.000	0.250	0.144	1.000
Ba2	Ba	8	o	0.750	0.000	0.357	1.000
Cu1	Cu	4	g	0.750	0.000	0.000	1.000
Cu2	Cu	4	j	0.000	0.250	0.500	1.000
O1	O	2	a	0.000	0.000	0.000	1.000
O2	O	4	e	0.250	0.250	0.000	1.000
O3	O	8	o	0.750	0.000	0.143	1.000
O4	O	8	n	0.000	0.250	0.359	1.000
O5	O	2	d	0.000	0.000	0.500	1.000
O6	O	2	c	0.500	0.000	0.500	1.000

Table 6.2: Principal paramaters for the crystal structure of BCO as proposed in this work and shown in Figure 6.6(b).

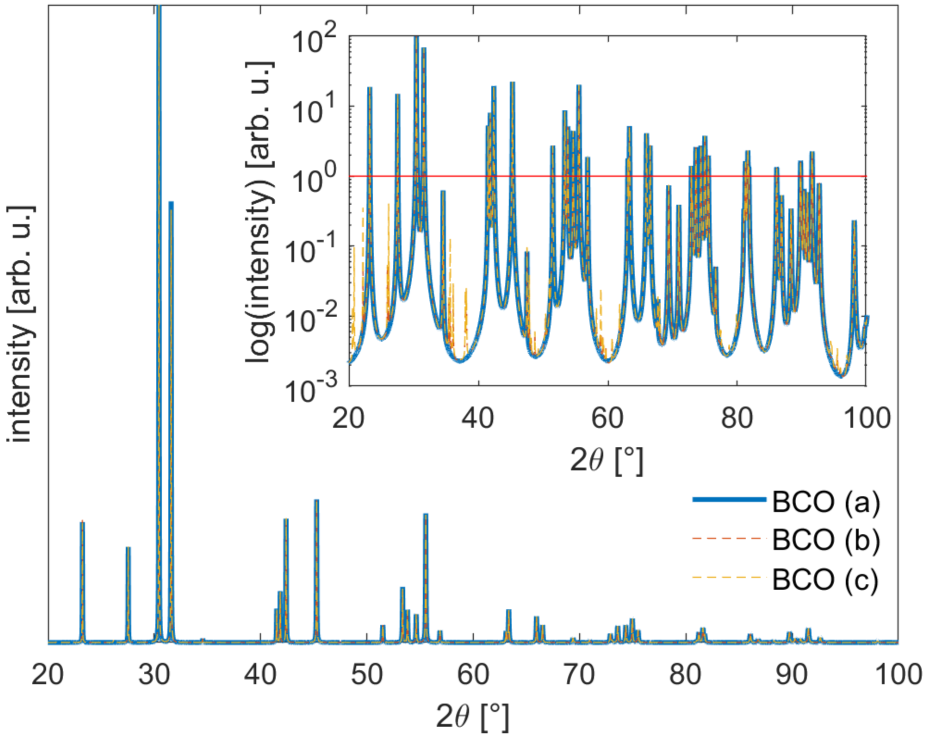

Figure 6.7: Simulated pXRD patterns for the crystal structures reported in Figure 6.6(a), (b) and (c).

Space group : *Cmmm* (# 65) $a = b = 8.006$ Å, $c = 12.942$ Å							
label	symbol	mult.	Wyckoff	x	y	z	occupancy
Ba1	Ba	8	o	0.250	0.000	0.144	1.000
Ba2	Ba	8	n	0.000	0.750	0.357	1.000
Cu1	Cu	4	i	0.000	0.750	0.000	1.000
Cu2	Cu	4	h	0.250	0.000	0.500	1.000
O1	O	4	e	0.250	0.250	0.000	1.000
O2	O	2	a	0.000	0.000	0.000	1.000
O3	O	8	n	0.000	0.750	0.143	1.000
O4	O	8	o	0.250	0.000	0.359	1.000
O5	O	4	f	0.250	0.250	0.500	1.000

Table 6.3: Principal paramaters for the crystal structure of BCO as proposed in this work and shown in Figure 6.6(c).

phonons and the peak at 200 meV to magnetic excitations (paramagnons)[5, 22]. Based on this interpretation, we will try in the following to give an estimate of magnetic interactions in BCO.

The *ab*-plane crystal structure of BCO is shown in the inset of Figure 6.9(b), where Cu-O-Cu super-exchange paths exist between nearest-neighbour Cu^{2+} ions along three bonds, only. The fourth magnetic bond is broken by the systematic absence of oxygen ions, thus preventing the system from forming the square magnetic lattice common to all cuprates. Magnetic excitations are in general highly dispersive, *i.e.* their energy depends on the magnitude and orientation of the transferred momentum, so precautions should be taken before drawing conclusions on magnetic interactions because, for a powder sample, the RIXS signal is averaged over the fraction of reciprocal space accessible by the available transferred momentum.

Assuming an isotropic (Heisenberg) antiferromagnetic coupling J between the nearest-neighbor spins $^1/_2$, we calculated the structure factor of magnetic excitations using linear spin wave theory, as implemented in SpinW [255]. The results are reported in Figure 6.9: the momentum transfer dependence of the magnetic structure factor for a powder sample is shown in panel (a) to be bounded at $1.5J$, as expected; a cut at 0.91 Å^{-1} momentum transfer, corresponding to performing RIXS at $2\theta = 150°$ scattering angle, as in our experiment, is reported in panel (b) and mostly consists of a single peak at an energy of $1.5J$. The comparison with our RIXS data, then, suggests a superexchange coupling constant $J \approx 130$ meV, in line with the magnitude of the antiferromagnetic magnetic interaction in most cuprates.

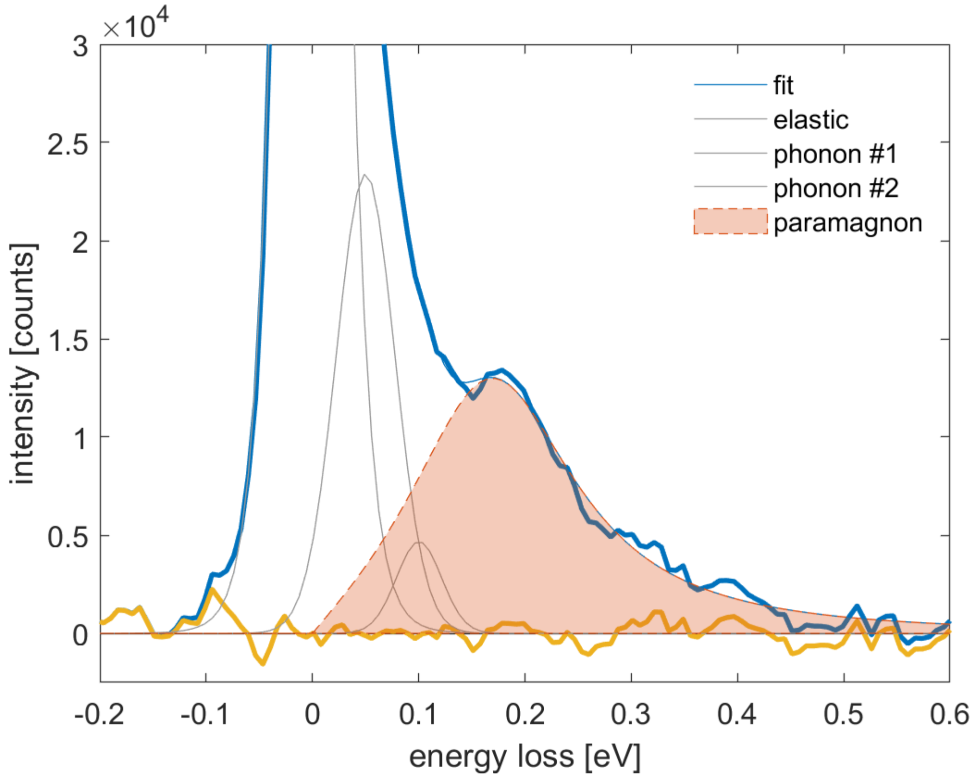

Figure 6.8: Close-up view of the RIXS spectrum of powder BCO measured at 936.7 eV incident photon energy (solid blue line) and its fit to an elastic line, two low-energy modes tentatively assigned to phonons (grey lines) and an asymmetric paramagnetic contribution (dashed red line with shaded area).

6.5 Conclusions

In our work, we probe the electronic structure of BCO by combining XAS and RIXS techniques. We argue that our measurements are inconsistent with the crystal structure previously proposed for BCO and propose an alternative structure that is compatible with both previous pXRD measurements and recent theoretical calculations. The proposed structure features two inequivalent Cu sites and naturally justifies the double peak structure in the XAS profile. Moreover, the systematic vacancies of oxygens in the $z = 0$ layer explains the absence of a high energy crystal field excitation in the RIXS spectra and leads to an estimate of the magnetic interactions in BCO in line with most common cuprates.

We have thus demonstrated an alternative use of XAS and RIXS, which were employed to set constraints on the plausible crystal structure of a recently synthesized cuprate system. Unfortunately, our present experimental

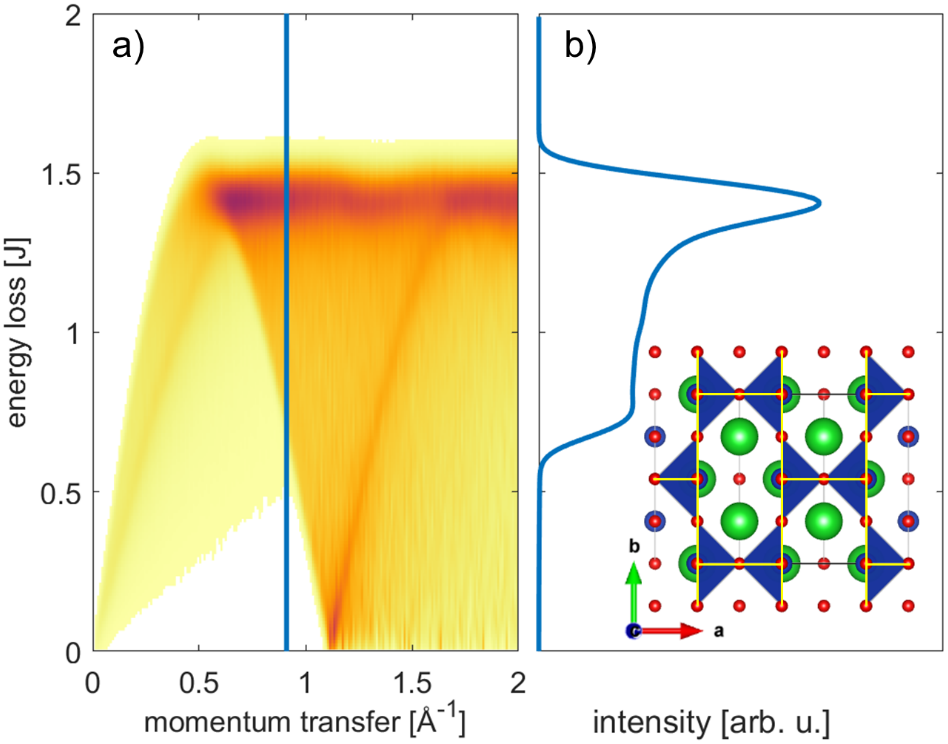

Figure 6.9: (a) Simulated momentum dependence of the magnetic structure factor and (b) its cut at 0.91 Å^{-1}, corresponding to scattering angles of $\theta = 150°$ for powder BCO. The considered nearest-neighbours superxchange interactions can be seen from the *ab*-plane crystal structure of BCO, also shown.

data on powder BCO are insufficient to provide information about the ground state symmetry, but will possibly serve as a basis for future investigations on single crystal BCO samples.

Conclusions

This thesis, besides presenting some important Cu L_3 RIXS results on cuprates obtained in the conventional way, *i.e.*, by summing over the polarizations of the scattered photons, presents a comprehensive review of polarization-resolved RIXS measurements. The experiments were carried out with the ERIXS spectrometer at the new ID32 beamline of the ESRF The European Synchrotron, an instrument that, since 2015, has set new standards in high resolution soft X-ray RIXS: higher energy resolution, full control of the scattering geometry with diffraction quality standards, and linear polarization analysis of the scattered photon.

This thesis work reports the first systematic high-resolution polarization resolved RIXS study of low energy (magnons and phonons) and orbital excitations in the high Tc superconductor $Nd_2BaCu_3O_{6+\delta}$, which sereve also as a prove of the capability and reliability of polarimetric measurements. Here we used a pure ionic picture to study the experimental results calculating the theoretical RIXS cross sections for all the possible excitations. Furthermore, we are able to describe and interpret the different polarized resolved contributions in terms of Stokes parameters. The thesis presents also other examples where the full polarization analysis has significantly contributed to the interpretation of the normal RIXS spectra. For example, polarization-resolved measurements confirmed the charge nature of the order parameter discovered in overdoped $(Bi,Pb)_2(Sr,La)_2CuO_{6+\delta}$, the assignment to spin excitations of the enhanced dynamic response at the charge order vector in $Nd_{2-x}Ce_xCuO_4$ and finally the confirmation of the charge nature of the fast-dispersing zone-center excitations in $La_{2-x}Ce_xCuO_4$. The polarization analysis has been applied also to systems other than cuprates, such as $CeRh_2Si_2$, where the use of the polarimeter allowed to assign the energy and symmetry of *ff* excitations.

The thesis presents also the study of the momentum-dependence of orbital excitations in RIXS spectra of 1D and 2D cuprates. In correlated oxides electronic excitations tend to have localized a character and are usually described by orbital and spin quantum numbers in a symmetry adapted atomic picture: usually orbital excitations do not disperse, irrespective of their spin character. On the contrary, pure spin excitations have collective nature: spin-waves (or magnons) display large energy dispersion vs momentum. Theory predicts that at low dimensionality orbital excitations can split their orbital and spin components, giving rise to complex dispersion. So far orbital excitations with sizeable dispersion had been observed and theoretically analyzed only in quasi-1D materials. We have investigated the Cu L_3-edge RIXS spectra of the quasi-1D AF Ca_2CuO_3, which display two dispersive orbital excitations. Unexpectedly, also the data of the 2D infinite layer $CaCuO_2$ show a non-negligible dispersion of the dd excitations, a phenomenon that cannot be explained by the model used in the 1D case.

Finally, we used Cu L_3-edge RIXS to directly probe the orbital structure and the energy scale of the in-plane exchange interaction of a polycrystalline $Ba_2CuO_{3+\delta}$ sample. This novel cuprate superconductor has recently challenged the universality of the assumption where insulating parent compounds are characterized by a $d_{x^2-y^2}$ ground state, giving rise to a *d*-wave superconductivity upon doping. In fact, it has been proposed that $Ba_2CuO_{3+\delta}$ is presumably characterized by a predominant $3d_{3z^2-r^2}$ or a markedly mixed ($3d_{3z^2-r^2}$-$3d_{x^2-y^2}$) character of the ground state. Our experimental results suggest, partially in agreement with previous theoretical predictions, that the crystalline structure of $Ba_2CuO_{3+\delta}$ is made by two inequivalent Cu sites with the oxygen vacancies lying in the planar CuO_2 planes. Despite this fact, the in-plane magnetic interaction strength is similar to the one displayed by other cuprates. We have thus demonstrated that, by exploiting the capabilities offered by RIXS to probe a specific atomic species, it is also possible to infer about the crystal structure and the atomic arrangement in materials such as cuprates. However, our experimental data are insufficient to obtain crucial information on the energy and symmetry of the Cu $3d$ states in this novel material, and for this scope crystalline (or thin films) samples are needed.

In the last decade RIXS has become one of the most used techniques for the study of strongly correlated electron systems. ERIXS at the ID32 beamline of the ESRF has set a new standard and is being followed by equally or even more ambitious projects at storage rings and free electron lasers. The future developments in the RIXS instrumentations will bring to a better energy resolution, count rate and sample environments: all together, these new achievements will lead to study with more accuracy cuprates and other interesting and fascinating materials. In this thesis work we have shown another possible use of this technique, as demonstrated in the last Chapter. Here we infer about the crystal structure of the novel $Ba_2CuO_{3+\delta}$ superconductor by carefully studying the energy of the different spectral features. In the hard X-rays regime this kind of investigation is routinely performed because, despite providing more indirect information than soft-RIXS, it is easy to carry out especially in the case of non 'ideal' samples.

This thesis provides useful contents for both the two future applications of high-resolution RIXS. In fact, we have shown how this technique can be useful for the investigation of the low-energy physics (superconductivity, spin orders, charge and orbitals) and of the chemistry of materials (crystalline field). Finally, the possibility to infer about the polarization of the scattered photons can provide extra information to disambiguate a specific problem.

Appendix A

Theoretical model and methods

Ca_2CuO_3 is a strong Mott insulator, with one hole in the $|x^2-y^2\rangle$ orbital. Hence spin and orbital excitations are described by a Kugel-Khomskii Hamiltonian with the generic form described by equation (5.1). The operators $A(T_i^\beta, T_j^\alpha)$ and $K(T_i^\beta, T_j^\alpha)$ describe the dynamics of the orbital degrees of freedom and are obtained by the second order perturbation theory from the multi-orbital Hubbard model, assuming: 1.) dominant onsite Coluomb repulsion ('Hubbard' U is much larger than the hopping between the ground state orbital t_1), i.e. omitting charge fluctuations; 2.) strong crystal field splitting, to polarize the ground state in the lower orbital; and 3.) one excited orbital at most. They read

$$\begin{aligned} A(T_i^\beta, T_j^\alpha) = {} & \frac{2t_1^2}{U}\frac{1}{1-\left(\frac{J_H}{U}\right)^2}\left(T_i^z-\frac{1}{2}\right)\left(T_j^z-\frac{1}{2}\right)+ \\ & +\frac{2t_1t_2}{U'}\frac{1}{1-\left(\frac{J_H}{U'}\right)^2}\left[T_i^+T_j^-+\text{h.c.}\right]+ \\ & +\frac{(t_1^2+t_2^2)}{U'}\frac{\frac{J_H}{U'}}{1-\left(\frac{J_H}{U'}\right)^2}\left[\left(T_i^z-\frac{1}{2}\right)\left(T_j^z+\frac{1}{2}\right)+(i\leftrightarrow j)\right], \end{aligned} \tag{2}$$

and

$$\begin{aligned} K(T_i^\beta, T_j^\alpha) = {} & -\frac{2t_1^2}{U}\frac{1}{1-\left(\frac{J_H}{U}\right)^2}\left(T_i^z-\frac{1}{2}\right)\left(T_j^z-\frac{1}{2}\right)+ \\ & +\frac{2t_1t_2}{U'}\frac{\frac{J_H}{U'}}{1-\left(\frac{J_H}{U'}\right)^2}\left[T_i^+T_j^-+\text{h.c.}\right]+ \\ & +\frac{t_1^2+t_2^2}{U'}\frac{1}{1-\left(\frac{J_H}{U'}\right)^2}\left[\left(T_i^z-\frac{1}{2}\right)\left(T_j^z+\frac{1}{2}\right)+(i\leftrightarrow j)\right]. \end{aligned} \tag{3}$$

Here, t_1 and t_2 are the hopping parameters of the ground state, *i.e.* between neighboring $|x^2-y^2\rangle$ orbitals, and the excited orbital, *i.e.* $|xy\rangle$, $|yz\rangle$ or $|xz\rangle$, respectively. ($\vec{S}_i$, T_i^α and all other model parameters are defined in the main text.) As an approximation we set the inter-orbital repulsion $U' = U - 2J_H$, as in the case of the atomic orbitals subject to a spherically symmetric potential [256]. Note however, that a small departure from this relation does not alter the results significantly [216].

To calculate *dd*-excitation spectrum probed by RIXS we define the spectral function for orbital excitations and spin-orbital excitations. The orbital spectral function is

$$O(q,\omega) = \frac{1}{\pi}\,\mathrm{Im}\,\langle \mathrm{gs}|\, T^x_{-k} \frac{1}{\omega + E_{\mathrm{gs}} - H - i\Gamma_L} T^x_k\, |\mathrm{gs}\rangle\,, \tag{4}$$

where T_k^x is the Fourier transform of T_i^x, $|\mathrm{gs}\rangle$ is the ground state of Eq. (5.1), and Γ_L is the Lorentzian broadening to mitigate finite-size artefacts. We set $\Gamma_L = 0.06\,\mathrm{eV}$. The spin-orbital excitation function $SO(\mathbf{q},\omega)$ is defined analogously, with T_i^x replaced by $S_i^z T_i^x$.

We calculate the excitation spectra using exact diagonalization in combination with the spin cluster perturbation theory [257] on a 20 site chain. Additionally, we derive in Appendix B an effective Hamiltonian, which yields an analytic relation between bandwidth of the excitation and the Hund's coupling.

Appendix B

Effective Hamiltonian for spin-orbital excitation

Here we derive an effective Hamiltonian, which captures accurately the spin-orbital excitation spectrum $SO(q,\omega)$ of Hamiltonian (5.1) and which can be mapped onto the t–J model. The latter enables us to find an analytic relation between the Hund's coupling and the bandwidth W of the excitation spectrum.

The ground state of Hamiltonian (5.1) is antiferromagnetically (AF) and ferro-orbitally (FO) ordered. Hence we approximate the ground state $|\mathrm{gs}\rangle$ at a bond $\langle i,j\rangle$ as spin-singlet with an FO order

$$|\mathrm{gs}\rangle \propto \left|\begin{smallmatrix} - & - \\ \uparrow & \downarrow \end{smallmatrix}\right\rangle - \left|\begin{smallmatrix} - & - \\ \downarrow & \uparrow \end{smallmatrix}\right\rangle . \tag{5}$$

The excited state for $SO(q,\omega)$ excitation is then given by

$$S_j^z T_j^+ \, |\mathrm{gs}\rangle \propto \left|\begin{smallmatrix} - & \downarrow \\ \uparrow & - \end{smallmatrix}\right\rangle + \left|\begin{smallmatrix} - & \uparrow \\ \downarrow & - \end{smallmatrix}\right\rangle . \tag{6}$$

Thus, we are now allowed to skip the parts in Hamiltonian (5.1) which hinder the mapping onto a t–J model. This yields an effective Hamiltonian of the form (5.1), with the modified orbital operators

$$\begin{aligned}\widetilde{A}(T_i^\beta, T_j^\alpha) = {} & \frac{2t_1^2}{U}\frac{1}{1-\left(\frac{J_H}{U}\right)^2}\left(T_i^z-\frac{1}{2}\right)\left(T_j^z-\frac{1}{2}\right)+ \\ & +\frac{2t_1t_2}{U'}\frac{1}{1-\frac{J_H}{U'}}\left[T_i^+T_j^- + \mathrm{h.c.}\right] ,\end{aligned} \tag{7}$$

and

$$\begin{aligned}\widetilde{K}(T_i^\beta, T_j^\alpha) = &-\frac{2t_1^2}{U}\frac{1}{1-\left(\frac{J_H}{U}\right)^2}\left(T_i^z-\frac{1}{2}\right)\left(T_j^z-\frac{1}{2}\right)+\\ &+\frac{t_1^2+t_2^2}{U'}\frac{1}{1-\frac{J_H}{U'}}\left[\left(T_i^z-\frac{1}{2}\right)\left(T_j^z+\frac{1}{2}\right)+(i\leftrightarrow j)\right].\end{aligned} \tag{8}$$

Note that the effective Hamiltonian can now be mapped onto a t–J model [214].

The mapping on the t–J model gives analytic expressions for upper and lower boundaries of the spinon-orbiton continuum [258, 259], which read

$$\begin{aligned}\epsilon_{\mathrm{lo}}(k) = &\Delta+\mathcal{J}-2\frac{t_1^2+t_2^2}{U'}\frac{1}{(1-J_H/U')}-\\ &\begin{cases}\sqrt{\mathcal{J}^2+4\tilde{t}^2-4\tilde{t}\mathcal{J}\cos(k)} & ,k<k_0\\ 2\tilde{t}\sin(k) & ,k>k_0\end{cases},\end{aligned} \tag{9a}$$

$$\begin{aligned}\epsilon_{\mathrm{up}}(k) = &\Delta+\mathcal{J}-2\frac{t_1^2+t_2^2}{U'}\frac{1}{(1-J_H/U')}+\\ &\begin{cases}\sqrt{\mathcal{J}^2+4\tilde{t}^2-4\tilde{t}\mathcal{J}\cos(k)} & ,k>k_0\\ 2\tilde{t}\sin(k) & ,k<k_0\end{cases},\end{aligned} \tag{9b}$$

Here k_0 is given by $\cos(k_0)=\mathcal{J}/(2\tilde{t})$ and the rescaled hopping and rescaled superexchange constants are given by

$$\tilde{t}=2\frac{t_1t_2}{U'}\frac{1}{(1-J_H/U')} \quad \text{and} \quad \mathcal{J}=J_{\mathrm{AF}}\frac{1}{1-(J_H/U)^2} \tag{10}$$

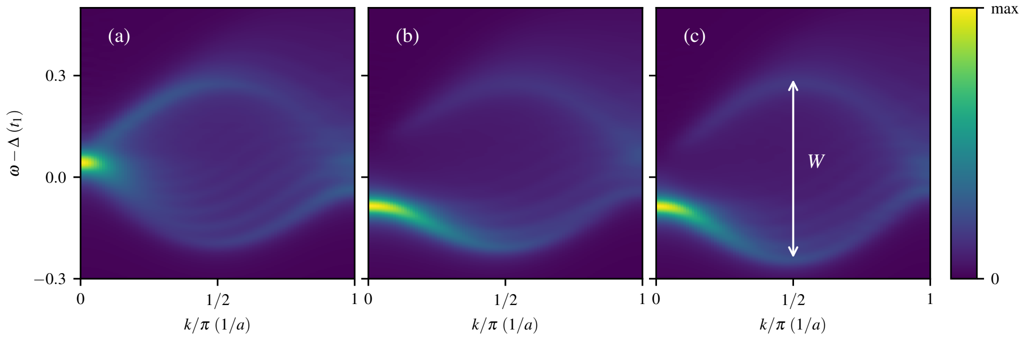

Figure 10: Orbital (a) and spin-orbital (b) spectral function of the full Hamiltonian. (c) Spin-orbital spectral function of the effective Hamiltonian. W indicates the bandwidth of the excitation. Parameters of d_{yz} orbital are used.

respectively. The bandwidth is then given by

$$W = \epsilon_{\text{up}}(k = \pi/2) - \epsilon_{\text{lo}}(k = \pi/2) = 4\tilde{t}. \tag{11}$$

This relation can be used to extract Hund's coupling from the bandwidth of the excitation spectrum.

Figure 10 shows the orbital (a) and the spin-orbital (b) excitation spectrum of the full Hamiltonian as well as the spin-orbital (c) excitation spectrum of the effective Hamiltonian, for parameters modeling the yz orbital excitation in Ca21. The effective Hamiltonian reproduces the shape as well as the intensity of the spin-orbital excitations of the full Hamiltonian. RIXS measures a combination of orbital and spin-orbital excitation, however due to the same bandwidth of $O(k,\omega)$ and $SO(k,\omega)$ this does not affect the expression of the bandwidth (11).

Acknowledgments

Undertaking this PhD has been a truly life-changing experience for me and it would not have been possible to do without the support and guidance that I received from many people.

First of all my deepest gratitude goes to my supervisor Prof. Giacomo Ghiringhelli and to the senior Prof. (and Emeritus of the ESRF) Lucio Braicovich. For them I have the greatest respect, not only as a scientists but also for the persons they are. They represented a continuous and always available reference for me and almost everything I know in physics, I owe to them. It has been more than a pleasure to share with them endless days at the beamlines and nice scientific discussions: every time I was impressed by their motivations and unsurpassed knowledge. Their enthusiasm and dedication have been a constant source of inspiration as a driving force to brilliant achievements. I would like to pay my special regards to Giacomo for the great opportunity he gave me to do the PhD at Politecnico di Milano, and for trusting me. Thanks for encouraging me everyday to do my best. This thesis would not have been possible without his timely suggestions despite of his busy schedule.

I am particularly indebted to Prof. Marco Moretti (sometimes Sala). Everything started 5 years ago, when he hosted me at the ID20 beamline of the ESRF in order to develop my master thesis. He introduced me to the wonderful world of resonant inelastic X-ray scattering and transition metal oxides, enlightening me the first glance of research. Thanks for his guidance, support, and above all friendship.

I thank my fellow office-mates and other members of the Milano RIXS group Ying Ying Peng, Matteo Rossi, Riccardo Arpaia, Giovanni De Vecchi, Mattia Pagetti and Leonardo Martinelli for the stimulating discussions, for

the sleepless nights we were working together, and for all the fun we have had (especially drinking Chartreuse in Grenoble) in the last years.

I would like to thank Dr. Nick Brookes, who kindly hosted me for seven months at the ID32 beamline. Thanks for all the time he devoted to me during endless beam-times, I really appreciated his continuous support. And of course, thanks to all the ID32 beamline staff (Kurt, Flora, Andrea) for endless coffee and nice discussions after every delicious lunch at the canteen. A very special thanks goes to the best local contact (and friend) that I could ever had, Davide. Thanks for his assistance (even in remote) during all my beam-times, and as a reward, thanks for the best croissants that he always brought to me after nights spent performing experiments.

Thanks to all people I met at the ESRF and in Grenoble, in particular Emilie R. and the other PhD students who joined with me the Hercules school. I can not forget every moment spent with you.

I wish to thank all the people whose assistance was a milestone in the completion of the projects presented in this thesis. Thanks to Jonas Heverhagen, Maria Daghofer, Krzysztof Wohlfeld, Enrico Schierle, Marco Salluzzo, Daniele Di Castro, Wei Sheng Lee, Marco Grilli, Floriana Lombardi, Hu Miao, Mark Dean, Jonathan Pelliciari, Riccardo Comin, Hunho Kim, Matteo Minola, Matthieu Le Tacon and all the other several collaborators. Without their passionate participation and input, all the results obtained in the last years could not have been successfully conducted. Thanks for the fruitful and pleasant collaborations.

I would like to express my sincere gratitude to Prof. Matthieu Le Tacon and Prof. Krzysztof Wohlfeld to agreed to referee this thesis work and honor me with their presence in the PhD committee.

Thanks to my travel companions in this years, in particular Cameron Dashwood and Andrea Amorese, for giving me the possibility to really enjoy the conferences in the United States. From San Francisco to New York, I will always remember the lovely days spent together.

Very special thanks go to Matteo Minola, not only a colleague, but also a brother for me. We shared unforgettable moments, from interminable beam-times spent side by side to extraordinary moments spent all over around the world. From him I learned how beautiful is to travel and discover new places and cultures. Thanks for the continuous help, for all valuable advices “to survive”, to be my best English teacher and for always making me feel so welcome in Stuttgart.

I would particularly like to thank my friends of a life, Rasco, Bobo, Andre, Otto, Turo, Teo, Ale, Ste, Anza, Facco, Chiara and Clara, always available and ready to give me a smile, especially in tough periods.

Last but not the least, I would like to thank my family: my parents and to my sister and her beautiful family, for supporting me spiritually throughout these years and with my life in general. Thanks for always believing in me and encouraging me to follow my dreams.

And finally, Valentina. Thanks for all your support and unconditional love, without which everything would have been much more difficult. You have been amazing, always by my side even when I was on the other side of the world. I can't thank you enough for encouraging me throughout this experience.

Bibliography

[1] C. Dallera, E. Puppin, G. Trezzi, N. Incorvaia, A. Fasana, L. Braicovich, N. B. Brookes, and J. B. Goedkoop, "Soft X-ray emission spectroscopy at ESRF beamline 26 based on a helical undulator," Journal of Synchrotron Radiation **3**, 231 (1996).

[2] M. Dinardo, A. Piazzalunga, L. Braicovich, V. Bisogni, C. Dallera, K. Giarda, M. Marcon, A. Tagliaferri, and G. Ghiringhelli, "Gaining efficiency and resolution in soft X-ray emission spectrometers thanks to directly illuminated CCD detectors," Nuclear Instruments and Methods in Physics Research **570**, 176 (2007).

[3] G. Ghiringhelli, A. Piazzalunga, C. Dallera, G. Trezzi, L. Braicovich, T. Schmitt, V. Strocov, R. Betemps, L. Patthey, X. Wang, and M. Grioni, "SAXES, a high resolution spectrometer for resonant X-ray emission in the 400–1600 eV energy range," Review of Scientific Instruments **77**, 113108 (2006).

[4] L. J. P. Ament, M. van Veenendaal, T. P. Devereaux, J. P. Hill, and J. van den Brink, "Resonant inelastic X-ray scattering studies of elementary excitations," Review of Modern Physics **83**, 705 (2011).

[5] L. Braicovich, J. van den Brink, V. Bisogni, M. M. Sala, L. J. P. Ament, N. B. Brookes, G. M. De Luca, M. Salluzzo, T. Schmitt, V. N. Strocov, and G. Ghiringhelli, "Magnetic excitations and phase separation in the underdoped $La_{2-x}Sr_xCuO_4$ superconductor measured by resonant inelastic X-ray scattering," Physical Review Letters **104**, 077002 (2010).

[6] J. G. Bednorz and K. A. Müller, “Possible high-T_c superconductivity in the Ba-La-Cu-O system,” Zeitschrift für Physik B Condensed Matter **64**, 189 (1986).

[7] B. Keimer, S. A. Kivelson, M. R. Norman, S. Uchida, and J. Zaanen, “From quantum matter to high-temperature superconductivity in copper oxides,” Nature **518**, 179 (2014).

[8] N. B. Brookes, F. Yakhou-Harris, K. Kummer, A. Fondacaro, J. C. Cezar, D. Betto, E. Velez-Fort, A. Amorese, G. Ghiringhelli, L. Braicovich, R. Barrett, G. Berruyer, F. Cianciosi, L. Eybert, P. Marion, P. van der Linden, and L. Zhang, “The beamline ID32 at the ESRF for soft X-ray high energy resolution resonant inelastic X-ray scattering and polarisation dependent X-ray absorption spectroscopy,” Nuclear Instruments and Methods A **903**, 175 (2018).

[9] G. G. Stokes, “On the composition and resolution of streams of polarized light from different sources,” Transactions of the Cambridge Philosophical Society **9** (1851).

[10] M. J. Walker, “Matrix calculus and the Stokes parameters of polarized radiation,” American Journal of Physics **22**, 170 (1954).

[11] M. Moretti Sala, V. Bisogni, C. Aruta, G. Balestrino, H. Berger, N. B. Brookes, G. M. De Luca, D. Di Castro, M. Grioni, M. Guarise, P. G. Medaglia, F. Miletto Granozio, M. Minola, P. Perna, M. Radovic, M. Salluzzo, T. Schmitt, K. J. Zhou, L. Braicovich, and G. Ghiringhelli, “Energy and symmetry of *dd* excitations in undoped layered cuprates measured by Cu L_3 resonant inelastic X-ray scattering,” New Journal of Physics **13**, 043026 (2011).

[12] W. M. Li, J. F. Zhao, L. P. Cao, Z. Hu, Q. Z. Huang, X. C. Wang, Y. Liu, G. Q. Zhao, J. Zhang, Q. Q. Liu, R. Z. Yu, Y. W. Long, H. Wu, H. J. Lin, C. T. Chen, Z. Li, Z. Z. Gong, Z. Guguchia, J. S. Kim, G. R. Stewart, Y. J. Uemura, S. Uchida, and C. Q. Jin, “Superconductivity in a unique type of copper oxide,” Proceedings of the National Academy of Sciences **116**, 12156 (2019).

[13] C. T. Chen, L. H. Tjeng, J. Kwo, H. L. Kao, P. Rudolf, F. Sette, and R. M. Fleming, “Out-of-plane orbital characters of intrinsic and doped holes in $La_{2-x}Sr_xCuO_4$,” Physical Review Letters **68**, 2543 (1992).

[14] A. P. Ramirez, “Colossal magnetoresistance,” Journal of Physics: Condensed Matter **9**, 8171 (1997).

[15] S.-W. Cheong and M. Mostovoy, "Multiferroics: a magnetic twist for ferroelectricity," Nature Materials **6**, 13 (2007).

[16] M. Imada, A. Fujimori, and Y. Tokura, "Metal-insulator transitions," Review of Modern Physics **70**, 1039 (1998).

[17] J. Bardeen, L. N. Cooper, and J. R. Schrieffer, "Theory of superconductivity," Physical Review **108**, 1175 (1957).

[18] Y. Y. Peng, G. Dellea, M. Minola, M. Conni, A. Amorese, D. D. Castro, G. M. D. Luca, K. Kummer, M. Salluzzo, X. Sun, X. J. Zhou, G. Balestrino, M. L. Tacon, B. Keimer, L. Braicovich, N. B. Brookes, and G. Ghiringhelli, "Influence of apical oxygen on the extent of in-plane exchange interaction in cuprate superconductors," Nature Physics **13**, 1201 (2017).

[19] M. A. G. Aranda, "Crystal structures of copper-based high-T_c superconductors," Advanced Materials **6**, 905 (1994).

[20] J. Ghijsen, L. H. Tjeng, H. Eskes, G. A. Sawatzky, and R. L. Johnson, "Resonant photoemission study of the electronic structure of CuO and Cu_2O," Physical Review B **42**, 2268 (1990).

[21] E. Dagotto, "Correlated electrons in high-temperature superconductors," Review of Modern Physics **66**, 763 (1994).

[22] M. L. Tacon, G. Ghiringhelli, J. Chaloupka, M. M. Sala, V. Hinkov, M. W. Haverkort, M. Minola, M. Bakr, K. J. Zhou, S. Blanco-Canosa, C. Monney, Y. T. Song, G. L. Sun, C. T. Lin, G. M. De Luca, M. Salluzzo, G. Khaliullin, T. Schmitt, L. Braicovich, and B. Keimer, "Intense paramagnon excitations in a large family of high-temperature superconductors," Nature Physics **7**, 725 (2011).

[23] M. Dean, G. Dellea, R. Springell, F. Yakhou-Harris, K. Kummer, N. Brookes, X. Liu, Y. Sun, J. Strle, T. Schmitt, L. Braicovich, G. Ghiringhelli, I. Bozovic, and J. P. Hill, "Persistence of magnetic excitations in $La_{2-x}Sr_xCuO_4$ from the undoped insulator to the heavily overdoped non-superconducting metal," Nature Materials **12**, 1019 (2013).

[24] C. L. Teske and H. Mller-Buschbaum, "Über ErdalkalimetallOxocuprate. II. Zur Kenntnis von Sr_2CuO_3," Z. Anorg. Allg. Chem. **371**, 325 (1969).

[25] M. Hjorth and J. Hyldtof, "Crystal structure of dicalcium cuprate Ca_2CuO_3," Acta Chemica Scandinavica **44** (1990), 10.3891/acta.chem.scand.44-0516.

[26] H. Rosner, H. Eschrig, R. Hayn, S.-L. Drechsler, and J. Málek, "Electronic structure and magnetic properties of the linear chain cuprates Sr_2CuO_3 and Ca_2CuO_3," Physical Review B **56**, 3402 (1997).

[27] H. Matsuzaki, H. Nishioka, H. Uemura, A. Sawa, S. Sota, T. Tohyama, and H. Okamoto, "Ultrafast charge and lattice dynamics in one-dimensional Mott insulator of CuO-chain compound Ca_2CuO_3 investigated by femtosecond absorption spectroscopy," Physical Review B **91**, 081114 (2015).

[28] K. I. Kugel' and D. I. Khomski, "The Jahn-Teller effect and magnetism: transition metal compounds," Soviet Physics Uspekhi **25**, 231 (1982).

[29] F. C. Zhang and T. M. Rice, "Effective Hamiltonian for the superconducting Cu oxides," Physical Review B **37**, 3759 (1988).

[30] H. Eskes and G. A. Sawatzky, "Tendency towards local spin compensation of holes in the high-T_c copper compounds," Physical Review Letters **61**, 1415 (1988).

[31] C. C. Tsuei and J. R. Kirtley, "Pairing symmetry in cuprate superconductors," Review of Modern Physics **72**, 969 (2000).

[32] D. A. Wollman, D. J. Van Harlingen, W. C. Lee, D. M. Ginsberg, and A. J. Leggett, "Experimental determination of the superconducting pairing state in YBCO from the phase coherence of YBCO-Pb dc SQUIDs," Physical Review Letters **71**, 2134 (1993).

[33] C. C. Tsuei, J. R. Kirtley, C. C. Chi, L. S. Yu-Jahnes, A. Gupta, T. Shaw, J. Z. Sun, and M. B. Ketchen, "Pairing symmetry and flux quantization in a tricrystal superconducting ring of $YBa_2Cu_3O_{7-\delta}$," Physical Review Letters **73**, 593 (1994).

[34] A. Mathai, Y. Gim, R. C. Black, A. Amar, and F. C. Wellstood, "Experimental Proof of a Time-Reversal-Invariant Order Parameter with a π shift in $YBa_2Cu_3O_{7-\delta}$," Physical Review Letters **74**, 4523 (1995).

[35] D. A. Wollman, D. J. Van Harlingen, J. Giapintzakis, and D. M. Ginsberg, "Evidence for $d_{x^2-y^2}$ pairing from the magnetic field modulation

of $YBa_2Cu_3O_7$-Pb Josephson junctions," Physical Review Letters **74**, 797 (1995).

[36] L. Liu, H. Yao, E. Berg, S. R. White, and S. A. Kivelson, "Phases of the infinite U Hubbard model on square lattices," Physical Review Letters **108**, 126406 (2012).

[37] P. A. Lee, N. Nagaosa, and X.-G. Wen, "Doping a Mott insulator: Physics of high-temperature superconductivity," Reiew of Modern Physics **78**, 17 (2006).

[38] M. Norman, H. Ding, M. Randeria, J. Campuzano, T. Yokoya, T. Takeuchi, T. Takahashi, T. Mochiku, K. Kadowaki, P. Guptasarma, and D. G. Hinks, "Destruction of the Fermi surface in underdoped high-T_c superconductors," Nature **392**, 157 (1998).

[39] T. Timusk and B. Statt, "The pseudogap in high-temperature superconductors: an experimental survey," Reports on Progress in Physics **62**, 61 (1999).

[40] J. M. Tranquada, B. J. Sternlieb, J. D. Axe, Y. Nakamura, and S. Uchida, "Evidence for stripe correlations of spins and holes in copper-oxide superconductors," Nature **375**, 561 (1995).

[41] K. Yamada, C. H. Lee, K. Kurahashi, J. Wada, S. Wakimoto, S. Ueki, H. Kimura, Y. Endoh, S. Hosoya, G. Shirane, R. J. Birgeneau, M. Greven, M. A. Kastner, and Y. J. Kim, "Doping dependence of the spatially modulated dynamical spin correlations and the superconducting-transition temperature in $La_{2-x}Sr_xCuO_4$," Physical Review B **57**, 6165 (1998).

[42] P. Abbamonte, A. Rusydi, S. Smadici, G. D. Gu, G. A. Sawatzky, and D. L. Feng, "Spatially modulated 'Mottness' in $La_{2-x}Ba_xCuO_4$," Nature Physics **1**, 155 (2005).

[43] T. Wu, H. Mayaffre, S. Krämer, M. Horvatić, C. Berthier, W. Hardy, R. Liang, D. Bonn, and M.-H. Julien, "Magnetic-field-induced charge-stripe order in the high-temperature superconductor π shift in $YBa_2Cu_3O_y$," Nature **477**, 191 (2011).

[44] T. Wu, H. Mayaffre, S. Krämer, M. Horvatić, C. Berthier, P. L. Kuhns, A. P. Reyes, R. Liang, W. Hardy, D. Bonn, and M. H. Julien, "Emergence of charge order from the vortex state of a high-temperature superconductor," Nature Communications **4**, 2113 (2013).

[45] G. Ghiringhelli, M. Le Tacon, M. Minola, S. Blanco-Canosa, C. Mazzoli, N. B. Brookes, G. M. De Luca, A. Frano, D. G. Hawthorn, F. He, T. Loew, M. M. Sala, D. C. Peets, M. Salluzzo, E. Schierle, R. Sutarto, G. A. Sawatzky, E. Weschke, B. Keimer, and L. Braicovich, "Long-range incommensurate charge fluctuations in $(\mathrm{Y,Nd})\mathrm{Ba_2Cu_3O_{7-\delta}}$," Science **337**, 821 (2012).

[46] Y. Y. Peng, M. Salluzzo, X. Sun, A. Ponti, D. Betto, A. M. Ferretti, F. Fumagalli, K. Kummer, M. Le Tacon, X. J. Zhou, N. B. Brookes, L. Braicovich, and G. Ghiringhelli, "Direct observation of charge order in underdoped and optimally doped $\mathrm{Bi_2(Sr,La)_2CuO_{6+\delta}}$ by resonant inelastic X-ray scattering," Physical Review B **94**, 184511 (2016).

[47] W. Tabis, Y. Li, M. Le Tacon, L. Braicovich, A. Kreyssig, M. Minola, G. Dellea, E. Weschke, M. Veit, M. Ramazanoglu, A. Goldman, T. Schmitt, G. Ghiringhelli, N. Barisic, M. Chan, C. J. Dorow, G. Yu, X. Zhao, B. Keimer, and M. Greven, "Charge order and its connection with Fermi-liquid charge transport in a pristine high-T_c cuprate," Nature Communications **5**, 5875 (2014).

[48] R. Comin, A. Frano, M. M. Yee, Y. Yoshida, H. Eisaki, E. Schierle, E. Weschke, R. Sutarto, F. He, A. Soumyanarayanan, Y. He, M. Le Tacon, I. S. Elfimov, J. E. Hoffman, G. A. Sawatzky, B. Keimer, and A. Damascelli, "Charge order driven by Fermi-arc instability in $\mathrm{Bi_2Sr_{2-x}La_xCuO_{6+\delta}}$," Science **343**, 390 (2014).

[49] E. H. da Silva Neto, R. Comin, F. He, R. Sutarto, Y. Jiang, R. L. Greene, G. A. Sawatzky, and A. Damascelli, "Charge ordering in the electron-doped superconductor $\mathrm{Nd_{2-x}Ce_xCuO_4}$," Science **347**, 282 (2015).

[50] M. M. Sala, *Magnetic and orbital resonant inelastic soft X-ray scattering*, Ph.D. thesis, Politecnico di Milano (2011).

[51] M. Minola, *Magnetic, orbital and charge fluctuations in layered cuprates studied by resonant soft X-ray scattering*, Ph.D. thesis, Politecnico di Milano (2013).

[52] R. Arpaia, S. Caprara, R. Fumagalli, G. De Vecchi, Y. Y. Peng, E. Andersson, D. Betto, G. M. De Luca, N. B. Brookes, F. Lombardi, M. Salluzzo, L. Braicovich, C. Di Castro, M. Grilli, and G. Ghiringhelli, "Dynamical charge density fluctuations pervading the phase diagram of a Cu-based high-T_c superconductor," Science **365**, 906 (2019).

[53] R. Coldea, S. M. Hayden, G. Aeppli, T. G. Perring, C. D. Frost, T. E. Mason, S.-W. Cheong, and Z. Fisk, "Spin waves and electronic interactions in La_2CuO_4," Physical Review Letters **86**, 5377 (2001).

[54] M. Hepting, L. Chaix, E. W. Huang, R. Fumagalli, Y. Y. Peng, B. Moritz, K. Kummer, N. B. Brookes, W. C. Lee, M. Hashimoto, T. Sarkar, J. F. He, C. R. Rotundu, Y. S. Lee, R. L. Greene, L. Braicovich, G. Ghiringhelli, Z. X. Shen, T. P. Devereaux, and W. S. Lee, "Three-dimensional collective charge excitations in electron-doped cuprate superconductors," Nature **563**, 374 (2018).

[55] J. Schlappa, K. Wohlfeld, K. J. Zhou, M. Mourigal, M. W. Haverkort, V. N. Strocov, L. Hozoi, C. Monney, S. Nishimoto, S. Singh, A. Revcolevschi, J. Caux, L. Patthey, H. M. Rønnow, J. V. D. Brink, and T. Schmitt, "Spin-orbital separation in the quasi-one-dimensional Mott insulator Sr_2CuO_3," Nature **485**, 82 (2012).

[56] S. Sasaki, K. Kakuno, T. Takada, T. Shimada, K.-i. Yanagida, and Y. Miyahara, "Design of a new type of planar undulator for generating variably polarized radiation," Nuclear Instruments and Methods in Physics Research **331**, 763 (1993).

[57] G. Dellea, *Collective excitations in high temperature superconducting cuprates studied by resonant inelastic soft X-ray scattering*, Ph.D. thesis, Politecnico di Milano (2016).

[58] G. Hopkinson, "Charge diffusion effects in CCD X-ray detectors: I. Theory," Nuclear Instruments and Methods in Physics Research **216**, 423 (1983).

[59] A. Amorese, C. Langini, G. Dellea, K. Kummer, N. Brookes, L. Braicovich, and G. Ghiringhelli, "Enhanced spatial resolution of commercial soft X-ray CCD detectors by single-photon centroid reconstruction," Nuclear Instruments and Methods in Physics Research **935**, 222 (2019).

[60] R. Fumagalli, L. Braicovich, M. Minola, Y. Y. Peng, K. Kummer, D. Betto, M. Rossi, E. Lefrançois, C. Morawe, M. Salluzzo, H. Suzuki, F. Yakhou, M. Le Tacon, B. Keimer, N. B. Brookes, M. M. Sala, and G. Ghiringhelli, "Polarization-resolved Cu L_3-edge resonant inelastic x-ray scattering of orbital and spin excitations in $NdBa_2Cu_3O_{7-\delta}$," Physical Review B **99**, 134517 (2019).

[61] P. Marra, S. Sykora, K. Wohlfeld, and J. van den Brink, "Resonant inelastic X-ray scattering as a probe of the phase and excitations of the order parameter of superconductors," Physical Review Letters **110**, 117005 (2013).

[62] A. Damascelli, Z. Hussain, and Z.-X. Shen, "Angle-resolved photoemission studies of the cuprate superconductors," Review of Modern Physics **75**, 473 (2003).

[63] H. Suzuki, M. Minola, Y. Lu, Y. Peng, R. Fumagalli, E. Lefrançois, T. Loew, J. Porras, K. Kummer, D. Betto, S. Ishida, H. Eisaki, C. Hu, X. Zhou, M. Haverkort, Haverkort, N. B. Brookes, L. Braicovich, G. Ghiringhelli, M. Le Tacon, and B. Keimer, "Probing the energy gap of high-temperature cuprate superconductors by resonant inelastic X-ray scattering," npj Quantum Materials **3**, 65 (2018).

[64] I. Vishik, M. Hashimoto, R.-H. He, W.-S. Lee, F. Schmitt, D. Lu, R. Moore, C. Zhang, W. Meevasana, T. Sasagawa, S. Uchida, K. Fujita, S. Ishida, M. Ishikado, Y. Yoshida, H. Eisaki, Z. Hussain, T. P. Devereaux, and Z. X. Shen, "Phase competition in trisected superconducting dome," Proceedings of the National Academy of Sciences **109**, 18332 (2012).

[65] S. Ideta, K. Takashima, M. Hashimoto, T. Yoshida, A. Fujimori, H. Anzai, T. Fujita, Y. Nakashima, A. Ino, M. Arita, H. Namatame, M. Taniguchi, K. Ono, M. Kubota, D. H. Lu, Z.-X. Shen, K. M. Kojima, and S. Uchida, "Enhanced superconducting gaps in the trilayer high-temperature $Bi_2Sr_2Ca_2Cu_3O_{10+\delta}$ cuprate superconductor," Physical Review Letters **104**, 227001 (2010).

[66] M. R. Norman, M. Randeria, H. Ding, and J. C. Campuzano, "Phenomenological models for the gap anisotropy of $Bi_2Sr_2CaCu_2O_8$ as measured by angle-resolved photoemission spectroscopy," Physical Review B **52**, 615 (1995).

[67] M. Salluzzo, G. M. de Luca, D. Marrè, M. Putti, M. Tropeano, U. Scotti di Uccio, and R. Vaglio, "Thickness effect on the structure and superconductivity of $Nd_{1.2}Ba_{1.8}Cu_3O_z$ epitaxial films," Physical Review B **72**, 134521 (2005).

[68] R. Arpaia, E. Andersson, E. Trabaldo, T. Bauch, and F. Lombardi, "Probing the phase diagram of cuprates with $YBa_2Cu_3O_{7-\delta}$ thin films and nanowires," Physical Review Materials **2**, 024804 (2018).

[69] G. Seibold, R. Arpaia, Y. Peng, R. Fumagalli, L. Braicovich, C. Di Castro, M. Grilli, G. Ghiringhelli, and S. Caprara, "Marginal Fermi Liquid behaviour from charge density fluctuations in cuprates," arXiv preprint arXiv:1905.10232 (2019).

[70] A. Amoretti, D. Areán, B. Goutéraux, and D. Musso, "Universal relaxation in a holographic metallic density wave phase," Physical Review Letters **123**, 211602 (2019).

[71] D. J. Scalapino, "A common thread: The pairing interaction for unconventional superconductors," Review of Modern Physics **84**, 1383 (2012).

[72] X. J. Zhou, J. Shi, T. Yoshida, T. Cuk, W. L. Yang, V. Brouet, J. Nakamura, N. Mannella, S. Komiya, Y. Ando, F. Zhou, W. X. Ti, J. W. Xiong, Z. X. Zhao, T. Sasagawa, T. Kakeshita, H. Eisaki, S. Uchida, A. Fujimori, Z. Zhang, E. W. Plummer, R. B. Laughlin, Z. Hussain, and Z.-X. Shen, "Multiple bosonic mode coupling in the electron self-energy of $(La_{2-x}Sr_x)CuO_4$," Physical Review Letters **95**, 117001 (2005).

[73] P. W. Anderson, "Is there glue in cuprate superconductors?" Science **316**, 1705 (2007).

[74] L. Pintschovius, "Electron–phonon coupling effects explored by inelastic neutron scattering," Physica Status Solidi (b) **242**, 30 (2005).

[75] D. Reznik, "Giant electron-ponon anomaly in doped La_2CuO_4 and other cuprates," Advances in Condensed Matter Physics **2010** (2010).

[76] Z. An-Min and Z. Qing-Ming, "Electron—phonon coupling in cuprate and iron-based superconductors revealed by Raman scattering," Chinese Physics B **22**, 087103 (2013).

[77] M. Rossi, R. Arpaia, R. Fumagalli, M. Moretti Sala, D. Betto, K. Kummer, G. M. De Luca, J. van den Brink, M. Salluzzo, N. B. Brookes, L. Braicovich, and G. Ghiringhelli, "Experimental determination of momentum-resolved electron-phonon coupling," Physical Review Letters **123**, 027001 (2019).

[78] T. P. Devereaux, A. M. Shvaika, K. Wu, K. Wohlfeld, C. J. Jia, Y. Wang, B. Moritz, L. Chaix, W.-S. Lee, Z.-X. Shen, G. Ghiringhelli, and L. Braicovich, "Directly characterizing the relative strength and

momentum dependence of electron—phonon coupling using resonant inelastic X-ray scattering," Physical Review X **6**, 041019 (2016).

[79] W. S. Lee, S. Johnston, B. Moritz, J. Lee, M. Yi, K. J. Zhou, T. Schmitt, L. Patthey, V. Strocov, K. Kudo, Y. Koike, J. van den Brink, T. P. Devereaux, and Z. X. Shen, "Role of lattice coupling in establishing electronic and magnetic properties in quasi-one-dimensional cuprates," Physical Review Letters **110**, 265502 (2013).

[80] S. Moser, S. Fatale, P. Krüger, H. Berger, P. Bugnon, A. Magrez, H. Niwa, J. Miyawaki, Y. Harada, and M. Grioni, "Electron-phonon coupling in the bulk of anatase TiO_2 measured by resonant inelastic X-ray spectroscopy," Physical Review Letters **115**, 096404 (2015).

[81] S. Fatale, S. Moser, J. Miyawaki, Y. Harada, and M. Grioni, "Hybridization and electron-phonon coupling in ferroelectric $BaTiO_3$ probed by resonant inelastic X-ray scattering," Physical Review B **94**, 195131 (2016).

[82] S. Johnston, C. Monney, V. Bisogni, K.-J. Zhou, R. Kraus, G. Behr, V. N. Strocov, J. Málek, S.-L. Drechsler, J. Geck, J. GEck, T. Schmitt, and J. Van den Brink, "Electron-lattice interactions strongly renormalize the charge-transfer energy in the spin-chain cuprate Li_2CuO_2," Nature Communications **7**, 10563 (2016).

[83] D. Meyers, K. Nakatsukasa, S. Mu, L. Hao, J. Yang, Y. Cao, G. Fabbris, H. Miao, J. Pelliciari, D. McNally, M. Dantz, E. Paris, E. Karapetrova, Y. Choi, D. Haskel, P. Shafer, E. Arenholz, T. Schmitt, T. Berlijn, S. Johnston, J. Liu, and M. P. M. Dean, "Decoupling carrier concentration and electron-phonon coupling in oxide heterostructures observed with resonant inelastic X-ray scattering," Physical Review Letters **121**, 236802 (2018).

[84] L. Braicovich, M. Rossi, R. Fumagalli, Y. Peng, Y. Wang, R. Arpaia, D. Betto, G. M. De Luca, D. Di Castro, K. Kummer, M. Moretti Sala, M. Pagetti, G. Balestrino, N. B. Brookes, M. Salluzzo, S. Johnston, J. van den Brink, and G. Ghiringhelli, "Determining the electron-phonon coupling in superconducting cuprates by resonant inelastic X-ray scattering: methods and results on $NdBa_2Cu_3O_{7-\delta}$," arXiv preprint arXiv:1906.01270 (2019).

[85] L. Braicovich, M. Moretti Sala, L. J. P. Ament, V. Bisogni, M. Minola, G. Balestrino, D. Di Castro, G. M. De Luca, M. Salluzzo, G. Ghir-

inghelli, and J. van den Brink, “Momentum and polarization dependence of single-magnon spectral weight for Cu L_3-edge resonant inelastic X-ray scattering from layered cuprates,” Physical Review B **81**, 174533 (2010).

[86] D. Vaknin, S. K. Sinha, D. E. Moncton, D. C. Johnston, J. M. Newsam, C. R. Safinya, and H. E. King, “Antiferromagnetism in $\mathrm{La_2CuO_{4-y}}$,” Physical Review Letters **58**, 2802 (1987).

[87] D. Vaknin, E. Caignol, P. K. Davies, J. E. Fischer, D. C. Johnston, and D. P. Goshorn, “Antiferromagnetism in $\mathrm{(Ca_{0.85}Sr_{0.15})CuO_2}$, the parent of the cuprate family of superconducting compounds,” Physical Review B **39**, 9122 (1989).

[88] D. Vaknin, S. K. Sinha, C. Stassis, L. L. Miller, and D. C. Johnston, “Antiferromagnetism in $\mathrm{Sr_2CuO_2Cl_2}$,” Physical Review B **41**, 1926 (1990).

[89] L. J. P. Ament, G. Ghiringhelli, M. M. Sala, L. Braicovich, and J. van den Brink, “Theoretical demonstration of how the dispersion of magnetic excitations in cuprate compounds can be determined using resonant inelastic X-ray scattering,” Physical Review Letters **103**, 117003 (2009).

[90] M. W. Haverkort, “Theory of resonant inelastic X-ray scattering by collective magnetic excitations,” Physical Review Letters **105**, 167404 (2010).

[91] S. Fatale, C. G. Fatuzzo, P. Babkevich, N. E. Shaik, J. Pelliciari, X. Lu, D. E. McNally, T. Schmitt, A. Kikkawa, Y. Taguchi, Y. Tokura, B. Normand, H. M. Rønnow, and M. Grioni, “Electronic and magnetic excitations in the half-stuffed Cu-O planes of $\mathrm{Ba_2Cu_3O_4Cl_2}$ measured by resonant inelastic X-ray scattering,” Physical Review B **96**, 115149 (2017).

[92] M. Kang, J. Pelliciari, Y. Krockenberger, J. Li, D. E. McNally, E. Paris, R. Liang, W. N. Hardy, D. A. Bonn, H. Yamamoto, T. Schmitt, and R. Comin, “Resolving the nature of electronic excitations in resonant inelastic X-ray scattering,” Physical Review B **99**, 045105 (2019).

[93] A. J. Achkar, F. He, R. Sutarto, C. McMahon, M. Zwiebler, M. Hucker, G. D. Gu, R. Liang, D. A. Bonn, W. N. Hardy, J. Geck, and D. G. Hawthorn, “Orbital symmetry of charge-density-wave order

in $La_{1.875}Ba_{0.125}CuO_4$ and $YBa_2Cu_3O_{6.67}$," Nature Materials **15**, 616 (2016).

[94] L. Braicovich, M. Minola, G. Dellea, M. Le Tacon, M. Moretti Sala, C. Morawe, J.-C. Peffen, R. Supruangnet, F. Yakhou, G. Ghiringhelli, and N. B. Brooked, "The simultaneous measurement of energy and linear polarization of the scattered radiation in resonant inelastic soft X-ray scattering," Review of Scientific Instruments **85**, 115104 (2014).

[95] M. Minola, G. Dellea, H. Gretarsson, Y. Y. Peng, Y. Lu, J. Porras, T. Loew, F. Yakhou, N. B. Brookes, Y. B. Huang, J. Pelliciari, T. Schmitt, G. Ghiringhelli, B. Keimer, L. Braicovich, and M. Le Tacon, "Collective nature of spin excitations in superconducting cuprates probed by resonant inelastic X-ray scattering," Physical Review Letters **114**, 217003 (2015).

[96] Y. Peng, R. Fumagalli, Y. Ding, M. Minola, S. Caprara, D. Betto, M. Bluschke, G. De Luca, K. Kummer, E. Lefrançois, M. Salluzzo, H. Suzuki, X. J. Zhou, N. B. Brookes, B. Keimer, L. Braicovich, M. Grilli, and G. Ghiringhelli, "Re-entrant charge order in overdoped $(\mathrm{Bi,Pb})_{2.12}Sr_{1.88}CuO_{6+\delta}$ outside the pseudogap regime," Nature Materials **17**, 697 (2018).

[97] E. H. da Silva Neto, M. Minola, B. Yu, W. Tabis, M. Bluschke, D. Unruh, H. Suzuki, Y. Li, G. Yu, D. Betto, K. Kummer, F. Yakhou, N. B. Brookes, M. Le Tacon, M. Greven, B. Keimer, and A. Damascelli, "Coupling between dynamic magnetic and charge-order correlations in the cuprate superconductor $Nd_{2-x}Ce_xCuO_4$," Physical Review B **98**, 161114 (2018).

[98] A. Amorese, N. Caroca-Canales, S. Seiro, C. Krellner, G. Ghiringhelli, N. B. Brookes, D. V. Vyalikh, C. Geibel, and K. Kummer, "Crystal electric field in $CeRh_2Si_2$ studied with high-resolution resonant inelastic soft X-ray scattering," Physical Review B **97**, 245130 (2018).

[99] M. Born and E. Wolf, *Principle of Optics* (Cambridge University Press, 1999).

[100] D. H. Goldstein, *Polarized light* (CRC Press, 2011).

[101] E. Collett, *Field guide to polarization*, Vol. 15 (SPIE press Bellingham, 2005).

[102] C. Detlefs, M. Sanchez del Rio, and C. Mazzoli, “X-ray polarization: General formalism and polarization analysis,” The European Physical Journal Special Topics volume **208**, 359 (2012).

[103] R. C. Jones, Journal of the Optical Society of America **31**, 488 (1941).

[104] B. E. A. Saleh and M. C. Teich, *Fundamental of Photonics* (John and Wiley and Sons, 2007).

[105] J. Kessler, *Polarized Electrons* (Springer, Berlin, 1985).

[106] D. S. Ellis, Y.-B. Huang, P. Olalde-Velasco, M. Dantz, J. Pelliciari, G. Drachuck, R. Ofer, G. Bazalitsky, J. Berger, T. Schmitt, and A. Keren, “Correlation of the superconducting critical temperature with spin and orbital excitations in $(Ca_xLa_{1-x})(Ba_{1.75-x}La_{0.25+x})Cu_3O_y$ as measured by resonant inelastic X-ray scattering,” Physical Review B **92**, 104507 (2015).

[107] M. Salluzzo, I. Maggio-Aprile, and O. Fischer, “Properties of superconducting $Nd_{1-x}Ba_{2-x}Cu_3O_{7-\delta}$ thin films deposited by dc magnetron sputtering,” Applied Physics Letters **73**, 683 (1998).

[108] M. Salluzzo, G. M. de Luca, D. Marrè, M. Putti, M. Tropeano, U. Scotti di Uccio, and R. Vaglio, “Thickness effect on the structure and superconductivity of $Nd_{1.2}Ba_{1.8}Cu_3O_z$ epitaxial films,” Physical Review B **72**, 134521 (2005).

[109] C. Thomsen and G. Kaczmarczyk, “Vibrational Raman Spectroscopy of High-temperature Superconductors,” in *Handbook of Vibrational Spectroscopy* (American Cancer Society, 2006).

[110] V. Bisogni, L. Simonelli, L. J. P. Ament, F. Forte, M. Moretti Sala, M. Minola, S. Huotari, J. van den Brink, G. Ghiringhelli, N. B. Brookes, and L. Braicovich, “Bimagnon studies in cuprates with resonant inelastic x-ray scattering at the O K edge. I. Assessment on La_2CuO_4 and comparison with the excitation at Cu L_3 and Cu K edges,” Physical Review B **85**, 214527 (2012).

[111] H. Sakakibara, H. Usui, K. Kuroki, R. Arita, and H. Aoki, “Two-orbital model explains the higher transition temperature of the single-layer Hg-cuprate superconductor compared to that of the La-cuprate superconductor,” Physical Review Letters **105**, 057003 (2010).

[112] M. Le Tacon, M. Minola, D. C. Peets, M. Moretti Sala, S. Blanco-Canosa, V. Hinkov, R. Liang, D. A. Bonn, W. N. Hardy, C. T. Lin, T. Schmitt, L. Braicovich, G. Ghiringhelli, and B. Keimer, "Dispersive spin excitations in highly overdoped cuprates revealed by resonant inelastic X-ray scattering," Physical Review B **88**, 020501 (2013).

[113] M. P. M. Dean, A. J. A. James, R. S. Springell, X. Liu, C. Monney, K. J. Zhou, R. M. Konik, J. S. Wen, Z. J. Xu, G. D. Gu, V. N. Strocov, T. Schmitt, and J. P. Hill, "High-energy magnetic excitations in the cuprate superconductor $Bi_2Sr_2CaCu_2O_{8+\delta}$: towards a unified description of its electronic and magnetic degrees of freedom," Physical Review Letters **110**, 147001 (2013).

[114] Y. Y. Peng, M. Hashimoto, M. M. Sala, A. Amorese, N. B. Brookes, G. Dellea, W.-S. Lee, M. Minola, T. Schmitt, Y. Yoshida, K.-J. Zhou, H. Eisaki, T. P. Devereaux, Z.-X. Shen, L. Braicovich, and G. Ghiringhelli, "Magnetic excitations and phonons simultaneously studied by resonant inelastic x-ray scattering in optimally doped $Bi_{1.5}Pb_{0.55}Sr_{1.6}La_{0.4}CuO_{6+\delta}$," Physical Review B **92**, 064517 (2015).

[115] M. Fujita, H. Goka, K. Yamada, and M. Matsuda, "Competition between charge- and spin-density-wave order and superconductivity in $La_{1.875}Ba_{0.125-x}Sr_xCuO_4$," Physical Review Letters **88**, 167008 (2002).

[116] J. Chang, E. Blackburn, A. Holmes, N. B. Christensen, J. Larsen, J. Mesot, R. Liang, D. Bonn, W. Hardy, A. Watenphul, M. v. Zimmermann, E. M. Forgan, and S. M. Hayden, "Direct observation of competition between superconductivity and charge density wave order in π shift in $YBa_2Cu_3O_{6.67}$," Nature Physics **8**, 871 (2012).

[117] W. Tabis, B. Yu, I. Bialo, M. Bluschke, T. Kolodziej, A. Kozlowski, E. Blackburn, K. Sen, E. M. Forgan, M. v. Zimmermann, Y. Tang, E. Weschke, B. Vignolle, M. Hepting, H. Gretarsson, R. Sutarto, F. He, M. Le Tacon, N. Barišić, G. Yu, and M. Greven, "Synchrotron X-ray scattering study of charge-density-wave order in $HgBa_2CuO_{4+\delta}$," Physical Review B **96**, 134510 (2017).

[118] E. H. da Silva Neto, P. Aynajian, A. Frano, R. Comin, E. Schierle, E. Weschke, A. Gyenis, J. Wen, J. Schneeloch, Z. Xu, S. Ono, G. Gu, M. Le Tacon, and A. Yazdani, "Ubiquitous interplay between charge ordering and high-temperature superconductivity in cuprates," Science **343**, 393 (2014).

[119] E. H. da Silva Neto, B. Yu, M. Minola, R. Sutarto, E. Schierle, F. Boschini, M. Zonno, M. Bluschke, J. Higgins, Y. Li, G. Yu, E. Weschke, F. He, M. Le Tacon, R. L. Greene, M. Greven, G. A. Sawatzky, B. Keimer, and A. Damascelli, "Doping-dependent charge order correlations in electron-doped cuprates," Science Advances **2** (2016).

[120] C.-W. Chen, J. Choe, and E. Morosan, "Charge density waves in strongly correlated electron systems," Reports on Progress in Physics **79**, 084505 (2016).

[121] J. González, "Charge instabilities near a Van Hove singularity," Physical Review B **63**, 045114 (2001).

[122] S. Wakimoto, H. Zhang, K. Yamada, I. Swainson, H. Kim, and R. J. Birgeneau, "Direct relation between the low-energy spin excitations and superconductivity of overdoped high-T_c superconductors," Physical Review Letters **92**, 217004 (2004).

[123] S. Wakimoto, K. Yamada, J. M. Tranquada, C. D. Frost, R. J. Birgeneau, and H. Zhang, "Disappearance of antiferromagnetic spin excitations in overdoped $La_{2-x}Sr_xCuO_4$," Physical Review Letters **98**, 247003 (2007).

[124] C. Jia, E. Nowadnick, K. Wohlfeld, Y. Kung, C.-C. Chen, S. Johnston, T. Tohyama, B. Moritz, and T. Devereaux, "Persistent spin excitations in doped antiferromagnets revealed by resonant inelastic light scattering," Nature Communications **5**, 1 (2014).

[125] E. W. Huang, D. J. Scalapino, T. A. Maier, B. Moritz, and T. P. Devereaux, "Decrease of d-wave pairing strength in spite of the persistence of magnetic excitations in the overdoped Hubbard model," Physical Review B **96**, 020503 (2017).

[126] T. Dahm, V. Hinkov, S. Borisenko, A. Kordyuk, V. Zabolotnyy, J. Fink, B. Büchner, D. Scalapino, W. Hanke, and B. Keimer, "Strength of the spin-fluctuation-mediated pairing interaction in a high-temperature superconductor," Nature Physics **5**, 217 (2009).

[127] M. Guarise, B. Dalla Piazza, H. Berger, E. Giannini, T. Schmitt, H. M. Rønnow, G. Sawatzky, J. Van Den Brink, D. Altenfeld, I. Eremin, and M. Grioni, "Anisotropic softening of magnetic excitations along the nodal direction in superconducting cuprates," Nature Communications **5**, 5760 (2014).

[128] M. P. M. Dean, A. J. A. James, A. C. Walters, V. Bisogni, I. Jarrige, M. Hücker, E. Giannini, M. Fujita, J. Pelliciari, Y. B. Huang, R. M. Konik, T. Schmitt, and J. P. Hill, "Itinerant effects and enhanced magnetic interactions in Bi-based multilayer cuprates," Physical Review B **90**, 220506 (2014).

[129] C. Monney, T. Schmitt, C. E. Matt, J. Mesot, V. N. Strocov, O. J. Lipscombe, S. M. Hayden, and J. Chang, "Resonant inelastic X-ray scattering study of the spin and charge excitations in the overdoped superconductor $La_{1.77}Sr_{0.23}CuO_4$," Physical Review B **93**, 075103 (2016).

[130] O. Ivashko, N. E. Shaik, X. Lu, C. G. Fatuzzo, M. Dantz, P. G. Freeman, D. E. McNally, D. Destraz, N. B. Christensen, T. Kurosawa, N. Momono, M. Oda, C. E. Matt, C. Monney, H. M. Rønnow, T. Schmitt, and J. Chang, "Damped spin excitations in a doped cuprate superconductor with orbital hybridization," Physical Review B **95**, 214508 (2017).

[131] D. Meyers, H. Miao, A. C. Walters, V. Bisogni, R. S. Springell, M. d'Astuto, M. Dantz, J. Pelliciari, H. Y. Huang, J. Okamoto, D. J. Huang, J. P. Hill, X. He, I. Božović, T. Schmitt, and M. P. M. Dean, "Doping dependence of the magnetic excitations in $La_{2-x}Sr_xCuO_4$," Physical Review B **95**, 075139 (2017).

[132] Y. F. Kung, E. A. Nowadnick, C. J. Jia, S. Johnston, B. Moritz, R. T. Scalettar, and T. P. Devereaux, "Doping evolution of spin and charge excitations in the Hubbard model," Physical Review B **92**, 195108 (2015).

[133] Y. Y. Peng, E. W. Huang, R. Fumagalli, M. Minola, Y. Wang, X. Sun, Y. Ding, K. Kummer, X. J. Zhou, N. B. Brookes, B. Moritz, L. Braicovich, T. P. Devereaux, and G. Ghiringhelli, "Dispersion, damping, and intensity of spin excitations in the monolayer $(Bi,Pb)_2(Sr,La)_2CuO_{6+\delta}$ cuprate superconductor family," Physical Review B **98**, 144507 (2018).

[134] N. S. Headings, S. M. Hayden, R. Coldea, and T. G. Perring, "Anomalous high-energy spin excitations in the high-T_c superconductor-parent antiferromagnet La_2CuO_4," Physical Review Letters **105**, 247001 (2010).

[135] E. Pavarini, I. Dasgupta, T. Saha-Dasgupta, O. Jepsen, and O. K. Andersen, "Band-structure trend in hole-doped cuprates and correlation with $T_{c\max}$," Physical Review Letters **87**, 047003 (2001).

[136] B. Dalla Piazza, M. Mourigal, M. Guarise, H. Berger, T. Schmitt, K. J. Zhou, M. Grioni, and H. M. Rønnow, "Unified one-band Hubbard model for magnetic and electronic spectra of the parent compounds of cuprate superconductors," Physical Review B **85**, 100508 (2012).

[137] K. W. Plumb, A. T. Savici, G. E. Granroth, F. C. Chou, and Y.-J. Kim, "High-energy continuum of magnetic excitations in the two-dimensional quantum antiferromagnet $Sr_2CuO_2Cl_2$," Physical Review B **89**, 180410 (2014).

[138] G. Fabbris, D. Meyers, J. Okamoto, J. Pelliciari, A. S. Disa, Y. Huang, Z.-Y. Chen, W. B. Wu, C. T. Chen, S. Ismail-Beigi, C. H. Ahn, F. J. Walker, D. J. Huang, T. Schmitt, and M. P. M. Dean, "Orbital engineering in nickelate heterostructures driven by anisotropic oxygen hybridization rather than orbital energy levels," Physical Review Letters **117**, 147401 (2016).

[139] D. Betto, Y. Y. Peng, S. B. Porter, G. Berti, A. Calloni, G. Ghiringhelli, and N. B. Brookes, "Three-dimensional dispersion of spin waves measured in NiO by resonant inelastic X-ray scattering," Physical Review B **96**, 020409 (2017).

[140] Y. Lu, D. Betto, K. Fürsich, H. Suzuki, H.-H. Kim, G. Cristiani, G. Logvenov, N. B. Brookes, E. Benckiser, M. W. Haverkort, G. Khaliullin, M. Le Tacon, M. Minola, and B. Keimer, "Site-selective probe of magnetic excitations in rare-earth nickelates using resonant inelastic X-ray scattering," Physical Review X **8**, 031014 (2018).

[141] G. L. Squires, *Introduction to the theory of thermal neutron scattering* (Cambridge university press, 2012).

[142] C. Jia, K. Wohlfeld, Y. Wang, B. Moritz, and T. P. Devereaux, "Using RIXS to uncover elementary charge and spin excitations," Physical Review X **6**, 021020 (2016).

[143] M. A. Kastner, R. J. Birgeneau, G. Shirane, and Y. Endoh, "Magnetic, transport, and optical properties of monolayer copper oxides," Review of Modern Physics **70**, 897 (1998).

[144] J. Lorenzana, G. Seibold, and R. Coldea, "Sum rules and missing spectral weight in magnetic neutron scattering in the cuprates," Physical Review B **72**, 224511 (2005).

[145] A. W. Sandvik and R. R. P. Singh, "High-energy magnon dispersion and multimagnon continuum in the two-dimensional Heisenberg antiferromagnet," Physical Review Letters **86**, 528 (2001).

[146] J.-i. Igarashi and T. Nagao, "1S-expansion study of spin waves in a two-dimensional Heisenberg antiferromagnet," Physical Review B **72**, 014403 (2005).

[147] J.-i. Igarashi and T. Nagao, "Magnetic excitations in L-edge resonant inelastic X-ray scattering from cuprate compounds," Physical Review B **85**, 064421 (2012).

[148] L. J. Ament and J. v. d. Brink, "Strong three-magnon scattering in cuprates by resonant X-rays," arXiv preprint arXiv:1002.3773 (2010).

[149] A. Donkov and A. V. Chubukov, "Momentum-dependent light scattering in a two-dimensional Heisenberg antiferromagnet: analysis of X-ray scattering data," Physical Review B **75**, 024417 (2007).

[150] J. Lorenzana and G. A. Sawatzky, "Phonon assisted multimagnon optical absorption and long lived two-magnon states in undoped lamellar copper oxides," Physical Review Letters **74**, 1867 (1995).

[151] J. Lorenzana and G. A. Sawatzky, "Theory of phonon-assisted multimagnon optical absorption and bimagnon states in quantum antiferromagnets," Physical Review B **52**, 9576 (1995).

[152] N. B. Christensen, H. M. Rønnow, D. F. McMorrow, A. Harrison, T. Perring, M. Enderle, R. Coldea, L. Regnault, and G. Aeppli, "Quantum dynamics and entanglement of spins on a square lattice," Proceedings of the National Academy of Sciences **104**, 15264 (2007).

[153] N. Tsyrulin, T. Pardini, R. R. P. Singh, F. Xiao, P. Link, A. Schneidewind, A. Hiess, C. P. Landee, M. M. Turnbull, and M. Kenzelmann, "Quantum effects in a weakly frustrated $S = 1/2$ two-dimensional Heisenberg antiferromagnet in an applied magnetic field," Physical Review Letters **102**, 197201 (2009).

[154] M. Fujita, H. Hiraka, M. Matsuda, M. Matsuura, J. M. Tranquada, S. Wakimoto, G. Xu, and K. Yamada, "Progress in neutron scattering studies of spin excitations in high-T_c cuprates," Journal of the Physical Society of Japan **81**, 011007 (2011).

[155] S. Tajima, “Optical studies of high-temperature superconducting cuprates,” Reports on Progress in Physics **79**, 094001 (2016).

[156] E. J. Singley, D. N. Basov, K. Kurahashi, T. Uefuji, and K. Yamada, “Electron dynamics in $\mathrm{Nd}_{1.85}\mathrm{Ce}_{0.15}\mathrm{CuO}_{4+\delta}$: evidence for the pseudogap state and unconventional c-axis response,” Physical Review B **64**, 224503 (2001).

[157] I. Bozovic, “Plasmons in cuprate superconductors,” Physical Review B **42**, 1969 (1990).

[158] J. Levallois, M. K. Tran, D. Pouliot, C. N. Presura, L. H. Greene, J. N. Eckstein, J. Uccelli, E. Giannini, G. D. Gu, A. J. Leggett, and D. van der Marel, “Temperature-dependent ellipsometry measurements of partial Coulomb energy in superconducting cuprates,” Physical Review X **6**, 031027 (2016).

[159] J. Fink, M. Knupfer, S. Atzkern, and M. Golden, “Electronic correlations in solids, studied using electron energy-loss spectroscopy,” Journal of electron spectroscopy and related phenomena **117**, 287 (2001).

[160] V. Z. Kresin and H. Morawitz, “Layer plasmons and high-T_c superconductivity,” Physical Review B **37**, 7854 (1988).

[161] Y. Ishii and J. Ruvalds, “Acoustic plasmons and cuprate superconductivity,” Physical Review B **48**, 3455 (1993).

[162] A. Bill, H. Morawitz, and V. Z. Kresin, “Electronic collective modes and superconductivity in layered conductors,” Physical Review B **68**, 144519 (2003).

[163] D. Grecu, “Plasma frequency of the electron gas in layered structures,” Physical Review B **8**, 1958 (1973).

[164] K. Ishii, M. Fujita, T. Sasaki, M. Minola, G. Dellea, C. Mazzoli, K. Kummer, G. Ghiringhelli, L. Braicovich, T. Tohyama, K. Tsutsumi, K. Sato, R. Kajimoto, K. Ikeuchi, K. Yamada, M. Yoshida, M. Kurooka, and J. Mizuki, “High-energy spin and charge excitations in electron-doped copper oxide superconductors,” Nature Communications **5**, 1 (2014).

[165] W. Lee, J. Lee, E. Nowadnick, S. Gerber, W. Tabis, S. Huang, V. Strocov, E. Motoyama, G. Yu, B. Moritz, H. Y. Huang, R. P. Wang, Y. B. Huang, W. B. Wu, C. T. Chen, D. J. Huang, M. Greven, T. Schmitt,

Z. C. Shen, and T. P. Devereaux, “Asymmetry of collective excitations in electron-and hole-doped cuprate superconductors,” Nature Physics **10**, 883 (2014).

[166] G. Dellea, M. Minola, A. Galdi, D. Di Castro, C. Aruta, N. B. Brookes, C. J. Jia, C. Mazzoli, M. Moretti Sala, B. Moritz, P. Orgiani, D. G. Schlom, A. Tebano, G. Balestrino, L. Braicovich, T. P. Devereaux, L. Maritato, and G. Ghiringhelli, “Spin and charge excitations in artificial hole- and electron-doped infinite layer cuprate superconductors,” Physical Review B **96**, 115117 (2017).

[167] A. Greco, H. Yamase, and M. Bejas, “Plasmon excitations in layered high-T_c cuprates,” Physical Review B **94**, 075139 (2016).

[168] J. E. Hoffman, E. W. Hudson, K. M. Lang, V. Madhavan, H. Eisaki, S. Uchida, and J. C. Davis, “A four unit cell periodic pattern of quasi-particle states surrounding vortex cores in $Bi_2Sr_2CaCu_2O_{8+\delta}$,” Science **295**, 466 (2002).

[169] C. Howald, H. Eisaki, N. Kaneko, and A. Kapitulnik, “Coexistence of periodic modulation of quasiparticle states and superconductivity in $Bi_2Sr_2CaCu_2O_{8+\delta}$,” Proceedings of the National Academy of Sciences **100**, 9705 (2003).

[170] A. J. Achkar, R. Sutarto, X. Mao, F. He, A. Frano, S. Blanco-Canosa, M. Le Tacon, G. Ghiringhelli, L. Braicovich, M. Minola, M. Moretti Sala, C. Mazzoli, R. Liang, D. A. Bonn, W. N. Hardy, B. Keimer, G. A. Sawatzky, and D. G. Hawthorn, “Distinct charge orders in the planes and chains of ortho-III-ordered $YBa_2Cu_3O_{6+\delta}$ Superconductors identified by resonant elastic X-ray scattering,” Physical Review Letters **109**, 167001 (2012).

[171] H. Jang, S. Asano, M. Fujita, M. Hashimoto, D. H. Lu, C. A. Burns, C.-C. Kao, and J.-S. Lee, “Superconductivity-insensitive order at $q \sim 1/4$ in electron-doped cuprates,” Physical Review X **7**, 041066 (2017).

[172] J. Zaanen and O. Gunnarsson, “Charged magnetic domain lines and the magnetism of high-T_c oxides,” Physical Review B **40**, 7391 (1989).

[173] K. Machida, “Magnetism in La_2CuO_4 based compounds,” Physica C: Superconductivity **158**, 192 (1989).

[174] M. Kato, K. Machida, H. Nakanishi, and M. Fujita, “Soliton lattice modulation of incommensurate spin density wave in two dimensional

hubbard model-a mean field study," Journal of the Physical Society of Japan **59**, 1047 (1990).

[175] S. A. Kivelson, E. Fradkin, and V. J. Emery, "Electronic liquid-crystal phases of a doped Mott insulator," Nature **393**, 550 (1998).

[176] J. C. S. Davis and D.-H. Lee, "Concepts relating magnetic interactions, intertwined electronic orders, and strongly correlated superconductivity," Proceedings of the National Academy of Sciences **110**, 17623 (2013).

[177] K. Efetov, H. Meier, and C. Pépin, "Pseudogap state near a quantum critical point," Nature Physics **9**, 442 (2013).

[178] S. Sachdev and R. La Placa, "Bond order in two-dimensional metals with antiferromagnetic exchange interactions," Physical Review Letters **111**, 027202 (2013).

[179] Y. Wang and A. Chubukov, "Charge-density-wave order with momentum $(2Q, 0)$ and $(0, 2Q)$ within the spin-fermion model: Continuous and discrete symmetry breaking, preemptive composite order, and relation to pseudogap in hole-doped cuprates," Physical Review B **90**, 035149 (2014).

[180] X. Wang, Y. Wang, Y. Schattner, E. Berg, and R. M. Fernandes, "Fragility of charge order near an antiferromagnetic quantum critical point," Physical Review Lett. **120**, 247002 (2018).

[181] S. Blanco-Canosa, A. Frano, T. Loew, Y. Lu, J. Porras, G. Ghiringhelli, M. Minola, C. Mazzoli, L. Braicovich, E. Schierle, E. Weschke, M. Le Tacon, and B. Keimer, "Momentum-dependent charge correlations in $YBa_2Cu_3O_{6+\delta}$ superconductors probed by resonant X-ray scattering: evidence for three competing phases," Physical Review Letters **110**, 187001 (2013).

[182] M. Hücker, N. B. Christensen, A. T. Holmes, E. Blackburn, E. M. Forgan, R. Liang, D. A. Bonn, W. N. Hardy, O. Gutowski, M. v. Zimmermann, S. M. Hayden, and J. Chang, "Competing charge, spin, and superconducting orders in underdoped $YBa_2Cu_3O_y$," Physical Review B **90**, 054514 (2014).

[183] T. Wu, H. Mayaffre, S. Krämer, M. Horvatić, C. Berthier, W. Hardy, R. Liang, D. Bonn, and M.-H. Julien, "Incipient charge order observed

by NMR in the normal state of π shift in $YBa_2Cu_3O_y$," Nature Communications **6**, 6438 (2015).

[184] E. Motoyama, G. Yu, I. Vishik, O. Vajk, P. Mang, and M. Greven, "Spin correlations in the electron-doped high-transition-temperature superconductor $Nd_{2-x}Ce_xCuO_{4\pm\delta}$," Nature **445**, 186 (2007).

[185] S. Gerber, H. Jang, H. Nojiri, S. Matsuzawa, H. Yasumura, D. A. Bonn, R. Liang, W. N. Hardy, Z. Islam, A. Mehta, S. Song, M. Sikorski, D. Stefanescu, Y. Feng, S. A. Kivelson, T. P. Devereaux, Z.-X. Shen, C.-C. Kao, W.-S. Lee, D. Zhu, and J.-S. Lee, "Three-dimensional charge density wave order in π shift in $YBa_2Cu_3O_{6.67}$ at high magnetic fields," Science **350**, 949 (2015).

[186] J. Chang, E. Blackburn, O. Ivashko, A. Holmes, N. B. Christensen, M. Hücker, R. Liang, D. Bonn, W. Hardy, U. Rütt, M. v. Zimmermann, E. M. Forgan, and S. M. Hayden, "Magnetic field controlled charge density wave coupling in underdoped $YBa_2Cu_3O_{6+x}$," Nature Communications **7**, 11494 (2016).

[187] H. Jang, W.-S. Lee, H. Nojiri, S. Matsuzawa, H. Yasumura, L. Nie, A. V. Maharaj, S. Gerber, Y.-J. Liu, A. Mehta, D. A. Bonn, R. Liang, W. N. Hardy, C. A. Burns, Z. Islam, S. Song, J. Hastings, T. P. Devereaux, Z.-X. Shen, S. A. Kivelson, C.-C. Kao, D. Zhu, and J.-S. Lee, "Ideal charge-density-wave order in the high-field state of superconducting YBCO," Proceedings of the National Academy of Sciences **113**, 14645 (2016).

[188] S. A. Kivelson, I. P. Bindloss, E. Fradkin, V. Oganesyan, J. M. Tranquada, A. Kapitulnik, and C. Howald, "How to detect fluctuating stripes in the high-temperature superconductors," Reiew of Modern Physics **75**, 1201 (2003).

[189] Y. Caplan, G. Wachtel, and D. Orgad, "Long-range order and pinning of charge-density waves in competition with superconductivity," Physical Review B **92**, 224504 (2015).

[190] T. Wu, R. Zhou, M. Hirata, I. Vinograd, H. Mayaffre, R. Liang, W. N. Hardy, D. A. Bonn, T. Loew, J. Porras, D. Haug, C. T. Lin, V. Hinkov, B. Keimer, and M.-H. Julien, "^{63}Cu-NMR study of oxygen disorder in ortho-II $YBa_2Cu_3O_y$," Physical Review B **93**, 134518 (2016).

[191] M. Bejas, H. Yamase, and A. Greco, "Dual structure in the charge excitation spectrum of electron-doped cuprates," Physical Review B **96**, 214513 (2017).

[192] S. Quezel, J. Rossat-Mignod, B. Chevalier, P. Lejay, and J. Etourneau, "Magnetic ordering in $TbRh_2Si_2$ and $CeRh_2Si_2$," Solid State Communications **49**, 685 (1984).

[193] S. Kawarazaki, M. Sato, Y. Miyako, N. Chigusa, K. Watanabe, N. Metoki, Y. Koike, and M. Nishi, "Ground-state magnetic structure of $CeRh_2Si_2$ and the response to hydrostatic pressure as studied by neutron diffraction," Physical Review B **61**, 4167 (2000).

[194] B. H. Grier, J. M. Lawrence, V. Murgai, and R. D. Parks, "Magnetic ordering in $\mathrm{Ce}M_2\mathrm{Si}_2$ $(M = \mathrm{Ag}, \mathrm{Au}, \mathrm{Pd}, \mathrm{Rh})$ compounds as studied by neutron diffraction," Physical Review B **29**, 2664 (1984).

[195] T. Graf, M. F. Hundley, R. Modler, R. Movshovich, J. D. Thompson, D. Mandrus, R. A. Fisher, and N. E. Phillips, "Magnetic phase transitions in $CeRh_2Si_2$: specific heat, susceptibility, and resistance studies," Physical Review B **57**, 7442 (1998).

[196] R. Movshovich, T. Graf, D. Mandrus, J. D. Thompson, J. L. Smith, and Z. Fisk, "Superconductivity in heavy-fermion $CeRh_2Si_2$," Physical Review B **53**, 8241 (1996).

[197] S. Araki, M. Nakashima, R. Settai, T. C. Kobayashi, and Y. Onuki, "Pressure-induced superconductivity in an antiferromagnet $CeRh_2Si_2$," Journal of Physics: Condensed Matter **14**, L377 (2002).

[198] C. Dallera, K. Giarda, G. Ghiringhelli, A. Tagliaferri, L. Braicovich, and N. B. Brookes, "Charge-transfer excitations in lanthanum compounds measured by resonant inelastic X-ray scattering at the M_5 edge," Physical Review B **64**, 153104 (2001).

[199] T. Willers, D. T. Adroja, B. D. Rainford, Z. Hu, N. Hollmann, P. O. Körner, Y.-Y. Chin, D. Schmitz, H. H. Hsieh, H.-J. Lin, C. T. Chen, E. D. Bauer, J. L. Sarrao, K. J. McClellan, D. Byler, C. Geibel, F. Steglich, H. Aoki, P. Lejay, A. Tanaka, L. H. Tjeng, and A. Severing, "Spectroscopic determination of crystal-field levels in $CeRh_2Si_2$ and $CeRu_2Si_2$ and of the $4f^0$ contributions in $\mathrm{Ce}M_2\mathrm{Si}_2$ (M=Cu, Ru, Rh, Pd, and Au)," Physical Review B **85**, 035117 (2012).

[200] R. Settai, A. Misawa, S. Araki, M. Kosaki, K. Sugiyama, T. Takeuchi, K. Kindo, Y. Haga, E. Yamamoto, and Y. Onuki, “Single crystal growth and magnetic properties of $CeRh_2Si_2$,” Journal of the Physical Society of Japan **66**, 2260 (1997).

[201] H. Abe, H. Kitazawa, H. Suzuki, G. Kido, and T. Matsumoto, “Magnetic properties of $CeRh_2Si_2$ and $CePd_2Si_2$ single crystals,” Journal of Magnetism and Magnetic Materials **177-181**, 479 (1998).

[202] S. Patil, A. Generalov, M. Güttler, P. Kushwaha, A. Chikina, K. Kummer, T. Rödel, A. Santander-Syro, N. Caroca-Canales, C. Geibel, S. Danzenbächer, Y. Kucherenko, C. Laubschat, J. W. Allen, and D. V. Vyalikh, “ARPES view on surface and bulk hybridization phenomena in the antiferromagnetic Kondo lattice $CeRh_2Si_2$,” Nature Communications **7**, 11029 (2016).

[203] A. Georges, L. d. Medici, and J. Mravlje, “Strong Correlations from Hund’s Coupling,” Annual Review of Condensed Matter Physics **4**, 137 (2013).

[204] Y. Tokura and N. Nagaosa, “Orbital physics in transition-metal oxides,” Science **288**, 462 (2000).

[205] J. Kanamori, “Superexchange interaction and symmetry properties of electron orbitals,” Journal of Physics and Chemistry of Solids **10**, 87 (1959).

[206] J. B. Goodenough, *Magnetism and the Chemical Bond* (Interscience, New York, 1963).

[207] D. I. Khomskii, *Transition Metal Compounds* (Cambridge University Press, Cambridge, 2014).

[208] F. Moussa, M. Hennion, J. Rodriguez-Carvajal, H. Moudden, L. Pinsard, and A. Revcolevschi, “Spin waves in the antiferromagnet perovskite $LaMnO_3$: A neutron-scattering study,” Physical Review B **54**, 15149 (1996).

[209] A. M. Oleś, G. Khaliullin, P. Horsch, and L. F. Feiner, “Fingerprints of spin-orbital physics in cubic Mott insulators: Magnetic exchange interactions and optical spectral weights,” Physical Review B **72**, 214431 (2005).

[210] K. Wohlfeld, S. Nishimoto, M. W. Haverkort, and J. van den Brink, "Microscopic origin of spin-orbital separation in Sr_2CuO_3," Physical Review B **88**, 195138 (2013).

[211] V. Bisogni, K. Wohlfeld, S. Nishimoto, C. Monney, J. Trinckauf, K. Zhou, R. Kraus, K. Koepernik, C. Sekar, V. Strocov, B. Büchner, T. Schmitt, J. van den Brink, and J. Geck, "Orbital control of effective dimensionality: from spin-orbital fractionalization to confinement in the anisotropic ladder system $CaCu_2O_3$," Physical Review Letters **114**, 096402 (2015).

[212] J. Kim, D. Casa, M. H. Upton, T. Gog, Y.-J. Kim, J. F. Mitchell, M. van Veenendaal, M. Daghofer, J. van den Brink, G. Khaliullin, and B. J. Kim, "Magnetic excitation spectra of Sr_2IrO_4 probed by resonant inelastic X-ray scattering: establishing links to cuprate superconductors," Physical Review Letters **108**, 177003 (2012).

[213] J. Kim, M. Daghofer, A. H. Said, T. Gog, J. van den Brink, G. Khaliullin, and B. J. Kim, "Excitonic quasiparticles in a spin-orbit Mott insulator," Nature Communications **5**, 4453 (2014).

[214] K. Wohlfeld, M. Daghofer, S. Nishimoto, G. Khaliullin, and J. van den Brink, "Intrinsic coupling of orbital excitations to spin fluctuations in Mott insulators," Physical Review Letters **107**, 147201 (2011).

[215] C. Kim, A. Y. Matsuura, Z.-X. Shen, N. Motoyama, H. Eisaki, S. Uchida, T. Tohyama, and S. Maekawa, "Observation of spin-charge separation in one-dimensional $SrCuO_2$," Physical Review Letters **77**, 4054 (1996).

[216] J. Heverhagen and M. Daghofer, "Spinon-orbiton repulsion and attraction mediated by Hund's rule," Physical Review B **98**, 085120 (2018).

[217] U. Gebhardt, N. Kasper, A. Vigliante, P. Wochner, H. Dosch, F. Razavi, and H.-U. Habermeier, "Formation and thickness evolution of periodic twin domains in manganite films grown on $SrTiO_3$ (001) substrates," Physical Review Letters **98**, 096101 (2007).

[218] A. Vailionis, H. Boschker, W. Siemons, E. P. Houwman, D. H. Blank, G. Rijnders, and G. Koster, "Misfit strain accommodation in epitaxial ABO_3 perovskites: Lattice rotations and lattice modulations," Physical Review B **83**, 064101 (2011).

[219] M. Weber, M. Guennou, N. Dix, D. Pesquera, F. Sánchez, G. Herranz, J. Fontcuberta, L. López-Conesa, S. Estradé, F. Peiró, , J. Iñiguez, and J. Kreisel, "Multiple strain-induced phase transitions in $\mathrm{LaNiO_3}$ thin films," Physical Review B **94**, 014118 (2016).

[220] R. Arpaia, E. Andersson, A. Kalaboukhov, E. Schröder, E. Trabaldo, R. Ciancio, G. Dražić, P. Orgiani, T. Bauch, and F. Lombardi, "Untwinned $\mathrm{YBa_2Cu_3O_{7-\delta}}$ thin films on MgO substrates: a platform to study strain effects on the local orders in cuprates," arXiv preprint arXiv:1908.02637 (2019).

[221] S. Kondoh, K. Fukuda, and M. Sato, "Magnetic susceptibility of $\mathrm{Ca_2CuO_3}$," Solid State Communications **65**, 1163 (1988).

[222] M. Karbach, G. Müller, A. H. Bougourzi, A. Fledderjohann, and K.-H. Mütter, "Two-spinon dynamic structure factor of the one-dimensional s=1/2 Heisenberg antiferromagnet," Physical Review B **55**, 12510 (1997).

[223] T. Giamarchi, *Quantum physics in one dimension*, Vol. 121 (Clarendon press, 2003).

[224] J.-S. Caux and R. Hagemans, "The four-spinon dynamical structure factor of the Heisenberg chain," Journal of Statistical Mechanics: Theory and Experiment **2006**, P12013 (2006).

[225] J.-S. Caux, J. Mossel, and I. P. Castillo, "The two-spinon transverse structure factor of the gapped Heisenberg antiferromagnetic chain," Journal of Statistical Mechanics: Theory and Experiment **2008**, P08006 (2008).

[226] B. Lake, D. A. Tennant, C. D. Frost, and S. E. Nagler, "Quantum criticality and universal scaling of a quantum antiferromagnet," Nature Materials **4**, 329 (2005).

[227] B. Lake, A. M. Tsvelik, S. Notbohm, D. A. Tennant, T. G. Perring, M. Reehuis, C. Sekar, G. Krabbes, and B. Büchner, "Confinement of fractional quantum number particles in a condensed-matter system," Nature Physics **6**, 50 (2010).

[228] M. Mourigal, M. Enderle, A. Klöpperpieper, J.-S. Caux, A. Stunault, and H. M. Rønnow, "Fractional spinon excitations in the quantum Heisenberg antiferromagnetic chain," Nature Physics **9**, 435 (2013).

[229] S. Glawion, J. Heidler, M. W. Haverkort, L. C. Duda, T. Schmitt, V. N. Strocov, C. Monney, K. J. Zhou, A. Ruff, M. Sing, and R. Claessen, "Two-spinon and orbital excitations of the spin-Peierls system TiOCl," Physical Review Letters **107**, 107402 (2011).

[230] S. Kourtis, J. van den Brink, and M. Daghofer, "Exact diagonalization results for resonant inelastic X-ray scattering spectra of one-dimensional Mott insulators," Physical Review B **85**, 064423 (2012).

[231] F. Forte, M. Cuoco, C. Noce, and J. van den Brink, "Doping dependence of magnetic excitations of one-dimensional cuprates as probed by resonant inelastic X-ray scattering," Physical Review B **83**, 245133 (2011).

[232] J. Schlappa, U. Kumar, K. J. Zhou, S. Singh, M. Mourigal, V. N. Strocov, A. Revcolevschi, L. Patthey, H. M. Rnnow, S. Johnston, and T. Schmitt, "Probing multi-spinon excitations outside of the two-spinon continuum in the antiferromagnetic spin chain cuprate Sr_2CuO_3," Nature Communications **9** (2018), 10.1038/s41467-018-07838-y.

[233] A. C. Walters, T. G. Perring, J.-S. Caux, A. T. Savici, G. D. Gu, C.-C. Lee, W. Ku, and I. A. Zaliznyak, "Effect of covalent bonding on magnetism and the missing neutron intensity in copper oxide compounds," Nature Physics **5**, 867 (2009).

[234] H. Suzuura, H. Yasuhara, A. Furusaki, N. Nagaosa, and Y. Tokura, "Singularities in optical spectra of quantum spin chains," Physical Review Letters **76**, 2579 (1996).

[235] K. Kugel and D. Khomskii, "Crystal-structure and magnetic properties of substances with orbital degeneracy," Soviet Journal of Experimental and Theoretical Physics **64**, 725 (1973).

[236] H. F. Pen, J. van den Brink, D. I. Khomskii, and G. A. Sawatzky, "Orbital ordering in a two-dimensional triangular lattice," Physical Review Letters **78**, 1323 (1997).

[237] B. Kim, H. Koh, E. Rotenberg, S.-J. Oh, H. Eisaki, N. Motoyama, S. Uchida, T. Tohyama, S. Maekawa, Z.-X. Shen, and C. Kim, "Distinct spinon and holon dispersions in photoemission spectral functions from one-dimensional $SrCuO_2$," Nature Physics **2**, 397 (2006).

[238] K. Wohlfeld, M. Daghofer, G. Khaliullin, and J. van den Brink, "Dispersion of orbital excitations in 2D quantum antiferromagnets," Journal of Physics: Conference Series **391**, 012168 (2012).

[239] G. Balestrino, R. Desfeux, S. Martellucci, A. Paoletti, G. Petrocelli, A. Tebano, B. Mercey, and M. Hervieu, "Growth of $CaCuO_2$ and $SrCa_{1-x}CuO_2$ epitaxial films on $NdGaO_3$ substrates by pulsed laser deposition," Journal of Materials Chemistry **5**, 1879 (1995).

[240] J. J. Lee, B. Moritz, W. S. Lee, M. Yi, C. J. Jia, A. P. Sorini, K. Kudo, Y. Koike, K. J. Zhou, C. Monney, V. Strocov, L. Patthey, T. Schmitt, T. P. Devereaux, and Z. X. Shen, "Charge-orbital-lattice coupling effects in the dd excitation profile of one-dimensional cuprates," Physical Review B **89**, 041104 (2014).

[241] D. Li, K. Lee, B. Y. Wang, M. Osada, S. Crossley, H. R. Lee, Y. Cui, Y. Hikita, and H. Y. Hwang, "Superconductivity in an infinite-layer nickelate," Nature **572**, 624 (2019).

[242] X. Wu, D. Di Sante, T. Schwemmer, W. Hanke, H. Y. Hwang, S. Raghu, and R. Thomale, "Robust $d_{x^2-y^2}$ s-wave superconductivity of infinite-layer nickelates," arXiv preprint arXiv:1909.03015 (2019).

[243] H. Sakakibara, H. Usui, K. Suzuki, T. Kotani, H. Aoki, and K. Kuroki, "Model construction and a possibility of cuprate-like pairing in a new d^9 nickelate superconductor $(Nd,Sr)NiO_2$," arXiv preprint arXiv:1909.00060 (2019).

[244] A. S. Botana and M. R. Norman, "Similarities and differences between infinite-layer nickelates and cuprates and implications for superconductivity," arXiv preprint arXiv:1908.10946 (2019).

[245] M. Jiang, M. Berciu, and G. A. Sawatzky, "Doped holes in $NdNiO_2$ and high-T_c cuprates show little similarity," arXiv preprint arXiv:1909.02557 (2019).

[246] T. Maier, T. Berlijn, and D. J. Scalapino, "Two pairing domes as Cu^{2+} varies to Cu^{3+}," Physical Review B **99**, 224515 (2019).

[247] D. G. Hawthorn, K. M. Shen, J. Geck, D. C. Peets, H. Wadati, J. Okamoto, S.-W. Huang, D. J. Huang, H.-J. Lin, J. D. Denlinger, R. Liang, D. A. Bonn, W. N. Hardy, and G. A. Sawatzky, "Resonant elastic soft X-ray scattering in oxygen-ordered $YBa_2Cu_3O_{6+\delta}$," Physical Review B **84**, 075125 (2011).

[248] D. Manske, *Theory of unconventional superconductors: cooper-pairing mediated by spin excitations*, Vol. 202 (Springer Science & Business Media, 2004).

[249] T. Siegrist, S. M. Zahurak, D. W. Murphy, and R. S. Roth, "The parent structure of the layered high-temperature superconductors," Nature **334**, 231 (1988).

[250] L. Hozoi, L. Siurakshina, P. Fulde, and J. Van Den Brink, "Ab initio determination of Cu $3d$ orbital energies in layered copper oxides," Scientific reports **1**, 65 (2011).

[251] I. B. Bersuker, *Electronic structure and properties of transition metal compounds* (John Wiley & Sons, 2010).

[252] Y. Li, S. Du, Z.-Y. Weng, and Z. Liu, "In-plane ordering of O vacancies in a high-T_c cuprate superconductor with compressed Cu-O octahedrons: a first-principles cluster expansion study," arXiv preprint arXiv:1909.08304 (2019).

[253] K. Liu, Z.-Y. Lu, and T. Xiang, "Electronic structures of quasi-one-dimensional cuprate superconductors $Ba_2CuO_{3+\delta}$," Physics Review Materials **3**, 044802 (2019).

[254] C. Le, K. Jiang, Y. Li, S. Qin, Z. Wang, F. Zhang, and J. Hu, "Electronic structure and superconductivity in unconventional cuprates π shift in $Ba_2CuO_{3+\delta}$," arXiv preprint arXiv:1909.12620 (2019).

[255] S. Toth and B. Lake, "Linear spin wave theory for single-Q incommensurate magnetic structures," Journal of Physics: Condensed Matter **27**, 166002 (2015).

[256] J. S. Griffith, *The theory of transition metal ions* (Cambridge University Press, Cambridge, 1971).

[257] A. S. Ovchinnikov, I. G. Bostrem, and V. E. Sinitsyn, "Cluster perturbation theory for spin Hamiltonians," Theoretical and Mathematical Physics **162**, 179 (2010).

[258] M. Brunner, F. Assaad, and A. Muramatsu, "Single hole dynamics in the one-dimensional - model," The European Physical Journal B **16**, 209 (2000).

[259] H. Suzuura and N. Nagaosa, "Spin-charge separation in angle-resolved photoemission spectra," Physical Review B **56**, 3548 (1997).

List of publications

1. M. Rossi, M. Retegan, C. Giacobbe, R. Fumagalli, A. Efimenko, T. Kulka, K. Wohlfeld, A. I. Gubanov, and M. Moretti Sala, “Possibility to realize spin-orbit induced correlated physics in iridium fluoride”, *Physical Review B* **95**, 235161 (2017);

2. Y. Y. Peng, R. Fumagalli, Y. Ding, M. Minola, S. Caprara, D. Betto, M. Bluschke, G. M. De Luca, K. Kummer, E. Lefranois, M. Salluzzo, H. Suzuki, M. Le Tacon, X. J. Zhou, N. B. Brookes, B. Keimer, L. Braicovich, M. Grilli and G. Ghiringhelli, “Re-entrant charge order in overdoped (Bi,Pb)$_{2.12}$Sr$_{1.88}$CuO$_{6+\delta}$”, *Nature Materials* **17**, 697 (2018);

3. Y. Y. Peng, E. W. Huang R. Fumagalli, M. Minola, Y. Wang, X. Sun, Y. Ding, K. Kummer, X. J. Zhou, N. B. Brookes, B. Moritz, L. Braicovich, T. P. Devereaux, and G. Ghiringhelli, “Dispersion, damping, and intensity of spin excitations in the monolayer (Bi,Pb)$_{2.12}$Sr$_{1.88}$CuO$_{6+\delta}$ cuprate superconductor family”, *Physical Review B* **98**, 144507 (2018);

4. M. Hepting, L. Chaix, E. W. Huang, R. Fumagalli, Y. Y. Peng, B. Moritz, K. Kummer, N. B. Brookes, W. C. Lee, M. Hashimoto, T. Sarkar, J.-F. He, C. R. Rotundu, Y. S. Lee, R. L. Greene, L. Braicovich, G. Ghiringhelli, Z. X. Shen, T. P. Devereaux, and W. S. Lee, “Three-dimensional collective charge excitations in electron-doped copper oxide superconductors cuprate superconductor family”, *Nature* **563**, 374 (2018);

5. H. Suzuki, M. Minola, Y. Lu, Y. Y. Peng, R. Fumagalli, E. Lefran-

cois, T. Loew, J. Porras, K. Kummer, D. Betto, S. Ishida, H. Eisaki, C. Hu, X. Zhou, M. W. Haverkort, N. B. Brookes, L. Braicovich, G. Ghiringhelli, M. Le Tacon and B. Keimer, “Probing the energy gap of high-temperature cuprate superconductors by resonant inelastic X-ray scattering”, *npj Quantum Materials* **3**, 65 (2018);

6. R. Fumagalli, L. Braicovich, M. Minola, Y. Y. Peng, K. Kummer, D. Betto, M. Rossi, E. Lefranois, C. Morawe, M. Salluzzo, H. Suzuki, F. Yakhou, M. Le Tacon, B. Keimer, N. B. Brookes, M. Moretti Sala, and G. Ghiringhelli, “Polarization-resolved Cu L_3-edge resonant intelastic X-ray scattering of orbital and spin excitations in NdBa$_2$Cu3O$_{7-\delta}$”, *Physical Review B* **99**, 134517 (2019) Editors suggestion;

7. M. Rossi, R. Arpaia, R. Fumagalli, M. Moretti Sala, D. Betto, G. M. De Luca, K. Kummer, J. Van Den Brink, M. Salluzzo, N. B. Brookes, L. Braicovich, and G. Ghiringhelli, “Experimental determination of momentum-resolved electron-phonon coupling”, *Physical Review Letters* **123**, 027001 (2019);X

8. H. Miao, R. Fumagalli, M. Rossi, J. Lorenzana, G. Seibold, F. Yakhou, K. Kummer, N. B. Brookes, G. D. Gu, L. Braicovich, G. Ghiringhelli, and M. P. M. Dean, “Formation of incommensurate charge density waves in cuprates”, *Pysical Review X* **9**, 031042 (2019);

9. M. Rossi, C. Henriquet, J. Jacobs, C. Donnerer, S. Boseggia, A. Al-Zein, R. Fumagalli, Y. Yao, J. G. Vale, E. C. Hunter, R. S. Perry, I. Kantor, G. Garbarino, W. Crichton, G. Monaco, D. F. McMorrow, M. Krisch, and M. Moretti Sala, “Resonant inelastic X-ray scattering of magnetic excitations under pressure”, *Journal of Synchrotron Radiation* **26**, 1725-1732 (2019);

10. R. Arpaia, S. Caprara, R. Fumagalli, G. De Vecchi, Y. Y. Peng, E. Andersson, D. Betto, G. M. De Luca, N. B. Brookes, F. Lombardi, M. Salluzzo, L. Braicovich, C. Di Castro, M. Grilli, and G. Ghiringhelli, “Dynamical charge density fluctuations pervading the phase diagram of a Cu-based high-T_c superconductor”, *Science* **365**, 6456 (2019);

11. G. Seibold, R. Arpaia, Y. Y. Peng, R. Fumagalli, L. Braicovich, C. Di Castro, M. Grilli, G. Ghiringhelli, and S. Caprara, “Marginal Fermi liquid behavior from charge density fluctuations in cuprates”, arXiv:1905.10232 (2019);

12. L. Braicovich, M. Rossi, R. Fumagalli, Y. Y. Peng, Y. Wang, R. Arpaia, D. Betto, G. M De Luca, D. Di Castro, K. Kummer, M. Moretti Sala, M. Pagetti, G. Balestrino, N. B. Brookes, M. Salluzzo, S. Johnston, J. van den Brink and G. Ghiringhelli, "Determining the electron-phonon coupling in superconducting cuprates by resonant inelastic X-ray scattering: methods and results on $Nd_{1+x}Ba_{2-x}Cu_3O_{7-\delta}$", arXiv:1906.01270 (2019);

13. R. Fumagalli, J. Heverhagen, D. Betto, R. Arpaia, M. Rossi, D. Di Castro, N.B. Brookes, M. Moretti Sala, M. Daghofer, L. Braicovich, K. Wohlfeld, and G. Ghiringhelli, "Mobile orbitons in Ca_2CuO_3: crucial role of the Hund's exchange", manuscript in preparation;

14. R. Fumagalli, M. Moretti Sala *et al.*, "The crystal and magnetic structure of $Ba_2CuO_{3+\delta}$ from X-ray absorption and resonant inelastic X-ray scattering", manuscript in preparation;

15. E. Andersson, R. Arpaia, M. Rossi, R. Fumagalli, E. Trabaldo, N. B. Brookes, L. Braicovich, G. Ghiringhelli, T. Bauch, and F. Lombardi, "Restoring the Planckian regime via suppression of charge order in underdoped ultrathin films of a cuprate superconductor", manuscript in preparation.